The University
Of
Sheffield.

Department
Of
Mechanical
Engineering.

Aerodynamics and Self-Starting of Vertical Axis Wind Turbines with J-Shaped Aerofoils

Yunus CELIK

A thesis submitted in partial fulfilment of the requirements for the degree of Doctor of Philosophy

The University of Sheffield
Energy2050
Faculty of Engineering
Department of Mechanical Engineering

June 2021

Dedicated to

My beloved son, Cinar Emre and my wife, Gonul.

Many of life's failures are people who did not realize how close they were to success when they gave up. - **Thomas Edison**

Acknowledgments

First of all, I would like to thank Allah (God) for giving me the strength and the patient without which thesis would never have been possible.

I will always be exceptionally grateful to my beloved wife (Gonul Celik), who left her career in Turkey and followed me on this journey in a completely different country. I would not be myself in my PhD without her continuous support and love. The most profound thanks must go to my family. Words cannot express how grateful I am to my father (Fehmi Celik), mother (Seval Celik), sister (Mislinur Celik) and all other family members. I would not have completed the PhD study without their support and prayer.

Last but not least, a special thank goes to my beloved son Cinar Emre, who is the best gift given by Allah. The thing that motivated me the most during this challenging time was to dream of hugging him again after a long period in which we were away from each other.

List of the publications

Journals:

Celik, Y., Ma, L., Ingham, D. and Pourkashanian, M., **2020**. "Aerodynamic investigation of the start-up process of H-type vertical axis wind turbines using CFD". *Journal of Wind Engineering and Industrial Aerodynamics*, *204*, p.104252.

Celik, Y., Ma, L., Ingham, D. and Pourkashanian, M., "Impact of the J-shaped aerofoil on the dynamic start-up behaviour of H-type vertical axis wind turbine". *Journal of Sustainable Energy Technologies and Assessments. (Under review)*

Future publications:

Celik, Y., Ma, L., Ingham, D. and Pourkashanian, M., **2020**. "Investigation on the aerodynamic characteristics of the J-shaped aerofoil considering the Darrieus motion and dynamic start-up behaviour".

Celik, Y., Ma, L., Ingham, D. and Pourkashanian, M., "Hybrid blade design to enhance the self-starting ability of the H-type VAWTs".

Conference:

Celik, Y. and Kaya, M.N., **2018**. "Numerical investigation of the starting behaviour of H-type Vertical Axis Wind Turbine with different airfoils". *International Conference on Innovative Engineering Applications, 938, Sivas, Turkey.*

Kaya, M.N. and **Celik, Y., 2018**. "Vertical Axis Wind Turbines for Turkey: Overview to Application Opportunities". *International Conference on Innovative Engineering Applications, 947, Sivas, Turkey.*

Posters:

Celik, Y., Ma, L., Ingham, D. and Pourkashanian, M., **2017**. "Self-starting Optimisation for SB-Vertical Axis Wind Turbine Blades". *Energy 2050 Symposium, Sheffield, South Yorkshire, United Kingdom.*

Celik, Y., Ma, L., Ingham, D. and Pourkashanian, M., **2019**. "Modelling and Investigating of Self-starting Behaviour of H-Type VAWT using CFD Method". *Mechanical Engineering Poster Day, University of Sheffield, Sheffield, South Yorkshire, United Kingdom.*

Celik, Y., Ma, L., Ingham, D. and Pourkashanian, M., **2020**. "Aerodynamic characteristics of the J-shaped aerofoil undergoing the Darrieus motion". *ETP 9th Annual Conference 2020, Glasgow, United Kingdom.*

Abstract

In light of the continuously increasing level of greenhouse gases, global warming has led to many investigations into the different types of renewable energy technologies, in particular wind turbines. The small-scale H-type Vertical Axis Wind Turbine (H-type VAWT) has been selected as the scope of this thesis due to its several significant advantages over the more commonly adopted Horizontal Axis Wind Turbines (HAWTs). However, the self-starting capability of these types of turbines is still one of the main challenging aspects and this limits their utilisation for the small-scale power generation. Unless the causes that prevent the turbine to self-start are understood sufficiently and designed to overcome the self-starting problem, they may be unsuitable for small-scale power generation. Hence, the present thesis aims to provide a detailed understanding of the self-starting behaviour of the small-scale H-type VAWTs and shed more light on the literature of the self-starting research by conducting a comprehensive analyse considering various design parameters.

The Computational Fluid Dynamics (CFD) simulations are utilised as a modelling approach after conducting the accuracy checks in order to obtain high fidelity analysis considering the reasonable accurate and computationally economic aspects. 2D-based turbine dynamic start-up simulations illustrate that not only lift force is required for the turbine to self-start but also the drag force contributes to the turbine torque generation at the critical turbine starting stage where the tip speed ratio (λ)<1. This finding encourages enhancing the positive contribution of the drag force by modifying the conventional aerofoil shape. In addition, the effect of the several physical properties, such as the moment of inertia, solidity, and the mechanical resistances on both the overall and the self-starting performance of the turbine is investigated.

In contrast with the conventional aerofoils, such as NACA0018, the resistive type, such as the J-shaped aerofoil, is investigated in detail to provide an in-depth understanding of the aerodynamic performance of these kinds of aerofoils considering the oscillating motion and whole turbine aspects. The investigation

of the J-shaped aerofoil under the oscillating motion, which is also a novel study for the J-shaped aerofoils, to highlight the advantages and disadvantages of the J-shaped aerofoils under the different operating conditions is found to assist in obtaining a further understanding of the aerodynamic characteristics of the J-shaped aerofoils when they are used in the turbine applications. In addition, the present work presents the first turbine time-varying start-up behaviour investigation for the turbine with the J-shaped aerofoils contrary to other studies in the literature. Even though the J-shaped profile increases the turbine performance in the upstream part of the turbine, increasing the opening length over the aerofoil surface causes a significant aerodynamic efficiency loss in the downstream part of the turbine, in particular when the turbine is rotating faster. Therefore, the utilisation of the optimum J-shaped profile is found to be of utmost importance not only to optimise turbine self-starting performance but also to maintain the performance efficiency at higher rotational speeds.

Furthermore, this thesis proposed a novel hybrid blade design for the first time, which combines a conventional aerofoil NACA0018 and its cutting-off counterpart J-shaped aerofoil, to enhance the torque generation at the starting of the turbine with low tip speed ratio λ values, on the other hand, minimise the efficiency loss at the high λ values. Although the utilisation of the J-shaped aerofoil in the turbine configurations illustrates an increase in the torque generation at the low λ values compared to the conventional aerofoils, a hybrid blade configuration that allows using the J-shaped profile in some portion of the blade span is required to reduce the significant performance loss at high λ values due to the inherent shape of the J-shaped aerofoil. For this purpose, the 3D-based CFD simulations have been conducted for the different configurations of the hybrid blades with the various opening length percentage of the J-shaped aerofoil used. In contrast with the losses due to the J-shaped aerofoils, the hybrid blade designs, especially a design with the closed-tip, is found to be an appropriate selection in terms of a faster start-up time and a higher final rotational speed when the turbine reaches its steady-state conditions.

Declaration of authorship

I declare that all the work presented in this thesis is my own effort. This work has not been submitted for any other award or degree at the University of Sheffield or any other university or institution. Where other sourced used in the present thesis has been acknowledged.

Signed by:

Yunus Celik

Table of Contents

List of Figures

xiii

List of Tables

Symbols and Abbreviations

Symbols (Greek letters)

α	Angle of attack [°]
α_1	Angle of attack with pitching angle [°]
$\dot{\alpha}$	Pitch rate [rad/s]
β	Blade pitch angle [°]
ρ	Air density [kg/m^3]
μ	Dynamic air viscosity [Pa.s]
v	Air volume [m^3]
λ	Tip speed ratio
ω	Rotational speed of the turbine [rad/s]
θ	Azimuthal angle [°]
σ	Solidity
τ	Non-dimensional time constant
Δt	Time step size [s]

Symbols (Latin letters)

a	Axial flow induction factor
A	Turbine swept area ($A=H{\times}D$) [m^2]
c	Blade chord length [m]
C_p	Power coefficient
C_{pr}	Pressure coefficient
C_l	Lift coefficient
C_d	Drag coefficient
C_t	Torque coefficient
C_m	Moment coefficient
C_c	Chordwise force coefficient
C_{fr}	Bearing frictional coefficient
C_μ	Empirical constant
D	Diameter of the turbine [m]
E	Kinetic Energy [J]
F_t	Tangential force component [N]
F_n	Normal force component [N]

F_l	Lift force [N]
F_d	Drag force [N]
H	Height of the turbine blade [m]
I	Turbine moment of inertia [kgm^2]
k	Reduced frequency
l_t	Turbulent length scale
m	Mass [kg]
$\dot{m}$	Mass flow rate
N	Number of blades
P	Power [W]
R	Radius of the turbine [m]
Re	Reynolds number
$Re_{\theta t}$	Momentum thickness Reynolds number
t	Time [s]
T	Torque [N.m]
T_w	Wind torque [N.m]
T_g	Generator torque [N.m]
T_f	Bearing frictional torque [N.m]
T_{res}	Resistive torque [N.m]
V_a	Actuator velocity [m/s]
V_b	Blade velocity [m/s]
V_D	Downstream wind velocity [m/s]
V_{rel}	Relative resultant flow velocity [m/s]
V_w	Wake velocity [m/s]
V_x	X-velocity [m/s]
V_∞	Free stream wind velocity [m/s]
w_z	Z-vorticity
y^+	Dimensionless wall distance

Abbreviations

2D	Two Dimensional
3D	Three Dimensional
6DOF	Six-Degree of Freedom
BEM	Blade Element Momentum model

CFD	Computational Fluid Dynamics
CFL	Courant Number
DES	Detached Eddy Simulation
DMST	Double Multiple Streamtube Model
DNS	Direct Numerical Simulation
FEM	Finite Element Method
FDM	Finite Difference Method
FVM	Finite Volume Method
GCI	Grid Convergence Index
HAWT	Horizontal Axis Wind Turbine
HPC	High-Performance Computing
LE	Leading Edge of an aerofoil
LES	Large Eddy Simulation
LEV	Leading Edge Vortex
NACA	National Advisory Committee for Aeronautics
NFL	Natural Laminar Flow
OLP	Opening Length Percentage
OR	Opening Ratio over the J-shaped aerofoil
PIV	Particle Image Velocity
RANS	Reynold Average Navier-Stokes equations
RNG	Renormalization Group turbulence model
RPM	Revolutions per minute
S–A	Spalart–Allmaras turbulence model
SST	Shear Stress Transport
TE	Trailing Edge of an aerofoil
UDF	User-defined Function
VAWT	Vertical Axis Wind Turbine
VTM	Vorticity Transport Model

Chapter 1

Introduction

1.1 The environment and wind energy

A general consensus has been made in the recent years that as a result of human activities, such as the burning of fossil fuels, the greenhouse gases in the atmosphere have been increasing, and this causes climate change [1]. Changing the climate has become one of the most important problems and the foremost pressing environmental threats to the world. For this purpose, there has been an urgent need to minimize emissions by using alternative technologies, which are able to extract the energy from the atmosphere while being non-polluting and sustainable. Several alternative sources to fossil fuels can be categorised as wind energy, solar energy, hydrogen energy, biomass and hydro [2]. These are known as 'renewable energy sources' and have been attracting significant research attention in the last few decades. Renewable energy offers our planet a chance to decrease carbon emissions, make the environment cleaner, and put our

civilisation on a more sustainable footing [3]. Among the renewable energy sources, wind energy usage has grown rapidly and will play an increasingly crucial role in the future economy.

The wind is everywhere and as long as the Earth continues to provide the appropriate conditions, it will continue that way. The air moves from the regions of the high pressure to the regions of the low pressure, which results in wind generation. Due to the mass of air that moves, it contains energy. The wind turbines are commonly employed to convert this energy into the electricity but only a limited portion of the world's electricity is produced by wind. Nevertheless, the need for wind energy has been increasing due to the rapid depletion of fossil fuels.

In 2019, the global new wind power installation's output surpassed 60GW with a 19% increment from the previous year's capacity and thus bringing the total installed capacity to 650GW [4]. Although the Asia Pacific continues to lead in global wind power development, accounting for 50.7% of the global new installations last year, the European countries, such as the United Kingdom and Spain also play a significant role in the wind power installation. Furthermore, it has been expected that over 355 GW of new capacity will be added and that is nearly 71 GW of new installations each year until 2024 [4].

1.2 Types of wind turbines

In order to use the potential of the wind, wind turbines are generally employed. A wind turbine is a device that converts the wind energy into mechanical energy by using blades and a shaft. By using a generator, this form of energy is converted into electricity. There are mainly two types of wind turbines, namely horizontal axis wind turbines (HAWTs) and vertical axis wind turbines (VAWTs). In addition, VAWTs have two different types. One is the Savonius rotor, which is a drag-based turbine, and the second is the Darrieus rotor, which is a lift-based turbine. At present, HAWTs are commonly used and they currently dominate the field of large-scale wind power generation both on land and in the

sea due to their high power coefficient compared to VAWTs. Nevertheless, the disadvantages of HAWTs include the requirement of a yaw mechanism to turn the rotor towards the wind, poor performance in urban regions where the flow is highly unsteady and difficult maintenance [5].

With respect to the Vertical Axis Wind Turbines, although many studies on VAWTs have been performed from the late 1970s to the early 1980s, it can be observed that the recent studies and works on VAWTs are not as numerous as those studying HAWTs, essentially due to the higher efficiency of HAWTs. As a matter of fact, VAWTs also have their advantages. First and foremost, VAWTs can generate power independently of the wind direction and therefore, there is no need to use a yaw control device for the VAWTs [6].

Even though vertical axis wind turbines are the main scope of the present thesis, the advantages and disadvantages of both types of wind turbines will be discussed in detail in the following sections.

1.2.1   Horizontal Axis Wind Turbines

One of the most popular wind turbines is the HAWT that is widely utilised for electricity generation. HAWTs are generally employed to the major wind farms around the world in order to provide sufficient electricity generation for the small towns, large cities, and the national grids.

The blades of a HAWT work to extract energy from the linear motion of the wind by generating lift, then leading to the torque generation that drives the generator. In order to achieve this process, in particular for large HAWTs, active pitch control systems can be utilised to make sure that each blade is placed to continue providing an optimal angle of attack to extract as much power as possible from the wind for a particular wind speed.

However, there are many disadvantages of HAWT. These turbines are usually very tall in order to operate in a relatively uniform wind and this makes turbine maintenance very difficult. Due to HAWTs consisting of many complex parts,

such as the control system, and they require more moving parts, the installation process takes much more time than that for a VAWT [7]. Moreover, a HAWT needs a yaw control system to readjust the rotor to the wind direction. These make the system more expensive and they have a complex design for the tower than do VAWTs. A typical horizontal wind turbine is shown in Figure 1.1.
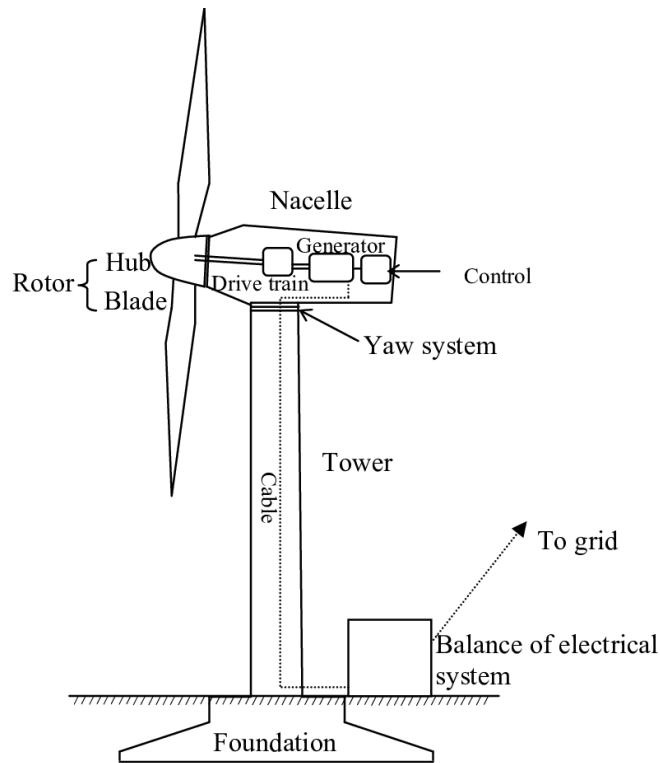
Figure 1.1. A typical horizontal axis wind turbine (HAWT) and its components [8].

1.2.2   Vertical Axis Wind Turbines

Vertical Axis Wind Turbines (VAWTs) have been gaining much attention due to the fact that the interest in green energy solutions has been increasing. The companies all over the world have been marketing these devices, in particular for the stand-alone applications. VAWTs target individual homes, small businesses, farms as a way of providing local, personal wind energy and offshore applications.

The axis of rotation of VAWT is perpendicular to the wind direction, and they can receive the wind from any direction. This characteristic of them can eliminate the complicated yaw control mechanism that occurs in HAWTs.

One of the most well-known lift-driven Vertical Axis Wind Turbines (VAWTs) is the Darrieus turbine, which was patented by Georges Jean Marie Darrieus, a French aeronautical engineer in 1931, (see Figure 1.2 (a) and (b)) [9]. The Darrieus type VAWT composed of a set of vertically oriented blades connected to the main rotor shaft and is characterised by its C-shape and H-shape rotor blades. They are generally constructed with two or three blades and according to experimental result [10], lift-driven Darrieus machines is able to produce a maximum power coefficient of about 0.4.

(a) C-type Darrieus   (b) H-type Darrieus   (c) Savonius
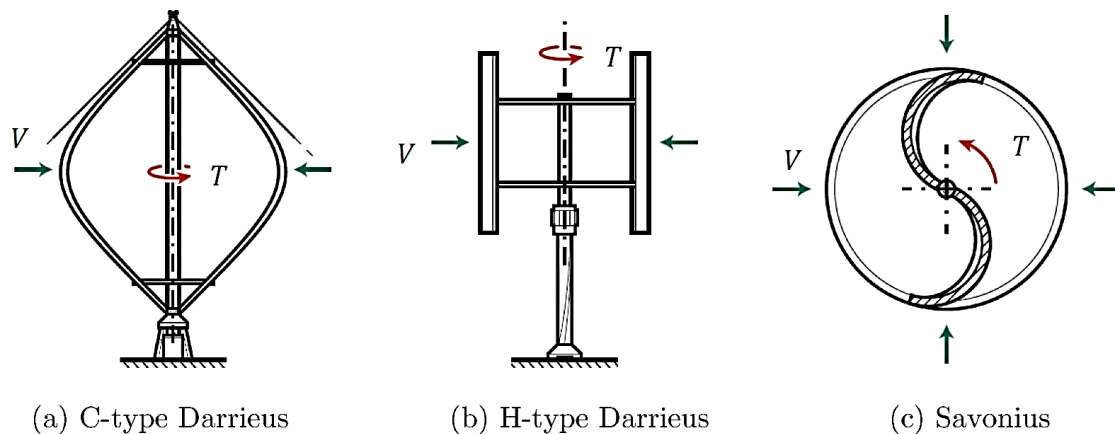
Figure 1.2. (a) and (b) Schematics of lift-driven Darrieus wind turbines, and (c) Drag-driven Savonius VAWT [9].

Previous studies have claimed that the Darrieus machines develop little or no torque at low speed conditions and are not able to self-start [11, 12] which shows that motors are required to 'start it up', thus making the machine inefficient and unsuitable for stand-alone operation. In contrast, other studies have illustrated that, based on a careful aerofoil selection, three-bladed SB-VAWTs have the capability to self-start [13, 14].

Due to this conflicting data and conclusions in the literature with regard to the self-starting capability of the H-type Darrieus wind turbine, one of the aims of this thesis is to improve the understanding of the self-starting process and set a basis for future analysis and optimisation.

1.2.3 Advantages and disadvantages of VAWTs over HAWTs

Even though it is believed that HAWTs are better than VAWTs in terms of maximum efficiency when compared on the same scale, the research interests on VAWTs have been increasing in recent times due to the inherent advantages that the VAWTs have over the HAWTs. As a summary, the advantages of the H-type VAWT over the commonly utilised HAWT, especially when used in the built environment, are as follows:

- VAWTs do not need a complex yaw mechanism since they rotate in a plane parallel to the wind direction and the blades are attached to the rotor at equally spaced angles of 120° for the three-bladed machines [15].
- Optimal blades for VAWTs are simple in design, being an aerofoil of constant shape along its span without any twist or taper. This simplicity makes the blades relatively easy to manufacture by fabrication [16].
- Aerodynamic noise from the VAWTs is lower than HAWTs due to the lower tip speed ratio. HAWTs can achieve their maximum power at higher tip speed ratios and so produce a loud noise. As the number of wind turbine numbers increases, the noise level is emerging as one of the main objections to onshore wind farms and so this aspect is very important [17].
- Compared to the HAWTs, according to the studies [18, 19], the VAWTs can be installed closer to each other, which results in a considerable increase in the power density per square meter.
- Under the complex urban wind conditions, VAWTs can achieve a better performance. In this urban wind environment, the wind speed is low and unsteady with high levels of turbulence [20]. This makes the VAWTs more

suitable in regions where tall devices are prohibited by the planning permission and law.

On the other hand, VAWTs also have some drawbacks compared to HAWTs:

- Due to the changing azimuthal angle and angle of attack during the rotation, the flow around the turbine is highly unsteady. The turbine blades will experience all possible angles of attack during the operation and so this makes the aerodynamic predictions more complex, which are already not fully understood [16].

- Darrieus VAWTs may fail to self-start even under no-load conditions, depending on the types of aerofoils used, the upstream wind speed and turbine solidity. On the other hand, the HAWTs are able to self-start under no-load conditions [17].

It is postulated that the main problems and some of the drawbacks of the VAWTs can be overcome with the careful research and utilization of the optimized aerofoil sections.

1.3   Kinematics of vertical axis wind turbine (VAWT)

Although analysing the H-type VAWT is difficult due to complicated rotor aerodynamics, a simplified kinematic approach in 2D is able to clarify its behaviour and identify the governing parameters. Therefore, this section assists one to understand the basic 2D aerodynamics of the H-type VAWTs.

The aerodynamics of the turbines are dependent on the kinematics and, the kinematics of the turbine affects the overall performance of the turbine and the flow physics. Therefore, aerodynamics is very important in the understanding of the fluid dynamics in the study of wind turbines. In this case, the fluid is air, and it contains kinetic energy. The main purpose of the wind turbine is to convert this kinetic energy into other forms of energy, such as electrical or mechanical energy. In order to calculate the available kinetic energy in the wind, the following equation is used:

$$Energy\ (E) = \frac{1}{2}\rho v V_\infty^2 \qquad (1.1)$$

and the power available in the wind is given by:

$$Power\ (P) = \frac{1}{2}\rho A V_\infty^3 \qquad (1.2)$$

where ρ is the air density, v is the air volume, V_∞ is the free stream wind velocity and A is the swept area.

As can be seen clearly from these equations, the wind velocity, the air density, and the area of the rotor affect the wind energy and wind power. However, there are other factors, which indirectly affect wind energy, such as air temperature, air pressure, etc.

Even though the wind contains kinetic energy, the wind turbines cannot transform all of this kinetic energy into the electrical energy. The ratio of the power extracted by the wind turbine to the total energy available in the wind is defined as the coefficient of power (C_p) [21],

$$C_p = \frac{Power\ extracted\ by\ the\ wind\ turbine}{Total\ power\ available\ in\ the\ wind\ (\frac{1}{2}\rho A V_\infty^3)} \qquad (1.3)$$

It is important to note that there are many factors that affect the power coefficient. In order to improve the power coefficient of a turbine, which is also known as the efficiency of the turbine, generally, a good optimisation of some of the design parameters, such as the blade geometry, the number of blades, and blade arrangements can be carried out.

The aerodynamic performances are based on the design parameters, such as the chord length, aspect ratio, solidity, etc. and scientists and engineers have been attempting to improve the turbine design as well as the blade design in order to maximize the power extraction from the wind. The most influential design parameters are explained in Section 2.2.

As the blades rotate, the aerodynamic forces of lift (F_l) and drag (F_d) are generated, which can change depending on the azimuthal position of the blade and the tip speed ratio. As can be seen from Figure 1.3, the aerodynamic forces can be obtained by resolving the normal force component (F_n), which plays an important role when considering the structure of the turbine, and the tangential force component (F_t), which is the creating torque (T) can be expressed as follows:

$$T = F_t R \tag{1.4}$$

$$F_n = F_l cos\alpha + F_d sin\alpha \tag{1.5}$$

$$F_t = F_l sin\alpha - F_d cos\alpha \tag{1.6}$$

In addition, the tangential force acting on the turbine blades can be calculated as follows:

$$Tangential\ Force\ (F_t) = \frac{1}{2}\rho A V_\infty^2 C_t \tag{1.7}$$

and the theoretical torque:

$$Torque\ (T) = \frac{1}{2}\rho A V_\infty^2 C_t R \tag{1.8}$$

where N is the number of the blades, A is the swept area, C_t is the torque coefficient and R is the radius of the turbine.

The torque coefficient is another important parameter and it is the ratio of the torque generated by the turbine and the theoretical torque as follows:

$$Torque\ Coefficient\ (C_t) = \frac{T}{\frac{1}{2}\rho A V_\infty^2 R} \tag{1.9}$$

where T is the torque.

The ratio of the blade wind velocity and the free stream wind velocity is one of the most influential parameters that affects the turbine overall performance and this ratio is commonly referred to as the tip speed ratio (λ). Most of the undisturbed wind will pass through the gaps between the blades when the turbine turns slowly, which results in a small amount of power extraction. On the contrary, when the turbine turns too fast, the turbine blades act as a solid wall and they obstruct the wind flow, and again the power extraction will be decreased. Therefore, to extract as much as possible power from the wind, the wind turbines should be designed to operate at their optimum tip speed ratio [22]. The tip speed ratio is defined as follows:

$$\lambda = \frac{V_b}{V_\infty} = \frac{\omega R}{V_\infty} \tag{1.10}$$

where V_b is the blade wind speed, ω is the rotational speed of the turbine.

From the equations (1.3) and (1.9), we can also express the relationship between the power coefficient and the torque coefficient as follows:

$$\lambda = \frac{C_p}{C_t} \tag{1.11}$$

As the turbine rotates, the Reynolds number varies depending on the turbine rotational speed. However, considering the rotationally-averaged Reynolds number allows a simple comparison between the VAWTs. The Reynolds number is defined as follows:

$$Re = \frac{\rho V_b c}{\mu} \tag{1.12}$$

where ρ is the air density, c is the chord length of the blade and μ is the dynamic air viscosity.

The blades experience large and rapid changes in the angle of attack (α) while the turbine rotates. As the blade travels around in a circle, α changes depending on the changes in both the azimuthal angle (θ) and the tip speed ratio (λ). Figure

1.3 illustrates the velocities and aerodynamic forces that act on the blades of the H-type VAWT.
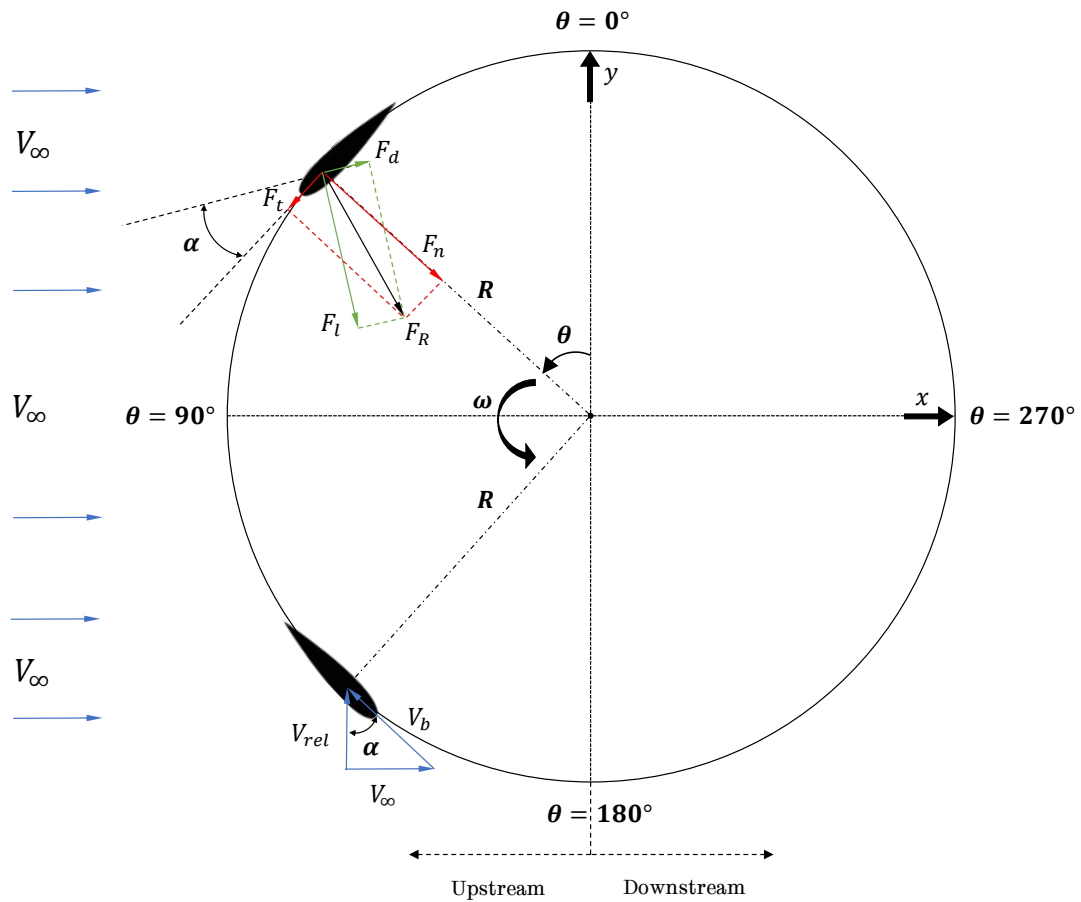
Figure 1.3. Schematic diagram of the velocity and force vectors for a constant rotational turbine speed (ω).

In the schematic diagram, V_∞ is the free upstream wind, V_b is the blade velocity and V_{rel} is the relative resultant flow velocity.

It is usual to define an axial flow induction factor 'a' which is the fractional decrease in velocity between the free stream and the turbine [23] as follows:

$$a = (V_\infty - V_D)/V_\infty \tag{1.13}$$

where V_D is the downstream wind velocity.

With the assumption of the induction factor as zero, based on the schematic diagram of the velocity components illustrated in Figure 1.3, the instantaneous relative wind speed V_{rel} and the geometrical angle of attack (α) can be derived as follows, respectively;

$$V_{rel} = V_\infty \times \sqrt{\lambda^2 + 2\lambda cos\theta + 1} \qquad (1.14)$$

$$\alpha = tan^{-1} \frac{sin\theta}{\lambda + cos\theta} \qquad (1.15)$$

Figure 1.4 illustrates the variation of the ratio of the relative wind speed to the free stream wind speed and the geometrical angle of attack versus azimuthal angle with changes in tip speed ratio (λ). The figure shows that the tip speed ratio plays an important role in the aerodynamics and performance of the H-type VAWT. The tip speed ratio affects the H-type VAWT aerodynamics and performance by determining the angle of attack and the relative velocity of the air to the turbine blades. In order to illustrate the effect of λ on the variations of the angle of attack and relative velocity, three different λ values namely λ=1.5, 2.5, and 3.5, which allow an apparent comparison, have been selected. Based on the geometrical angle of attack, the variation of the maximum and minimum angle of attack is low at a high tip speed ratio and it increases accordingly with the decrease in the tip speed ratio (see Figure 1.4 (a)). Furthermore, at the start (when $\alpha = 0°$), the maximum value of the relative wind speed can be obtained and the relative wind speed reaches the minimum value at 180° azimuthal angle (see Figure 1.4 (b)). At the same time, the figure illustrates that when the tip speed ratio increases, the ratio of the relative wind speed to the free stream increases. These variations of the relative wind speed and the angle of attack as a function of the azimuthal angle for the tip speed ratio investigated can influence positively and negatively on the aerodynamic forces and the blade stall of an H-type VAWT.
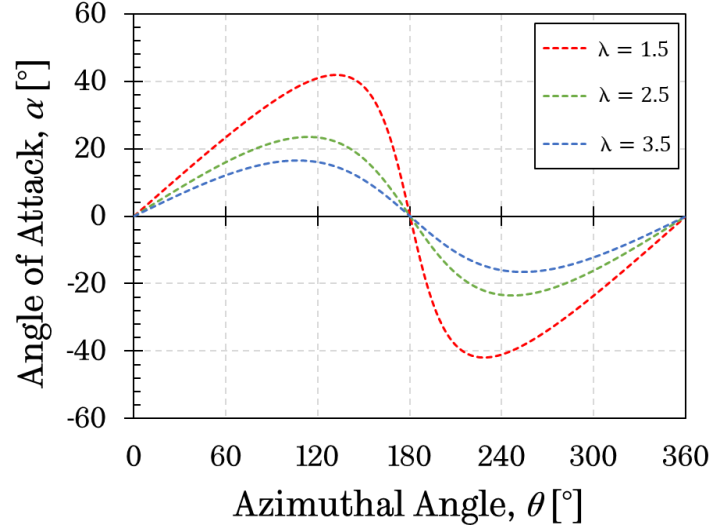
(a)
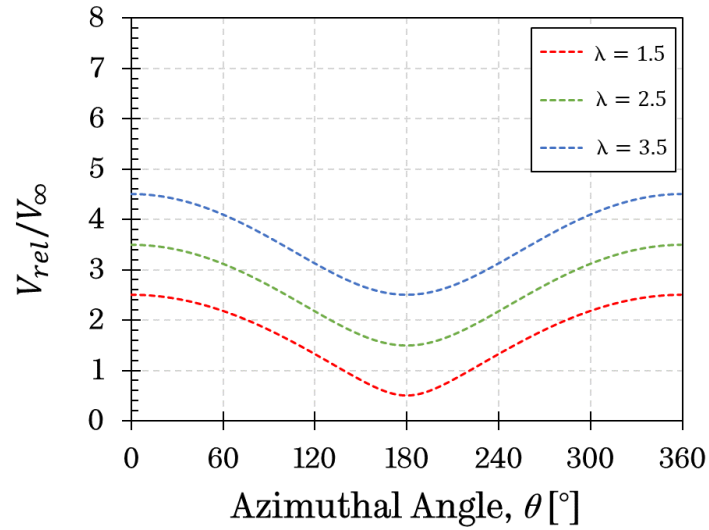
(b)

Figure 1.4. Variation of (a) the ratio of the relative wind speed to the free stream wind speed and (b) the angle of attack as a function of azimuthal angle for λ = 1.5, 2.5 and 3.5.

From the above summary and simplified kinematic description of the H-type VAWTs, several basic observations can be made briefly:

- The power coefficient (C_p) plays an important role in designing a wind turbine. Therefore, in order to improve the C_p, a good optimisation of some design parameters, such as the number of blades, blade geometry, etc. must be employed.

- In order to compare different VAWTs at different operating conditions then, in general, the relative wind speed can be used, instead of using the upstream wind speed.

- As the blade travels through a circle, the angle of attack depends on the changes in azimuthal angle (θ) and tip speed ratio (λ).

- From the turbine performance, F_n only has a contribution when considering the structure of the turbine and so it is not the major interest of the present thesis. Nevertheless, at the small tip speed ratios, F_n can be higher than F_t [16] and because of this, both forces must be considered during the design procedure.

The simple analyses of the kinematics of the H-type VAWTs have been explained above. According to this, the rotor effect on the freestream wind has not been taken into account. However, the presence of the rotor in the freestream affects the actual wind velocity that is experienced by the blades, especially for the downstream part of the turbine where the flow velocity magnitude can be lower than that of in the upstream due to the power extraction in the upstream part of the turbine. Additionally, due to the vortex shedding from the blades in the upstream region and the turbulent wake from the shaft, the effective angle of attack might be different to that predicted in the above simplified analyses, and this results in the possibility of the machine performance varying relative to the predicted results.

1.4 Aims and objectives of the study

Among all the wind technologies, the H-type VAWTs provide a promising future in the energy field and more benefit for small-scale applications in the urban regions. However, one of the most challenging aspects of this type of energy conversion systems is the ability to self-start. Since limited numbers of researchers have focused on this issue, there exists a large knowledge gap in the understanding of the aerodynamics and self-starting performance of VAWTs. Therefore, the current thesis is motivated at providing an in-depth understanding and enhancing the knowledge of how an H-type VAWT can gain

self-starting characteristics by a detailed investigation of the start-up process, aerodynamically.

Although the present literature also shows that the utilization of the different types of an aerofoil in the H-type VAWT can significantly affect the turbine performance, in particular at the low tip speed ratio regions, very limited studies have been conducted to investigate the effect of the resistive type aerofoils, such as a J-shaped profile, considering the oscillating motion and whole turbine simulations. Therefore, it is one of the aims of the current work to fill some of the gaps in the literature and provide a considerably improved knowledge of the aerodynamics of the J-shaped profile. However, the critical linking of the performance and aerodynamics is also the key point that will provide an in-depth understanding of the characteristics of the J-shaped aerofoils. In addition, the current thesis is extended to design an H-type VAWT with the novel hybrid blade profile with the aim of enhancing the self-starting and power efficiency simultaneously.

These aims will be achieved through the fulfilment of the following specific objectives:

- Development of the numerically-verified 2D and 3D CFD models with own user-defined function for the full turbine and single aerofoil analyses, which accurately allows the comparison with the available experimental data.

- An in-depth aerodynamic investigation on the turbine self-starting process considering its critical stages to provide substantial knowledge of the self-starting characteristics.

- Quantitative and qualitative analyses of the aerodynamic performance of the J-shaped aerofoil in a comparison with its counterpart-aerofoil profile under the dynamic and static conditions.

- Investigation of the J-shaped profiles with different configurations on both the turbine overall and self-starting performance considering different design parameters by underlining their advantages and disadvantages.

- Proposing a design methodology will assist to predict the performance of the turbine with the novel hybrid blade designs in comparison with the conventional and J-shaped aerofoils.

- Comparative analysis of the proposed hybrid blade design with different blade configurations when taking into consideration both the dynamic start-up behaviour and the power performance at low and high tip speed conditions.

1.5 Thesis outline

The thesis is divided into three major parts, namely the introduction, literature review, and the novel research.

The introduction part, presented in Chapter 1, introduces the thesis and addresses the need for the renewable energy sources and emphasises the wind energy, the various types of the wind turbines, comparison between the Vertical Axis Wind Turbines (VAWTs) and the Horizontal Axis Wind Turbines (HAWTs) by discussing their advantages and disadvantages. In addition, a simplified kinematics approach for the H-type VAWT in 2D, which assists us to better understand its aerodynamic behaviour and identify the governing parameters. Finally, the aims and objectives of the present study are also introduced here.

Chapter 2 presents a literature review related to the VAWTs, including a review of the performance parameters that affect the turbine overall performance and its self-starting characteristics. Furthermore, this chapter also includes a detailed review of the self-starting issue of the H-type VAWT and a discussion on the possible solution strategies to improve the self-starting performance.

Different numerical modelling techniques that can be employed to predict the performance of the H-type VAWTs are discussed in Chapter 3 where the advantages and disadvantages of each numerical model are explained. Apart from the numerical modelling, the various turbulence models are also critically evaluated to select the most appropriate models for the H-type VAWT applications.

In Chapter 4, a 2D Computational Fluid Dynamic (CFD) start-up model has been built with new user-defined function (UDF) after conducting sensitivity studies, such as domain size, time step size, and the number of nodes around the aerofoil to obtain an accurate CFD model. Once an accurate model has been obtained, the output results have been compared with the experimental data in order to observe their capability in predicting the turbine performance, such as the aerodynamic force coefficients and self-starting behaviour.

In Chapter 5, with the validated 2D CFD model, a detailed aerodynamic investigation of the start-up process of the H-type VAWT is performed. Furthermore, the contributions of the aerodynamic lift and drag of the turbine blade at various azimuthal positions to the turbine starting up are investigated. Then, the effects of the several physical properties, such as the inertia of the blades, the number of blades, the chord length, and the mechanical resistance on its dynamic self-starting behaviour and power performance are evaluated by using the dynamic start-up model instead of employing several constant rotational speeds of the turbine.

In Chapter 6, a detailed investigation of the aerodynamic behaviour of the J-shaped aerofoil with several opening ratios in comparison with conventional aerofoil NACA0018 under the dynamic and static conditions is presented. Additionally, the development of the CFD-based numerical model for the oscillating and static conditions is presented and validated against experimental studies, respectively. Furthermore, the quantitative (flow visualisation) and the qualitative (aerodynamic force coefficients, such as lift, drag and chordwise) are presented to compare the aerodynamic performance of the J-shaped aerofoil in a comparison with the conventional aerofoil. The overall aim of this chapter is to shed much light on the advantages and disadvantages of the J-shaped aerofoil from an aerodynamic point of view when it is used in the turbine applications.

In Chapter 7, the impact of the J-shaped aerofoil with the different values of the opening ratio on the dynamic start-up behaviour of the H-type VAWT has been investigated considering the different performance parameters. This

chapter also provides a comparison of the contributions of the J-shaped aerofoil and its conventional profile to the starting torque generation when the turbine is stationary at different starting positions.

In Chapter 8, the hybrid blade design methodology has been proposed here and depending on this methodology, the performance of the different hybrid blade designs have been proposed and investigated in terms of the overall and self-starting point of view. A 3D CFD start-up model has been built with own user-defined function after conducting the mesh independence analysis and compared with the 2D CFD start-up model that has been built in Chapter 4 and the experimental data.

All the major findings gained from the investigations are summarised in Chapter 9. Following this, the recommendations of the topics requiring future work are also presented.

Chapter 2

Literature review

2.1 Introduction

Research interest on the Vertical Axis Wind Turbines (VAWTs) has been increasing compared to the Horizontal Axis Wind Turbines (HAWTs) due to several inherent advantages of the VAWTs, such as suitable for being installed in the urban regions, and this chapter reviews the relevant literature pertaining to the study of VAWTs in this thesis. The main topics reviewed in this chapter are the performance parameters, such as solidity, types of the aerofoil, blade pitching, and dynamic stall, that affect the overall efficiency and the self-starting behaviour of H-type VAWTs. In addition, the possible solution strategies to enhance the self-starting performance of the H-type VAWT as well as previous studies on self-starting have been discussed. Furthermore, a critical discussion of the previous studies on the J-shaped aerofoils is presented. This chapter also

explains the motivations behind this research and indicates the knowledge gaps in the literature.

2.2 The H-type VAWT performance and the self-starting assessment parameters

It is generally believed that the Darrieus type of wind turbines are not reliable to self-start due to weak or negative torque generation at the low tip speed ratios. Figure 2.1 illustrates the negative torque region generated, which is often called a dead band, in the turbine performance curve. The reason for this generated negative torque is a result of the large angle of attack variations encountered at the low tip speed ratios. In this circumstance, the majority of the portion of the angle of attacks exceeds the stall angle and consequently, the turbine blades experience significant stall. When the blades stall, a considerable amount of the negative torque, which prevents the turbine to accelerate to the higher tip speed ratios, is generated due to both the decreasing in the lift force and the increasing in the drag force. Therefore, in the present thesis, an in-depth understanding of the self-starting behaviour of the H-type VAWT and the circumstances that cause the turbine not to self-start will be provided.
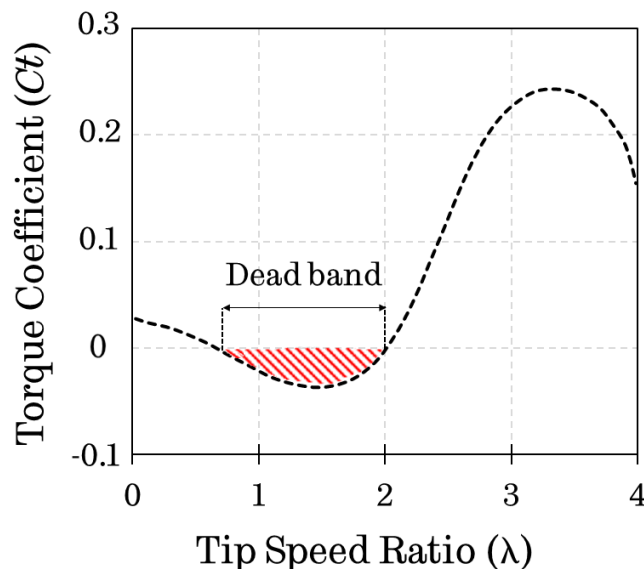
Figure 2.1. An illustration of the dead band region in the torque coefficient curve.

In order to evaluate the performance and the self-starting behaviour of an H-type VAWT, many design parameters, which have a significant influence on the turbine, should be carefully investigated and thoroughly understood. However, this process is not easy and straight forward due to each variable having more than one effect on the performance of the turbine. Nevertheless, the efforts in understanding the individual effects of each of the parameters have been numerous and a summary of these parameters is presented in this section.

The purpose of this section is to review the current state of the understanding of the main assessment parameters that may play an important role in the overall performance and self-starting behaviour of the H-type VAWTs based on studies from the literature.

2.2.1 Turbine solidity

Solidity is one of the most influential parameters that affects the turbine performance and the torque coefficient variation with the tip speed ratio (λ) and the maximum efficiency. The solidity of the H-type VAWT is determined as a ratio between the area of the blades and the turbine swept area, $\sigma = \frac{Nc}{2R}$. However, this definition appears to be less common in the literature, therefore, the generally adopted definition of the solidity is used in the present thesis as follows [16]:

$$\sigma = \frac{Nc}{R} \tag{2.1}$$

where N is the number of blades, c is the chord length and R is the radius of the turbine.

Increasing the solidity results in a greater blockage of the flow and this may cause a change in the effective incoming flow velocities and the variation in the blade angle of attack. As a result of the greater blockage, the tip speed ratio at which the blades stall decreases to a lower tip speed ratio values due to the lower angles of attack in the upstream part of the turbine. Thus, the turbine rotation

becomes slower and the maximum power coefficient obtained moves to the lower tip speed ratio values. However, the continued decrease in the angle of attack as the tip speed ratio increases causes the reduction in the aerodynamic torque generation of the high solidity turbines compared to the low solidity turbines at the higher tip speed ratios. Furthermore, the performance of high solidity turbines drops away quickly either side of the optimum tip speed ratio while the power coefficient to tip speed ratio curve is flatter for low solidity turbines. On the other hand, increasing the turbine solidity may also help the turbine to increase the torque output at the low tip speed ratios, which is beneficial for the self-starting ability. The low solidity means that the blade has a smaller area interface with the incoming wind and therefore it should depend on the high tip speed ratio to cover the same swept area, thus generating a smaller torque. On the contrary, a turbine with a higher solidity operates at low tip speed ratios and produces more torque. Therefore, the machines that require a high starting torque output, such as H-type VAWTs, may be required to have high solidity.

Templin [24] appears to be the first author in the literature who investigated the VAWT solidity. He developed a computational programme, which was based on the single stream tube model, in order to investigate the influence of the blade solidity on the turbine performance considering the range of the solidity 0.005 to 0.5. Furthermore, the effects of the high solidity on the vertical axis windmills performance have been studied by Mays and Holmes [25] using a momentum model. These two study results were compiled and compared by Kirke [21], which is shown in Figure 2.2.
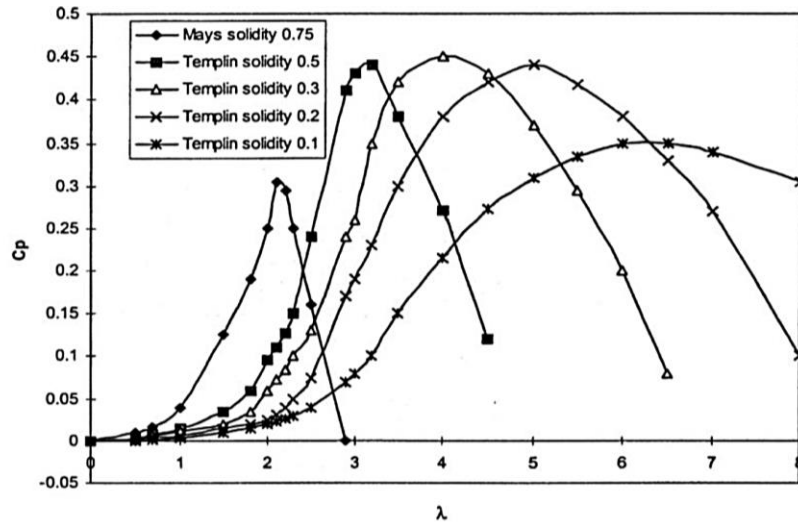
Figure 2.2. Variation of the power coefficient as a function of the tip speed ratio for various values of the solidities from the study by Kirke [21].

As can be seen in Eq. 2.1, one way of changing the solidity is to vary the number of blades (*N*) while keeping the chord and radius constant. In this way, the curvature and blade Reynolds number remain the same for each case. Consul et al. [26] conducted a set of 2D CFD based numerical analyses for the turbine with two and four blades using the NACA0015 aerofoil profile. The solidities employed in this study were $\sigma = 0.019$ and $\sigma = 0.038$. As can be seen in Figure 2.3, when the number of blades was increased from two to four, an increment in the peak power coefficient from 0.43 to 0.53 has been observed. Therefore, the entire performance of the testing with a higher solidity turbine is shifted to lower values of λ, hence obtaining the maximum power coefficient at λ=4 while the smaller solidity turbine reached a peak power coefficient at λ=6. A larger impedance to the flow is achieved with the four-bladed turbine, which results in a decrease in the streamwise velocity between the lower and higher solidity configurations with the values 14% and 26%, respectively [26]. The influence of the impedance on the turbine power coefficient depends on the tip speed ratio. An increase in the solidity results in a higher impedance at the high tip speed ratios, which causes a reduction in the power as the angle of attack is low and a higher impedance reduces it further, hence resulting in a reduced lift and torque.

The power efficiency of the VAWT increases with the increase in the solidity, as the blade of low solidity turbines may experience significant stall at low tip speed ratios. The findings in the study of Consul et al. [26] are found to be consistent with previous experimental studies [27, 28] and computational studies [29].
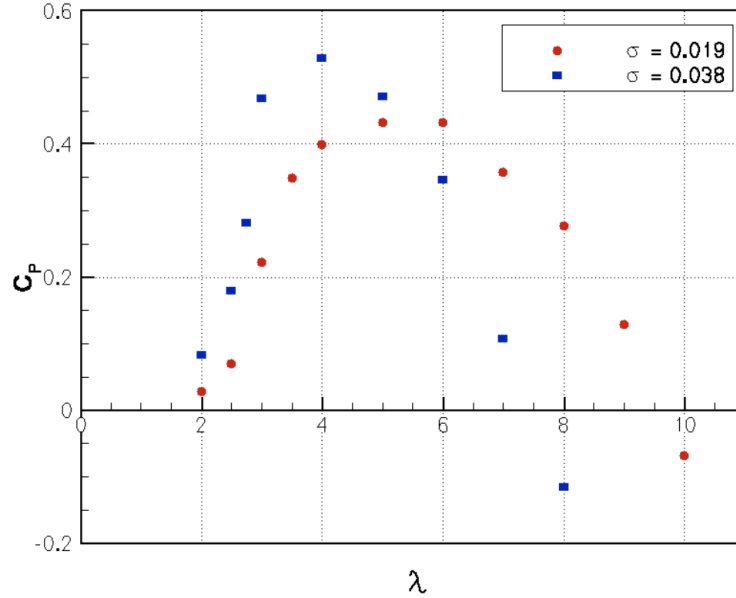
Figure 2.3. Variation of the power coefficient as a function of the tip speed ratio for values of 0.019 and 0.038 solidities for two and four-bladed turbines from Consul et al. [26].

Moreover, the significance of the solidity to determine the tip speed ratio, where the turbine reaches its maximum power coefficient, has been pointed out by Howell et al. [30] and they conducted an experimental study on the performance of small two and three-bladed H-type VAWTs. The results illustrated that the two-bladed turbine reached a higher power coefficient at a higher tip speed ratio. However, the three-bladed VAWT reached a higher power coefficient at a lower tip speed ratio. Furthermore, Castelli et al. [31] also examined the influence of the number of blades on a straight-bladed vertical axis wind turbine. In their study, they compared three, four and five-bladed H-type-VAWTs with a NACA0015 aerofoil profile in a 2D CFD model. As can be seen from Figure 2.4, the results obtained show that the peak power coefficient decreases with increase in the turbine solidity, which means that a larger number of blades

allows the attainment of the peak power coefficient for lower tip speed ratios but is caused a significant power performance loss.
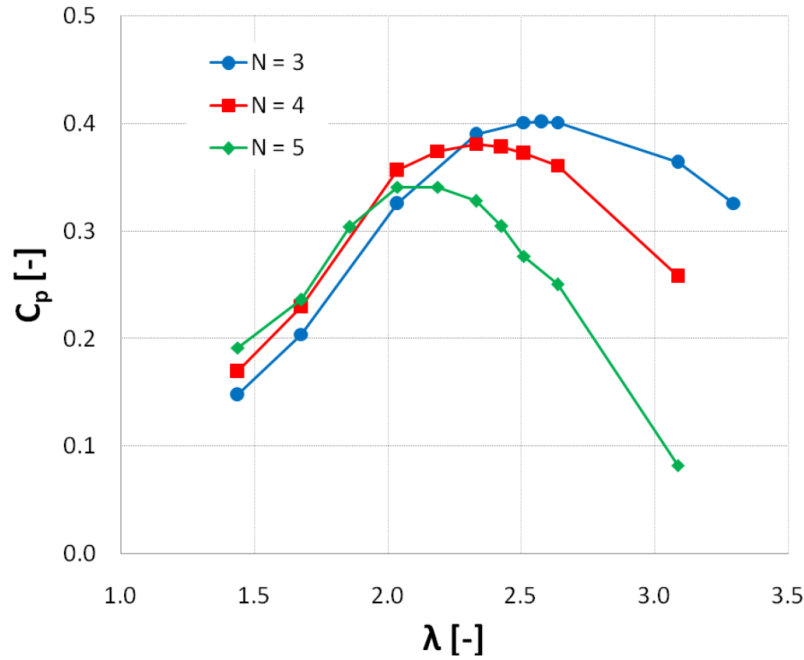
Figure 2.4. The variation of the power coefficient as a function of the tip speed ratio for three, four and five bladed turbine from Castelli [31].

Although the low solidity turbines produce a relatively higher power output for a large tip speed ratio range, as can be seen in Figure 2.2, a much lower power is produced at the low tip speed ratios. The associated low power produced at low tip speed ratios is always a difficulty for stand-alone applications, which means that this kind of applications requires self-starting. Although Kirke [21] pointed out that a load-disengaging device could be employed in order to avoid any resistance from the generator, if the solidity is too low then this means that the blade would not be effective in producing an unsteady aerodynamic force and this small force does not assist the turbine to escape from the 'dead band' back to the region that it could generate positive torque again [17]. It is argued that the advantage of a turbine having a higher peak power coefficient will lose its significance if the turbine cannot self-start or required an external force for self-starting in built environments under complex wind conditions.

Several studies have been carried out in order to examine the effects of the solidity on the turbine self-starting behaviour. Musgrove and Mays [32], Simhan [33] and Mays and Holmes [25] have suggested that increasing the VAWT solidity would assist in having a large starting torque. In Musgrove and Mays [32], a VAWT with solidity 0.6 and aspect ratio 4 showed significant torque throughout the 'dead band' region, unlike in an earlier turbine with solidity 0.17 and high blade aspect ratio. The improved self-starting ability of the turbine was ascribed to the 'increased solidity and reduced aspect ratio'. Although later corrected by Kirke [21] in that low aspect ratio reduces the starting torque, the increasing solidity improved the turbine self-starting capability. Nevertheless, Mays and Holmes [25] claimed that the high solidity generated a 'useful starting torque'.

Both Simhan [33] and Kirke and Lazzuskas [34] studied a theoretical analysis by increasing the chord length in order to increase the solidity. The results showed that increasing the chord length increases the non-dimensional starting torque coefficient. The reason for the increasing starting torque coefficient is that the Reynolds number is increased, thus leading to a better blade performance and the blade area is increased, then resulting in more aerodynamic force being generated by the blade in the rest position.

As we can infer from the above literature review of the effect of the solidity on the turbine performance, most studies [26, 27, 31, 35, 36] are concerned only with the turbine peak power output, and hence the measurements and simulations are generally conducted at relatively large tip speed ratios, such as $\lambda > 2$. Limited numerical studies have shown that a turbine with higher solidity can produce more torque, which means more power, at low tip speed ratios. This is an important point for the capability of turbine self-starting. Therefore, in this thesis, the H-type VAWT under different solidities will be investigated in terms of both the overall performance and the turbine dynamic start-up behaviour.

2.2.2 The selection of the aerofoil profile

The NACA00XX symmetrical profiles, such as NACA0012, NACA0015 and NACA0018, have been commonly utilised in the early investigations of the Darrieus type of VAWTs. The available data that covers a wide range of the conditions for these aerofoil profiles assists in the well understanding of their aerodynamic characteristics. This makes the theoretical prediction of the power coefficient and aerodynamic design easier. Nevertheless, it was later realised that these types of aerofoil profiles had been developed for aviation and might not be the best option to utilise for the VAWT [37]. A specially designed aerofoil profile, such as a laminar flow aerofoil, a cambered aerofoil and an increase in the thickness profile was suggested to enhance the performance of the turbine.

For this reason, many studies have been conducted in order to choose the optimum aerofoil profile for VAWT applications. Migliore and Fritschen [37] investigated a various range of aerofoil profiles and their influence on the turbine aerodynamic performance. The utilisation of the NACA6-series aerofoils was found to produce a wider power curve while the maximum power coefficient was comparable to that of the NACA00XX profiles. According to their results, if $NACA63_2 - 015$ were used, the energy yield can be increased by about 17% for the turbine with a 0.07 solidity to 27% for a turbine with solidity 0.21. However, their study was focused on a Darrieus rotor with a high Reynolds number and high tip speed ratio. It can be observed from these findings that they have little relevance to small-scale wind turbines under real field conditions.

On the other hand, Sandia researchers [38, 39] have developed a wide range of aerofoil profiles. The main objective was to develop the natural laminar flow aerofoils, which maintain a laminar boundary layer over the aerofoil surface as much of their length as possible. This series consists of three sections, such as SAND0015/47, SAND0018/50 and SAND0021/50. The classification of their aerofoils is similar to the NACA00XX series that were used as a reference for the design of the SAND00XX/XX. These aerofoil profiles have been presented by Berg [38] as in Figure 2.5.
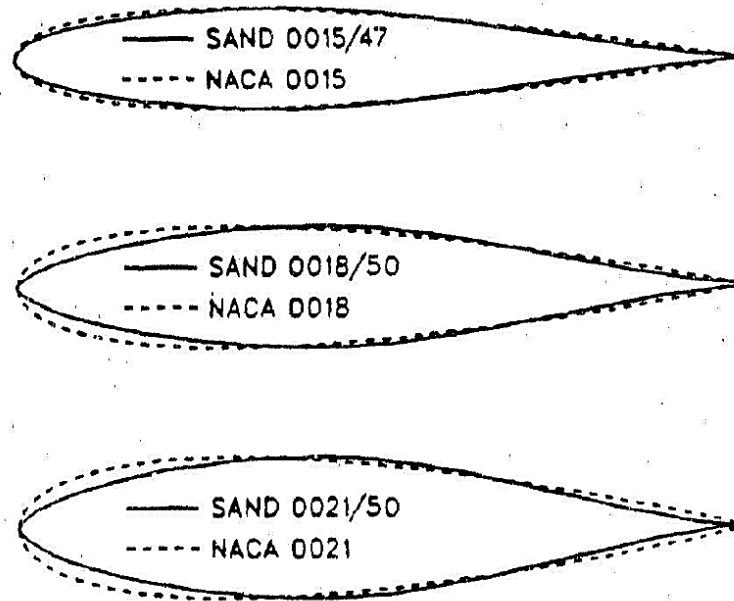
Figure 2.5. The SAND00XX/XX and NACA00XX profiles [38].

Klimas et al. [39] performed an analysis of VAWTs and showed that the natural laminar flow (NFL) aerofoil SAND0015/47 produces a lower peak efficiency due to its earlier stall behaviour. Moreover, Masson et al. [40] also demonstrated that for the 17m Sandia VAWT, the SAND0015/47 could only improve the performance slightly at high tip speed ratios compared with the NACA0015 baseline. The static lift and drag coefficients illustrated that the SAND0015/47 was the better at low angles of attack; however, the NACA0012 aerofoil showed better performance at a high angle of attack due to the early stall of the SAND0015/47.

On the other hand, Healy [41] conducted one of the first studies on the effect of the blade camber by using the momentum model. The results showed that a cambered aerofoil, which is closer to being symmetrical, has better power output. Moreover, Healy [41] claimed that the thicker aerofoils show better performance compared to the thinner aerofoils, in particular at low Reynolds numbers. The reason for this may be due to the thicker aerofoils resistance to stall. However, in contrast to the study by Healy, Kirke [21] indicated that a cambered S1210 aerofoil produced a higher maximum power output with a much improved turbine self-starting by using the multiple stream tube model. Kirke

also claimed that cambered aerofoils, which are used for aircraft applications, might perform better than the traditional symmetrical aerofoils. Furthermore, Kirke and Lazauskas [34] also predicted that a turbine with the cambered NACA4415 aerofoil having 0.32 m chord length should easily self-start in a 10 m/s wind, nevertheless, under the same conditions, the NACA0015 aerofoil has a negative torque range, which is called 'dead band', see in Figure 2.6.
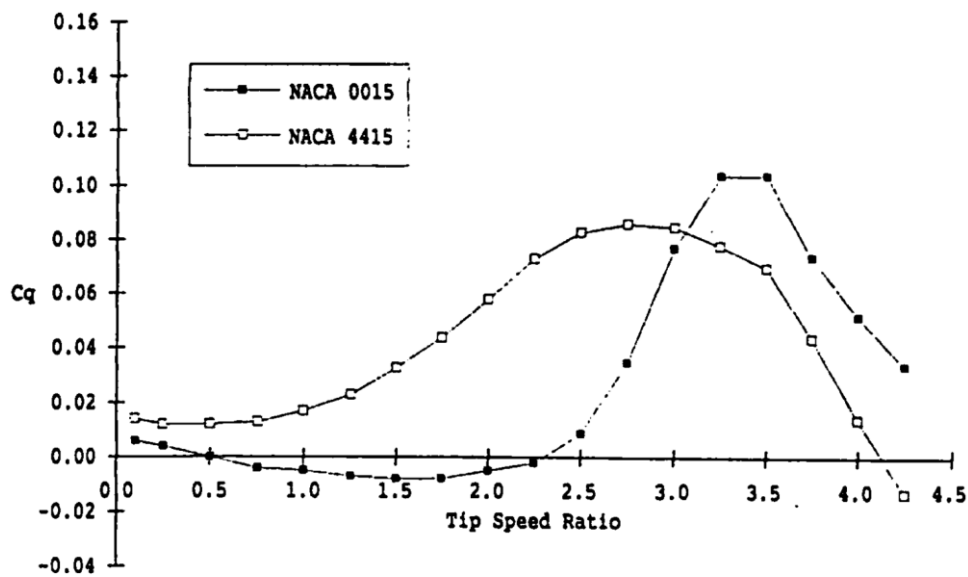
Figure 2.6. Influence of cambered aerofoils on the turbine performance, by Kirke and Lazauskas [34].

Bianchini et al. [42] presented a numerical code for the investigation of the transient behaviour of H-type Darrieus turbines. In their study, in order to evaluate the main secondary and parasitic effects, the time-dependent code, which was based on the theoretical approach derived from the momentum models, has been used. A sensitivity analysis has been also performed to examine the start-up behaviour of the small-scale three-bladed H-type VAWT. Particularly, for a fixed turbine layout, the effect of the aerofoil type, such as symmetrical NACA0015 or lightly cambered NACA4415 aerofoils, and the blade shape, such as a straight blade or helix-shaped, have been investigated

considering the initial position of the turbine and the oncoming wind velocity. According to their results, the cambered aerofoil shows significant start-up capabilities for all the investigated wind velocities, as shown in Figure 2.7.
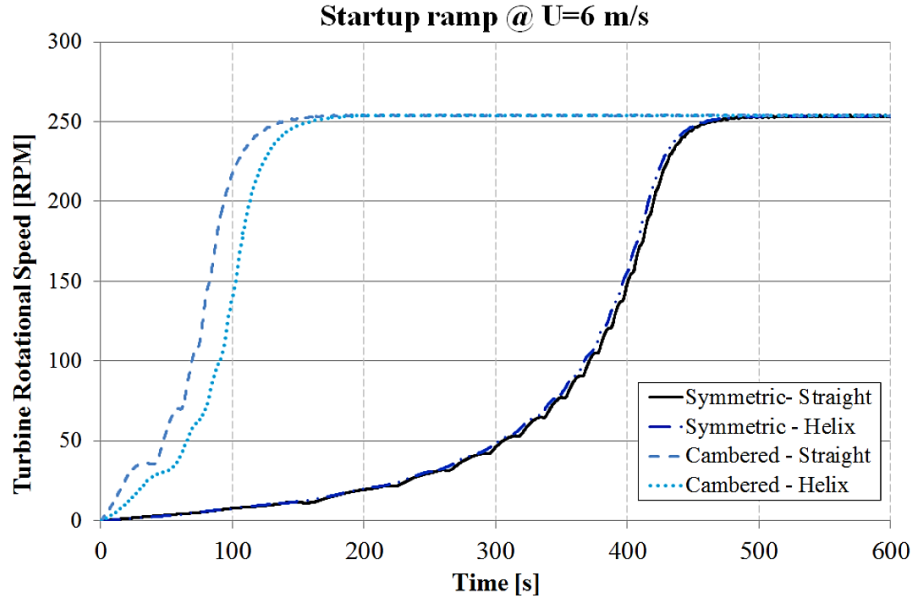
Figure 2.7. The turbine rotational speed as a function of time in 6m/s wind as a function of time for various blades [42].

The symmetrical profiles have been also investigated by increasing their thickness since a thicker aerofoil may be more beneficial to the VAWT. Angell et al. [43] have illustrated that increasing the aerofoil thickness up to approximately 21% may be utilised with no reduction in the turbine performance. Islam [44], Healy [41] and Kirke and Lazauskas [34] also found that the potential benefits of thicker aerofoils, including enhancement of the start-up performance and lower noise, may be achieved.

McIntosh [45] used a 2D Vorticity Transport Model (VTM) code in order to predict the potential change in the turbine power coefficient with a three-bladed turbine. For this study, different symmetrical NACA00XX aerofoils were used. The author concluded that the thinner aerofoils have a higher peak power coefficient at higher tip speed ratios while the thicker aerofoil profiles have a broader peak with a relatively lower value as shown in Figure 2.8. Furthermore,

at low tip speed ratios, thicker aerofoil profiles generate much more power than thinner aerofoils, which is desirable for the turbine design to achieve self-starting.
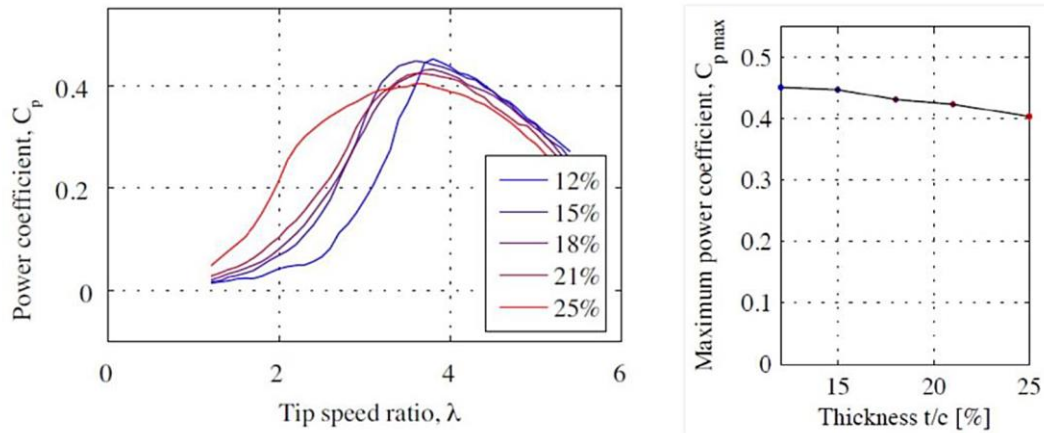
Figure 2.8. Power coefficient as a function of tip speed ratio for symmetrical NACA aerofoils with different thicknesses computed by using a 2D VTM model from McIntosh [45].

Claessens [46] proposed a new aerofoil design, namely DU06W200, to comply with the Delft aerofoil designation system. This aerofoil was designed specifically for VAWT application with a 0.8% camber and 20% thickness. In their study, they compared their newly designed aerofoil with the commonly used aerofoil NACA0018, and the results obtained are shown in Figure 2.9. The DU06W200 shows a 5% increase in the maximum power coefficient when compared to the NACA0018. As can be also seen from Figure 2.9, the shape of the curve is shifted to the left and this indicates that the new proposed aerofoil could generate more power (torque) at low λ values, which may help to increase in the turbine self-starting capability.
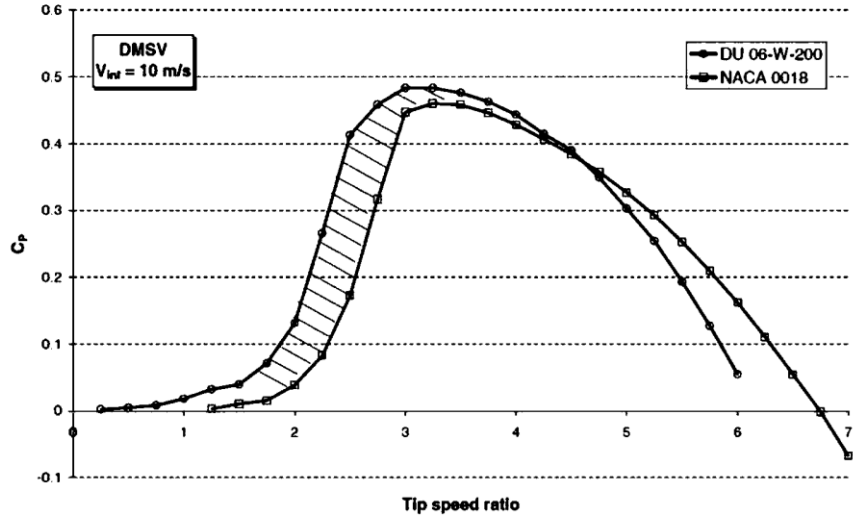
Figure 2.9. Turbine power coefficient as a function of the tip speed ratio for the DU06W200 and NACA0018 aerofoil profiles [46].

According to the above literature review concerning the aerofoil profile of H-type VAWTs, it can be concluded that even though symmetric NACA00XX aerofoils are commonly used for numerical and experimental investigations, asymmetric aerofoils may also be employed due to their more positive influences on the self-starting capability of H-type VAWTs. For this purpose, the investigation on the effects of the aerofoil profile on the turbine overall performance and dynamic start-up behaviour will be conducted by using several cambered and symmetrical aerofoils. The focus will be placed on examining the H-type VAWT performance at low λ values and the self-starting capability of the turbine with different aerofoil profiles, which have not been fully studied and presented in the literature.

2.2.3 Pitching

One of the disadvantages of VAWTs is the cyclical variation of the blade angle of attack as the turbine rotates. In this circumstance, optimal loading cannot be sustained for all azimuthal angles, thus resulting in an inherent reduction in the aerodynamic performance. As the blades depart from their optimum ${Cl}/{Cd}$ ratio at most azimuthal angles, this situation is further aggravated. In addition to this,

the pulsating lift results in significant fluctuations in the torque and power generated. The ability to pitch the blades as they rotate would address these advantages to some extent by sustaining the optimum angle of attack for most of the azimuthal angles as the blade rotates [47]. Generally, the definition of the blade pitch (β) is shown in Figure 2.10 and this definition is used in this thesis. In this figure, α is the blade theoretical angle of attack with no pitching while α_1 is the angle of attack with pitch angle. It is also important to note that the blade trailing edge moving inward is considered as the positive pitch angle.
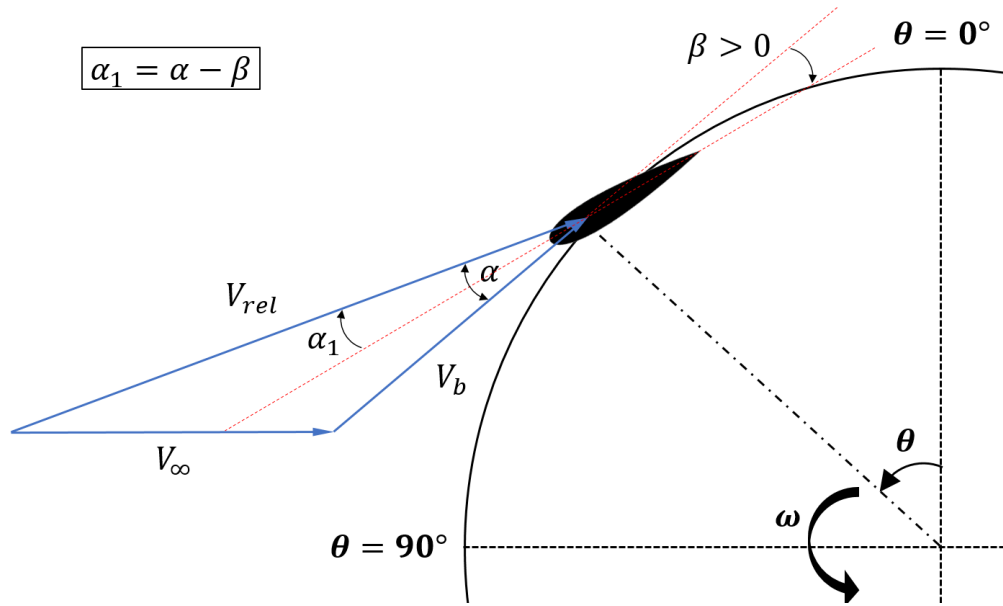
Figure 2.10. Schematic definition of the pitch angle.

2.2.3.1 Active pitch control

Over the past decades, the studies towards pitching control have gained much attention in order to improve wind turbine performance, especially HAWTs [1]. The regulations on the pitching are not only improving the power extraction but also achieving secondary objectives with the most important being the capability to decrease the transient structural loads [48]. It is also known that active pitching control can significantly improve the torque generation and the self-starting capability of VAWTs. Grylls et al. [49] performed a study on VAWT

using a simple sinusoidal pitch variation. The experimental results illustrated that a large pitch amplitude produces a good performance at low tip speed ratios but a poor performance at high tip speed ratios, whilst a small pitch amplitude produces a poor performance at low tip speed ratios but a good performance at high tip speed ratios.

Furthermore, Soraghan et al. [50] used a Double Multiple Streamtube model in order to simulate an H-type VAWT under a sinusoidal pitch motion as demonstrated in Figure 2.11 (a), which is designed to improve the peak aerodynamic performance, and the results are shown in Figure 2.11 (b). The results demonstrated that although the variable pitch successfully increases the peak performance of the turbine, it causes a reduction in the turbine performance at high and low tip speed ratios [50].
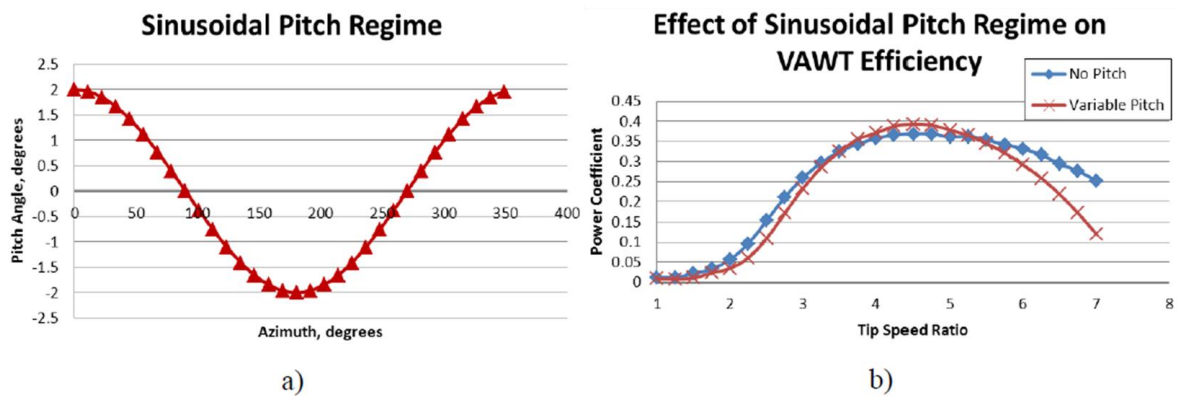
Figure 2.11. (a) The sinusoidal pitch regime designed to improve peak aerodynamic performance and (b) turbine power performance under a sinusoidal pitch control compared with no pitch [50].

2.2.3.2 Fixed pitch

If a blade could have its pitch varying with the azimuthal angle to achieve the optimum angle of attack for a complete revolution, then the dynamic stall problems of a VAWT could be avoided. In practice, the varying pitch is mechanically very challenging and often very complex for turbines, in particular relatively small-scale turbines, which is the main concern of this thesis. In spite

of using the active pitching, non-zero fixed pitch angles could improve the turbine performance. In this respect, various non-zero pitch angles will be investigated in order to investigate the effect of the fixed pitch angle on the self-starting ability of H-type VAWTs.

As illustrated in Figure 2.10, the angle of attack in the upstream part of the turbine decreases with a positive pitch angle, while it increases in the downstream part of the turbine. This pre-set positive pitch angle could affect the blades as follows:

- Since the angles of attack in the upstream part of the turbine are decreased, the blade stall angle would be delayed to further angles of attack. This would lead to the blade generating torque for a greater portion of the azimuthal angles in a complete turbine revolution.

- In the downstream part of the turbine, the onset of the blade dynamic stall would be earlier since the angles of attack are increased. This causes a decrease in the torque generation in the downstream part of the turbine.

Klimas and Worstell [51] experimentally investigated the effects of the blade pre-set pitch on the curved-bladed Darrieus type of VAWT performance and the results obtained are shown in Figure 2.12. It can be clearly seen that an increased turbine performance is found at low tip speed ratios and the peak power coefficient for the scenarios with $\beta = -2$ and $\beta = -4$. However, for the negative pitch angle of $\beta = -7$, the turbine performance for all the range of the tip speed ratios significantly decreases. Thus, it can be concluded that a too large negative pitch angle or a positive pitch angle will decrease the overall performance of the turbine. However, in this study relatively high tip speed ratios have been tested, and therefore data for the turbine performance during the start-up period is not available. In this study, the inward motion of the blade trailing edge has been considered as the negative pitching angle.
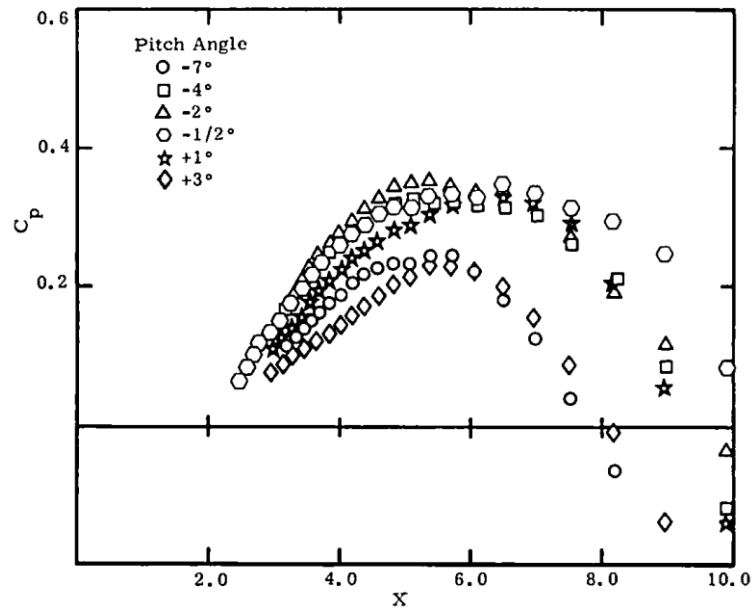
Figure 2.12. Turbine power coefficient as a function of the tip speed ratio(x) for different fixed pitch angles [51].

2.2.4 Dynamic stall

When the angle of attack of a stationary aerofoil exceeds the critical angle of attack, the static stall occurs and the lift coefficient drops from its maximum value. However, a more complex phenomenon, which is the dynamic stall, appears due to the continuous change in the effective angle of attack of a VAWT blade, particularly at the low tip speed ratios. The dynamic stall is one of the most important parameters that affects the VAWT performance and comprises of the initiation of the flow separation from the blade's surface, full boundary layer separation, detachment, shedding of vorticities and the flow reattachment to the aerofoil surface.

Beyond a certain critical angle of attack, which is depends on the aerofoil profile, the flow separates from the aerofoil surface resulting in the dynamic stall with a significant reduction in the lift and a large increase in the drag. For this inherent aerodynamic characteristic of a VAWT blade, the effect of the dynamic stall is required to be correctly investigated to assess the performance of the

VAWTs. This phenomenon depends on several factors, such as the Reynolds number, the aerofoil geometry, the angle of attack and the tip speed ratio [52].

McCroskey et al. [53] and Carr et al. [54] were the first authors who investigated the dynamic stall characteristics of the aerofoils. In order to examine the flow, hot films and hot wires were employed by McCroskey et al. [53]. The impact of the dynamic stall on the flow field separation, flow reattachment, and pitching moments was investigated. Carr et al. [54] applied a smoke visualisation method to study the effects of the dynamic stall and they have found that the dynamic stall depends on a large number of factors, including the Reynolds number, flow speed, pitching rate and aerofoil profile.

Ferreira et al. [55] investigated the influence of the dynamic stall by using a single-bladed rotor. In this study, the Detached Eddy Simulation (DES) and Large Eddy Simulation (LES) models were employed and the results showed that the blades would experience highly unsteady loading during the dynamic stall, which appears to be consistent with those of Tsang et al. [56] who performed the high frequency load measurements. Wang et al. [57] used a CFD method to model the dynamic stall and they found that a highly unstable flow region was produced due to the flow reversal on the suction side, thus resulting in a number of small vortices generation near the aerofoil surface. They indicated that it was this advection of small vortices over the blade that was responsible for the unsteadiness observed in the blade loads.

A small model in a water tank has been used in order to investigate the streamlines using an injection technique by Fujisawa and Shibuya [58]. To analyse the flow during the dynamic stall around single-bladed VAWT, the Particle Image Velocimetry (PIV) technique was employed. This study demonstrated the shedding of intense vortices during the dynamic stall, and these vortices could be seen through the blade to the downstream part of the turbine where vortices are likely to interact with the blade, and this is shown in Figure 2.13.
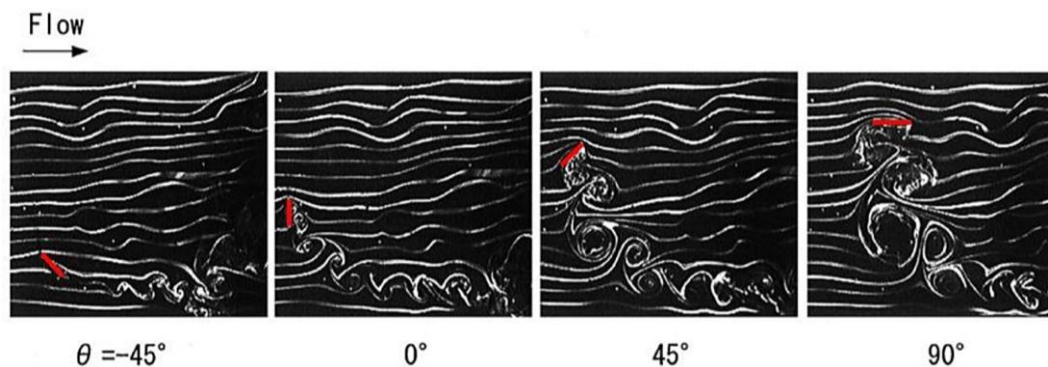
Figure 2.13. Flow visualisation of dynamic stall on a VAWT [58]. Red lines are the blades.

Although all these studies have provided an in-depth understanding for the dynamic stall phenomena, detailed identification of the dynamic stall process has been conducted by the following sequence of events by Lishman [59] and illustrated in Figure 2.14:

Stage 1: Due to the fact that the static stall angle is exceeded, a reverse flow develops at the aerofoil trailing edge. With the further increase in the angle of attack, the flow in the boundary layer starts to reverse at the aerofoil surface towards the leading edge.

Stage 2: Although the angle of attack exceeded the static stall angle, the lift coefficient increased further. In addition, the reversed flow considerably moved to the aerofoil leading edge, which results in flow separation.

Stage 2-3: The vortex size increased over the aerofoil surface and moved towards the blade trailing edge with an attendant increased in the lift until the maximum lift is obtained.

Stage 3-4: Since the vortices shed into the wake, the flow is fully separated from the aerofoil surface, which causes a sudden drop in the lift coefficient at the maximum angle of attack.

Stage 4-5: The inception of the flow reattachment has taken place with the decrease in the angle of attack. This reattachment process starts from the leading edge and moves toward the trailing edge.
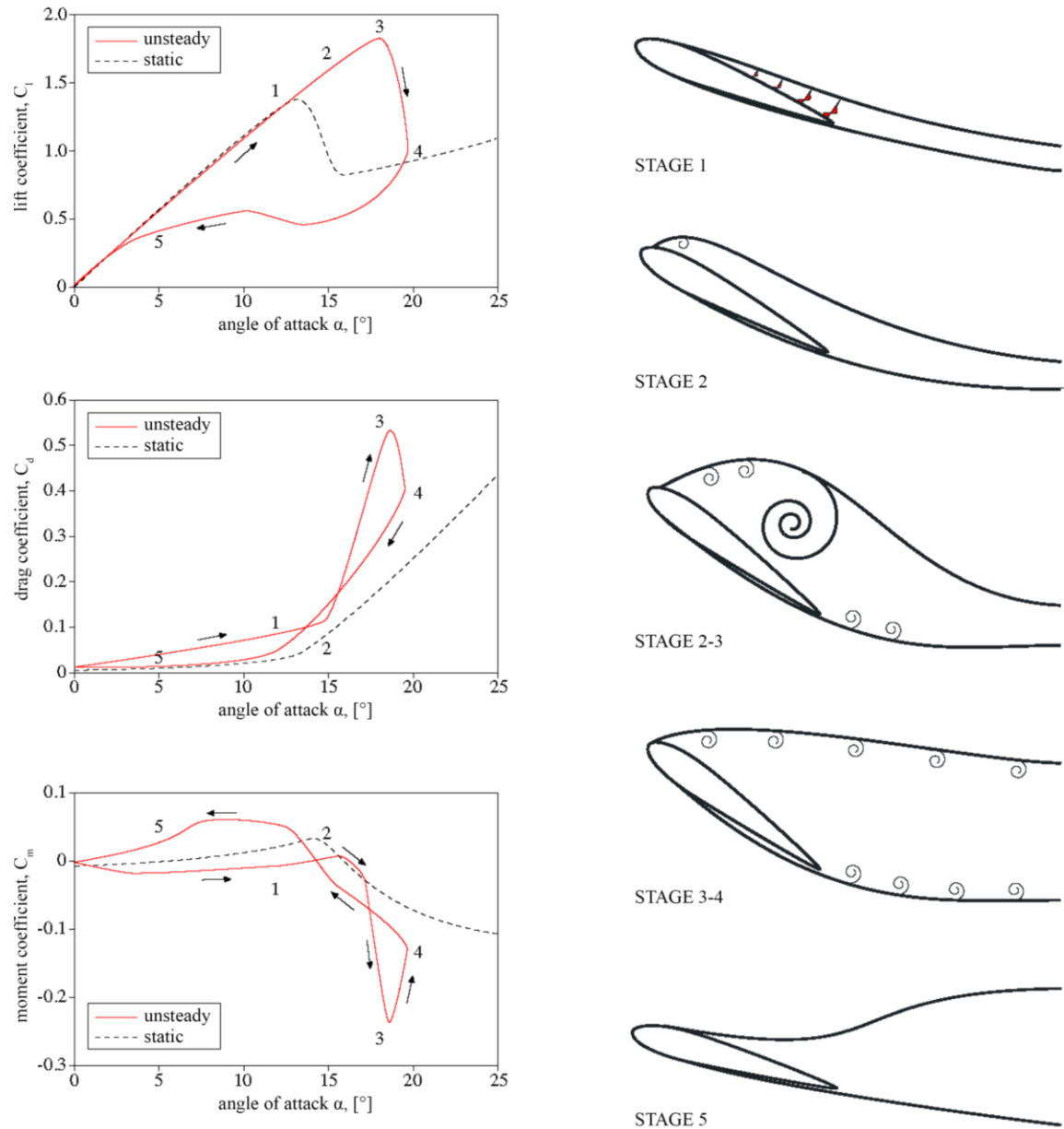
Figure 2.14. The stages of the dynamic stall process [45].

There are several theoretical models that have been designed to analyse dynamic stall, such as momentum models, [50, 93]. However, these models are not as accurate as of the computational fluid dynamics modelling of the viscous boundary layer. Therefore, the computational fluid dynamics model can be employed in this thesis to ensure relatively accurate modelling of the boundary layer flow in order to analyse the design of the H-type VAWT.

2.3   The H-type VAWT self-starting behaviour

Self-starting needs to be defined carefully. Although a Darrieus turbine is able to produce a small amount of forward torque when it is in a stationary condition, it may create a net torque per revolution at the initial starting stage, but it may then produce negative torque under certain circumstances over a range of tip speed ratios from about 0.5 to 2 depending on the blade geometry. Baker [12] describes this negative net torque region as the 'dead band'. According to his study, a turbine, which has this characteristic, may just start but it will not be able to escape this dead band in order to achieve its optimal working speed.

There are several types of definitions of self-starting. Even though they have a similar meaning, the way of explaining it is different. The self-starting was described by Ebert and Wood [60] as the self-starting process is completed when the significant power extraction begins. At the same time, Kirke [21] introduced a comparable definition that considers a turbine to be self-starting only if it can accelerate from rest to the stage where it can begin producing useful energy output. If we look at these two definitions, it can be understood that the meaning that the terms' significant power' and 'useful output' are themselves imprecise. A more specific definition of the self-starting has been adopted by Lunt [61]. He claims that the self-starting occurs only if the turbine accelerates from the rest to the steady-state condition, where turbine speeds exceed the free wind speed (λ>1). Under these circumstances, the positive drag contribution to the torque generation can no longer be existing while a significant lift is generated in a complete revolution. Even though this definition is more precise, it also has its limitations, as it does not guarantee that the turbine will continue to accelerate when it reaches a point where it starts to produce a significant lift in a complete revolution. In this thesis, the turbine is considered to be self-starting only if it accelerates from rest to its final operating tip speed ratio, where the turbine has already passed the plateau stage, without any need of the external power.

2.3.1 Review of the self-starting

The self-starting behaviour of the H-type VAWT has been a topic of intense conflict among the researches. It is essential in the instalment as an auxiliary motor might be required to start the turbine that would increase the whole system cost. Therefore, the studies have been carried out by the researchers in order to indicate the difficultly and capability of the turbine to self-start. For this purpose, the literature survey on both experimental and numerical studies conducted for the self-starting analyses of the H-type VAWTs are carried out in the present section.

There is a limited number of experimental data that has provided information on the stating behaviour of the H-type VAWT. In Chua's experimental study [62], in order to provide an airflow to the turbine investigated, three fans have been utilised. A tachometer was fitted to the shaft of the unloaded turbine to measure the rotational speed of the turbine. It is observed from his measurements; see Figure 2.15 (a), that the turbine had a relatively high initial acceleration rate for approximately 30 seconds. After that, the increasing of the rotor speed approached a steady rate. The rotor continued spinning at this steady rate for about 160 seconds when the turbine experienced another high-speed acceleration to its final tip speed ratio of 3.2 after about 200 seconds. The torque curve, as shown in Figure 2.15 (b), is consistent with the observation for the turbine acceleration. It can be seen from Figure 2.15 (b), at the beginning of the operation stage, the torque coefficient is large, and this means a fast increase in the turbine speed. However, the blades for the tip speed ratio ranging from 0.5 and 1.5 generate only a very small net torque, which is responsible with the slower of the acceleration. After the tip seed ratio 1.5, the torque increases quickly, then resulting in a fast turbine acceleration starting at about 150 seconds as shown in Figure 2.15 (a).

(a) rotor speed   (b) torque coefficient
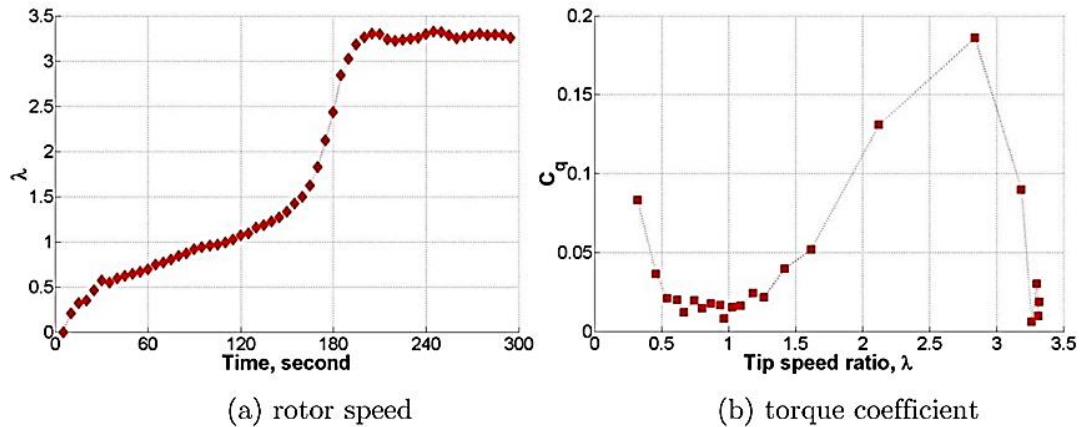
Figure 2.15. H-type Darrieus wind turbine performance from Chua's study [62]. (a) Tip speed ratio against time and (b) Torque coefficient against tip speed ratio.

Hill et al. [63] have performed another experimental study in which the turbine self-starting behaviour was further investigated. In the experimental measurements, a three-bladed H-type Darrieus wind turbine with a NACA0018 aerofoil was tested in a wind tunnel with a cross-section area of $2m^2$. The turbine was held until the speed in the wind tunnel had stabilized at its predetermined value, 6m/s, and then the release of the turbine triggered the start of the data capture process. A random starting position was applied to the turbine in each trial and it was found that the different starting position did not significantly affect the turbine performance, which is consistent with that of Dominy et al. [64] who found that a three-bladed turbine self-started regardless of its starting position. Contrary to general knowledge in the literature, they showed that a Darrieus type VAWT with the symmetrical aerofoils could still be reliable in terms of the self-starting.

According to Hill et al. [63], as it can be seen in Figure 2.16, there are four main stages occurring during the start-up period, which are (i) linear acceleration, (ii) plateau stage, (iii) rapid acceleration, and (iv) steady operation. The first stage of the start-up process is a linear acceleration from rest, followed by a plateau stage where the increase of the turbine rotational speed becomes very slow. In the rapid acceleration stage, the tip speed ratio gradually increases to about 1.5, and

then the rotor accelerates rapidly to its maximum speed when the tip speed is 3. After that, the tip speed ratio enters its steady operating stage and it is observed that Hill et al. [63] results are in good agreement with those of Chua [62]. Slopes of the curves are similar to those given by Hill et al. [63] and Chua [62].
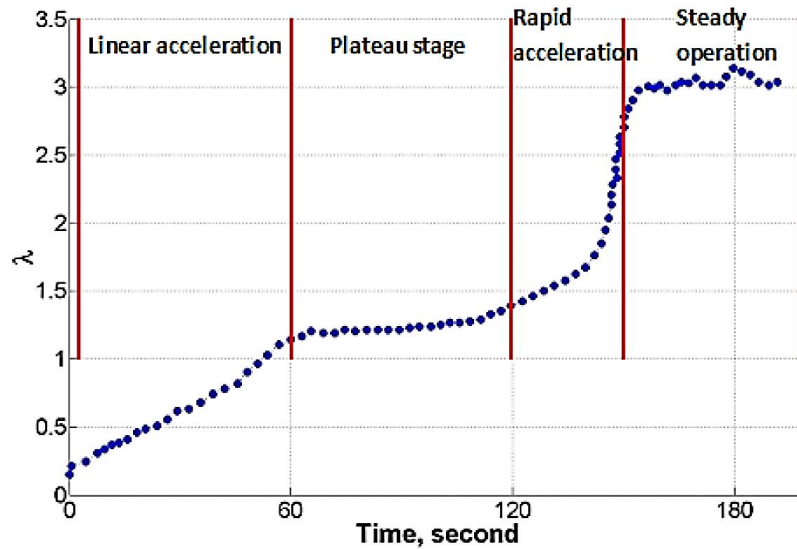
Figure 2.16. Measured H-type Darrieus turbine starting behaviour from Hill et al. [63].

Dumitrescu et al. [65] also studied the performance of an H-type Darrieus wind turbine, including the critical starting period. The turbine rotor consisted of two vertically arranged stages. In each stage, there are three straight blades, which form the basic configuration of the rotor. The three blades were arranged axially at 120° azimuthal position and 0°, 3°, 6° or 9° pitch angles. According to their measurements, see Figure 2.17, the two-stage H-type Darrieus wind turbine with a 3° blade-pitch angle experiences a small liner acceleration from rest and this is followed by a higher acceleration. Finally, it reaches a constant rotational velocity of 650 RPM. The shape of the torque curve looks similar to that measured by Hill et al. [63], the authors claim that the turbine has self-starting capabilities, and a detailed examination found this two-stage turbine only reaches a tip speed ratio of approximately 1.4.
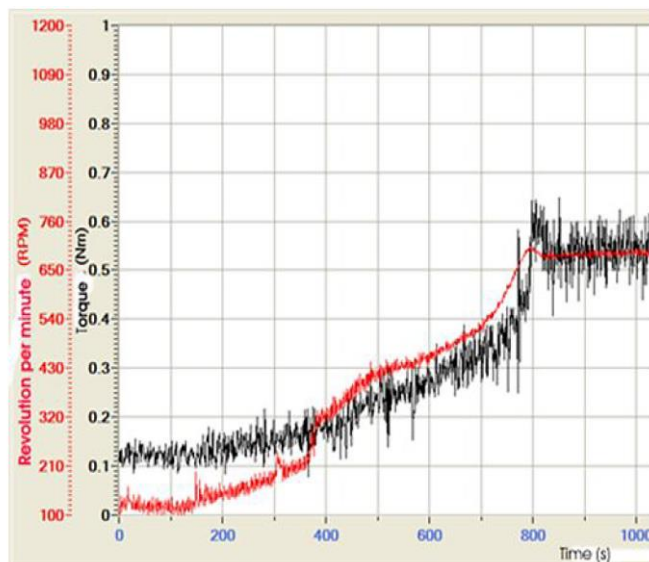
Figure 2.17. Measured H-type Darrieus turbine self-starting behaviour from Dumitrescu et al. [65].

More recently, Du et al. [66] conducted the experimental study to further enhance the understanding of the H-type VAWTs performance in terms of self-starting. The influence of the critical design parameters, such as turbine solidity, blade profile, surface roughness, pitch angle, and aspect ratio on the turbine performance has been analysed, especially when the turbine operates in the built environment. The results show that the turbine self-starting capability increases with the high solidity turbine configuration (σ>0.81), in addition to this, the thick symmetrical aerofoil with a slightly negative pitch angle (β>=-2) is superior to a cambered aerofoil. Furthermore, increasing the blade roughness may also assist the turbine to self-start.

Besides the experimental studies, there are a number of numerical studies using different numerical models conducted to investigate the self-starting behaviour of the H-type VAWTs. Beri et al. [67] investigated the effect of the modified aerofoil trailing edge on the self-starting behaviour of the H-type vertical axis wind turbines at low tip speed ratio using the computational fluid dynamic (CFD) method. The aerofoil modified from conventional aerofoil NACA0018 to be flexible at 15° from the main blade axis has been used for the

study. The modified aerofoil has been analysed at lower λ values, such as 0.1, 0.25, 0.5, 0.75, and 1. Figure 2.18 (a) shows the turbine torque values for the modified NACA0018 and NACA2415 at these λ values. The results show that the average turbine torque at each λ values are positive, which indicates that the turbine with both modified NACA0018 and NACA2415 aerofoils is able to self-start. In addition to this, in order to compare and show the effect of the camber on the blade, NACA2415 cambered aerofoil has been analysed in the same way using the same parameters. The results show that even the torque values at the different azimuthal position are positive for NACA2415; the values are lower than the modified aerofoil. Figure 2.18 (b) shows the comparison on average torque values for both aerofoils. The results indicate that the modified aerofoil has shown better self-starting performance due to the higher coefficient of the moment for all the azimuth angles than the cambered aerofoil.

(a)

(b)
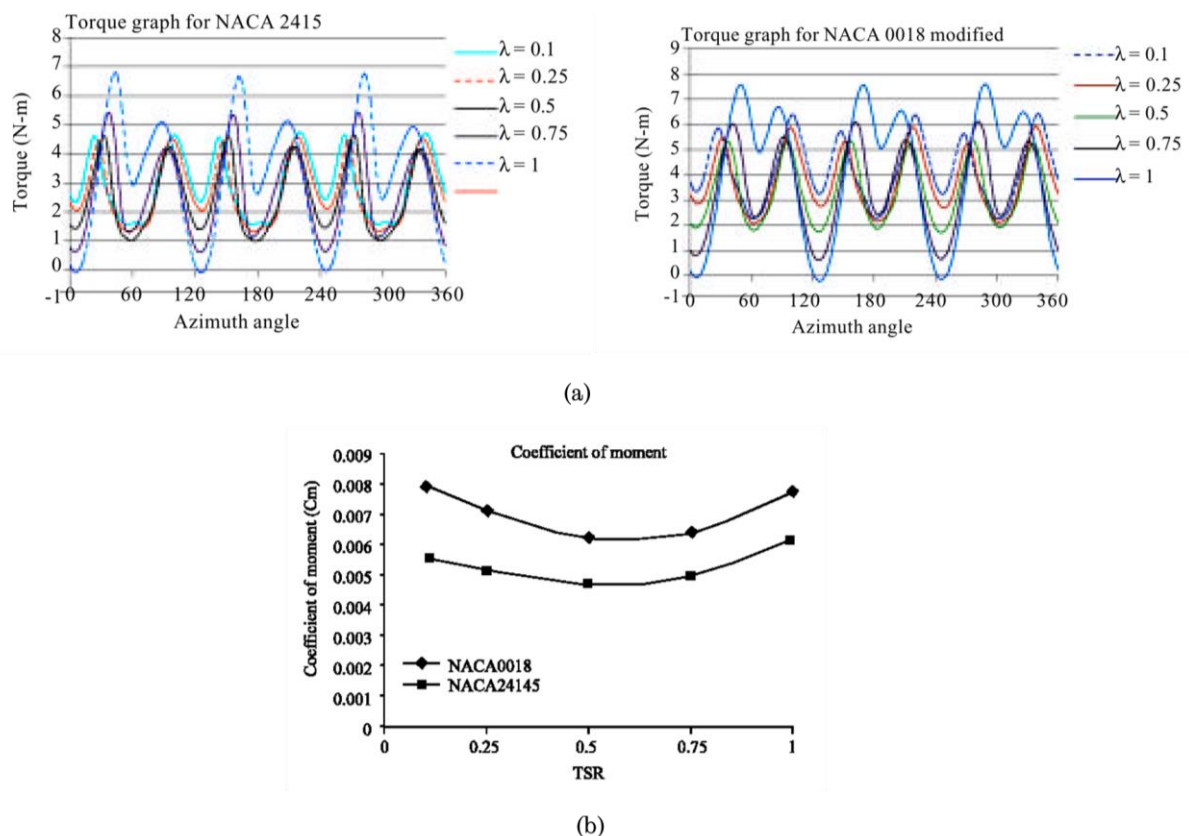
Figure 2.18. (a) Torque as a function of the azimuthal angle for NACA2415 and modified NACA0018 aerofoils, and (b) comparison of moment coefficient (Cm) as a function of the tip speed ratio for NACA2415 and modified NACA0018 aerofoils [67].

Untaroiu et al. [68] replicated an experimental prototype by employing 2D and 3D CFD models of a three-bladed vertical axis wind turbine. The results showed that even though 2D transient CFD simulations can predict the turbine operating speed with a 12% error, the performance of the turbine is not accurately captured by 2D CFD simulations compared to the 3D CFD simulations. This is due to the generation of tip vortices from the 3D model, which do not appear in 2D, and this considerably reduces the speed of the rotating of the turbine. The authors further recommended using $k - \omega$ formulations near the wall and transition during the separations to predict the initial plateau and tip vortices in 3D CFD simulations.

Worasinchai et al. [69] have created a Blade Element Momentum (BEM) based-model in order to evaluate the self-starting behaviour of the VAWT. In addition, the authors investigated the flow physics of the flapping-wing mechanism and its relation to the Darrieus turbine blade. According to their conclusion, the flapping analogy suggests that the symmetrical aerofoil with a careful configuration of the chord-to-diameter ratio, blade aspect ratio, and the number of blades may increase the driving torque generation and the ability of the self-start.

Rossetti et al. [70] compared the Blade Element Momentum (BEM) model with two and three-dimensional CFD approaches to describe the self-starting behaviour of the H-type VAWT. In order to assess self-starting behaviour, tip speed ratio versus power coefficient and thrust forces over a blade revolution have been highlighted. The BEM model indicates remarkable limits to explain the self-starting characteristic of the turbine due to the lack of well-documented aerofoil databases for the low Reynolds number and the inappropriate modelling of the dynamic stall. Even though 2D CFD simulation demonstrates the unsteady flow characteristics and the presence of complex vortices patterns, a substantial reduction in the vortices intensity inside the turbine has been found in the 3D CFD simulation results. The reduction of the vortices intensity increased the turbine expected mean torque at λ=1, which is compatible with the self-start.

Chen and Kuo [71] have investigated the effect of changing the pitch angle and the blade profiles on the turbine self-starting characteristics. They have found that the larger camber provides a better self-starting ability to the turbine. The NACA2412 had a higher root mean square moments than that of the NACA4412 and NACA0012. Singh et al. [71] conducted an experimental investigation of the self-starting behaviour and high rotor solidity on the performance of a three S1210 blades H-type Darrieus rotor. Self-starting characteristics of a three-bladed turbine with the range of solidities (from 0.8 to 1.2) at various azimuth positions have been investigated. The results show that the asymmetrical airfoil with increased rotor solidity can be chosen in order to produce a potential solution for the self-starting problem. The present configuration demonstrates high static torque coefficient at the all blade azimuthal angles for all solidities investigated. In addition, when compared to the existing symmetrical and asymmetrical aerofoils, the present design exhibits about four-time greater average static torque. It means that the turbine does not produce any negative torque during the start-up, which may assist the turbine self-starting.

On the other hand, Batista et al. [72] has developed a novel blade profile EN 0005 in order to improve the self-starting capability of the Darrieus type VAWTs. The results show that the Darrieus turbine with the EN 0005 profile achieved higher C_p values than conventional aerofoils, such as NACA0012 and NACA0018; however, the manufacturing of such blade design can cost high. Practically, the new turbine was able to start independently at a wind velocity as low as 1.25 m/s and showed stable behaviour at 25 m/s.

Zhu et al. [73] provided a systematic analysis of the fluid-turbine interaction process in terms of the self-starting behaviour of the H-type VAWT based on Computational Fluid Dynamics (CFD) method. Once the model has been obtained, then the effect of the solidity and fixed pitch angle on the self-starting behaviour have been investigated. According to the results, the solidity is not able to make the turbine have a fast self-starting and high power performance, simultaneously. However, a $-2.5°$ fixed pitch angle can make the turbine have

both a faster self-starting time and a larger power coefficient. Furthermore, Zhu et al. [74] numerically analysed the self-starting aerodynamic characteristics of the vertical axis wind turbine under fluctuating wind conditions. Contrary to the previous studies, the turbine angular velocity (ω) is not constant, and the dynamic interaction between the fluctuating wind and turbine determines the rotational speed. They claimed that if the fluctuating wind with appropriate fluctuation amplitude and frequency is determined, the capability of the self-starting behaviour of the VAWT could be improved.

Torabi et al. [75] studied the self-starting behaviour of the VAWT by using an appropriate CFD modelling setup. In contrast to the conventional approach, the turbine starts to accelerate based on the torque experienced over time. In addition, symmetrical and asymmetrical aerofoils of various thicknesses with a wide range of pitch angles have been investigated with the validated CFD model. The results showed that the asymmetrical aerofoil NACA2418, with the positive pitch angle of 1.5°, shows a significant enhancement in the rotor acceleration as 27% faster speed-up.

Sengupta et al. [76] investigated symmetrical and cambered aerofoils with high solidity in terms of self-starting behaviour of the H-type VAWT. For this study, two cambered aerofoils, namely S815 and EN 0005 and one symmetrical NACA0018 aerofoil, have been examined for both numerical and experimental investigations. It has been found that the turbine with an asymmetrical E815 aerofoil has higher dynamic torque and higher power coefficient than other aerofoils. Douak et al. [77] aimed to propose an optimised H-type VAWT having the start-up capability at the low wind speeds conditions. For this purpose, the angle of attack (α) was controlled, which may allow a self-starting under these circumstances. Then, in order to obtain a profile with a good starting torque, a general method has been introduced. Finally, an experimental study has been conducted to investigate the impacts of the angle of attack and the solidity on the force and torque generation. The results indicated that the optimal angle of attack in order to obtain a maximum torque is $\alpha = 15°$. They claim that this

angle increases the capability of the self-starting at low wind speeds conditions, and the three-bladed turbine has the self-starting capability, regardless of the starting position of the turbine.

In conclusion, the literature review shows that there is a number of experimental and numerical studies existing, with respect to H-type VAWT self-starting behaviour. However, due to its complex aerodynamics and flow structures experienced by the turbine blades, the self-starting problem is still not well understood. Therefore, one of the main aims of this thesis is to shed further light on this problem in order to provide a better understanding of the turbine self-starting behaviour by investigating the start-up stages numerically.

2.3.2 Possible solutions for the self-starting

There are several approaches to overcome the self-starting problem of the H-type VAWTs, such as pitching the blades, hybrid turbine designs, and optimising the turbine geometry including turbine solidity, blade thickness and camber, etc. Although these approaches may enhance the turbine self-starting capability, these can cause some of the major problems, such as a reduction in the final rotational speed at the steady-state condition and an efficiency loss in the peak power coefficient. Therefore, external electricity feed-in is generally needed to self-start the turbine. However, this external assistance results in much of this kind of turbine's advantages being lost.

In recent years, many Hybrid VAWT designs have been proposed for making the H-type VAWT self-starting. The Hybrid VAWTs can be a combination of the lift-based and drag-based turbines such as Darrieus and Savonius turbines, respectively. The main objective of the Hybrid turbine is to overcome the drawbacks of each turbine design, such as obtaining the self-starting characteristics at low tip speed ratios and high power output at relatively high tip speed ratios. [78].

A considerable amount of the literature has been published on the Hybrid VAWT design. The contribution of the Savonius turbine to Hybrid turbine design

has been investigated by Gavalda et al. [79] and it has been found that the Savonius turbine provides an important benefit to the turbine self-starting capability under a wider variety of wind velocities and directions. Gupta and Biswas [80] have also conducted numerical analyses in order to investigate the influence of the design parameters such as the overlap ratio and bucket size of the hybrid VAWT design, which consists of eggbeater Darrieus turbine and a 3-bladed Savonius turbine, as shown in Figure 2.19. In order to do this, five overlap ratios, namely 16.2%, 20%, 25%, 30%, and 35%, at the λ values 0.215 and 0.451 have been investigated. They have found that the highest lift-to-drag ratio at the low Reynolds numbers can be obtained with the overlap ratio of 16.2%.
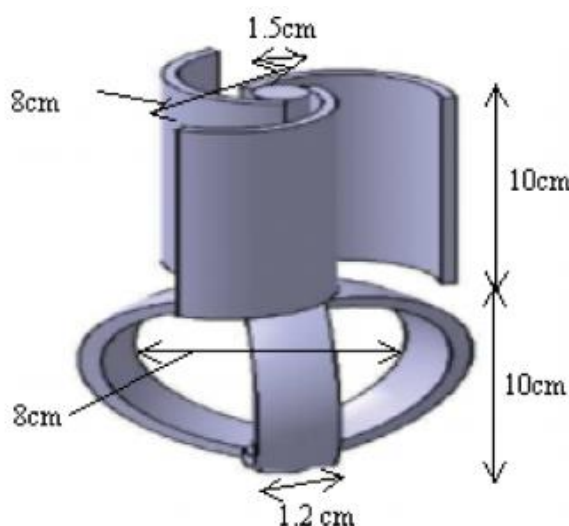
Figure 2.19. Schematic of the combined three-bucket Savonius three-bladed Darrieus turbine [80].

On the other hand, in terms of the start-up capability of the Hybrid VAWT design, Bhuyan and Biswas [81] have analysed and compared the start-up requirements of the Hybrid VAWT and conventional H-type VAWT. The results showed an improved start-up capability of the Hybrid VAWT design at any azimuthal angle and Reynolds number in comparison with the conventional H-type VAWT. However, the Savonius turbine can act as a brake at higher wind speeds for the Hybrid VAWT designs, thus decreasing the maximum possible power generation. Liang et al. [82] carried out a numerical analysis in order to

gain the optimum diameter ratio and the number of turbine blades for the Hybrid VAWT designs. It has been found that the Hybrid VAWT with two blades on the Darrieus turbine and a 0.25 diameter ratio provides the optimum performance, which is the start-up requirements for as low as 0.1 Nm under the low wind speed of 2m/s and a maximum power coefficient (C_p) of 0.363 at the tip speed ratios between 2.6 and 3.2. This combination increases the overall efficiency and the start-up torque at lower tip speed ratios.

Furthermore, an optimum aerofoil profile of the H-type VAWT is also expected to possess some desirable characteristics to obtain the optimum performance during the different turbine operating conditions, especially at the low tip speed ratios for the turbine self-starting ability. Therefore, as discussed in Section 2.2.2, a large number of the experimental and numerical studies on the effects of the aerofoil profile on the turbine overall performance and the self-starting behaviour have been carried out. However, as an alternative solution that can address the self-starting issue, the J-shaped profile has been applied to the VAWTs by a very small number of researchers. The J-shaped aerofoil profile is formed by removing a portion of the conventional aerofoil from either the pressure side or the suction side in order to utilize both the lift and drag forces at appropriate tip speed ratios. On the other hand, since the J-shaped aerofoil is made of a relatively thin sheet material compared to the conventional aerofoil, the selection of the blade material may play an important role for the cost-effective and high-strength design of the H-type VAWT having the J-shaped aerofoil, particularly at high rotational speeds. In most application, blade reinforcement technologies need to be considered, such as using support ribs, etc. Therefore, the types and the thickness of the material used for the J-shaped aerofoil would be an interesting topic for investigation.

Chen et al. [83] investigated different surface opening ratios (the ratio of the cut-off length and the full aerofoil length) for the J-shaped aerofoil in order to overcome the issue of the self-starting of H-type VAWT. Several opening ratios employed to the aerofoil surface were located on both the inner and outer sides

of the turbine. The results show that in terms of the power performance at the optimum tip speed ratio and the starting torque generation, the desirable turbine can be obtained with the J-shaped aerofoil with 0.48 and 0.60 inner opening ratios while that of 0.72 and 0.84 outer opening ratios. Zamani et al. [84] studied a 3kW H-type VAWT by implementing the newly proposed J-shaped aerofoil profile. The main purpose of this study was to improve the starting torque of H-type VAWT using the J-shaped profile. The findings indicate that the optimum turbine performance can be obtained using the J-shaped profile, which has the opening from the maximum thickness toward the trailing edge. More recently, Mohamed [85] criticised the J-shaped Darrieus type VAWT using different types of the aerofoils, such as NACA0015, NACA0021 and S1046, in terms of the turbine performance and noise generation. The author claims that J-shape aerofoil reduced the performance and did not reduce the turbine noise. However, this study was not carried out in accordance with the main purpose of J-shaped aerofoils. Since it is known that J-shaped aerofoils increase the performance of the turbine at the low λ values (generally less than 2), while it decreases the performance at the high λ values. However, the λ range investigated by the author was 2 to 5, but this range is not appropriate to evaluate the main purpose of J-shaped aerofoils.

The literature survey on the J-shaped aerofoil demonstrated that although some of the previous researches on the influence of the J-shaped aerofoil on the turbine self-starting capability have shown that the turbine's self-starting performance can be improved when adopting the J-shaped profile, the aerodynamic characteristics of the J-shaped aerofoil is not fully understood due to the lack of detailed studies addressing its importance in terms of the aerodynamics. Therefore, a detailed investigation of the aerodynamic behaviour of the J-shaped aerofoil in comparison with its conventional profile should be carried out when it is employed for VAWT.

2.4   Conclusion

The literature review shows that there are a considerable number of studies on the effect of the turbine design parameters on the overall performance and the self-starting behaviour of the H-type VAWTs by employing different methods, such as the Computational Fluid Dynamics method (CFD) and Blade Element Momentum method (BEM) and experiments. These parameters investigated are not of equal significance and they should be included in the evaluation of the turbine performance and design process in order to obtain an efficient H-type VAWT design. Most of these studies have been conducted to investigate the effect of the design parameters, such as solidity, pitch angle, blade profile, etc., on the self-starting behaviour with the calculated instantaneous torque and power coefficients at low tip speed ratios (e.g. $\lambda < 1$). However, little attention has been paid to the turbine time-varying start-up data together with the overall power performance data obtained from the dynamic start-up simulations. Therefore, the design parameters reviewed in this chapter are investigated in order to provide an in-depth understanding of their effect on the overall and the self-starting performance of the H-type VAWTs using the dynamic start-up model.

The present literature also shows that the different types of the aerofoils have been employed to the H-type VAWT applications in order to enhance turbine torque generation, in particular at the low tip speed ratios. Among all the aerofoil types, the J-shaped aerofoil provides a promising feature that enhances the instantaneous positive drag contribution in a complete rotor revolution, especially at the low tip speed ratios (e.g. $\lambda < 1$). In this circumstance, the positive drag can overcome the negative lift and thus a positive instantaneous torque can be produced at an instantaneous azimuthal position, which assists the turbine to enhance torque generation. However, very limited studies have been performed to analyse the effect of the J-shaped aerofoil in the turbine overall, and the self-starting performance and aerodynamic characteristics of the J-shaped aerofoil are not still well understood. In addition, based on the above discussion, the Darrieus type VAWT has been selected as a main subject of the

development in the existing literature due to its promising advantages, such as higher efficiency and low manufacturing cost. Even though this turbine has illustrated a high performance at the high tip speed ratios, the starting torque is one of the important drawbacks. Thus, several approaches have been proposed in order to improve the self-starting capability of the Darrieus type VAWTs.

Among all the possible approaches, although the Hybrid turbine rotors (Savonius & Darrieus) appear to be a promising method in order to overcome the self-starting issue, it has several challenges, such as efficiency penalties at high speed, new forms of the vortex shedding and the complexity of the system design that may result in the vibrations and associated high capital and maintenance costs due to additional moving parts, etc. Therefore, it is believed that the H-type VAWT with a novel hybrid blade design, which consists of the lift-based and drag-based aerofoils, may be a potential solution and replace the existing methods in order to overcome the weakness of the Hybrid turbines. The Hybrid Blade design emerged with the goal of combining the advantages of the lift-based and drag-based aerofoils in one design. In addition, apart from the aerodynamic advantages of the turbine having a novel hybrid blade design over the traditional hybrid turbine design, the utilization of these turbines can be beneficial in terms of the economical aspect since the fabrication and installation of the hybrid blade, especially the cutting part, would be easier than the installation of a separate Savonius turbine to the shaft. Therefore, it is expected to be much cheaper to produce the turbine having a novel hybrid blade. Furthermore, when encountering other technical problems, the maintenance of the hybrid turbine would be more complicated than that of a hybrid blade since the hybrid turbine consists of two different types of turbines. To the best of my knowledge, the overall performance and the self-starting characteristics of the H-type VAWT with a hybrid blade have never been explored in the literature.

Based on the critical discussions in the literature review, the following knowledge gaps are revealed and fully investigated in the present thesis:

- While the majority of the investigations in the literature rely on the calculated torque and power coefficients at the low tips peed ratio (e.g. λ<1) for the investigation of the VAWT self-starting behaviour, it is important to evaluate the turbine start-up characteristics with the turbine time-varying start-up data with the overall performance data obtained from dynamic start-up simulations. Thereby, both the turbine acceleration behaviour and the performance at the steady-state conditions can be analysed, simultaneously.

- The current understanding of the aerodynamic characteristics of the J-shaped aerofoils is not clear and there are several studies that rely on the static aerofoil performance as an indication of the desirable J-shaped aerofoil for the H-type VAWTs. Therefore, it is essential to investigate the behaviour of the J-shaped aerofoils under dynamic conditions.

- There is an inconsistency in the literature regarding the effect of the J-shaped aerofoil on the turbine dynamic start-up behaviour. Therefore, a comprehensive analysis of the aerodynamic characteristics of the J-shaped aerofoil considering the different design parameters under the turbine simulations is required in order to provide an in-depth understanding.

- It is essential to design a hybrid blade profile, which consists of the conventional aerofoil and the J-shaped aerofoil, to eliminate the drawbacks of the existing designs, such as the hybrid turbine.

Chapter 3

The H-type VAWT modelling theory and methods

3.1   Introduction

The main objective of this chapter is to review the theory and different numerical models applied to the investigation of the aerodynamic performance of VAWTs while pointing out their advantages and disadvantages. Over the past few years, many attempts have been made to build a general understanding of the Vertical Axis Wind Turbine (VAWT) aerodynamics by developing many numerical models. Generally, these models can be classified into two categories: the mathematical models and computational fluid dynamic (CFD) model. In the mathematical models, the VAWT problems are explained with mathematical equations in which flow field and aerodynamic forces are solved using simplistic equations based on fundamental of aerodynamic theories. On the other hand,

the computational fluid dynamic (CFD) is based on solving several forms of Navier-Stokes equations and no assumption made as to the forces acting on each blade and no look-up data needed for the aerodynamic force coefficients, such as lift and drag coefficient. Therefore, these features make CFD a more reliable and useful tool compared to the mathematical models.

In CFD modelling, the selection of the turbulence model is one of the most important tasks for the prediction of the H-type VAWT performance. The scope of this thesis is to consider, mainly, the relatively low Reynolds number flow regime. Under these circumstances, the analysis of the aerodynamic forces at the vicinity of the aerofoils requires detailed consideration, especially near the aerofoil surface. Therefore, the selection of an appropriate turbulence model plays a crucial role and it depends on many factors, such as the accuracy of the defined problem, availability of computational power, etc.

In addition to the numerical models, Lyapunov stability theory [86] can be employed for the system-controller design of the H-type VAWTs since these kinds of turbines are a nonlinear time-varying system due to the wind variations. In this regard, a literature survey was conducted and it has been found that there is a very limited number of studies carried out in terms of the application of the Lyapunov stability theory for the H-type VAWTs. A study was conducted by Abdalrahman [87] in order to improve the overall and self-starting performance of an H-type VAWT employing the pitch angle control technique. In this study, stability analyses of the H-type VAWT having both a fixed and a variable pitch blade have been conducted using the Lyapunov stability theory. The results show that using this theory, the system is asymptotically stable when the proposed blade pitch control is employed, in particular at the low λ values (λ<1.2), where the turbine self-starting ability plays an important role, while the system is unstable at the relatively high λ values. However, in general, there is a lack of studies existing in the literature about the use of the Lyapunov stability theory for the investigation of the stability of H-type VAWTs.

In the subsequent sections, a literature review including the numerical modelling of the VAWT is presented. A discussion is also carried out for the advantages and disadvantages of each numerical model. In addition, the various turbulence models for CFD will be critically discussed in order to select the most appropriate turbulence models for the H-type VAWT applications.

3.2   Mathematical models of H-type VAWT

Although the aerodynamic characteristics of the H-type VAWTs is very complex, mathematical models have been developed to predict the performance of the turbines. These mathematical models have strengths and weakness depending on the turbine configuration, wind behaviour, etc. The most commonly used mathematical models can be classified into three categories: Blade Element Momentum model (BEM), Vortex model, and Cascade model.

3.2.1   Momentum models

The Momentum models, also known as Blade Element Momentum (BEM) models, are based on the rate of change of the momentum of air due to the streamwise force acting on the blades. This force is equal to the overall change of the velocity multiplied by the mass flow rate. For each stream tube, Bernoulli's equation is applied and the force is equal to the average pressure difference throughout the turbine [15]. However, the blade element momentum models have some drawbacks, and they are invalid in two cases: (i) when the tip speed is large, and (ii) when the solidity of the rotor is high. Due to these two main problems, the momentum equations become inadequate [88]. Over the last years, several attempts have been made in order to enhance the accuracy of the models based the momentum theory which results in single-stream tube model, double stream tube model, and multiple double stream tube model.

The single stream tube model is one of the simplest prediction models for the calculation of the turbine performance. Templin [89] made the first application of the momentum theory to predict the performance of the vertical axis wind turbines by using the single stream tube model. The prediction of the

performance by using this model is always higher than the experimental results due to the fact that it does not consider the wind variations across the rotor, which increases with the increase in the turbine tip speed ratio and solidity [90]. Furthermore, this model is based on some assumptions, such as [16]:

- No frictional drag from the stream tube boundary and the blades,

- No rotating wake behind the rotor,

- An infinite number of blades and the length of the blade,

- No change in the velocity magnitude across the disc due to the fact that the pressure across the rotor is assumed to be constant.

On the other hand, the single stream tube model has been improved by Wilson and Lissaman [91] as the multiple stream tube model. The flow in this model is assumed to be inviscid and incompressible in the calculations of the induced velocity along the stream tube. Also, Wilson and Lissaman employed the theoretical torque and the actuator disc velocity through the streamtube. However, even though some deficiency encountered with the single stream tube model has been corrected for the multiple stream tube model, this model could not always predict VAWT performance precisely when compared to the experimental data since the loading of the blade in the downstream part of the turbine is not still taken into account.

Another theory, which is also based on the multiple stream tube model, was proposed by Strickland [92] in 1976 as an improvement to the Wilson and Lissaman model. He included the drag force by equating the blade forces to the rate of change of the momentum for each stream tube. This model reasonably predicts the total performance of the turbine; in particular, it is valid for lightly loaded turbines. Furthermore, by considering the wind shear effect, this model allows us to predict the overall performance to be much closer to the experimental results over that of the single stream tube model.

Furthermore, Paraschivoiu [93] developed the double-multiple stream tube model in 1981 to overcome the drawbacks encountered with the multiple stream

tube model. The calculations of the upstream and the downstream part of the turbine are performed separately in this model. In the upstream and downstream parts of the turbine, the upstream-induced velocity and downstream-induced velocity can be obtained by using the principle of the two actuator discs simultaneously. This principle of the two actuator disc theory was originally given by Lapin [94] in 1975. In this concept, the turbine interacts with the wind twice due to an additional disc at the downstream half-cycle, which results in a more accurate prediction obtained compared to the multiple stream tube model.

The significant influence of some secondary effects, in particular at the high λ values, such as the rotating central tower, the effect of struts, and the blade geometry was pointed out by Paraschivoiu et al. [95]. Additionally, in order to obtain more accurate calculations for the aerodynamic loads, the variation of the induced velocity as a function of the blade azimuthal position was also considered. After all these improvements, the double-multiple stream tube model provides much better results that are close to the experimental results. However, this model still over predicts the power coefficient for the high solidity turbines, and shows a convergence problem for the turbine, particularly in the downstream part of the turbine and at the higher tip speed ratios [90].

The more details of the momentum-based models and the calculation procedure of the power coefficient are available in [90, 96].

3.2.2   Vortex model

The vortex model is another important model used for the calculation of the aerodynamic performance of vertical axis wind turbines. The main principle of this model is based on the influence of the vorticity on the velocity field. Larsen [97] introduced the first 2D vortex method to predict the performance of a Cyclogyro windmill, which consist of aerofoils rotating around a horizontal axis for both lift and thrust. However, the stall effect was neglected with the selection of a small angle of attack in his model. On the other hand, Fanucci and Walter

[98] also presented a 2D-based vortex model in order to study the straight-bladed vertical axis wind turbine; however, they did not consider the stall effect either.

In 2010, the vortex model was also used in order to predict the noise produced by vertical axis wind turbines. Dumitrescu et al. [99] have used a discrete vortex model to predict and to analyse the low-frequency noise produced by vertical axis wind turbines and the vortex method was used in order to perform the fluid dynamic analyses, and the Ffowcs Williams-Hawkings [100] equations were used for the noise prediction.

Compared to the BEM model, the computational time is one of the main drawbacks of the vortex model. Moreover, significant simplifications are still applied in the vortex model. For instance, the effect of the viscosity in the blade aerodynamics is included through an experimental force coefficient and potential flow is considered in the wake [101].

3.2.3   Cascade model

The concept of the cascade model is generally applied in turbomachines [90]; however, the first cascade principle was applied by Hirsch and Mandal [102] to analyse the vertical axis wind turbines. The main idea of the cascade model is that the blade aerofoils of a turbine are equally positioned on the surface at a length, which is equal to the turbine circumference. As in other types of models, the cascade model has both advantages and disadvantages. According to the limited studies performed in the literature, the main advantages of this model is the smooth convergence [15]. Furthermore, the effect of the dynamic stall can be taken into account in this model, and results show a good agreement with the experimental data [103].

3.2.4   Summary of the mathematical models

Several mathematical models have been analysed and discussed, and these can be employed for the performance prediction and design of H-type vertical axis wind turbines. Currently, the most commonly used mathematical models are the double-multiple stream tube model, the Vortex model, and the Cascade

model. Since all these models are based on different assumptions and require accurate aerofoil aerodynamic data at the appropriate Reynolds number, it has been found that each of these three models has their advantages and disadvantages, which are shown briefly in Table 3.1. Due to the aerodynamics of a VAWT being so complicated, these models are seen to suffer from their inability to accurately simulate complicated applications. Furthermore, the above traditional mathematical models are not able to provide insight into the flow physics around the aerofoil and the wake, despite the huge efforts that have been made. In addition, these models are not reliable in predicting the turbine dynamic self-starting behaviour due to the lack of the aerodynamic force coefficients at a various range of the Reynolds numbers. Nevertheless, if all the aerodynamic date is available then these models can be employed to predict the turbine starting behaviour. For example, in Figure 3.1, a comparison of the power coefficient curves of the H-type vertical axis wind turbine between the experimental data and various mathematical models are illustrated. Figure 3.1 also shows that by using these models, the negative power coefficient zone is created, especially at low tip speed regions (0.5<λ<2). A turbine having this kind of the power coefficient characteristic may just start but could not accelerate to its optimum operating speed and stop due to that negative region of power coefficient. It is believed that the reason of the negative zone might be due to the low quality of the aerofoil aerodynamic force coefficients employed, which are lift and drag, as the model input in the calculation of the turbine power coefficient.

Table 3.1. Comparison of the mathematical models of VAWTs.

Reference	Model	Advantages	Shortcomings
[89]	• Single stream tube model	• Very fast computational prediction	• Predict higher results than the experimental results

[91]	• Multiple stream tube model	• Fast computation prediction	• Predict lower results than the experimental results • Some convergence problems
[88], [94]	• Double multiple stream tube model	• Good agreement with the experimental results	• High tip speed ratios converge problem • High solidity cases over prediction of power coefficient
[97], [104]	• Vortex model	• High-precision prediction capabilities	• Requires a high computational effort
[102]	• Cascade model	• Smooth convergence • Dynamic stall effect is considered	• High computation time • Predictions based on empirically determined parameters
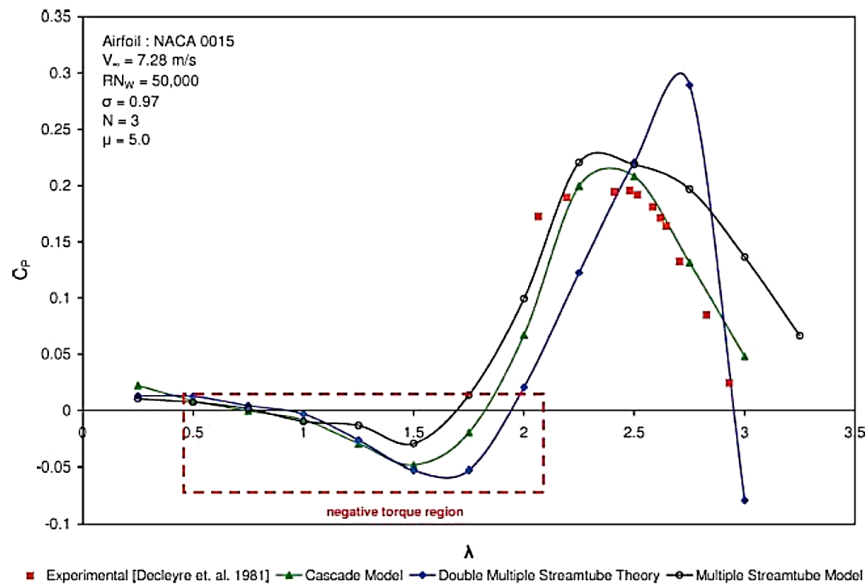
Figure 3.1. Comparison of the power coefficient curves of the H-type VAWT between the experimental data and different H-type VAWT models [90].

3.3   Computational Fluid Dynamics (CFD) modelling and turbulence models

3.3.1   An overview of the CFD methods

The history of the Computational Fluid Dynamics (CFD) started in the early 1970s. During that period of time, CFD became necessary for the combination of physical, numerical mathematics, and computer science aspects [105]. CFD is a very popular tool in order to solve a wide range of industrial and non-industrial problems, and it also plays an important role for VAWT research. CFD is also one of the most promising methods in the wind energy industry and it has been gaining more attention over recent years. Furthermore, CFD can be utilised in order to simulate the fluid flow in detail and it does not require as much cost for systematic analyses when compared to the traditional experimental methods.

The CFD simulations consist of three major steps. The first step is the pre-processing where the computational domain is constructed and discretised in the form of the computational mesh. This step also allows defining the flow properties and the boundary conditions. In the second step, to obtain the predicted results, the governing equations are solved iteratively. Finally, the post-processing is the third step in which the predicted results are analysed and can be visualised in different forms as the contour plots, streamlines, etc.

CFD promises several advantages, such as a far lower cost compared to the experimental investigations. However, in this case, the most important aspect is the fast speed of obtaining results. In addition, the visualization tools in the software help us to understand the underlying physics of the problem. Furthermore, the ability of CFD to calculate the aerodynamic forces acting on the blades eliminate the need for the external database, which is an inherent requirement for the momentum based models discussed above. Although the computational fluid dynamics is a powerful method for the analysing of VAWT applications, the computational results can be different from the experimental results if the model is not appropriately set up. Therefore, the CFD model

validation is necessary. CFD also has other limitations, in particular, the CPU time for the computations can be large and thus requires much computational power [15]. Therefore, simplification assumptions may be required. Nevertheless, CFD is the main model that will be used to analyse the aerodynamic performance and self-starting behaviour of the H-type VAWT in this thesis.

Most engineering fluid flow problems, which include wind turbines, involve turbulence and this has encouraged scientists and engineers to propose better techniques to model turbulence. There are three main approaches in simulating turbulent flows, namely Direct Numerical Simulation (DNS), Large Eddy Simulation (LES), and Reynolds-averaged Navier Stokes simulations (RANS) [106]. DNS resolves the whole spectrum of turbulent scales by numerically solving the full Navier-Stokes equations without employing any turbulence modelling techniques. In this method, a very fine mesh is required in order to capture all the scales from the smallest to the largest eddies, which extremely increases the computational cost and makes it impractical for most practical engineering problems involving high Reynolds number flows [152]. The RANS approach models the whole spectrum of the turbulence using a single turbulence model without the need to resolve the turbulence eddies and therefore a relatively coarse computational mesh can be employed that can substantially reduce the computational costs. The problem of RANS is that the simulation results may strongly depend on the turbulence model employed and no turbulence model is universally applicable. On the other hand, LES approach can improve the accuracy over RANS by resolving the large eddies and only modelling the small sub-grid scale eddies. This results in a significant reduction in the computational cost compared to the DNS but it is still higher than that for the RANS in terms of the both computer memory and calculation time [152]. Therefore, the current CFD research performed is based on the RANS with a carefully chosen turbulence model to reduce the computational time. Since the flow around the VAWT under the current setup is unsteady and incompressible, the unsteady Reynold Average Navier-Stokes (uRANS) equations for the incompressible flows will be employed and they can be expressed as follows:

$$\frac{\partial u_i}{\partial x_i} = 0 \tag{3.1}$$

where $i = 1, 2, 3$ for the three dimensional case.

The unsteady Reynolds-Averaged Navier-Stokes (uRANS) equations for incompressible flow can be also expressed as follows:

$$\frac{\partial}{\partial t}(\rho u_i) + \frac{\partial}{\partial x_j}(\rho u_i u_j) = \frac{\partial}{\partial x_j}\left(\sigma_{ij} - \rho\overline{u_i' u_j'}\right) \tag{3.2}$$

where

$$\sigma_{ij} = -p\delta_{ij} + \mu\left(\frac{\partial u_i}{\partial x_j} + \frac{\partial u_j}{\partial x_i}\right) \tag{3.3}$$

where ρ is the density, μ is the dynamic viscosity, p is the pressure, and $j = 1,2,3$. In addition, σ_{ij} is the pressure term and the viscus stress term, $\rho\overline{u_i' u_j'}$ is referred to as the Reynolds stress terms, which is depended on the velocity fluctuations in the flow, and only appear as a result of the Reynolds averaging process. Since this averaging process is for the separation of the mean and the fluctuating parts of the turbulent flow, these Reynolds stress terms need to be expressed in terms of mean flow quantities rather than the velocity fluctuations. This is called the closure problem. For this reason, these turbulence models are required in order to overcome the closure problem of Reynolds stresses.

3.3.2 Turbulence models

The objective of using the turbulence model for the RANS is to model the Reynolds stress tensor that appears in the RANS equations. It can be achieved typically by two main types of turbulence models. The first way is to adopt the Reynolds Stress Transport Model. This model solves six transport equations for the distinguished components of the Reynolds stress terms requiring a more detailed modelling and thus more computational demanding compared to the other turbulence models. The second way to model the Reynolds stress tensor is using the Eddy Viscosity based models, which relies on the Boussinesq

hypothesis. These models include zero-equation, one-equation, two-equation, and four-equation models.

The eddy viscosity in the zero-equation turbulence model is calculated based on the local mean flow quantities and a mixing length scale, rather than solving transport equations for turbulence quantities. The zero-equation models include the Mixing length, Cebeci-Smith, and Bladwin-Barth models [107]. However, these models are often too simple for use in most situations since the mixing length scale is not universal [108].

The Spalart-Allmaras model was presented by Spalart and Allmaras in 1992. This model was designed to overcome the limitations of the zero-equation models [109]. However, compared to the other types of turbulence models, the Spalart-Allmaras model is a simple one-equation turbulence model, where the flows with large separations and free shear flows cannot be captured accurately. Therefore, this model is less sensitive in the near wall treatment around the H-type VAWTs.

On the other hand, two equation turbulence models, such as $k-\varepsilon$ and $k-\omega$, are one of the most common types of turbulence models that are used for most types of engineering problems. In these models, there are two extra transport equations to represent the flow characteristic quantities, which are the turbulent kinetic energy (k), the turbulent dissipation rate (ε) or the specific energy dissipation rate (ω) and these depend on the turbulence model applied [110] and the quantities are defined as follows:

$$k = \frac{1}{2}(u_i'^2 + u_j'^2 + u_k'^2) \tag{3.4}$$

$$\varepsilon = \rho C_\mu \frac{k^2}{\mu_t} = \frac{k^{3/2}}{l_t} \tag{3.5}$$

$$\omega = \frac{\varepsilon}{k} \tag{3.6}$$

where l_t is the turbulent length scale, μ_t is the turbulent viscosity and C_μ is an empirical constant.

The $k - \varepsilon$ models are widely used due to their simplicity and they are mainly based on the two transport equations. Most popular models are the standard ($k - \varepsilon$), RNG $k - \varepsilon$, Realizable $k - \varepsilon$ and low Reynolds number $k - \varepsilon$ models. The main differences between these models are in the turbulent viscosity calculation, the Prandtl numbers for k and ε, and the dissipation term for ε [111].

The RNG $k - \varepsilon$ model is a modified version of the standard $k - \varepsilon$ model and was developed using the Re-Normalization Group methods developed by Yakhot et al. [112]. Concerning the standard $k - \varepsilon$ model, the eddy viscosity is determined from a single turbulence length scale, hence, the calculated turbulent diffusion only takes place at the specified length scale, while in fact, the turbulent diffusion is contributed by all scales in the motion. For this reason, the RNG approach causes a modified form of the ε equation that is responsible for the different scales of motion through changes in the production term [112].

The Realizable $k - \varepsilon$ model is an improvement over the standard $k - \varepsilon$ model. In this model, new eddy viscosity and dissipation rate formulations are introduced to the standard $k - \varepsilon$ model and this makes the model more consistent with the physics of the turbulent flow, and hence the name realizable. However, the realizable $k - \varepsilon$ model is not applicable in the situation where the domain consists of fixed and rotating parts [113].

Lastly, the fourth model is the Low Reynolds $k - \varepsilon$ model which is another modified form of the standard $k - \varepsilon$ model [114]. The modification is operated by applying a damping function to the near wall region. This allows the model to account for the low Reynolds number effect in the near wall region. In the standard $k - \varepsilon$ model, the assumption of the near wall treatment for ε is not suitable, and for this reason, an additional terms, such as the damping function, is necessary to be added to the production and dissipation terms of the transport equations [110]. The main drawback of this method is the convergence issues and the sensitivity of the solution to the mesh, where a very fine quality mesh is required.

Another two-equation model is the $k - \omega$ and this is one of the most commonly used turbulence models. The $k - \omega$ model consists of two extra transport equations to express the turbulent properties of the flow, namely the turbulence kinetic energy k, and the specific dissipation rate ω. This widely employed model was introduced by Wilcox [115], and there are two different types of k-ω model, which are the standard $k - \omega$ model and Shear Stress Transport (SST) $k - \omega$ model. Compared to the SST $k - \omega$ model, the standard k-ω model is much more sensitive to the free stream and an initial value of ω is required, which results in a major disadvantage of the standard $k - \omega$ model. On the other hand, the SST $k - \omega$ turbulence model has been proposed, which combines the $k - \omega$ and $k - \varepsilon$ models to form a hybrid model and it becomes more popular than the standard $k - \omega$ model. The $k - \omega$ model is employed for the near wall region and the $k - \varepsilon$ is used away from the wall. The $k - \omega$ formulation are directly applicable in the viscous sub-layer of the inner parts of the boundary layer, since $k - \omega$ model is a low-Reynolds number turbulence model that does not need any additional damping functions [116]. Furthermore, a gradual change from the standard $k - \omega$ model in the near-wall region to a high-Reynolds-number $k - \varepsilon$ model in the far-field is realised using a blend function [117]. However, the $k - \omega$ models need to be meshed well in order to analyse the flow near the wall, and therefore, the method may be much more expensive compared to the $k - \varepsilon$ model.

Another important turbulence model is the SST Transition model that was introduced by Menter et al. [118] and it is an extended version of the SST k-ω model. In this model, there are two extra additional transport equations, which are for the intermittency, γ, and for the transition onset based on the terms of the momentum thickness Reynolds number, $Re_{\theta t}$. These additional equations are coupled with the transport equations of the SST k-ω that makes the Transition SST model a four-equation model [111]. This model has the advantages over the SST model and accounts for the Laminar-Turbulent transition and therefore this model is suitable for modelling H-type VAWTs that exhibit transition in the boundary layer [119]. In addition, one of the major factors,

which needs to be considered, the grid should be modelled with the y^+<1 in order to capture the transition behaviour and allow the transition model to work.

On the other hand, an extra equation for the intermittency, γ, can be coupled with the SST $k - \omega$ model in order to predict the laminar-to-turbulent transition more accurately. This three-equation model is an alternative to the four-equation Transition SST model [118], which eliminates the requirement of the second transport equation for the momentum-thickness Reynolds number, which is employed in the Transition SST model. Therefore, SST $k - \omega$ with intermittency model is less computationally expensive, less complex, and includes lees number of correlations compared to the Transition SST model.

As a conclusion, employing the computational fluid dynamics requires a detailed review of the turbulence models, which has been discussed in this chapter. Selecting the suitable turbulence model is significant and requires prior knowledge of the strengths and weakness of each turbulence model. The laminar-to-turbulent transition, the separation of the flow, recirculation and presence of the adverse pressure are the important flow characteristics of the H-type VAWT applications. In addition, another challenging task for computational simulation is the convergence of the solution, which also depends on the selection of the turbulence model. In this context, the recent CFD studies and the turbulence model applied for VAWT in the literature will be review in the following sections carefully. Then, the most commonly used turbulence models for the H-type VAWTs applications can be selected for the future studies.

3.3.3 Recent CFD studies with turbulence model consideration

Howell et al. [30] carried out both numerical and experimental studies in order to analyse the aerodynamics and performance of the small-scale vertical axis wind turbine. Their computed results were compared with their experimental study, which was carried out in the University of Sheffield low-speed wind tunnel by using a three straight-bladed VAWT with a NACA0022 blade profile. The results obtained show that the employed turbulence model

(RNG $k - \varepsilon$) significantly over-predicts the power coefficient in the 2D model while under-predicting the power coefficient in the 3D model, as shown in Figure 3.2. It is believed that this discrepancy is a result of the presence of the large tip vortices occurring in the experimental and 3D simulations.
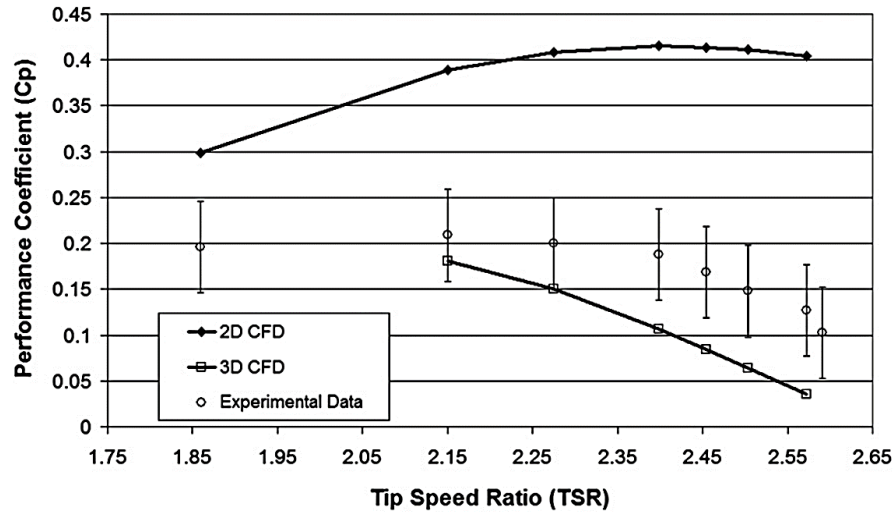
Figure 3.2. Performance coefficient for the model turbine and for the simulations [30].

Castelli et al. [120] introduced a new CFD-based model in order to predict the performance of the H-type vertical axis wind turbines. A rectangular outer domain with a circular inner domain was created. The sliding mesh method was used in order to connect the rectangular outer domain and the circular inner domain. In addition to this, a control region was built in order to improve the quality of the mesh elements in the vicinity of each blade. The realizable $k - \varepsilon$ turbulence model with enhanced wall treatment function was employed in this study. One of the main purposes of this study is to compare their results with the experimental measurements in the Bivisia low turbulence wind tunnel with a three straight-bladed VAWT using the NACA0021 aerofoil profile.

Figure 3.3 illustrates the variation of predicted power coefficient from different methods as a function of tip speed ratio. As can be seen from the figure, using the realizable $k - \varepsilon$ turbulence model with enhanced wall treatment function is able to successfully replicate the shape of the experimental curve. Although the CFD model captures the maximum power coefficient at the tip

speed ratio as obtained in the experimental result, which is about 2.65, it significantly over-predicts the performance.
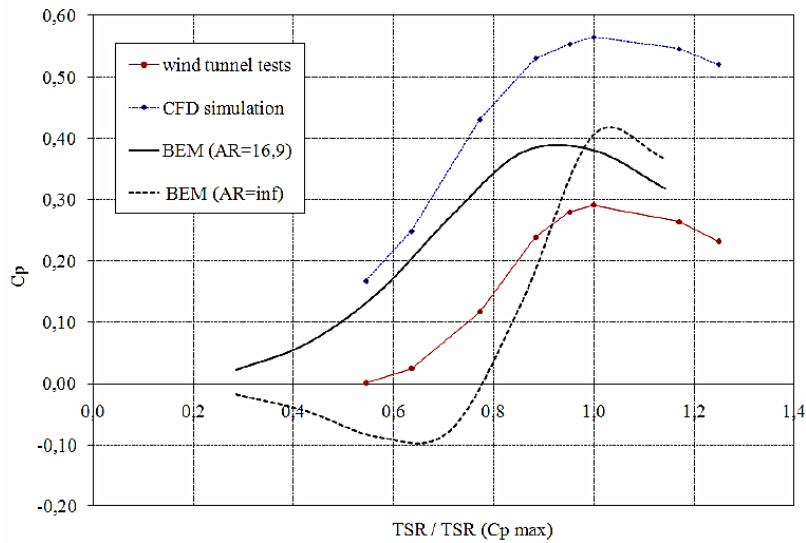
Figure 3.3. Comparison between the wind tunnel measured and CFD simulations [120].

Edwards et al. [121] employed the SST $k - \omega$ turbulence model in order to simulate a three-bladed H-type VAWT using the NACA0022 aerofoil profile and compared their numerical results with their experimental measurements. They claim that the SST $k - \omega$ turbulence model is the most appropriate model to employ and significantly better predicts the physics of the flow around the aerofoil. The results show that the 2D CFD model over-predicts the power output and this is due to the 3D effects and the losses at the blade tip. However, in terms of the flow field, the CFD flow field prediction indicates the similar pattern of the roll-up and shedding of pairs of stall vortices from the PIV measurements, as shown in Figure 3.4. Even though the delay on the stalling and reattachment in the CFD prediction can be observed, the SST $k - \omega$ turbulence model provides satisfactory results and has been performed by many authors (e.g. 122, 123, 124]). The reason for the observed delay in the CFD prediction might be due to the inability of the model to accurately predict transitional flow in the low Reynolds number region.
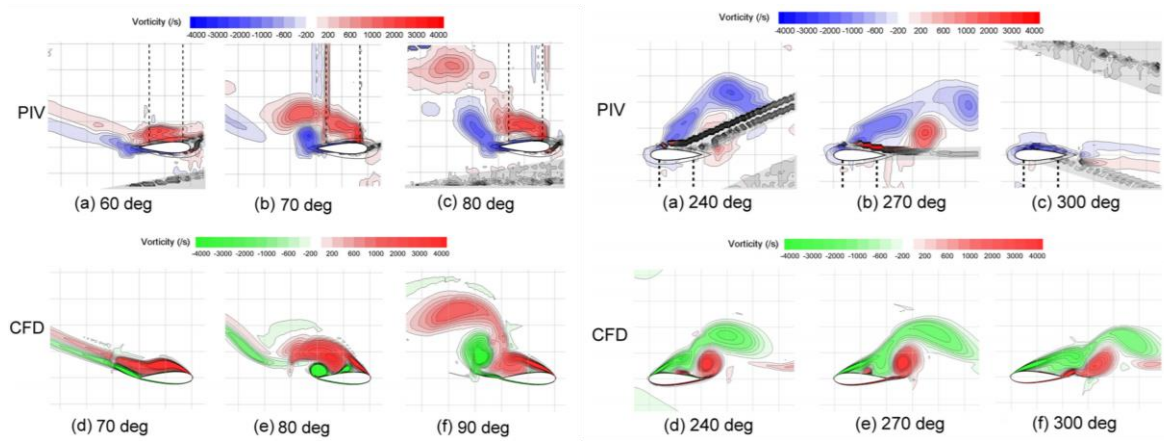
Figure 3.4. Predicted CFD flow field comparison with the experimental data [121].

Mohamed [35] conducted another comprehensive study in order to obtain the best aerofoil profile. A 2D CFD model was used to compare 20 different aerofoil profiles (Figure 3.5) by employing the realizable $k - \varepsilon$ turbulence model. The results show that the use of S-1046 aerofoil profile leads to a relative increase of the power coefficient by 28.83%, and an absolute increase in the efficiency by 10.87% compared to the widely used symmetrical NACA aerofoil profiles. Moreover, the low solidity was recommended for the H-type vertical axis wind turbines in order to obtain a wider operating range.
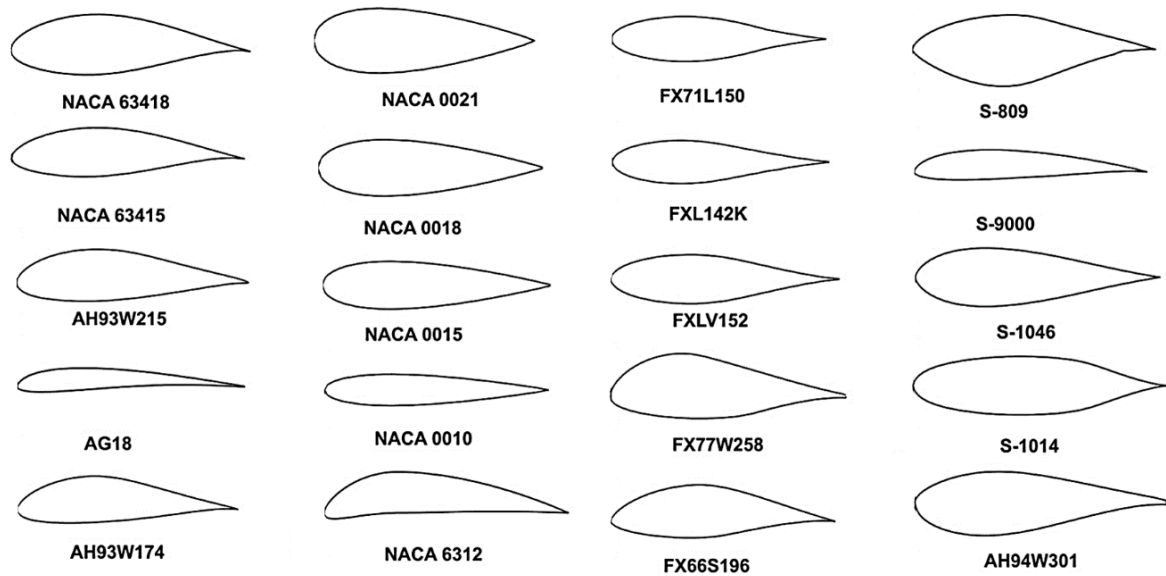
Figure 3.5. Different aerofoil profiles analysed by Mohamed [35].

Lanzafame et al. [125] modelled the H-type vertical axis wind turbine using the SST $k - \omega$ and the Transition SST turbulence models in order to evaluate the rotor performance. It has been found that the SST $k - \omega$ turbulent model over-predicts the lift coefficient (C_l) and under-predicts the drag coefficient (C_d) in the near stall region: however, a much closer prediction of the lift and drag coefficients is obtained with the Transition SST model for a wide range of the angles of attack (Figure 3.6). Moreover, the Transition SST model has been also applied to the whole turbine simulation to predict turbine power performance (Cp). The results show that due to the fact that tip vortices were neglected in the 2D CFD studies, the transition model slightly over-predicted the Cp.
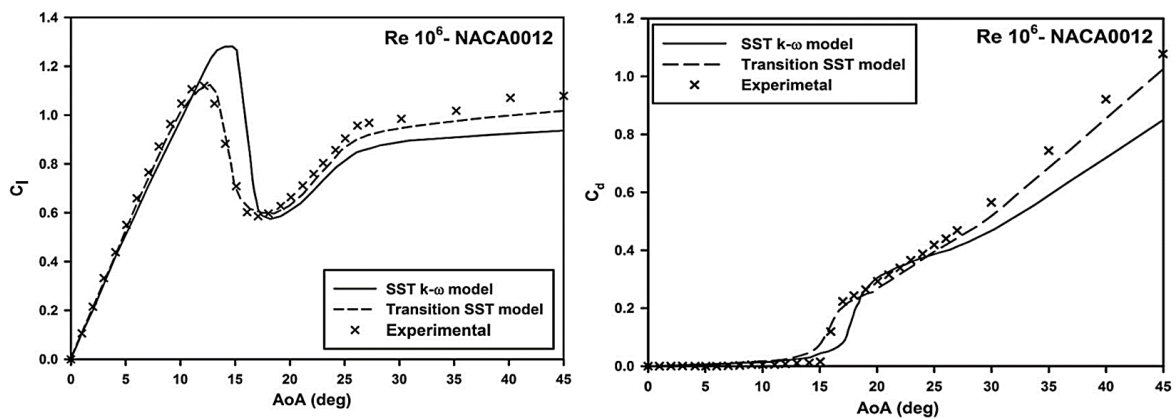
Figure 3.6. The variation of C_l and C_d with the angle of attack using different turbulence model and comparison with the experimental data [125].

A comprehensive study was conducted by Daróczy et al. [126] in order to obtain the most suitable turbulence model for the H-type vertical axis wind turbines. In this study, four different experimental results have been used to compare the numerical results by employing the realizable $k - \varepsilon$ with enhanced wall treatment and standard wall function, RNG $k - \varepsilon$, S–A, scale-adaptive simulation (SAS), SST $k - \omega$, $k - \omega$, transitional k– kl–ω, and Transitional SST turbulence models. They concluded that the realizable $k - \varepsilon$ with enhanced wall treatment model was able to predict the optimum tip speed ratio location correctly in all four cases. On the other hand, the SST k-ω model indicates an excellent prediction for the first three cases.

Balduzzi et al. [127] highlighted the important issues related to the CFD simulations and crucial parameters concerning the meshing and time step in the H-type VAWTs. The most critical parameters have been chosen to analyse their mutual effects when they are employed together. In addition, the advantages and disadvantages of the proposed approach were discussed. The most appropriate parameters have been applied in order to simulate the real turbine geometry by using the SST $k - \omega$ turbulence model. Then, the results obtained from the numerical studies were compared with the experimental study. As it can be seen from Figure 3.7 that the good prediction can be obtained by using the 2D CFD approach by employing the SST $k - \omega$ turbulence model.
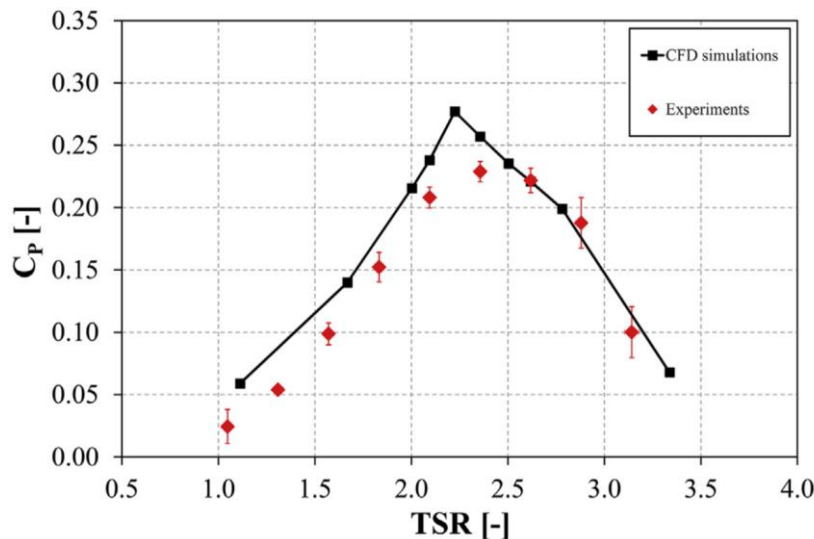
Figure 3.7. The comparison between numerical result and experimental data [127].

Subramanian et al. [128] employed 3D CFD models in order to investigate the effect of the solidity and the aerofoil profile on the performance of the H-type vertical axis wind turbines. The Transition SST turbulence model was used due to the fact that the turbine operates in the low Reynolds number region. The current findings were compared with the result obtained from the experimental study [129] and another 2D CFD study [130]. The results show that the current results and experimental data are in a good agreement with a maximum error of 16.3% corresponding to λ of 0.87, as shown in Figure 3.8. In addition, among all

the aerofoil profiles, the thicker aerofoil, which is the NACA0030, indicates the maximum power coefficient for the low tip speed ratios due to long durations of the attached flow. Moreover, the power coefficient observed in a 2-bladed turbine is higher than that of a 3-bladed turbine at the high tip speed ratios due to the increased occurrence of vortex interactions with the blades with higher solidities. However, at the low tip speed ratios, high solidity turbines are recommended because the interaction of the blades with the wind is better.
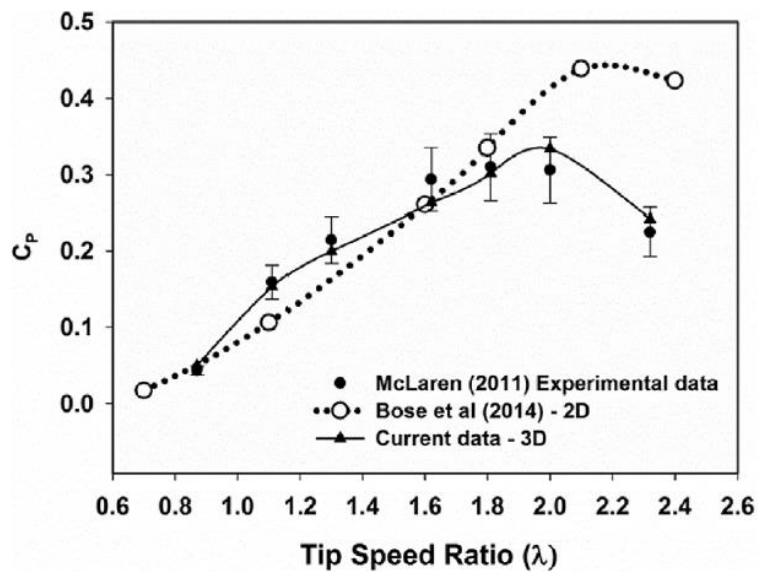
Figure 3.8. Comparison of results obtained by McLaren [129], Chandramouli et al. [130] and the current data [128].

Wang et al. [131] proposed a 2D CFD model to analyse the H-type vertical axis wind turbines with different thickness of the aerofoils and various type of aerofoil profiles. For the process of the turbulence model validation, the average Cp values of the turbine for SST $k - \omega$, realizable $k - \varepsilon$, and S–A turbulence models were compared with the results of Castelli et al. [120] as shown in Figure 3.9. The results show that the trend obtained with the SST $k - \omega$ turbulence model appears to be most accurate. On the other hand, the maximum power coefficient obtained by Wang was 0.3745, while Castelli et al. [47] obtained 0.56, which was very close to the Betz limit and appears to be impractical.
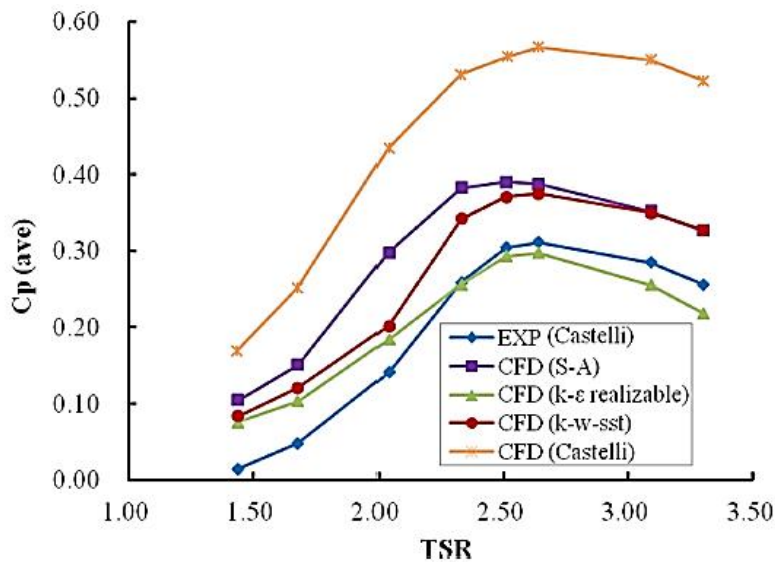
Figure 3.9. Comparison between experiment in a wind tunnel measurement and 2D CFD simulation results [131].

Ma et al. [132] adopted a 3D CFD model in order to calculate the aerodynamics of the H-type vertical axis wind turbines since the 3D model can generate more accurate results than a 2D CFD model. The aim of this study is the aerofoil optimization of a high solidity three-bladed H-type vertical axis wind turbine at the moderate tip speed ratios to improve the power performance of the turbine. For this purpose, the SST $k - \omega$ turbulence model was selected due to the consideration of the balance between accuracy and computational cost. Figure 3.10 illustrates the comparison results with the relative errors between numerical and experimental data. As it can be seen from the figure that the largest error occurs at λ=0.5 with the value of 17.15% and the second largest error appears with the value of 14.99% at λ=0.6. Overall, it can be concluded that the numerical results are reasonable and consistent with the experimental data.
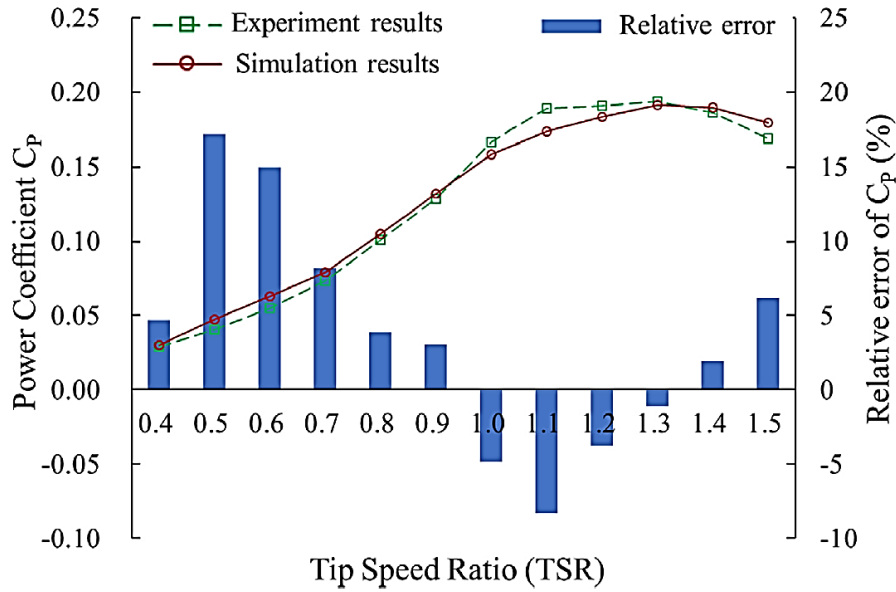
Figure 3.10. Comparison of average power coefficients between the experiment and as well as relative errors of them [132].

Elsakka et al. [133] proposed a new method in order to calculate and store the angle of attack during the CFD simulations. Therefore, the 2D CFD model with the SST $k - \omega$ turbulence model was created. The experimental and CFD data obtained by Li et al. [134] has been used for the model validation, and this includes the torque coefficient distribution over one cycle. The comparison illustrates that the predicted 2D CFD model under-predicts the torque coefficient in the range of azimuthal angle between 0° and 60°, while the model over-predicts the torque coefficient over the rest of the cycle, as shown in Figure 3.11. The authors claim that the main reason for this discrepancy between the 2D CFD prediction and the experimental data might be the negligence of the 3D effects, which are the supporting arms and blade tip losses. Therefore, the current 2D CFD results appear to be reasonably accurate, particularly downstream part of the turbine where complex flow structure exists.
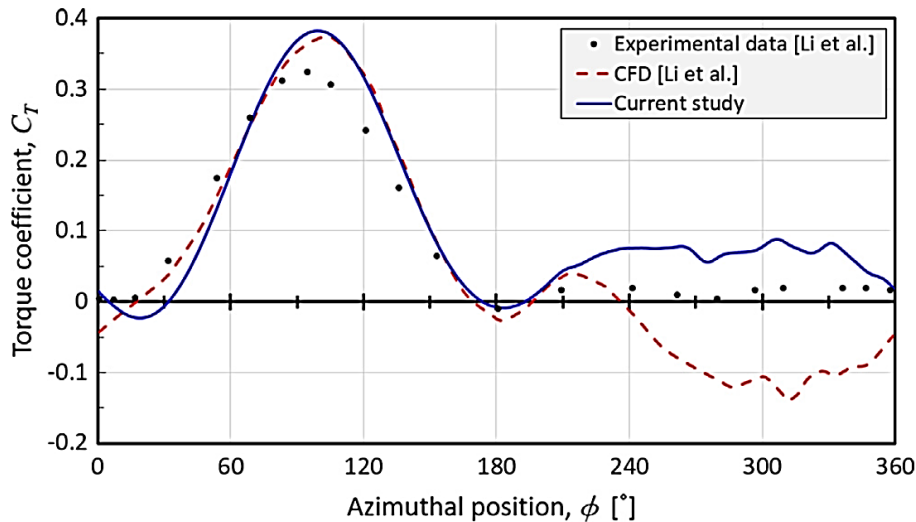
Figure 3.11. A comparison between the experimental and the numerical data for the single blade torque coefficient over a complete turbine rotation [133].

Mohamed et al. [135] presented a 2D CFD model in order to analyse the performance of the three-bladed H-type vertical axis wind turbine employing 25 different aerofoil profiles from different families. For this purpose, the quantitative and qualitative validation studies were presented. For the CFD validation studies, SST $k - \omega$ turbulence model was used and it was found that an acceptable agreement between the predicted CFD result and the published experimental data in the calculation of the power coefficient. Moreover, the authors claim that the optimum design of the Darrieus turbine consisting of an LS (1)-0413 aerofoil profile is very promising for wind energy conversion, in particular in remote and urban regions.

Mazarbhuiya et al. [136] investigated the effect of the blade thickness-to-chord ratio on the aerodynamic performance of an asymmetric NACA six series bladed H-type vertical axis wind turbine at different low wind speed conditions. The 4-equation turbulence model, Transition SST, has been applied in the 2D CFD calculations, and the results were compared with the experimental study. As can be seen in Figure 3.12, the results show that the trend on the power coefficient of the 2D CFD model over predicts in contrast to the experimental study. The authors claim that this discrepancy is mainly due to the blade tip losses, strut losses, which are not considered in the 2D CFD simulations.
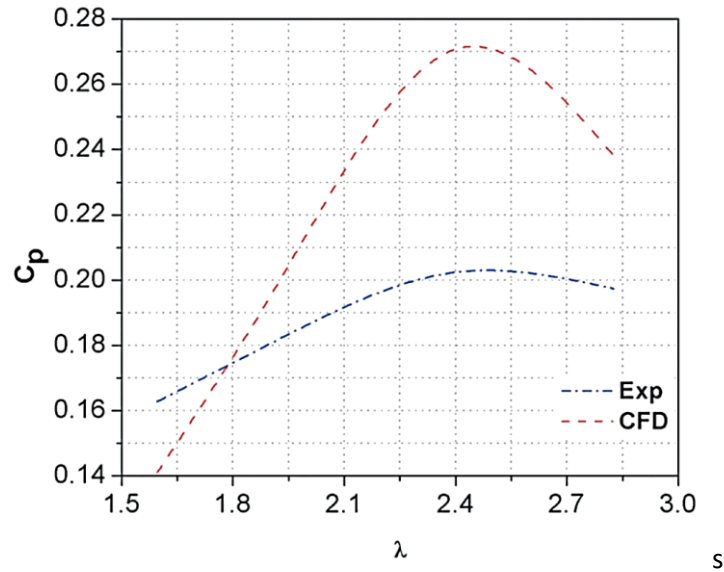
Figure 3.12. Validation of the CFD results with established experimental results [136].

3.3.4   Summary of the CFD models and turbulence models

In this thesis, the CFD models will be built to study the performance of the H-type VAWT as well as the self-starting behaviour of the turbine. According to the literature survey, the 2D model is able to reveal the most important factors that might affect turbine performance and flow physics. The overall performance of the turbine and the flow structure under different design parameters have been investigated and special attention has been paid to the performance of the turbine at low λ values.

In addition, selecting a suitable turbulence model is significant and prior knowledge of the strengths and weaknesses of the different turbulence models are essential. A detailed review of the turbulence models has been discussed in this chapter. Several turbulence models employed in the literature have been investigated in terms of turbine performance. It has been found that three turbulence models, namely k-ε Realizable turbulence model with the enhanced wall treatment function, SST $k - \omega$ turbulence model and Transition SST turbulence model, are generally employed. However, the Enhanced wall treatment $k - \varepsilon$ Realizable turbulence model generally over-predicts the results compared to the experimental data. In contrast, the results obtained by using

the SST $k - \omega$ and Transitional SST turbulence models provide much closer results to the experimental data. However, according to ANSYS [152] the Transition SST model is not recommended for the domains with moving walls. For this purpose, for the validation part of this thesis and future investigations, the SST $k - \omega$ turbulence model will be employed. A summary of the studies using different CFD models and turbulence models are listed in Table 3.2.

Table 3.2. Summary of recent CFD studies.

Authors	Year	Topics	Dimension	Turbulence model
Howell et al. [30]	2010	Solidity, Blade surface roughness, 3D effect	2D, 3D	RNG $k - \varepsilon$
Castelli et at. [120]	2011	Aerodynamic force, Power coefficient	2D	Realizable $k - \varepsilon$
Edwards et al. [121]	2012	Turbulence model validation, Flow structure analyse (PIV)	2D	SST $k - \omega$
Mohamed [135]	2012	Aerofoil profiles	2D	Realizable $k - \varepsilon$
Lanzafame et al. [125]	2014	Turbine performance, turbulence model comparison	2D	SST $k - \omega$, Transition SST
Daróczy et al. [126]	2015	Turbulence model comparison,	2D	Realizable and RNG $k - \varepsilon$, S–A, SAS, SST $k - \omega$, Transitional $k - kl - \omega$, Transitional SST
Balduzi et al. [127]	2016	CFD model validation with highlighted critical issues related to CFD	2D	SST $k - \omega$
Subramanian et al. [128]	2017	Solidity, Aerofoil profiles	3D	Transition SST
Wang et al. [131]	2018	Aerofoil thickness and profile	2D	SST $k - \omega$, Realizable $k - \varepsilon$, S-A
Ma et al. [132]	2018	Aerodynamic force, Power performance	3D	SST $k - \omega$
Elsakka et al. [133]	2019	AoA prediction	2D	SST $k - \omega$
Mohamed et al. [135]	2019	Aerofoil profiles	2D	SST $k - \omega$
Mazarbhuiya et al. [136]	2020	Blade thickness-to-chord ratio	2D	Transition SST

3.4   Conclusion

In the present chapter, the modelling techniques of H-type vertical axis wind turbines have been discussed in detail. These models can be classified into two categories, namely mathematical models, including momentum, vortex, and cascade models, and computational fluid dynamic model.

There are many aerodynamic models that have been employed to predict the performance of the H-type VAWT before performing the experimental measurements. However, many performance parameters that were investigated using the mathematical models are not appropriate for providing a full understanding of the flow physics. Nowadays, researchers have begun to take more precise approaches to investigate the flow physics, such as the development of CFD modelling and the improvements in the experimental capabilities, e.g. Particle Image Velocimetry (PIV). Therefore, researchers have been beginning to gain a better understanding of the effects of the fundamental design parameters and aerodynamic models in predicting the performance of the H-type VAWTs.

In conclusion, the CFD modelling approach based on the uRANS turbulence modelling is an appropriate way to be used due to its lower cost and fast speed of obtaining results compared to the more expensive DNS and LES. For the present thesis, the CFD model has been chosen for the numerical analyses of the turbine performance including the self-starting behaviour and the complex flow structure around the turbine blades. On the other hand, the selection of the turbulence model also plays a crucial role to obtain the predicted results accurately. In this context, among all turbulence models reviewed in the present chapter, the recommended SST $k - \omega$ turbulence model appears to one of the promising models that provide a much closer results to the experimental study compared to the other two-equation turbulence model. Therefore, the SST $k - \omega$ is employed in the CFD turbine investigations in this thesis.

Chapter 4

Development and validation of CFD models for turbine starting-up process

4.1   Introduction

The CFD may be applied to the vertical axis wind turbine (VAWT) simulations due to their ease and accurate predictions compared to the other types of methods such as the Blade Element Momentum model. The aerodynamic force coefficients, pressure distribution over the aerofoil surface, and the flow field can be easily examined using the CFD codes. The development of the computational model used in all the 2D CFD turbine simulations in this thesis is presented in this chapter. Furthermore, a detailed description of the computational model characteristics, such as the boundary conditions including the inlet and outlet, the mesh around the aerofoils and the stationary and rotating domains is presented. Then, the sensitivity studies of domain size, number of nodes around the aerofoil, and time-step size are also presented. Finally, the predicted numerical results are compared to the experimental

studies in order to observe their capability in predicting the performance, such as the aerodynamic force coefficients and self-starting behaviour.

4.2   2D CFD H-type VAWT study

A 2D CFD model has been employed to represent the H-type VAWT since the literature [121, 122, 123] has illustrated that 2D CFD models are able to reveal the most important factors that affect the overall performance of the turbine and the flow physics. There are 3D effects, such as the secondary flow in the span-wise direction and blade tip vortex that may be significant and these will be considered in Chapter 8 of the present thesis.

4.2.1   Model description

There are few experimental studies available in the literature in terms of the turbine self-starting. For this reason, a published experimental data, carried out by [137] has been selected in order to validate the CFD start-up model. One advantage of the selected experimental study is that it allows for a direct comparison of the transient behaviour of the turbine self-starting process rather than only the calculated overall torque and power coefficients. Furthermore, in the experimental study, an open jet wind tunnel, which eliminates the sidewall interference, has been used since open jet tunnels remove the blockage occurring in closed wall tunnels. In this thesis, the geometry of the investigated VAWT has been created based on the setup of the experiment by Rainbird [137]. The turbine is constructed of three NACA0018 aerofoils. The ANSYS Design Modeller has been used to create the CFD model, and Table 4.1 summarised the main characteristics of the wind turbine.

Table 4.1. Turbine Configurations.

Name	Value	Unit
Blade Profile	NACA0018	-
Number of blades	3	-
Span height	0.6	m
Chord length	0.083	m
Radius	0.375	m
Rotor moment of inertia	0.3	kgm^2

A pressure-based solver, SIMPLE, which uses a relationship between the velocity and the pressure corrections to enforce the mass conservation, was applied to the simulations with a gradient called Green-Gauss Node Based. The second-order upwind scheme that provides a better balance between accuracy and robustness is used for the discretization of the convection terms of the momentum and turbulence model equations [154]. In order to assess the sensitivity of the results in terms of the number of iterations and residual convergence criteria, the simulations have been run using a different number of iterations and the magnitudes of the convergence criteria. The results show that each time step requires at least 25 iterations to reduce all the residuals to five orders of magnitude, and this finding is in agreement with [138]. The turbulent intensity of the wind tunnel is unknown in the experimental study; therefore, a sensitivity analysis has been also conducted in order to define the turbulent intensity and viscosity ratio, and these have been chosen as 1% and 10, respectively.

In the conventional approach of the CFD simulations of VAWT, several constant rotational speeds are defined for the rotor, and the torque is calculated for each rotational speed. However, in this study, a method based on the interaction of the fluid and turbine has been employed. In this method, the solution starts where the turbine is at rest and the instantaneous aerodynamic torque corresponding to the turbine instantaneous position can be calculated using the aerodynamic lift and drag forces that are obtained through the solution of the Navier-Stokes equations. After that, in the next time step, the acceleration and the new rotational speed of the turbine can be obtained by using the equation of the motion taking into consideration the moment of inertia and the resistive torque (if available). This procedure will be repeated to calculate the new aerodynamic forces and the new rotational speed for the next time step and continued until the turbine reaches its final rotational speed at the steady-state condition. The mathematical procedure of the current method is demonstrated in Figure 4.1. According to this procedure, the 6 degrees of freedom (6DOF) user-defined function (UDF), which includes the physical characteristics of the

turbine and its moment of inertia, has been written in the C language and linked to the ANSYS Fluent solver under the dynamic mesh zone section. A typical example of the UDF code used in the 2D CFD start-up simulations is provided in the Appendix. In addition to this, only one degree of freedom, which rotates around the turbine z-axis, has been considered. In the experimental setup, the turbine moment of inertia was stated as $0.018 \, \text{kgm}^2$; however, the moment of inertia was recalculated for the 2D CFD simulations by considering the height of the turbine as 1m, instead of 0.6m (in the experiment). Therefore, the newfound value for the inertia was 0.03 and the predicted result is consistent with [139].

All simulations were performed on the HPC (High-Performance Computing) facilities provided by the University of Sheffield and when 16 cores were used, the time spent on each simulation was at least 7 hours.
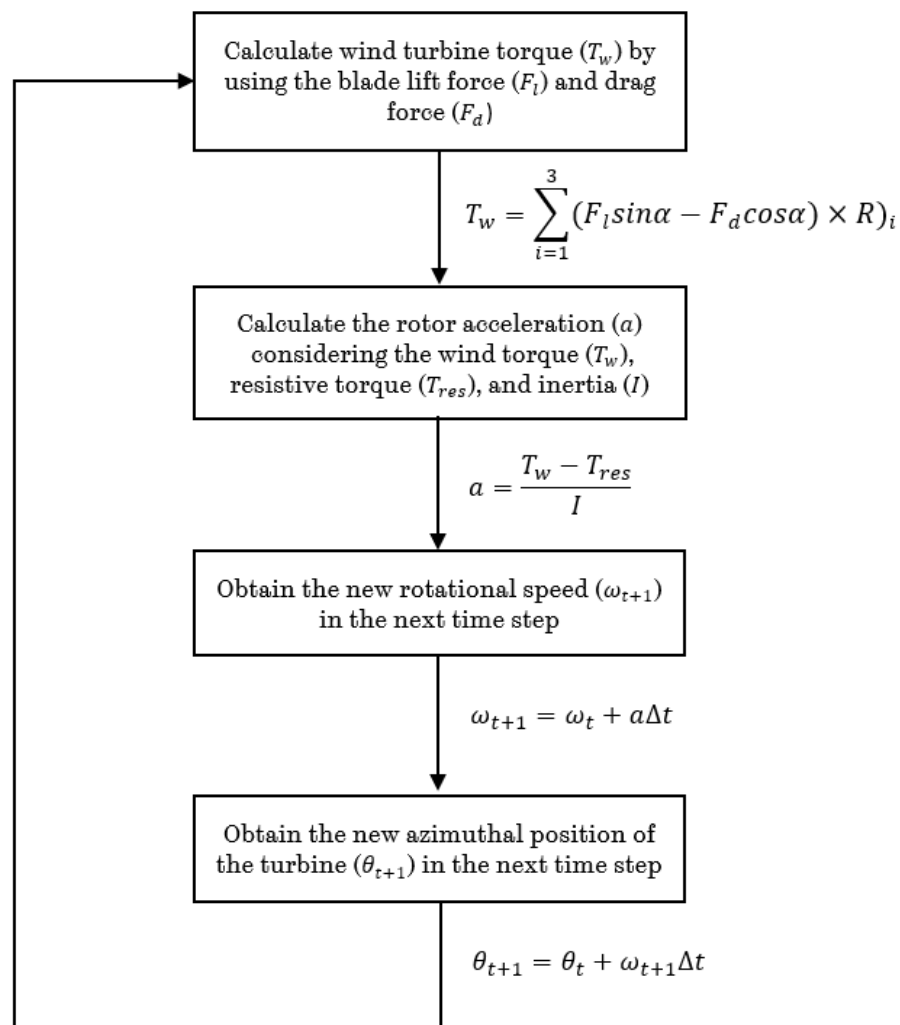
Figure 4. 1. Mathematical procedure of the current numerical model.

4.2.2 Model sensitivity studies

In this section, parametric studies were performed in order to yield a precise model that is used to make a comparison between the present results and the experimental data. It includes the domain size, number of nodes around the aerofoil, and time-step independence studies. The parametric studies were conducted at both low (λ=1.5) and relatively high (λ=3) tip speed ratios in order to ensure that each selected parameter in this study can produce accurate results for the entire self-starting procedure.

Furthermore, selecting the turbulence model plays a significant role, especially at the low λ due to the complex flow structures of the VAWT. Therefore, according to a detailed literature review on the turbulence models conducted in Chapter 3, it has been found that the two-equation turbulence models, such as k–ε and k–ω, are commonly used for the simulations, and the SST k–ω model has become very popular for VAWT simulations [140]. The model is directly applicable in the viscous sub-layer in the vicinity of the aerofoil without using additional damping functions [141]. In this context, the SST k–ω turbulence model has been preferred in many CFD simulations and validated experimentally by researchers [75, 127, 142, 143, 144, 145, 146, 147]. Therefore, the SST k–ω turbulence model is employed in the model sensitivity studies and further investigations.

4.2.2.1 Domain size study

The computational domain, as shown in Figure 4.2 is decomposed into a rotational domain, which contains the rotor, and a fixed rectangular outer domain. The two regions are connected using interface conditions to ensure that the continuity in the flow field is established. The velocity condition is applied to the left side of the computational domain with a constant velocity profile of *6m/s,* and this value is selected according to the experimental conditions [137]. A zero gauge pressure outlet is imposed on the right side of the computational domain, and the blade surfaces are considered as no-slip boundaries. Two symmetry boundary conditions were implemented at the top and bottom sides

of the computational domain in order to reduce the impact of the blockage effect [147].

As indicated in Figure 4.2, A is the distance between the velocity inlet and the centre of the turbine, B is the distance between the centre of the turbine and the pressure outlet, C is the distance between two symmetry boundaries, D is the radius of the circular subdomain that is associated with the region of the turbine, and E is the radius of the small circular subdomains that are located at the vicinity of the blades to increase the mesh intensity in these regions. In order to perform a sensitivity study to determine the required computational domain size, three different cases, namely Domain 1, Domain 2 and Domain 3, have been investigated, and the values of each case are shown in Table 4.2. The values for the Domain 1 have been selected according to Zhang et al. [148], and then these values have been proportionally increased for Domain 2 and Domain 3 to find optimum values for the size of the computational domain. The domain size independent study has been conducted at a relatively small tip speed ratio of 1.5 and at a tip speed ratio of 3 in order to ensure that the results do not show any discrepancies at these two very different tip speed ratios.

Table 4.2. Computational domain sizes for the validation study.

Name	Values				
	A	**B**	**C**	**D**	**E**
Domain 1	6r	24r	12r	2r	0.5r
Domain 2	8r	32r	16r	2.5r	1r
Domain 3	10r	40r	20r	3r	1.5r
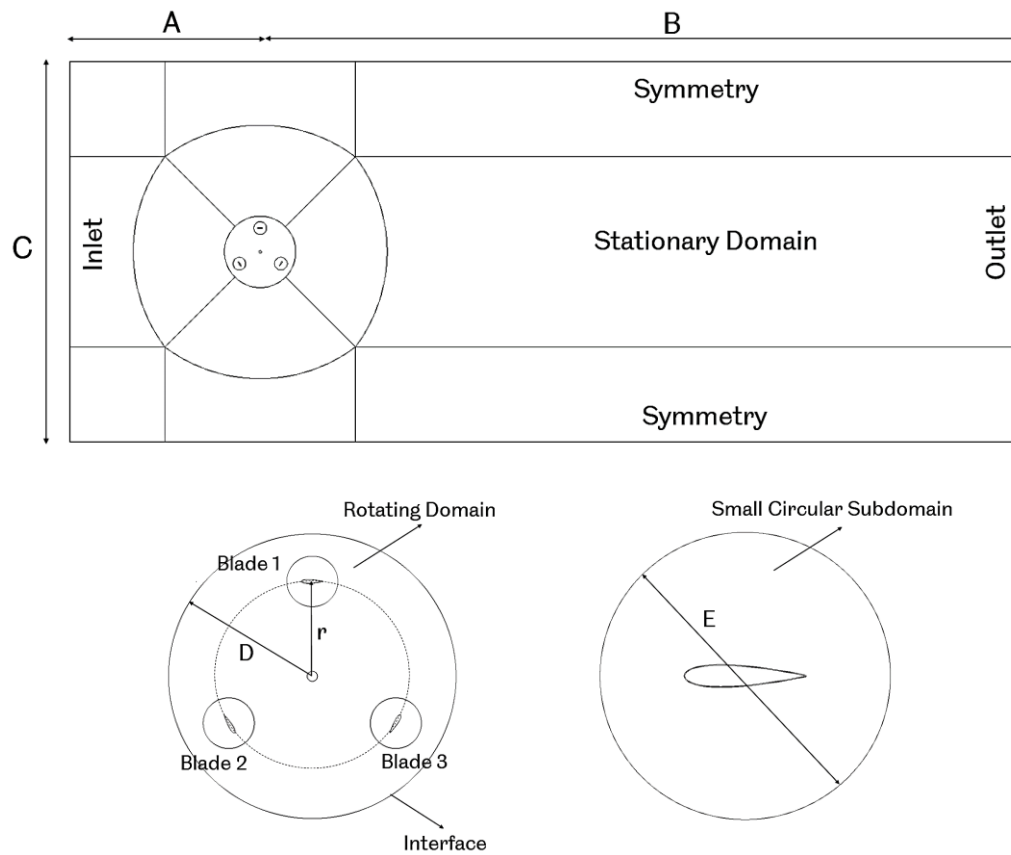
Figure 4.2. Schematic of the domain created for the computations.

The blade moment coefficient as a function of the azimuthal angle for both the tip speed ratios is plotted in Figure 4.3, and it is observed that the results for the Domain 2 matches closely to that of Domain 3 for both tip speed ratios while the result for the Domain 1 is different. Therefore, Domain 2, which has the dimensions of 40r and 16r in the directions parallel and perpendicular to the free stream velocity, respectively, has been chosen for the further self-starting simulations of VAWT in this thesis. Furthermore, using the computational domain with 32R distance from the turbine centre to the domain outlet is determined to be a safe choice in order for the domain to be sufficiently large so that the wake fully develops inside the computational domain, and this is consistent with other relevant studies [149, 150, 151].
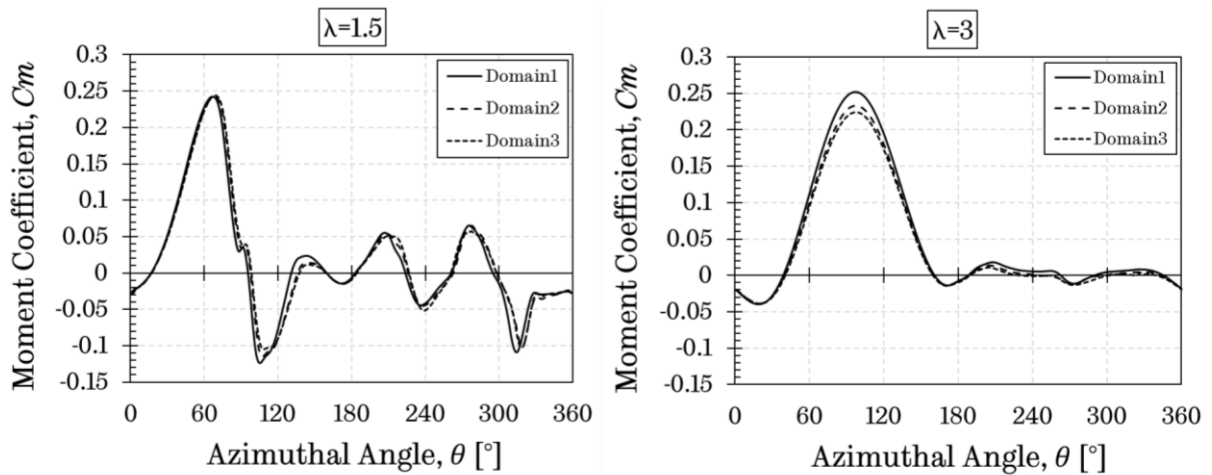
Figure 4.3. The moment coefficient as a function of the azimuthal angle for the domain size study at λ=1.5 and λ=3.

4.2.2.2 Grid topology

One of the most critical parts of the CFD simulations is the mesh generation due to its impact on the accuracy of the model. The behaviour of the flow within the boundary layer is a complicated phenomenon. Therefore, in order to define the order of the magnitude for the size of the cells in the boundary layer region, the dimensionless wall distance, namely y^+, should be determined according to the turbulence model [152]. In order to allow the turbulence model to predict the performance, at least 10 layers of cells should be employed within the boundary layer [153]. In the present study, 15 mesh layers with the first cell height of about 2×10^{-5}m have been used in order to obtain a maximum non-dimensional wall distance y^+ value of 2.5 and average $y^+ < 1$. By maintaining these values, a proper estimation of the aerodynamic forces in the boundary layer can be achieved [133, 154].

A hybrid mesh is chosen as the most appropriate mesh type in this study since the hybrid mesh provides a flexible approach and reduces the number of mesh elements in the computational domain. As can be seen from Figure 4.4, the hybrid mesh consists of a structured mesh used for both around the aerofoil and in the far field, while an unstructured mesh is employed for the rotating domain.
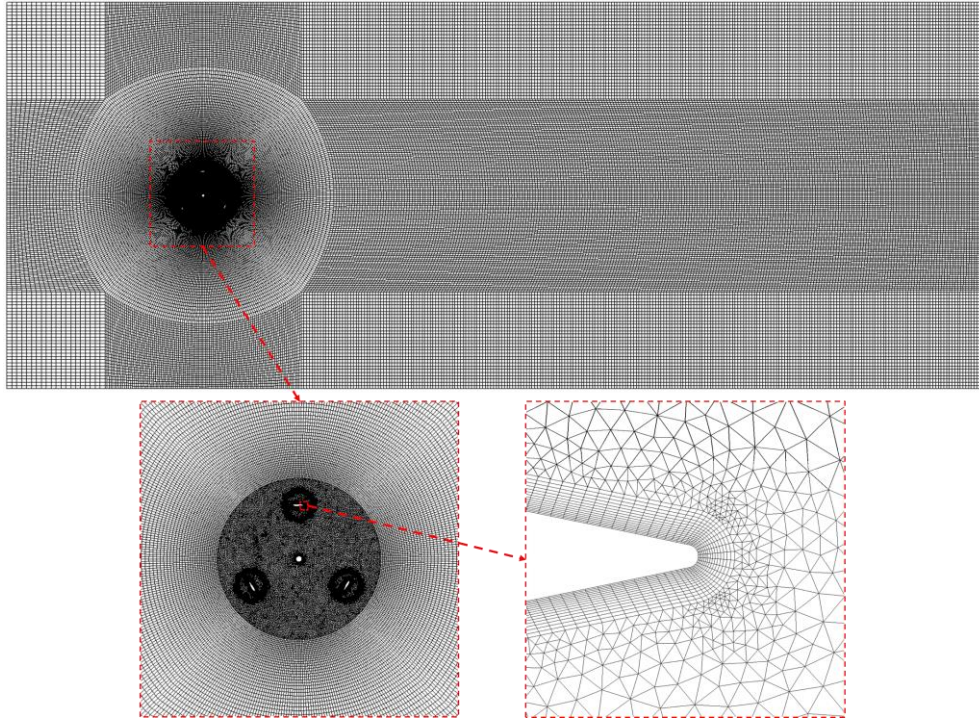
Figure 4.4. Grid configurations for the whole domain, the rotating domain and at the vicinity of the blade.

Three different number of nodes, as shown in Table 4.3, have been investigated to obtain an optimal number of nodes around the aerofoil at two different λ values. For this purpose, Nodes 1, 2, and 3, which have 800, 1000, and 1200 nodes, respectively, were created by using the ANSYS Meshing Module. The grid sensitivity study was performed based on these three sets of nodes around the aerofoil. The Grid Convergence Index (GCI) [155] was calculated based on the 2D turbine power coefficient using a safety factor 1.25 [156] for both tip speed ratios (λ=1.5 and λ=3). The $\mathrm{GCI_{fine}}$ for the Node 2 - Node 3 pair are found to be about 1.2×10^{-3} and 2.2×10^{-3} for λ=1.5 and λ=3, respectively and this corresponds to about 1.56% and 0.6% of the 2D turbine power coefficient, respectively.

Table 4.3. The number of nodes around the investigated aerofoil.

	Values		
	Node 1	**Node 2**	**Node 3**
Number of Nodes	800	1000	1200

Furthermore, a comparison of the results on the moment coefficients as a function of the blade azimuthal angle for the different number of nodes at the two λ are presented in Figure 4.5. As can be seen from the figures, there is a negligible difference in the moment coefficients over all azimuthal angles between Nodes 2 and 3 at both tip speed ratios while Node 1 is different. Therefore, the most reasonably accurate and computationally economic number of nodes are found to be 1000 at both λ values and chosen for the further self-starting simulations of the VAWT in this study. The mesh having 127,000 elements in the rotating domain and 77,000 elements in the fixed domain has been created after the sensitivity study was performed.
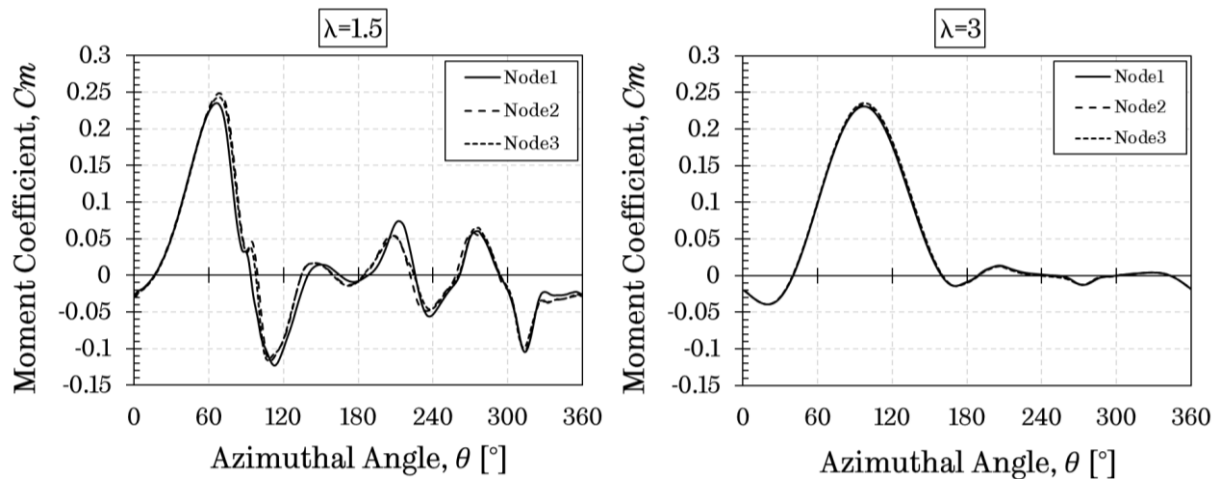
Figure 4.5. The moment coefficient as a function of azimuthal angle for the nodes study at λ=1.5 and λ=3.

4.2.2.3 Time step size study

For the time step size study, three time steps, which are $\Delta t1 = 0.00144$s, $\Delta t2 = 0.00072$s, and $\Delta t3 = 0.00036$s, were examined to evaluate the impact on the results concerning the length of time steps. According to the results, which are shown in Figure 4.6, there is only a slight difference observed between $\Delta t2$ and $\Delta t3$ with the identical trend in the moment coefficient at both tip speed ratios. Therefore, $\Delta t2 = 0.00072$s is selected for further simulations to reduce the computational time and it is consistent with other researches [75, 157].
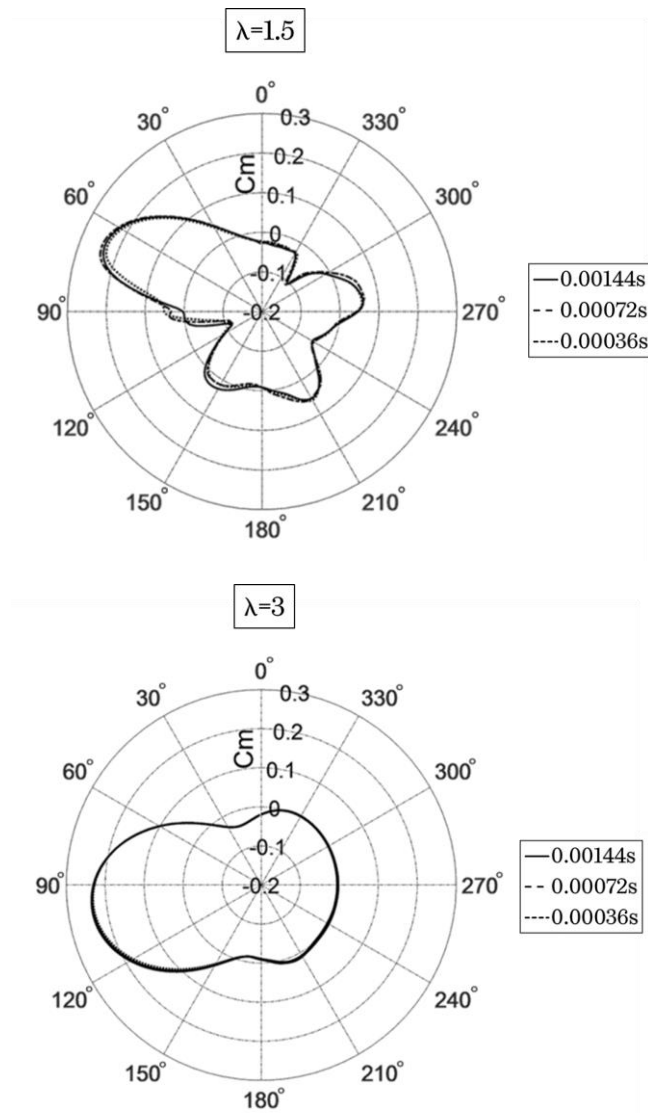
Figure 4.6. The moment coefficient as a function of azimuthal angle for the time step size study at λ=1.5 and λ=3.

It is important to note that in all the verification studies, namely the domain size, number of nodes around the aerofoil, and the time step size, the moment coefficients are calculated at the 20th revolution in order to reach the statically steady-state condition for both tip speed ratios investigated. This number of revolutions is sufficient and consistent with the published guideless for the CFD simulations of the VAWTs [156].

4.2.3 Model validation

Figure 4.7 shows a comparison between the current CFD prediction with the experimental data obtained by Rainbird [137]. It can be seen from the figure that the current CFD model is able to predict the self-starting behaviour of the turbine. However, to make it easier to understand the comparison between the experimental and the current numerical results, the non-dimensional time axis, which is defined as t/T (T is the time when the steady-state condition is reached) is employed. The time required to reach steady-state condition is about 150 seconds in the experiment while it is about 15 seconds in the present 2D CFD study. The finding of the current study is consistent with those of Untaroiu et al. [157], Zhu et al. [139], and Torabi et al. [75] who found the start-up time as about 18 seconds, 10 seconds, and 12 seconds, respectively.
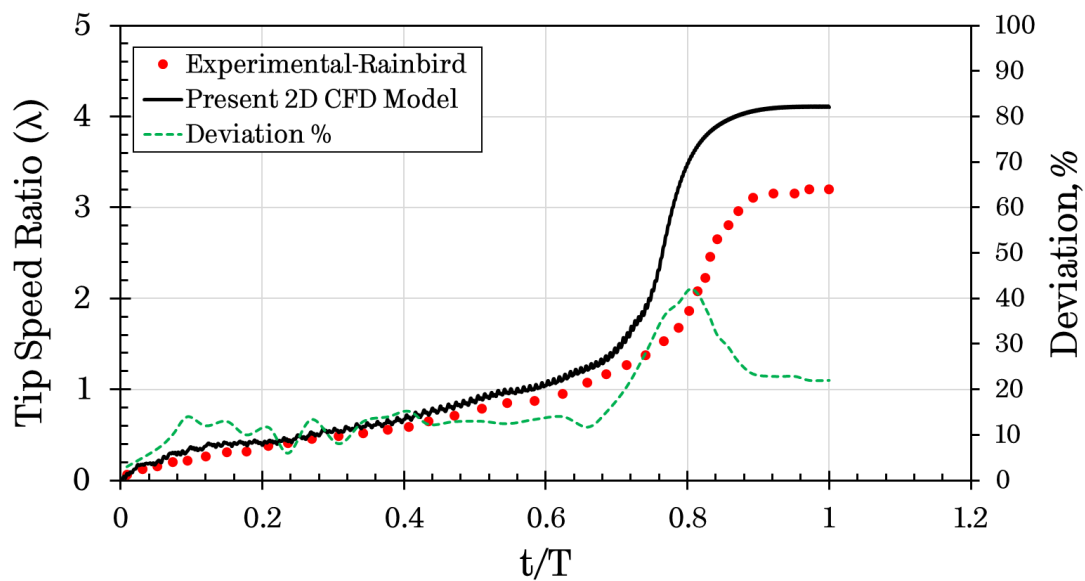
Figure 4.7. The variation of the tip speed ratio as a function of the normalized time for comparison of the present 2D CFD model with the experimental data, and deviation between CFD and experiment as a %.

As it can be seen in Figure 4.7 that the turbine accelerates continuously in the experiment and reaches its steady-state condition at a tip speed ratio of about 3.2, while the CFD model result shows a similar behaviour; however, the

operating λ is about 4.1. Furthermore, the deviation between the current CFD prediction and experimental data in terms of the instantaneous tip speed ratio is also presented in Figure 4.7. As it can be seen from the figure that the maximum discrepancy is observed to be around 40% in the acceleration region (0.7<t/T<0.82) due to a slight delay in approaching to the acceleration period. However, this discrepancy decreases to around 21% when the turbine reaches its steady-state position.

The observed discrepancies between the experimental data and 2D CFD results could be explained to be a result of the following:

- The existence of the 3D effects, such as the blade supporting arms and tip losses, which the 2D CFD model does not take into account [120, 139].

- Other additional sources of resistive torque, namely the bearing friction and generator losses, may result in the over-prediction of the predicted results compared to the experimental data [75].

- The uncertainties related to the experimental data, such as the blade-spoke connection is not clearly mentioned in the experiment data, carried out by Rainbird [137]. The effect of the location of the blade-spoke connection on the turbine power performance (C_p) is known to be more effective at higher λ [158]. This may be the reason for the larger deviation of the experiment data and predicted the rotational speed of the current CFD model, especially at the acceleration period and the steady-state condition.

- Limitations of the numerical modelling in the prediction of the complex flows around the turbine could be a reason of the observed deviations at low λ values, where the flow becomes more complex due to the dynamic stall.

Despite of a larger % differences observed between the 2D CFD and experimental data in term of starting time and the final rotational speed, the CFD correctly predicted the start of the turbine and has shown a good agreement (<~10%) between the current numerical model and experimental data for the critical tip speed ratio (λ<1), which plays a crucial role for the evaluation of the turbine self-starting behaviour.

4.3 Conclusion

In this chapter, a two-dimensional CFD start-up model technique has been built with own user-defined function (UDF) after conducting sensitivity studies, such as domain size, time step size, and the number of nodes around the airfoil to obtain an accurate CFD model. Once an accurate model has been obtained, the output results have been compared with experimental data.

It is very demanding to obtain a perfect match between the 2D CFD simulation results and experimental data, even in 3D, due to the limited accuracy of the numerical methods. It is postulated here that even though there is an understandable degree in the difference between the results obtained from the CFD simulations and experimental study, in particular the time taken by the turbine to fully start, the behaviour of the self-starting curve of the H-type VAWT obtained from the 2D CFD simulation using the SST $k - \omega$ turbulence model is in good agreement with the curve obtained from an experimental study. Therefore, the obtained CFD start-up model is found to be sufficient to provide valid and accurate investigations for the future studies of the self-starting behaviour of the H-type VAWT.

Chapter 5

Self-starting characteristics of an H-type VAWT

5.1 Introduction

As discussed in Chapter 2, there are a considerable number of studies on the self-starting characteristics of the VAWTs by employing different methods, such as the Computational Fluid Dynamics model (CFD) and Blade Element Momentum model (BEM). These studies have been conducted to investigate the effect of the physical parameters, such as solidity, pitch angle, blade profile, etc., on the self-starting behaviour with the calculated instantaneous torque and power coefficients at low tip speed ratios (e.g. $\lambda<1$). However, little attention has been paid to the turbine time-varying start-up data together with the overall power performance data obtained from the dynamic start-up simulations, especially in terms of the effects of the turbine moment of inertia, the number of blades, etc. on the self-starting. The effect of turbine inertia on the starting time

and in particular on the torque/power generation during the acceleration phase have been observed for the first time. Furthermore, the utilisation of the dynamic start-up model also allows comparing the self-starting performance of the H-type VAWTs in terms of the time of the turbine acceleration from the initial stationary conditions to the steady passive cycle rotation. According to the above discussions, the main importance of this chapter is to improve the understanding of the self-starting process and set a basis for further analysis and optimisation.

The main objectives of the work presented in this chapter are as follows:

- Enhance the knowledge of how vertical axis wind turbines can gain self-starting characteristics by a detailed investigation of the start-up process, aerodynamically.

- The contributions of the aerodynamic lift and drag of the turbine blade at various azimuthal positions to the turbine starting up will be analysed in detail that should provide important insights on optimizing an H-type VAWT design.

- The effects of the several physical properties, such as the moment of inertia, the number of blades, the chord length, and the mechanical resistance on its dynamic self-starting behaviour and power performance will be investigated by using the dynamic start-up model instead of employing several constant rotational speeds of the turbine.

The chapter is structured as follows: Section 5.2 aims to enhance the knowledge of how vertical axis wind turbines can gain self-starting characteristics by a detailed aerodynamic investigation of the start-up process. Furthermore, the contributions of the aerodynamic lift and drag of the turbine blade at various azimuthal positions to the turbine starting up have been analysed in great detail which provides important insights on optimizing an H-type VAWT design. Section 5.3 presents the effects of the moment of inertia of the blades on the aerodynamic behaviour of the self-starting and the turbine performance of the H-type VAWT using the dynamic start-up model instead of employing several constant rotational speeds to the turbine. Section 5.4 presents

how the solidity affects the dynamic self-starting behaviour and performance of the H-type VAWT considering the different number of blades and blade chord length, separately. Finally, Section 5.5 presents the effect of the mechanical resistance, such as bearing friction, applied to the turbine on its self-starting behaviour in terms of the start-up time and final tip speed ratio at the steady-state condition.

5.2 Aerodynamic investigation of the start-up process

In this section, the CFD dynamic start-up simulation has been carried out for the turbine having the properties as described in Chapter 4. The predicted time variation of both the moment coefficient and the tip speed ratio under a constant wind speed of 6m/s is shown in Figure 5.1. In order to show the time that is taken for each turbine revolution during start-up and how many revolutions are needed to reach steady-state condition, the values of the moment coefficients were averaged over one turbine revolution. Therefore, the width of each line demonstrates the period of one single rotation and the number of the individual lines indicates the number of turbine rotation in which 56 revolutions are needed to reach the steady-state condition. As the figure shows, since the turbine rotates slowly at the low λ values, the time required to complete one revolution is longer than that at the high λ values. In addition, there is only a small amount of the moment generated until a value of λ of 1 is achieved, where the turbine acceleration is very slow. This range is generally known as the critical region.

In order to critically analyse and provide a better understanding of the aerodynamic characteristics of the H-type VAWT during the start-up process, a complete starting curve has been divided into the several important zones, which are Zone 1, Zone 2, Zone 3, and Zone 4 indicated as the red squares in Figure 5.1. These four λ zones have been selected corresponding to the critical region (Zone 1 and Zone 2 at $\lambda \leq 1$), where the turbine acceleration is very slow due to the weak torque generation, the rapid acceleration region (Zone 3 at λ=2.57), where the turbine is fully lift-driven, and the final steady-state region (Zone 4 at λ=4.1), where the turbine reaches its final rotational speed.
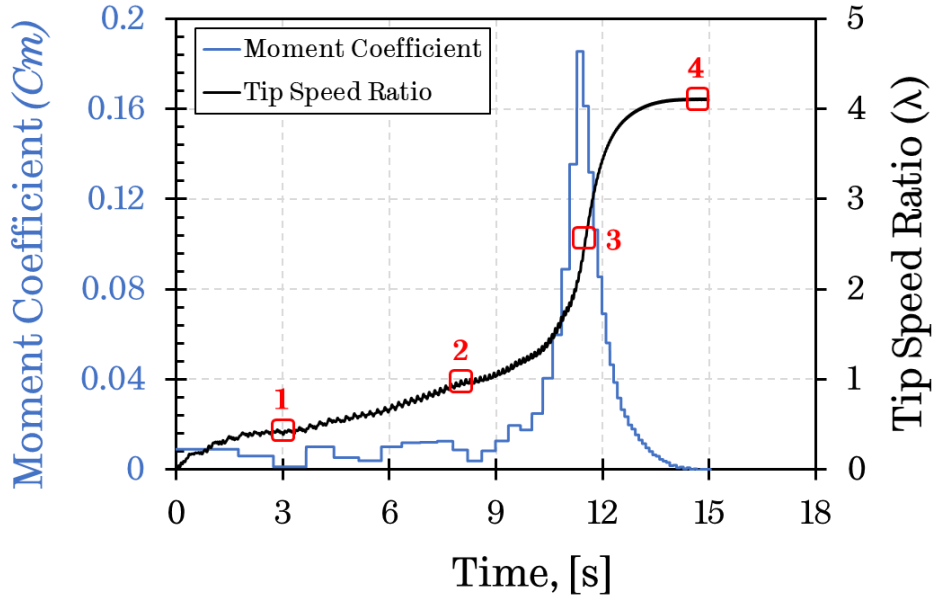
Figure 5.1. Moment coefficient and tip speed ratio as a function of the time for the CFD model.

One way of explaining the reason for the weak self-starting behaviour of the turbine in the critical region is to plot the variations of the theoretical angle of attack as a function of the blade azimuthal angle for different tip speed ratios, as in Figure 5.2. Without taking into account the effect of the induction factor, the theoretical angle of attack during the one complete revolution for different tip speed ratios can be calculated as follows [133]:

$$AoA(\alpha) = tan^{-1} \frac{sin\theta}{\lambda + cos\theta} \tag{5.1}$$

where θ is the blade azimuthal angle and λ is the tip speed ratio.

It should be noted that there is a slight difference between the theoretical angle of attack and the effective angle of attack, however; this difference can be neglected since the induction factor does not have a significant effect on the undisturbed wind velocity in the upstream part of the turbine, especially at low tip speed ratios. On the other hand, in the downstream part of the turbine, the magnitude of the effective angle of attack is smaller than the theoretical angle of

attack due to the effects of several phenomena, such as stream-tube expansion, the blade-wake interaction and the flow deceleration in the front of the turbine [133]. However, Figure 5.2 assists in observing the various phenomena of the H-type VAWTs. Also, the static stall angle, where the lift coefficient achieves its maximum value, for the NACA0018 airfoil at Re = 3.5×10^4 is also marked in the figure [159].
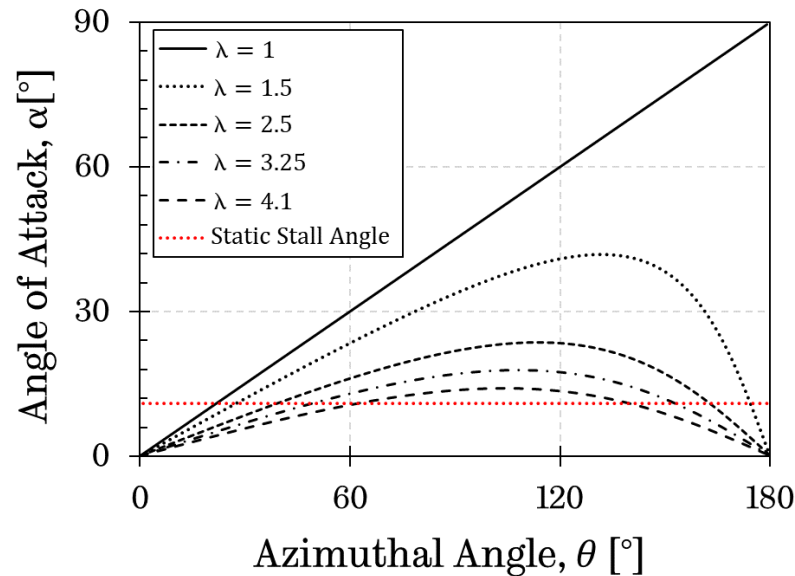
Figure 5.2. Blade theoretical angle of attack as a function of the blade azimuthal angle for different tip speed ratios.

As Figure 5.2 shows, the stall can be observed more strongly at the low tip speed ratios since the majority of the portion of the angle of attacks exceeds the static stall angle. Under these circumstances, the blade lift coefficient significantly decreases due to the large flow separations at large angles of attack while the blade drag coefficient increases. Therefore, this is a crucial reason why the start-up characteristic is poor when the tip speed ratio is less than 1. However, while the tip speed ratio increases, the possibility of the blade stall decreases, which results in an improvement of the turbine torque generation and its acceleration.

In addition, to investigate the effect of lift and drag on the turbine start-up process in the critical region, the contribution of the lift and drag coefficients to the torque coefficient as a function of the blade azimuthal angle for different tip speed ratios, such as 0.2, 0.4, 0.8, and 1.2, are illustrated in Figure 5.3. Although the H-type VAWTs is known as lift-driven machines, the drag force might have a positive effect on the turbine start-up in the critical region. As it can be observed from Figure 5.3, when the turbine is in the critical region, where the λ is less than 1, the turbine is not only driven by the lift force. The drag force also contributes to the turbine torque generation at some azimuthal angles of the complete rotor revolution; however, the positive drag contribution decreases while the tip speed ratio is approaching to 1. This finding suggests that the positive contribution of the drag force in the critical region should be enhanced in order to increase the self-starting ability of the H-type VAWT.
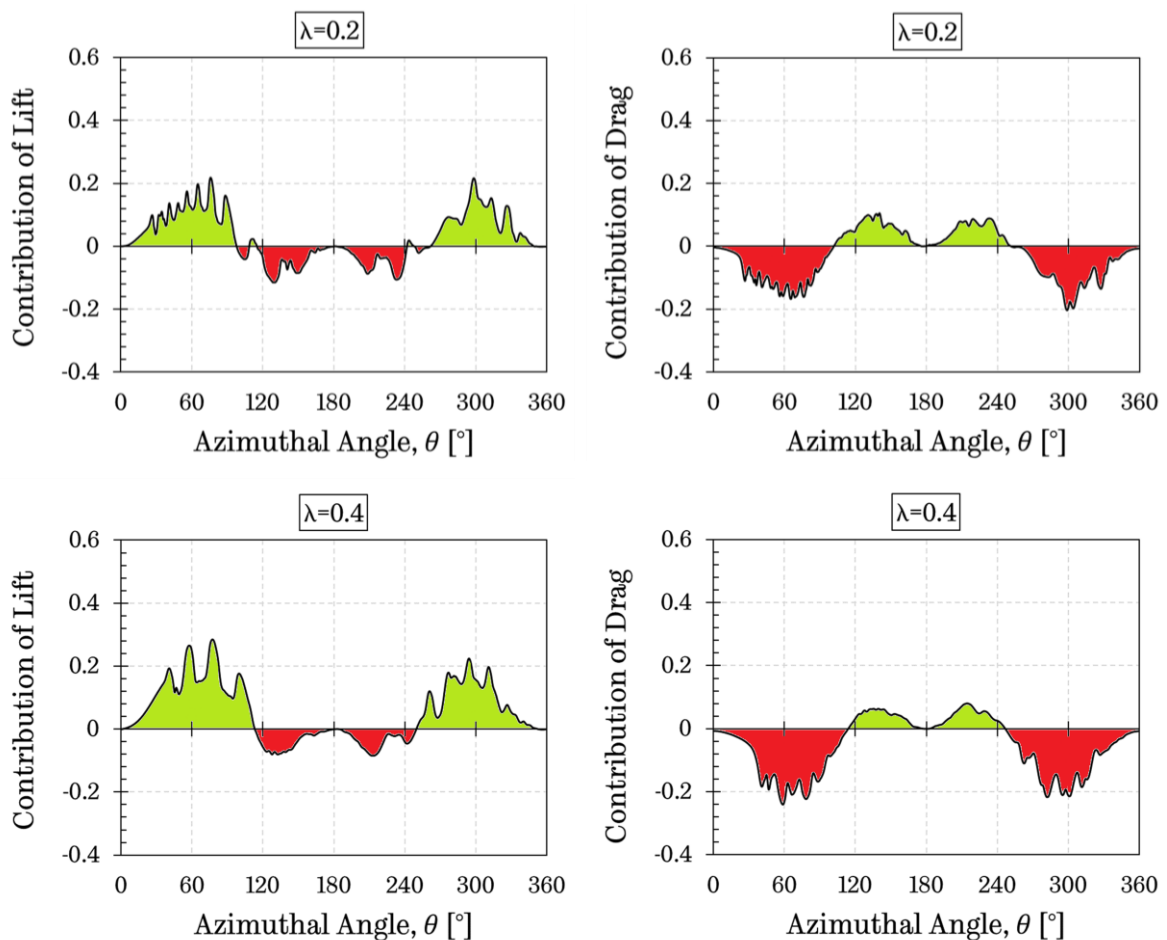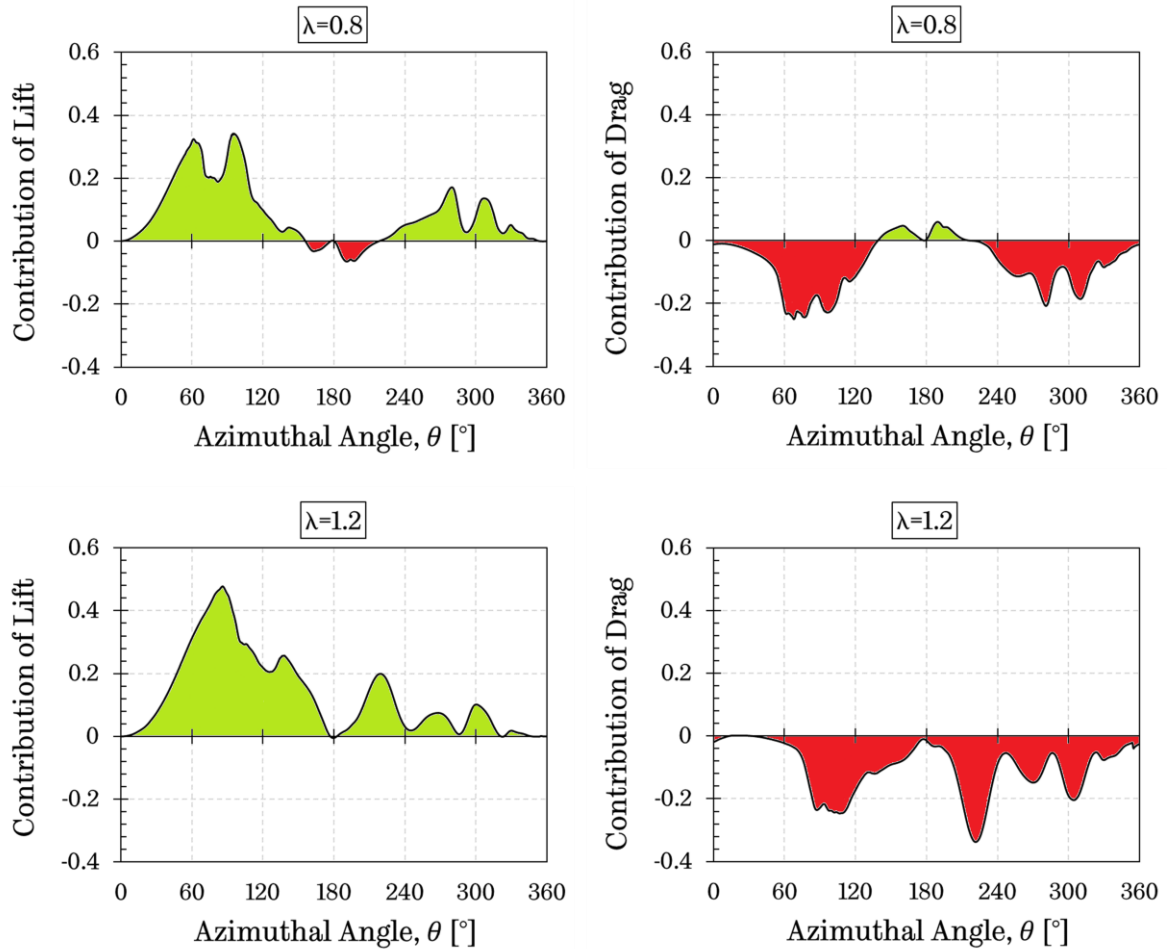
Figure 5.3. The contribution of the lift and drag to the torque generation as a function of blade azimuthal angle at tip speed ratios of 0.2, 0.4, 0.8, and 1.2.

It can also be observed in the figure that when the tip speed ratio is less than 1; the region of the positive lift contribution is more significant than the negative drag contribution, while the region of the positive drag contribution is more significant than the negative lift contribution in a complete rotor revolution. This situation leads to a positive average torque generation, which results in the increasing of the self-starting capability of the turbine. In addition, the average turbine torque coefficients as a function of the tip speed ratios are illustrated in Figure 5.4. Although the turbine might generate a negative instantaneous torque coefficient at some azimuthal angles in a complete rotor revolution, (see Figure 5.3), the overall average torque coefficients are positive and increase with

increasing the tip speed ratio, as shown in Figure 5.4, and this makes the turbine speeds up.
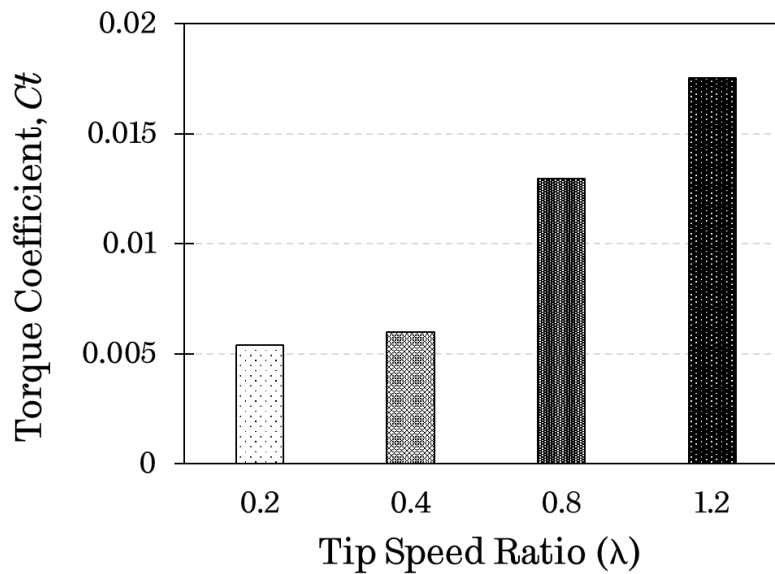
Figure 5.4. The turbine torque coefficient as a function of the different tip speed ratios of 0.2, 0.4, 0.8, and 1.2.

It should be also noted that, as stated above, the magnitude of the effective angle of attack, especially in the downstream part of the turbine, is smaller than the theoretical angle of attack. Therefore, according to the study [158], the measured α at the downstream part of turbine is almost halved compared to the theoretical value at high tip speed ratios and based on this assumption, the contribution of the lift and drag to the turbine torque generation has been calculated for the tip speed ratios of 0.4 and 0.8. The deviation between the theoretical angle of attack and effective angle of attack in the contribution of the lift and drag to the total torque is found to be less than 5% and the difference is expected to be even less at reduced tip speed ratios. Therefore the calculated lift and drag contributions to the torque generation based on the real angle of attack, which is not always readily available for the downstream part, is found to be only a little different from that based on the theoretical angle of attack in the turbine self-starting investigation.

As stated above, the dynamic start-up curve has been divided into four important zones to investigate the self-starting process of the Darrieus type VAWT in detail. Figure 5.5 illustrates the turbine moment coefficients as a function of the blade azimuthal angles in the four zones. As it can be seen in the figure, at low λ regions, such as Zone 1 and Zone 2, the complexity of the moment coefficient curve is due to the fact that in some azimuthal positions of a complete rotor revolution, the direction of the net aerodynamic forces acting on the blade is contrary to the direction to the turbine rotation, which results in a negative or weak net torque generation. The reason behind this situation is that the drag force overcomes the lift force, which results in an instantaneous negative torque generation. Even though the instantaneous torque is negative in a certain azimuthal position, the average torque at each tip speed ratio is positive, which may increase the possibility of the self-stating of the turbine, and this agrees with the findings of Beri and Yao [67]. As the turbine rotational speed increases up to Zone 3, the average turbine moment coefficient reaches its maximum value, and the moment coefficient curve becomes smoother. On the other hand, in Zone 4, the turbine reaches its steady-state position, where the average moment coefficient becomes almost zero, due to the balance between the generated positive lift and negative drag forces.
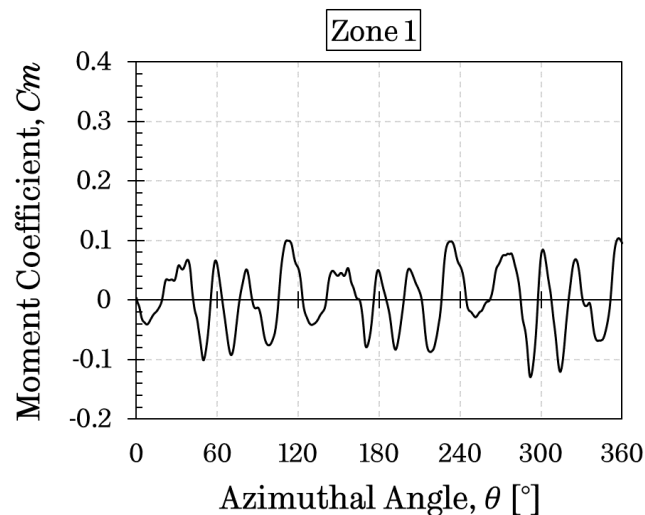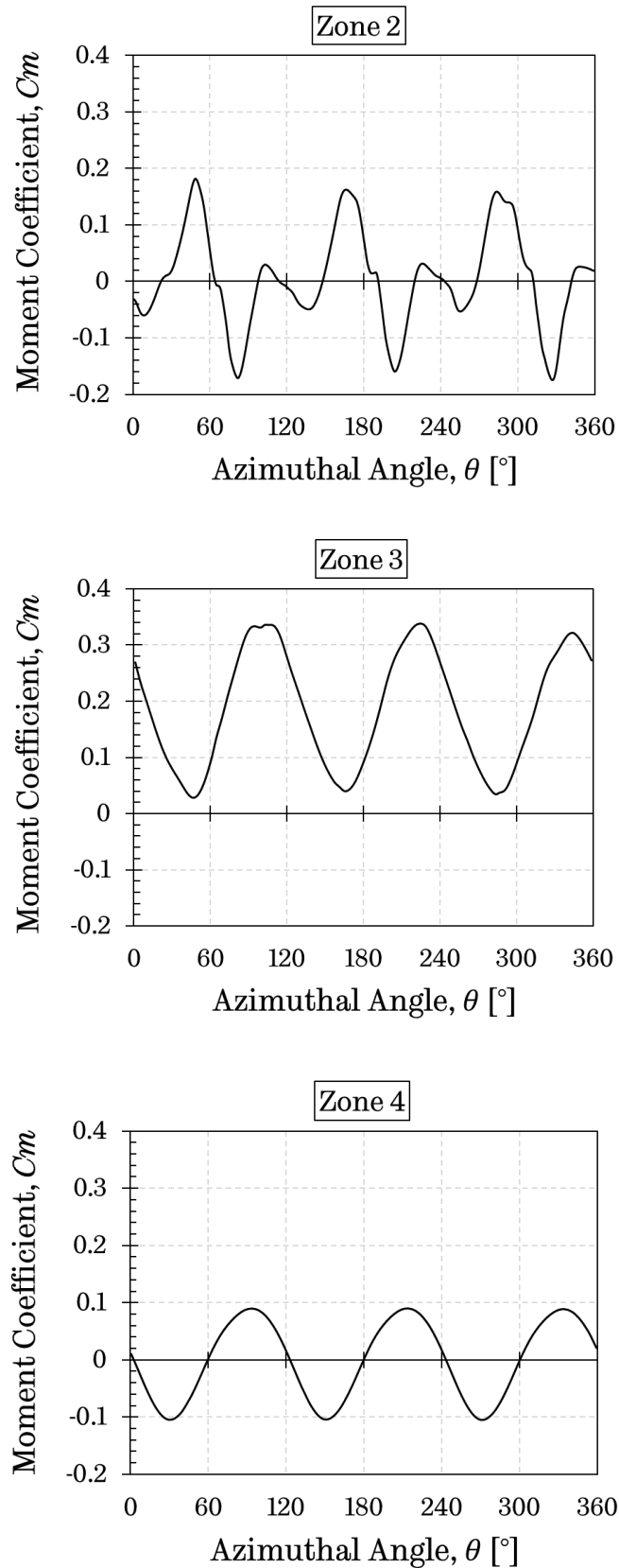
Figure 5.5. Turbine moment coefficients as a function of the blade azimuthal angle in the four zones.

For further analyses, the visualisation of the flow around the airfoils is shown in Figure 5.7, which compares the non-dimensional vorticity contours for each zone at azimuthal angles of 0°, 60°, 120°, and 180°. At low λ regions, such as Zone 1 and Zone 2, each blade experiences high and low angles of attack, which causes a complex flow pattern. The existence of these complex vorticities in Zone 1 and Zone 2 leads to a slower, or even no starting of the turbine, which may be mainly due to the lower lift force on the blade. When the tip speed ratio is greater than 1, the blade vortices become smaller, and the blades generate a higher lift force. For this reason, the turbine acceleration increases considerably, and this can be seen in Figure 5.1 between 9s and 14s. After 14s, although no separation occurs (Zone 4), the low angle of the attack reduces the maximum possible lift force on the blades. In addition, another situation may cause the reduction in the turbine performance in Zone 4, which is the blades increase the pressure in the front of the turbine and the turbine reacts like a solid wall, and there is a significant amount of the wind that passes around the turbine. In order to clarify this situation, the non-dimensional velocity magnitude contours for the turbine in Zone 1 and Zone 4 have been presented in Figure 5.6. As it can be seen in the figure, the amount of the wind passing towards the downstream part of the turbine in Zone 4 is less than in Zone 1 due to the high pressure in the front of the turbine. This condition is called the blockage effect, which reduces the lift force generation in the downstream part of the turbine and the overall turbine efficiency.
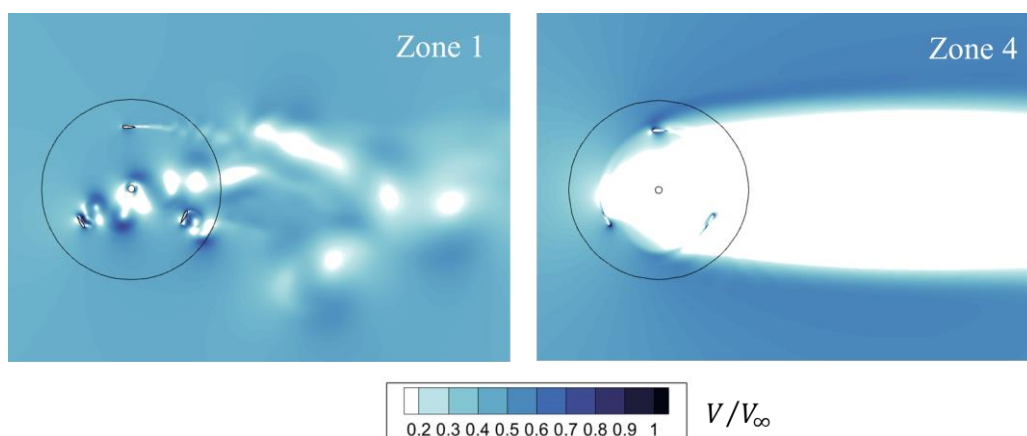
Figure 5.6. Dimensionless velocity magnitude around the blades for Zone 1 and Zone 4.

Eventually, it can be understood that one of the most critical parameters for the turbine to accelerate to a steady-state condition may be the gradually elimination of the initial complex vorticities. The reduction in the complex patterns can be observed in the non-dimensional vorticity contours from Zone 1 to Zone 4, see Figure 5.7.
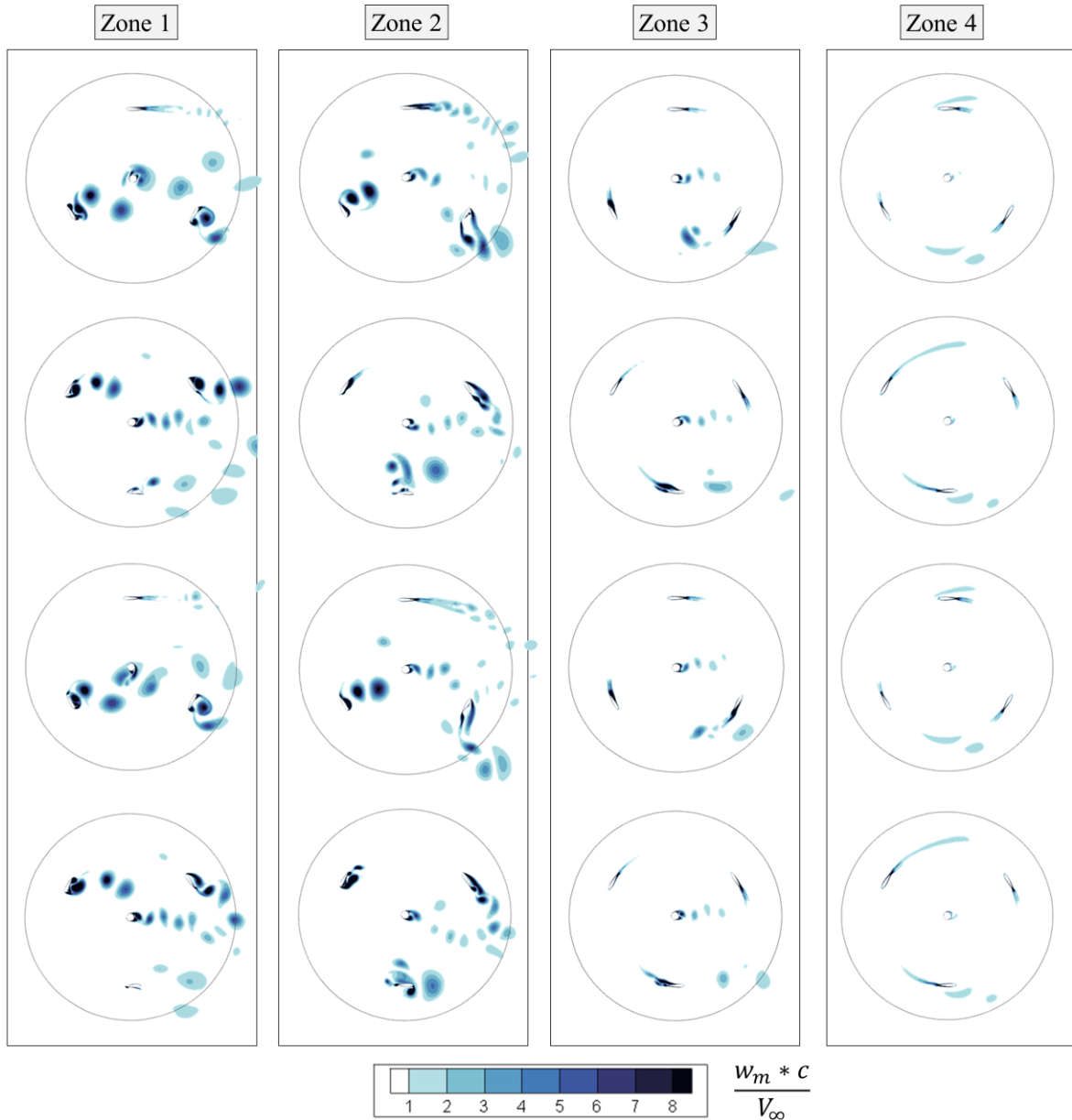
Figure 5.7. Non-dimensional vorticity contours around the blades for the four zones at 60° intervals of the azimuthal angle.

As a summary of the H-type of VAWT start-up process, the variation of tip speed ratio as a function of the normalised time is illustrated in Figure 5.8. What is interesting in the figure is that the H-type VAWTs operate in two different conditions during the start-up process, such as a combined stage, which is lift-drag driven, and the fully lift driven stage. The turbine in the combined stage proceeds until the λ=1. In this region, the positive drag contribution plays a significant role in the second and third quarter of the rotor revolution, where the azimuthal position varies between 100° and 253°, as shown in Figure 5.8. Once the λ>1, the turbine enters the fully lift-driven stage.
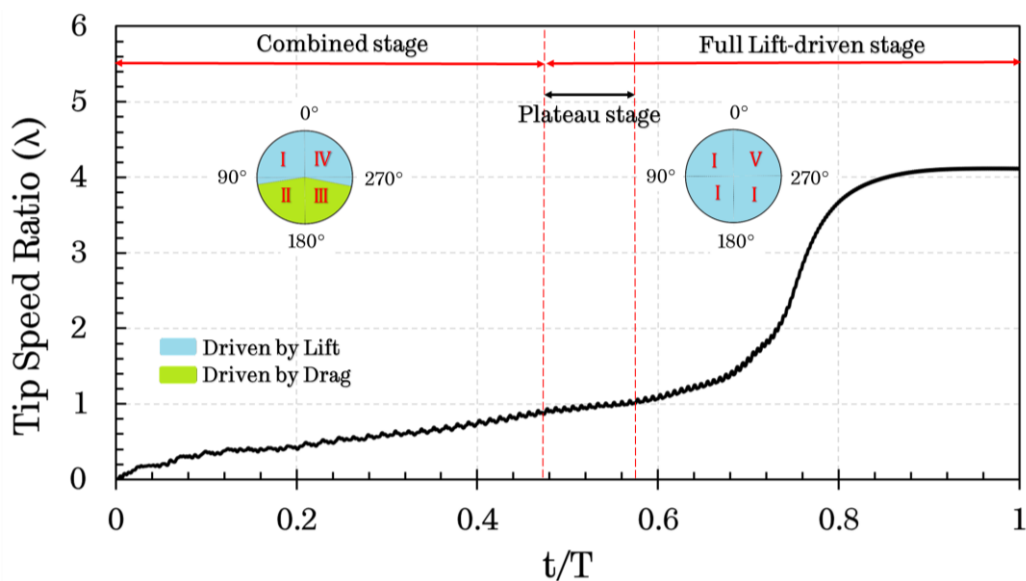
Figure 5.8. The variation of the tip speed ratio as a function of the normalised time to show the summary for the H-type VAWT start-up process.

Overall, these findings indicate that the main driving force of the turbine in the critical region is both the lift and drag forces. Therefore, in order to improve the self-starting capability of the H-type VAWT in the critical region, not only the lift force but also the drag force at the position, where the drag force assists the turbine rotating motion, should be increased. Additionally, when the λ≥1, the lift-driven is required to be maintained in order to achieve a complete start-up process.

5.3 Moment of inertia effect on the start-up performance of the turbine

The effect of the moment of inertia on the turbine start-up and the acceleration behaviour is another issue that requires a computational method based on the interaction of the fluid and turbine. This is because the moment of inertia changes the instantaneous blade speed at any given time, its acceleration rates and thus the characteristics of the flow over the blade. For this reason, in this part of the study, four different inertias, namely Inertia 1, Inertia 2, Inertia 3, and Inertia 4, which have the inertia values as *0.0105 kgm², 0.0211 kgm², 0.03 kgm², and 0.0422 kgm²*, respectively, were selected to investigate the inertia effect on the self-starting behaviour and turbine performance. Inertia 3 has been selected as the base case, where the blade mass is the same as in the experiment, and other mass values have been selected proportionally.

As stated above, the turbine starts rotating from rest and accelerates until its steady-state condition is reached, where the turbine rotational speed is oscillating around the same average value. Figure 5.9 shows the effects of different turbine moments of inertia on the turbine acceleration as a function of the non-dimensional time. It can be observed from the figure that increasing the turbine moment of inertia from *0.0105 kgm²* to *0.0422 kgm²* extends the time required to reach its steady-state condition.
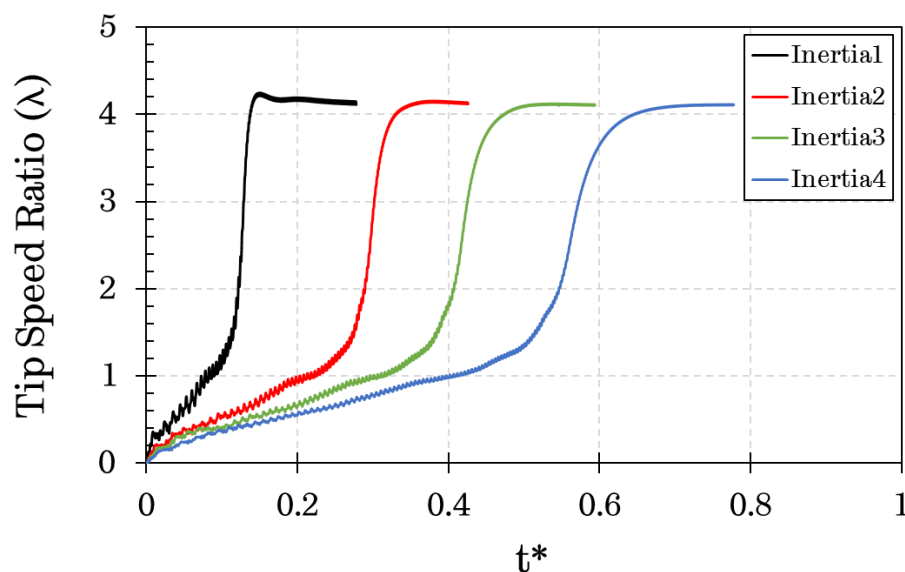
Figure 5.9. The tip speed ratio as a function of the non-dimensional time for different moments of inertia.

It is observed from this figure that even though the moment of inertia is changed, the average value of the turbine rotational speed at the steady-state condition is the same for all investigated inertia cases. The turbine moment of inertia effect at its steady-state condition is illustrated in Figure 5.10, and it can be observed that as the turbine moment of inertia increases, the amplitude of the fluctuation of the turbine rotational speed decreases. This situation can be explained by using the equation of the motion described in Eq. 5.3. Since the torque generated at the final steady-state condition is same for the turbines having the different moment of inertia (see Figure 5.11), if the moment of inertia is doubled, the amplitude of the oscillation is approximately halved; e.g., h2 is half of the h1.
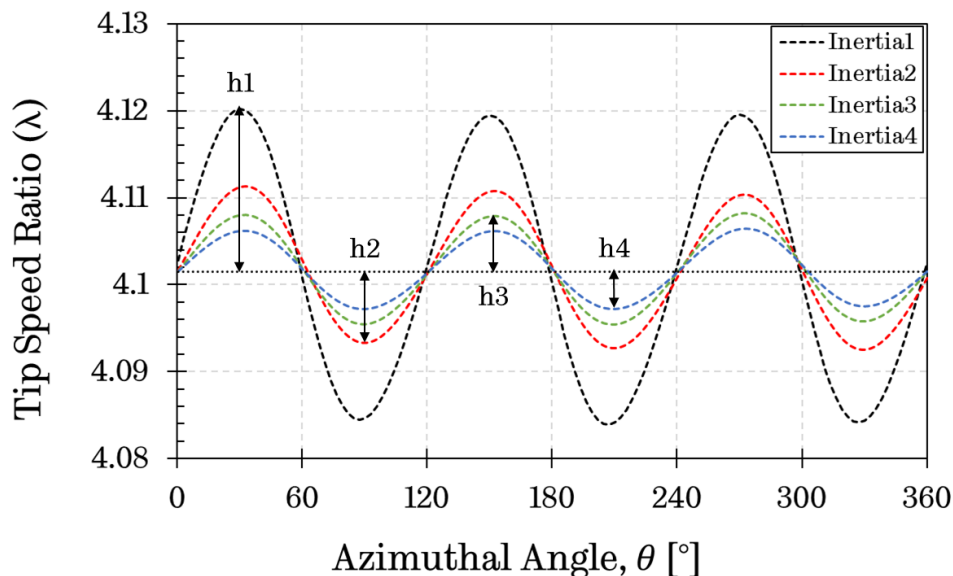
Figure 5.10. The tip speed ratio as a function of the blade azimuthal angle for the four inertias at the final steady-state condition.

In order to discuss the effect of the inertia on the performance of the turbine, the turbine power coefficient as a function of the tip speed ratio curve during the start-up process is plotted in Figure 5.11. It should be noted that the values of the power coefficients and the tip speed ratios have been averaged over one revolution of the turbine. Therefore, each point in the $Cp - \lambda$ curve indicates one

complete revolution for each inertia case. It can be observed in the figure that the four inertias produce a similar value for the power coefficients until the tip speed ratio reaches 2.6, where the turbine has passed the plateau stage and has started up as shown in Figure 5.1. After this point, the lighter turbine shows a higher instantaneous performance until the final steady tip speed ratio is reached, as illustrated in Figure 5.11 in the λ values marked as A, B, and C.
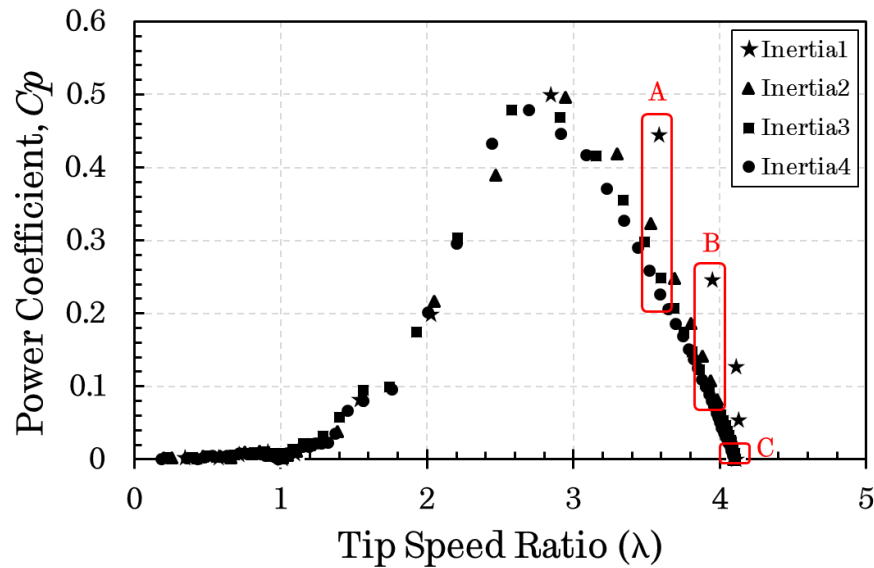
Figure 5.11. The power coefficient as a function of the tip speed ratio for the four inertias investigated.

To investigate the aerodynamic behaviour of the lighter turbine and compare it with other turbines after the λ of 2.6, the blade moment coefficients as a function of the azimuthal angle for Zone A, Zone B, and Zone C as indicated in Figure 5.11 are illustrated in Figure 5.12. It can be seen in the figures that in Zone A and Zone B, the blade instantaneous moment coefficient of the Inertia 1, especially in the upstream part of the turbine, is higher than the other turbines, which results in a higher power coefficient in these regions. In Zone C, the instantaneous moment coefficients of all inertia cases show similar behaviour and this is due to the turbine reaching steady-state conditions.
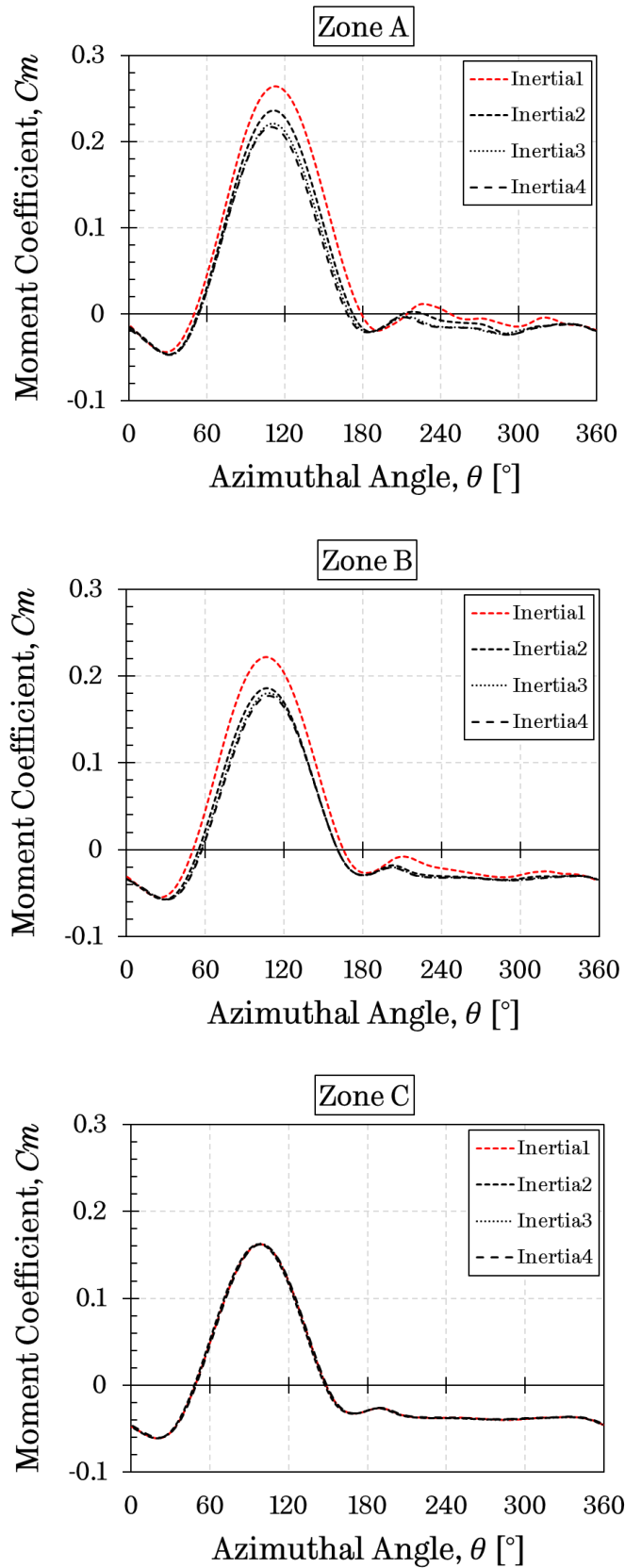
Figure 5.12. The moment coefficient as a function of azimuthal angle for Zone A, Zone B, and Zone C.

In addition, the lift and drag coefficient of the four inertia cases in Zone A are plotted in Figure 5.13 and it can be observed that the lighter turbine produces the higher lift coefficient and lower drag coefficient in this region, which may result in the higher power coefficient. Although the higher drag coefficient contributes to the starting torque at low tip speed ratios, it decreases the turbine performance at high tip speed ratios, as explained in the previous section.
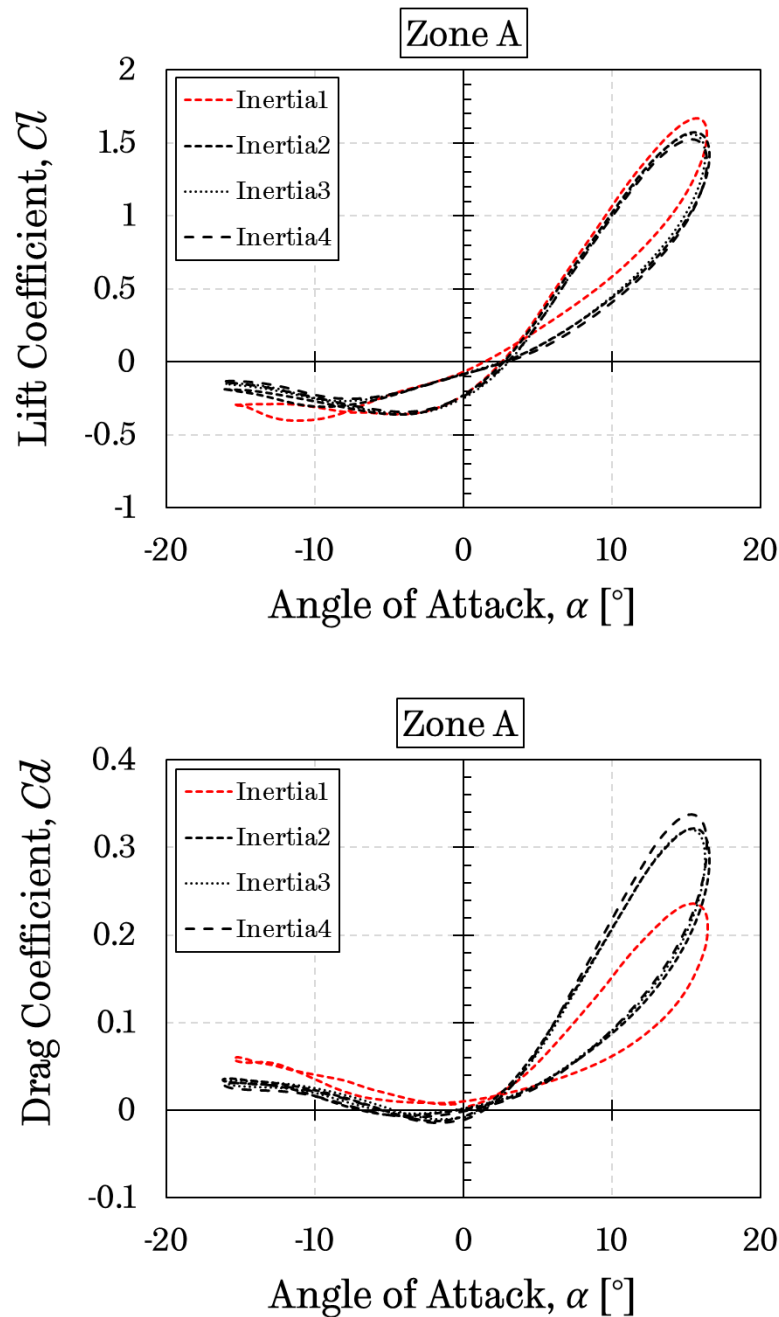
Figure 5.13. The lift and drag coefficients as a function of the angle of attack for Zone A.

Furthermore, investigating the acceleration rates of the four inertia cases may help to understand the reason for the higher power coefficient of the lighter turbine in Zone A and B. Therefore, the variation of the tip speed ratio as a function of the normalised time is plotted for the four inertia cases in Figure 5.14 (a). It is apparent from the figure that the tip speed ratios of all inertia cases increase similarly until the point 1, where the tip speed ratio is around 2.6, and then the discrepancy became clearer until the point 2, where deceleration starts before the steady-state condition. Between the point 1 and 2, the lighter turbine has a higher acceleration rate compared to other turbines, as seen in the enlarged view (Figure 5.14 (b)). Therefore, it is believed that the reason for the higher lift and lower drag coefficients of the lighter turbine, which results in higher power coefficient, might be due to this acceleration rate. However, it should be noted that these conclusions were based on the modelling results obtained. It would be useful to perform further experimental investigations to confirm the accuracy of the model results and shed more light on the topic.
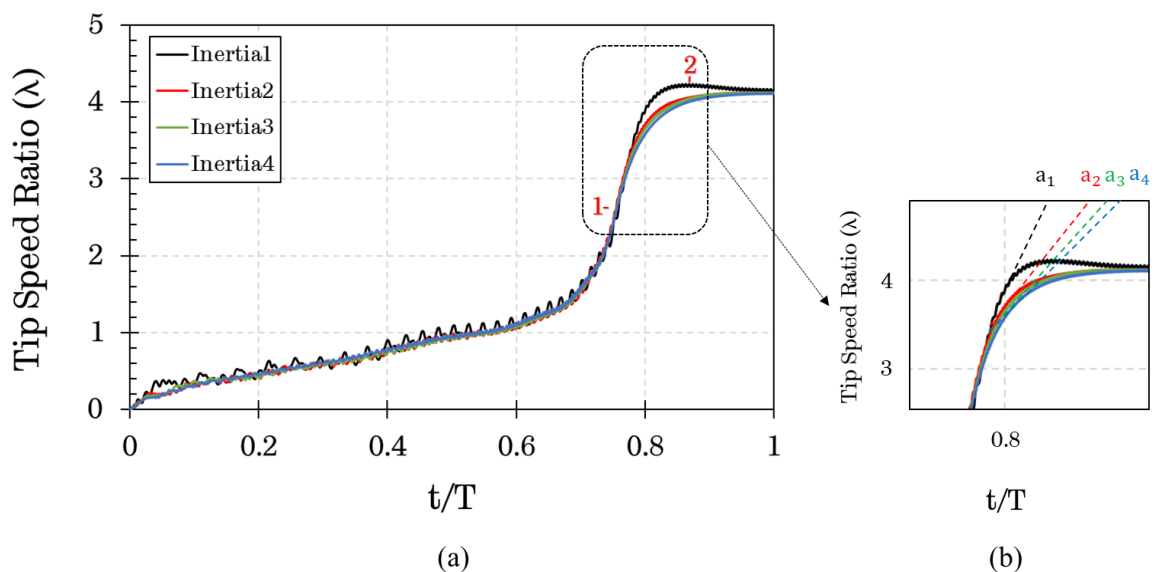
Figure 5.14. (a) The tip speed ratio as a function of the non-dimensional time axis for inertia cases and (b) its enlarged view.

In conclusion, increasing the moment of inertia of the turbine increases the time to reach the final rotational speed. However, it did not show a noticeable effect on the starting of the turbine and the final speed. In addition, the λ range

is the same in all the cases investigated, and the lighter turbine has a higher power coefficient after the peak power coefficient has been reached. Although the lighter turbine shows a better performance after the optimum λ, where the turbine produces maximum power output, the amplitude of oscillation of the rotational speed, which is in direct proportion to the torque, is increased during the start-up process (see Figure 5.9 and Figure 5.10). As a result, the vibration and fatigue stress acting on the turbine may increase [160]. For this reason, the optimum inertia could be determined in order to achieve quick turbine start-up while reducing the vibration and fatigue issues.

5.4 The effect of the solidity on the turbine self-starting with different number of blades and blade chord lengths

The solidity is one of the important parameters affecting the start-up performance of the H-type VAWTs. The is because the change in the solidity will change the aerodynamics and thus torque generations of the turbine. In this thesis, the turbine solidity is determined as a ratio between the area of the blades and turbine swept area, and simply defined as follows:

$$Solidity\ (\sigma) = \frac{Nc}{R} \tag{5.2}$$

where N is the number of blades, c is the chord length of the blade, and R is the radius of the turbine. As previously discussed in Section 2.2.1, the solidity can be modified either by changing the number of blades or the blade chord length with the consideration of a constant turbine radius. For this purpose, in this section, the effect of the number of blades and the blade chord length on the turbine self-starting behaviour are studied, separately.

In order to investigate the effect of the blade number on the self-starting behaviour and performance of the H-type VAWT with a NACA0018 blade profile, the blade numbers of the turbine are changed to 2, 3, 4, and 5 while the chord length and the radius of the turbine are kept constant. Turbine self-starting, time-varying data is presented for 2, 3, 4, and 5-bladed turbines in order to observe the number of blade effect on the turbine start-up behaviour.

Figure 5.15 shows the variation of the tip speed ratio as a function of the time for the investigated turbines. As it can be seen in the figure that the 2-bladed turbine fails to self-start; however, the times required to reach the steady-state condition are 15s, 11s, and 9.5s, when the numbers of blades are N=3, 4, and 5, respectively.
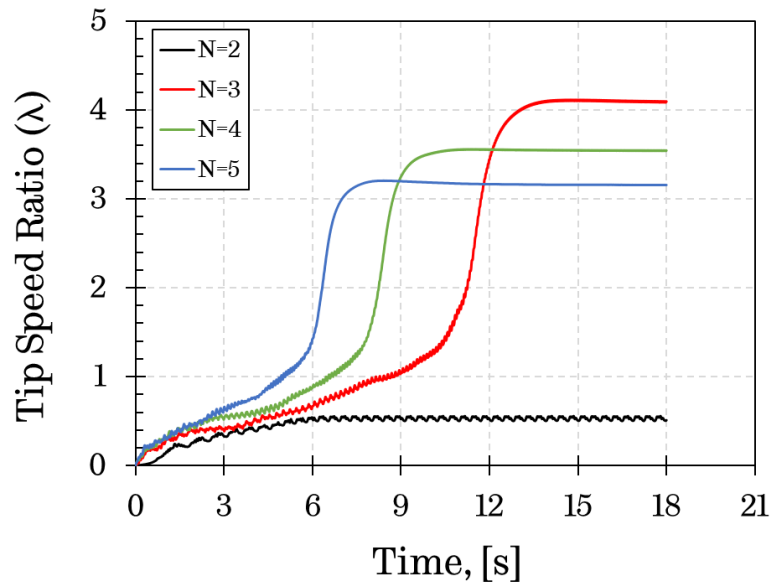
Figure 5.15. The variation of the tip speed ratio as a function of the time for 2, 3, 4, and 5-bladed turbines.

In order to assess the start-up behaviour and the performance of an H-type VAWT, three essential parameters, such as the start-up time, the peak power coefficient, and the optimum tip speed ratio, where the peak power coefficient is obtained, should be considered. Generally, shorter start-up time and a higher peak power coefficient at a higher optimum tip speed ratio are required in order to achieve optimum performance of an H-type VAWT. Therefore, the optimum tip speed ratio, the peak power coefficient, and the start-up time of H-type VAWT as a function of the different number of blades are illustrated in Figure 5.16. The optimum tip speed ratios are 2.57, 2.31, and 2.1, when the numbers of blades are N=3, 4, and 5, respectively. On the other hand, the peak power coefficient can be obtained as 0.478, 0.432, and 0.398, when the numbers of blades are N=3, 4, and 5, respectively. The findings in this part of the study revealed three important

phenomena on how the number of blades affects the turbine start-up characteristics. First, the optimum tip speed ratio, where the maximum power output is obtained, decreases with the increase of the number of blades. Second, the start-up time decreases with the increase of the number of blades. Third, the peak power coefficient also decreases with the increase of the number of blades. It should be noted that the information of the 2-bladed turbine does not exist in Figure 5.16 due to the fact that it does not show the self-starting characteristics.

(a)

(b)
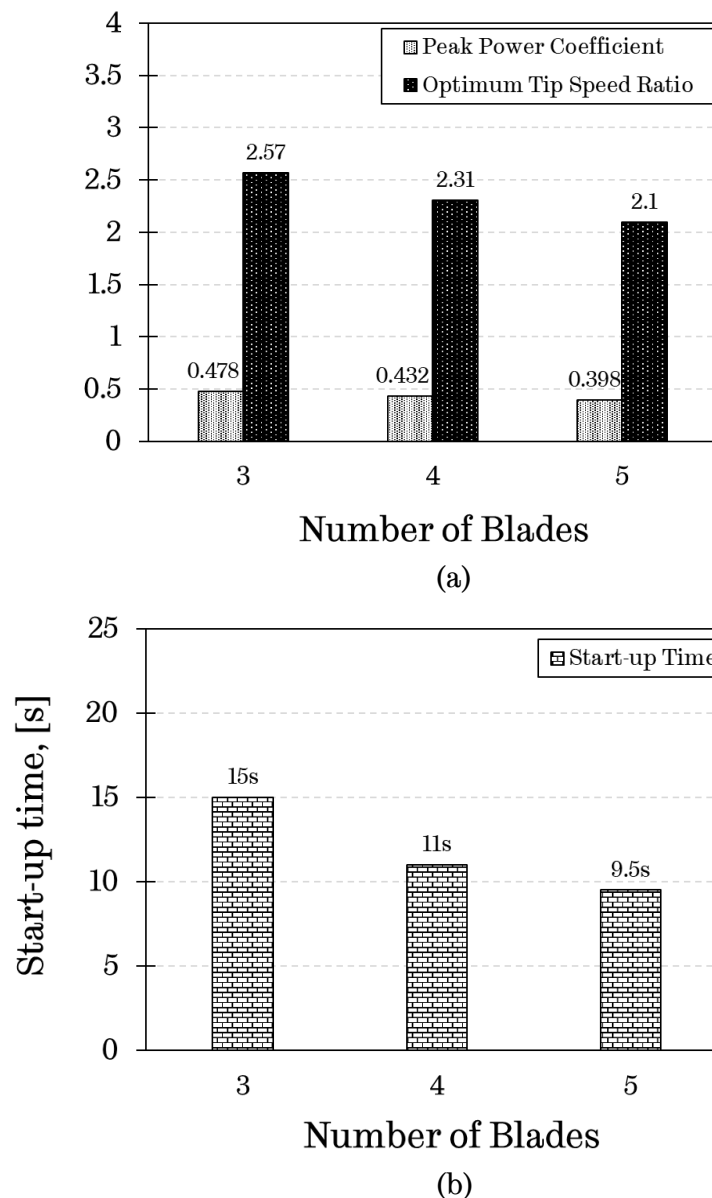
Figure 5.16. Aerodynamic characteristics of the H-type VAWT with the different number of blades: (a) optimum tip speed ratio and peak power coefficient, and (b) start-up time.

Furthermore, the turbine power coefficient in the low tip speed ratio region ($0<\lambda<1$) has been calculated and plotted in Figure 5.17. From this figure, it is noted that the values of the power coefficients and tip speed ratios have been averaged over one complete revolution of the turbine from the dynamic start-up simulations. In addition, the 2-bladed turbine is not included in Figure 5.17 since it does not show any self-starting characteristics. Figure 5.17 also illustrates that the larger is the number of blades then a slightly higher power coefficient at low tip speed ratios is obtained, which increases the self-starting capability of the turbine. This is largely because of the increase in the total blade surface area. On the contrary, at the high λ values, the increasing the turbine blade area increases the blockage to the oncoming free stream wind, which also prevents the air passing thought the upstream part towards the downstream part of the turbine and resulting in a significant reduction in the power performance in the downstream part of the turbine. This observed finding in the current study appears to be consistent with other researches [156, 161] and the previously discussed the effect of the complex vorticities on the turbine performance in Section 5.2.
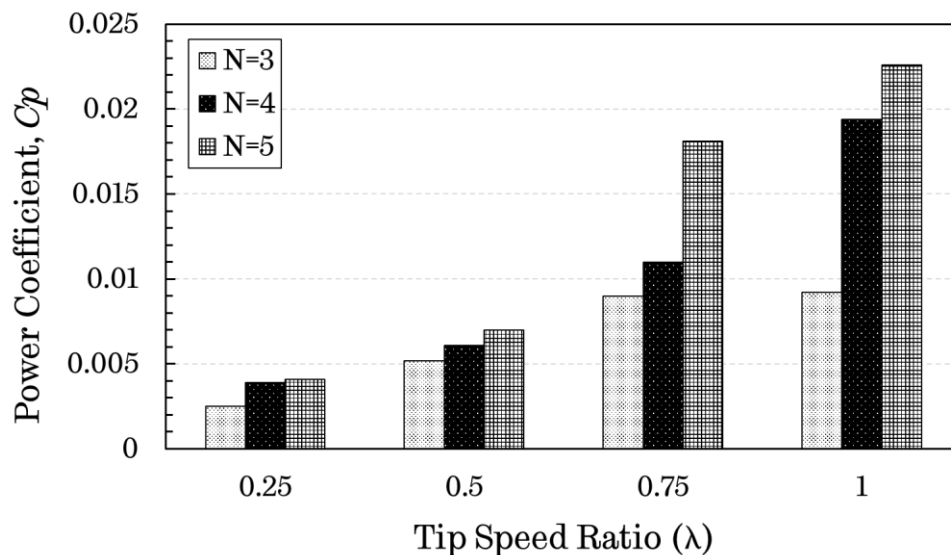
Figure 5.17. Turbine power coefficient as a function of the tip speed ratio for different number of blades.

Consequently, the good self-starting performance of the H-type VAWTs can be determined by a quick start-up time and a peak power coefficient at an optimum tip speed ratio. For the turbines studied in this section, the peak power coefficient is achieved when the number of blades is 3; however, the quicker time to reach steady-state condition is achieved when the number of blades is 5. Therefore, it is apparent that the blade number cannot make the turbine have both larger power coefficient and quicker start-up time. According to the CFD start-up simulation results, it can be argued that the optimum turbine performance might be obtained with 3 blades in terms of the start-up time and peak power coefficient.

Furthermore, another way to change the turbine solidity is to alter the blade chord length while keeping constant all the other variables, such as the number of blades and rotor radius. For this reason, in order to investigate the effect of the blade chord length on the turbine start-up behaviour and performance of the H-type VAWT with NACA0018 blade profile, five different chord lengths, namely Chord1, Chord2, Chord3, Chord4, and Chord5, which have the chord length values of $0.025m$, $0.05m$, $0.083m$, $0.1m$, and $0.125m$, respectively, have been selected, while the number of blades and the radius of the turbine are kept constant, i.e. 3 blades and a radius of 0.375m. It should be noted that the value of Chord3 has been chosen as the base case, and other chord length values have been proportionally increased and decreased for other cases.

Turbine dynamic start-up behaviour with different blade chord lengths is presented in the time-varying format as can be seen in Figure 5.18. As can be seen from the figure that there are clear advantages in increasing the blade chord length, particularly at the turbine start-up time. Increasing the chord length from $0.025m$ to $0.125m$ reduces the turbine start-up time. The turbine with a blade chord length of $0.125m$ reaches the steady-state condition in around 7s, while it is around 15s for the turbine with $0.083m$ blade chord length. In addition to this, the turbine with lower blade chord length, such as $0.025m$ and $0.05m$, do not show the self-starting characteristic. However, the final tip speed ratio at the

steady-state condition decreases with the increase of the blade chord length. Although the finding implies that, a turbine with a higher blade chord length provides an improved self-starting characteristic due to the larger Reynolds number at the low tip speed ratios, a considerable performance reduction is apparent at the high tip speed ratios, which may be due to increasing the frontal area of the turbine that obstructs the air passing towards the downstream part of the turbine.
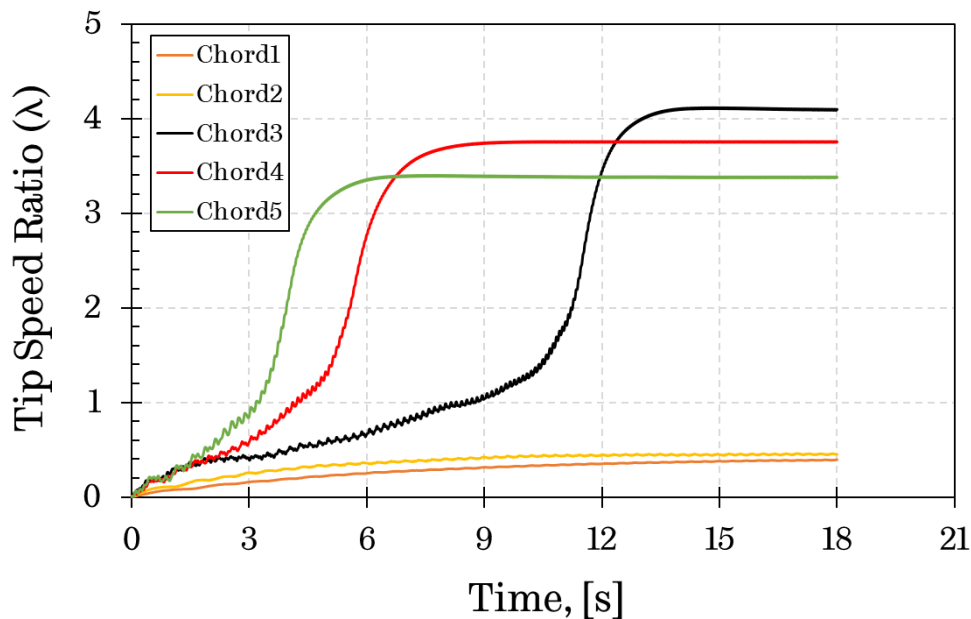
Figure 5.18. The variation of the tip speed ratio as a function of the time for the turbines with a chord length of $0.025m$, $0.05m$, $0.083m$, $0.1m$, and $0.125m$, respectively.

Although increasing the blade chord length enhances the turbine self-starting performance, especially at low tip speed ratios, the high blade chord length could bring some disadvantages, such as a reduction in the turbine performance at high tip speed ratios. Figure 5.19 shows the effect of the blade chord length on the turbine performance as a function of the tip speed ratio. It is noted that Chord1 and Chord2 are not presented in the figure since they do not show self-starting characteristics. As can be seen from the figure, the optimum power performance of the turbine can be obtained either at a combination of low blade chord length and high tip speed ratio or vice versa. This implies that at a given

wind speed, which is $6 m/s$ in this case, when the turbine is rotating faster (higher tip speed ratio), the optimum performance is obtained with a smaller blade area (lower blade chord length) while if the turbine is rotating slower (lower tip speed ratio), the optimum performance is achieved with a larger blade area (higher blade chord length). Therefore, the shift should be correlated with a balance in the power output and sufficient self-starting characteristics.
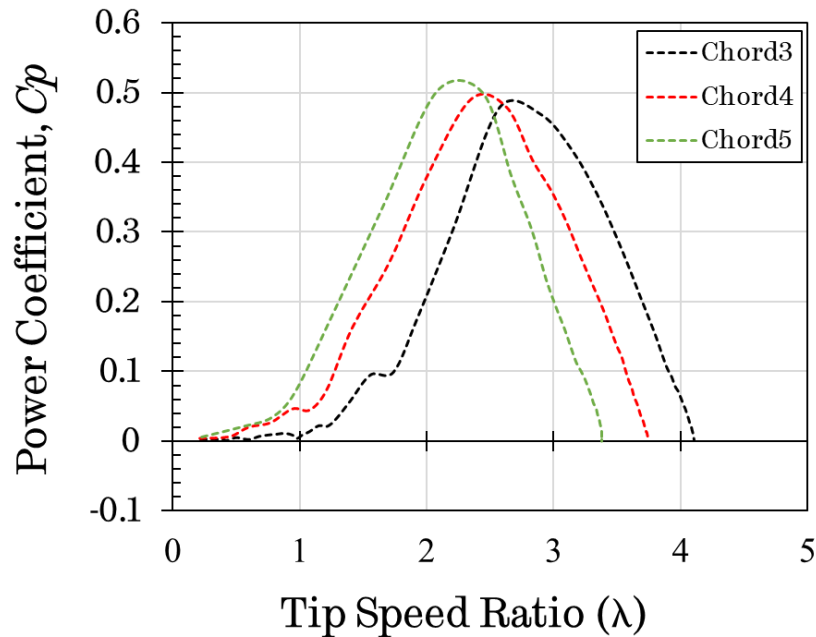
Figure 5.19. The power coefficient as a function of the tip speed ratio for the turbine investigated with different blade chord lengths.

5.5   The resistance to the turbine

As discussed in Section 4.2.3, the observed discrepancies between the experimental study and the current 2D CFD model results could be due to (i) the existence of the 3D effects, such as blade supporting arms and tip losses and (ii) other additional sources of resistive torque, such as the bearing friction. Because of the lack of the information provided in the experimental study, the implementation of the resistive torque effect on the turbine self-starting was not taken into account during the CFD model validation studies. However, it is worth estimating and implementing the bearing frictional losses depending on

the bearing system employed to the vertical axis turbine application in order to increase the quality and reliability of the current 2D CFD model for the future studies.

For this reason, firstly, it is important to understand how the turbine rotational speed is calculated. The rate of change of the rotational speed, ω, with the moment of inertia, I, is subject to the balance of the external torques. The relation between the turbine rotational speed and the external torques can be expressed using the rotor dynamics equation, as follows:

$$I\frac{d\omega}{dt} = T_w - T_g - T_f \tag{5.3}$$

where, T_w is the wind torque, T_g is the generator torque, and T_f is the bearing frictional torque, which is proportional to the rotational speed with a bearing frictional coefficient ($T_f = C_{fr} \times \omega$).

Due to the absence of any external load connected to the turbine in the experiment, the resistive effect from the generator was neglected, as stated in the experiment [137]. However, subject to the bearing friction can be estimated by implementing the friction coefficient caused by the bearing system to the current CFD model. For this reason, a literature survey has been conducted in order to obtain the optimum value of the coefficient based on the bearing system that is generally employed to the vertical axis wind turbines. The findings suggested that the deep-groove ball bearings and angular ball bearings are generally employed in the shaft units of the vertical axis wind turbines [162]. The bearing frictional coefficients for these types of the baring systems were found to be 0.0015 and 0.002, respectively [163]. Therefore, the several assumed-bearing frictional coefficients, C_{fr}, have been implemented in the current CFD model in order to observe their effects on the turbine dynamic start-up behaviour.

Figure 5.20 demonstrates the effects of the bearing frictional coefficient on the turbine dynamic self-starting behaviour. The results indicate that the turbine is very sensitive to changes in the bearing frictional coefficients. Further, it is clear

from the figure that the time to reach its final tip speed ratio, which is also known as the steady-state condition, increases with the increase of the bearing resistance, even the turbine losses its self-starting capability when the resistance is too much, such as 0.1 and 0.01. In addition to this, we observe that the final tip speed ratio of the turbine decreases with the increase of the resistance; even the turbine does not self-start.
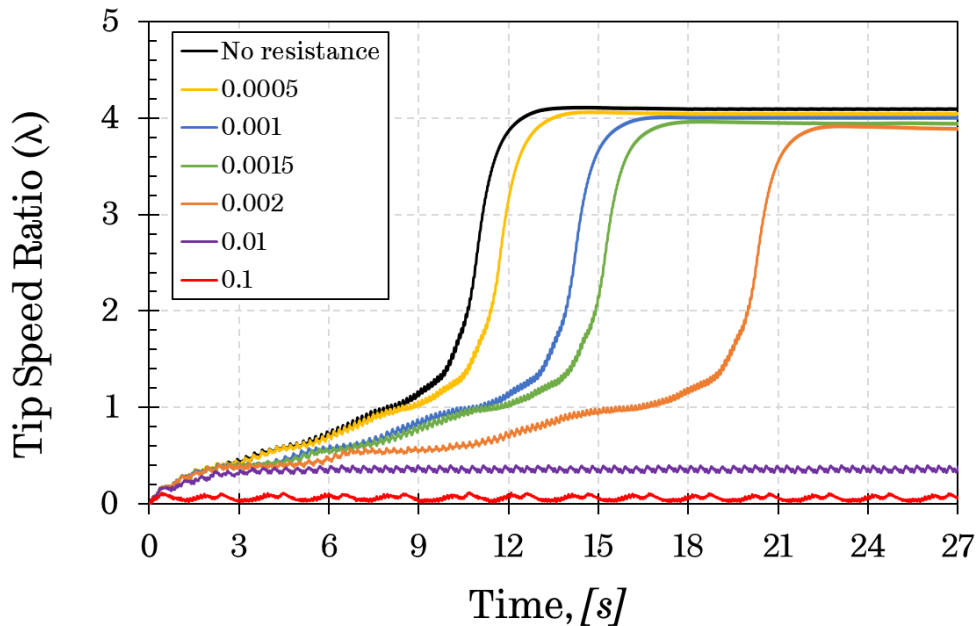
Figure 5.20. The variation of the tip speed ratio as a function of the time for different bearing frictional coefficients.

Furthermore, the effect of the different bearing frictional coefficients on the turbine start-up times and final tip speed ratios can be summarised in Figure 5.21 and Figure 5.22. As can be seen from figures that with the increase of the bearing frictional coefficients, start-up time is delayed; however, the final tip speed ratio decreases. It should also be noted that information on the turbines with bearing frictional coefficients of 0.1 and 0.01 do not exist in Figure 5.21 and Figure 5.22 since they have no self-starting characteristics.
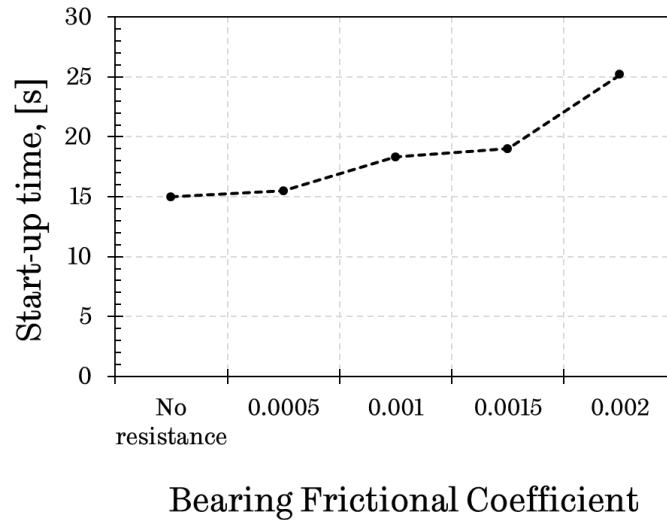
Figure 5.21. The start-up time as a function of the different bearing frictional coefficient.
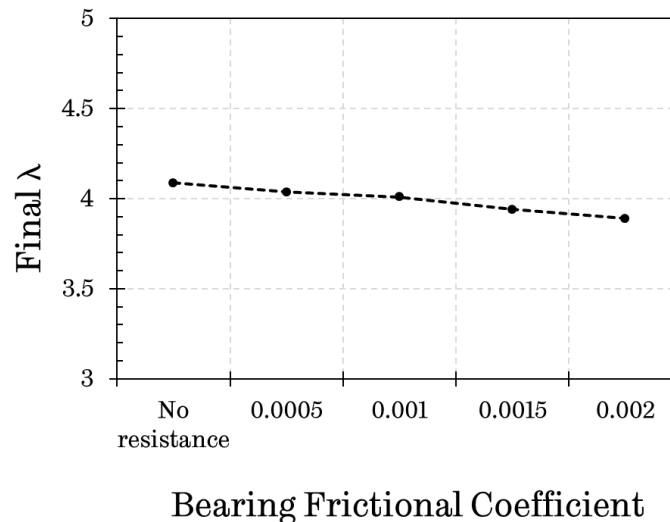
Figure 5.22. The final tip speed ratio as a function of the different bearing frictional coefficient.

Even though a small resistance plays a significant role on the turbine self-starting behaviour, it is clear that the turbine real start-up time and the final tip speed ratio are not possible to be predicted precisely due to the existence of the 3D effects, such as blade supporting arms and tip losses not being considered in the 2D CFD simulations. However, the results obtained from this study show how the resistance affects the turbine self-starting behaviour and these results provide important insights for future studies.

5.6   Conclusion

In this chapter, a CFD start-up model with own user-defined function (UDF) has been employed in order to provide an in-depth understanding of the self-starting behaviour of the H-type VAWTs with paying attention to the turbine different start-up stages. Furthermore, in contrast conventional numerical approach in the literature, the effect of the several physical properties, such as the inertia of the blades, the number of blades, the chord length, and the mechanical resistance on its overall and the self-starting performance has been investigated using the dynamic CFD start-up model, in which the rotation velocity of the turbine is driven by the turbine aerodynamic torque.

The important findings of the present study are as follows:

- In the critical region ($\lambda<1$), the positive drag contributes to the torque generation in the second and third quarters of the rotor revolution, where the range of the azimuthal angles vary between 100° and 253°. Once $\lambda>1$, the turbine enters a stage where the turbine is fully driven by the lift force.

- In order to improve the self-starting capability of the H-type VAWT in the critical region, not only the lift force but also the drag force, at the position where the drag force assists the turbine rotating motion, should be enhanced.

- When the $\lambda\geq1$, the lift-driven is required to be maintained in order to achieve a complete start-up process.

- Although increasing the moment of inertia of the turbine increases the time to reach the final rotational speed, it decreases the amplitude of the fluctuation of the turbine rotational speed at the steady-state condition.

- An instantaneous increase in the power efficiency is observed during the start-up process when the turbine escapes from the plateau stage due to an increase in the acceleration rate of the lighter turbine.

- The peak power coefficient is achieved when the number of blades is 3; however, a faster start-up time is achieved when the number of blades is 5. Therefore, a compromise between the start-up and the power efficiency may have to be made in the design of the turbine.

- The larger number of blades allows the reaching of a slightly higher power coefficient at low tip speed ratios ($\lambda<1$), which increases the self-starting capability of the turbine.

- When the turbine is rotating faster (higher tip speed ratio), the optimum performance is obtained with a smaller blade area (lower blade chord length) while if the turbine is rotating slower (lower tip speed ratio), the optimum performance is achieved for a larger blade area (higher blade chord length).

- With the increase in the bearing frictional coefficients, the start-up time is delayed; however, the final tip speed ratio decreases.

- The application of the resistance force in the CFD simulations make the results much more physically and practically important and reliable. In addition, it will assist in producing more realistic results in the future studies.

Chapter 6

Aerodynamic characteristics of J-shaped aerofoils

6.1 Introduction

The J-shaped aerofoil exhibits an alternative solution to the problem of self-starting of H-type VAWTs, due to the higher torque generation at the low λ values. Although some studies have been reported on the self-starting behaviour of the turbine with a J-shaped profile at isolated fixed rotational speeds, the dynamic characteristics of the J-shaped aerofoil performing Darrieus motion as occurs in VAWTs is not fully understood due to the lack of detailed aerodynamics analysis. This has significantly hindered the progress in effective designs of self-start VAWT using J-shaped aerofoil. There is an urgent need to gain an in-depth understanding of the aerodynamics of the J-shaped aerofoil under the operating conditions that mimic those of VAWTs, in order to optimise the design of the J-shape blade for self-starting VAWTs and minimise their loss at high λ values.

Therefore, the current study aims at providing a detailed aerodynamic investigation of the J-shaped aerofoil in comparison with its counterpart conventional profile when performing the Darrieus oscillating motion that simulates the fundamental fluid dynamics of the VAWT but in a much simple CFD setup. Three different opening ratios have been investigated, namely 30%, 60%, and 90%, in terms of the ratio of the opening size x to the aerofoil chord length c, as shown in Figure 6.1.
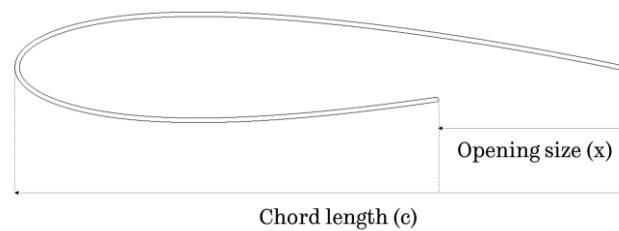
Figure 6.1. Schematic representation of a J-shaped aerofoil with an x/c=30% opening located at the pressure side of the aerofoil.

Firstly, the CFD simulations of an oscillating aerofoil performing Darrieus motion defined by Eq. 6.1, which matches the angle of attack motion of a VAWT, has been conducted to provide an appreciation of the aerodynamics, such as the dynamic stall phenomenon, for one of the most used conventional aerofoils NACA0018. Then the aerodynamics over the J-shaped aerofoil profiles produced by cutting off part of the NACA0018 were analysed. The crucial parameters, such as the tip speed ratio and pitch angle and their effect on the aerodynamic performance of the J-shaped aerofoil undergoing the Darrieus motion have been investigated and compared with the standard NACA0018 under the same flow conditions. The simulation results provide a comprehensive analyse both quantitatively and qualitatively of the differences in the aerodynamic performance of the conventional and J-shaped aerofoil profiles. Secondly, the simulations have been performed over stationary J-shaped aerofoils with different opening ratios, and then the results were compared with the NACA0018

at both positive and negative angles of attack. Consequently, the current study sheds much light on the characteristics of the J-shaped aerofoil from an aerodynamic point of view when it is used in the turbine applications.

6.2   Dynamic Performance

In this section, several of the most important parameters, such as aerofoil thickness, tip speed ratio, pitch angle, Reynolds number, and constantly varying relative velocity have been investigated using the J-shaped aerofoil and its counterpart conventional profiles, in order to address the need in better understanding the influence of these parameters governing to H-type VAWTs operation. Additionally, the visualization of the flow generated over the J-shaped aerofoil and a comparison with its conventional profile are presented in order to allow the qualitative comparisons of the aerodynamic characteristics of the aerofoils over the complete pitching motion cycle in which aerofoils oscillating within a certain angle of attack range.

6.2.1   Method

A VAWT aerofoil experiences dynamic stall due to the continuous change in its effective angle of attack, particularly at the low tip speed ratios. The dynamic stall phenomenon is characterised by the formation and shedding of the vortex from the aerofoil surface to the wake under changing the high angle of attacks and can also induce large unsteady aerodynamic loads and flow losses. An extensive number of experimental and numerical studies have been conducted in order to indicate the factors that most affect this complicated phenomenon on VAWTs [164, 165, 166, 167, 168]. These studies show that the dynamic stall is primarily dependent on the aerofoil shape, the amplitude of oscillation in the angle of attack, Reynolds number, and the rotational speed/reduced frequency. However, most of these previous studies concerned with the relatively high Reynolds number, which is around 1×10^6 or larger, and the generally oscillating aerofoil undergoing the sinusoidal pitching motion has been applied [165, 169, 170, 171]. This study will focus on relatively low Reynolds number flow.

One of the complicated features of the H-type VAWT is that the relative velocity experienced by the blade always changes as the azimuthal angle varies in a cyclic manner. In addition, as the turbine rotates, the angle of attack between the oncoming wind and rotating blades continuously changes as a function of the blade azimuthal position. Both the magnitude of the relative velocity and the angle of attack is also a function of the tip speed ratio, which results in the variable aerodynamic forces. This is generally referred to as the Darrieus motion [172]. Therefore, in this study, the Darrieus motion describing the blade angle of attack of a VAWT is systematically applied to the simulations in order to investigate the aerodynamic characteristics of J-shaped aerofoils and its conventional profile. The approach used to evaluate the influence of the operating conditions on the performance of the J-shaped aerofoil and its conventional profile can be explained as follows:

An investigation of the oncoming wind flow V_∞ with a constant magnitude passing over an oscillating aerofoil has been conducted, as shown in Figure 6.2. The oscillating aerofoil describes the angle of the attack motion of a VAWT blade given as follow:

$$\alpha(t) = tan^{-1}\left(\frac{\sin(\omega t)}{\lambda + \cos(\omega t)}\right) - \beta \tag{6.1}$$

where ω is the rotational speed, t is the time, λ is the tip speed ratio, and β is the pitch angle.

The angle between the chord and the incoming wind is represented as the angle of attack (α). Also, the positive pitch angle (β) described for this oscillating aerofoil is shown in Figure 6.2 (a) [88]. Furthermore, the definition of the upstroke and downstroke motions of the aerofoil in the positive and negative angles of attack regions used in the present study is also illustrated in Figure 6.2 (b).

(a)

(b)

1: Upstroke (↑) in positive angles of attack
2: Downstroke (↓) in positive angles of attack
3: Downstroke (↓) in negative angles of attack
4: Upstroke (↑) in negative angles of attack
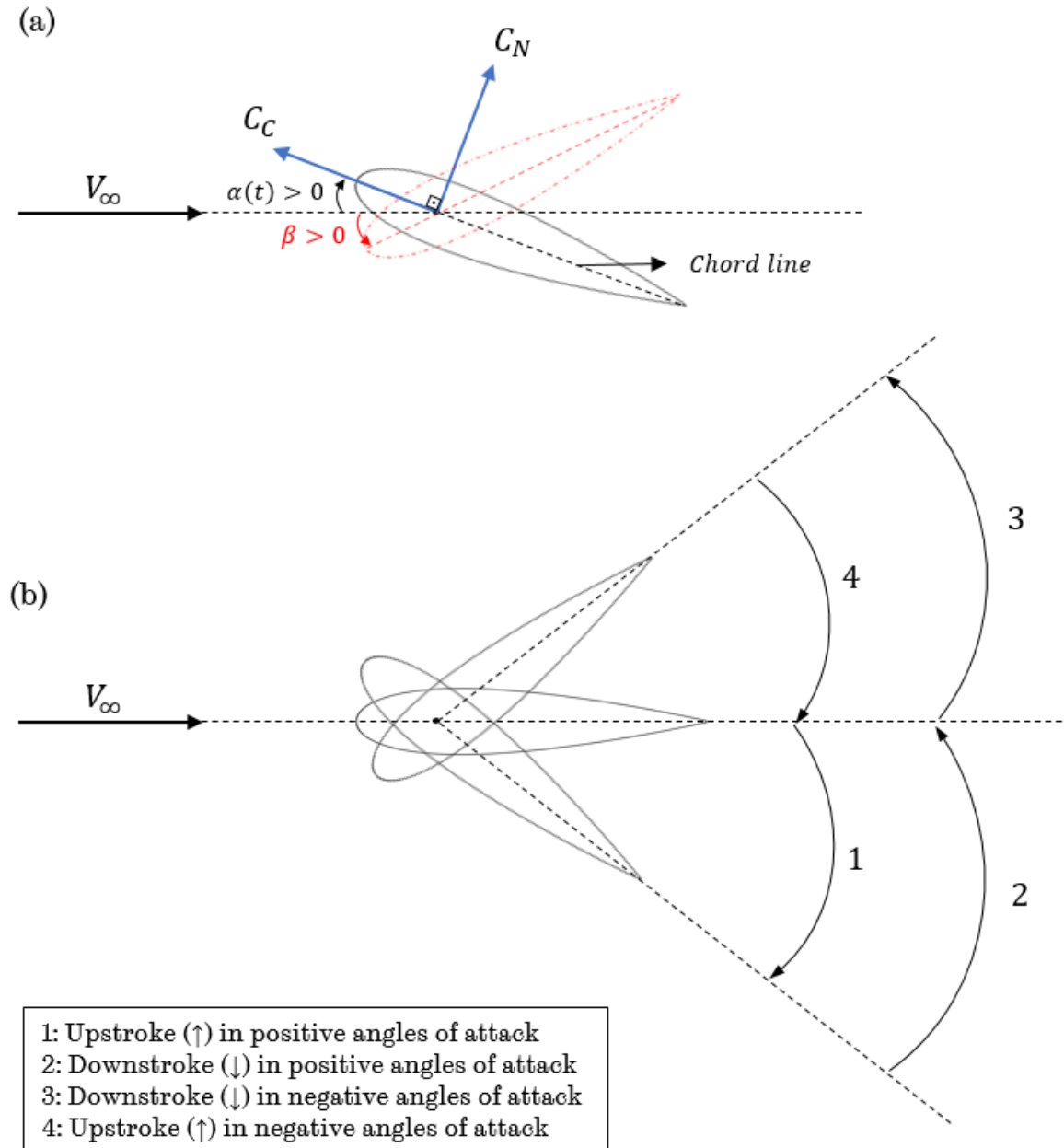
Figure 6.2. Schematics of the (a) flow past an oscillating aerofoil and (b) the upstroke and downstroke motions in the positive and negative angles of attack.

The value of the ωt varying between 0 and π represents the upstream part of the turbine while between π and 2π, it represents the downstream part of the turbine. Furthermore, positive angles of attack are also considered as the upstream part of the turbine and the negative angles of attack are considered as the downstream part of the turbine when the $\beta = 0°$.

To mimic the angle of attack motion described in the Eq. 6.1 in the CFD simulations, a user-defined function (UDF), which is presented in Appendix, has been developed and applied in ANSYS Fluent to control the pitching rate of the rotating domain according to the equation:

$$\dot{\alpha} = \omega \left(\frac{(1 + \lambda \cos(\omega t))}{(\lambda^2 + 2\lambda \cos(\omega t) + 1)} \right) \tag{6.2}$$

Using this method, the tip speed ratio and pitch angle that affects the angle of attack given in Eq. 6.1 at a constant Reynolds number have been investigated initially. The effect of the varying relative wind velocity will be examined later. The rotational speed (ω) of the oscillating aerofoil was expressed depending on the non-dimensional parameter, which is called the reduced frequency (k). Reduced frequency is the dimensionless number used in general for the case of unsteady aerodynamics and expressed as $k = \omega c / 2V_\infty$ [59]. In addition, different values of the Reynolds number were tested at a constant tip speed ratio.

The tip speed ratios examined in the present study are 2, 2.5, and 3.5 as these are usually identified to be small (λ=2) enough for higher possibility of the dynamic stall occurrence and relatively high (λ=3.5) enough to reduce the effect of the dynamic stall. Furthermore, the values of the Reynolds number investigated are 0.4×10^5, 0.72×10^5 and 1×10^5, which are appropriate to the urban applications of the H-type VAWTs and this range of the Reynolds number makes a contribution towards a much better understanding of the flow physics as well as the dynamic stall phenomena to assist in the design of the J-shaped aerofoil for the H-type VAWT applications [173, 174, 175]. Additionally, the values of the reduced frequency (k) used in the current study are 0.1 which is found to be in the range of the average reduced frequency in VAWTs [174].

As previously mentioned, the relative velocity experienced by the blade is always changing as the azimuthal angle varies in a cyclic manner in the H-type VAWT applications. Therefore, as the final step of the present investigation, a constantly-changing relative velocity will be taken into account in order to

observe its effect on the dynamic performance of a J-shaped profile undergoing a Darrieus motion. The oncoming relative velocity V_{rel} was a time-depended function given by the equation of the VAWTs as follows:

$$V_{rel} = V_\infty \sqrt{\lambda^2 + 2\lambda cos(wt) + 1} \tag{6.3}$$

Therefore, it will be beneficial to investigate the effect of the constantly-changing relative velocity expressed in Eq. 6.3 on the aerodynamic behaviour of the J-shaped aerofoil and its conventional profile. A user-defined function (UDF) was applied to ANSYS Fluent according to the Eq. 6.2 and Eq. 6.3 to implement the constantly-varying relative velocity to the simulations. A typical example of the UDF code used in the present investigations is presented in Appendix.

The stall-onset angle is one of the most crucial parameters to explain the dynamic stall process. The stall-onset angle shows the inception of the leading edge vortex (LEV) [169]. Under the static conditions, the stall angle can be recognised according to the angle where a rapid decrease in the lift force coefficient. However, more careful attention to the other type of aerodynamic features requires to be paid under the dynamic conditions. There are several ways employed in the calculations in order to recognise the stall-onset angle during the unsteady conditions. However, in this study, the angle where the maximum chordwise force coefficient obtained is considered for the calculation of the stall-onset angle. This criterion has been also suggested by several authors [176]. The chordwise force coefficient, C_c, for an oscillating aerofoil can be described as in Eq. 6.4.

$$C_c = C_l \sin(\alpha) - C_d \cos(\alpha) \tag{6.4}$$

where C_l is the dynamic lift force coefficient, C_d is the dynamic drag force coefficient, and α is the angle of attack. In the present study, the chordwise force coefficient is used to get some insight into the effect of the operating conditions on the dynamic characteristics of the J-shaped aerofoil and to predict the stall-onset angle.

6.2.2 CFD oscillating aerofoil study

6.2.2.1 Model description and numerical settings

The 2D CFD simulations employed for this investigation have been validated with the existing experimental data of an oscillating NACA0012 aerofoil conducted by Lee and Gerontakos [168]. The reason for selecting this experimental data is due to the lack of experimental studies in the literature at such low Reynolds number in terms of the oscillating motion for NACA0018, and it has been reproduced by many authors using the RANS [177, 178, 179] and LES [177]. Therefore, this is beneficial to compare and verify the numerical study conducted in the present study with the available numerical results. Table 6.1 provides the details for this experimental setup concerning: aerofoil shape, chord length, free stream velocity, Reynolds number, and pitching motion parameters.

Table 6.1. Validation case parameters

Aerofoil	NACA0012
Chord	0.15m
V_∞	14m/s
Reynolds number	135,000
Pitching motion	$\alpha = 10° + 15°\sin(\omega t)$
ω	18.67 rad/s
Reduced frequency (k)	0.1

In the present study, a pressure-based solver was used while the pressure-velocity coupling was handled using the Coupled algorithm. A 2nd order interpolation scheme for the pressure has been used along while a 2nd order upwind discretization scheme for all the other parameters. In addition, one of the advantages of using the Coupled method is that it is able to detect divergence and automatically reduces the Courant Number (CFL). In the CFD solver, the default value of the CFL number is 200 when the Coupled method is selected;

however, a reduction to 10-50 is recommended [176] if the simulations are struggling to converge, therefore a CFL=10 has been selected. Moreover, the convergence of the simulations was assessed by a low residual level of 10^{-5} with 50 iterations per time step. In order to obtain a converged solution, at least four complete oscillating cycles have been run for each simulation and the force coefficients, such as lift and drag, have been collected in the fourth cycle.

Furthermore, selecting the turbulence model plays a crucial role in the oscillating aerofoils due to the complex flow structures, such as stall phenomena and linear to the turbulent transitional process at low Reynolds numbers. Therefore, in the current study, the SST $k - \omega$ turbulence model with an intermittency function, which is the additional transport equation, has been chosen due to the Reynolds numbers studied, which are less than 135,000, where the boundary layer flow transition possibly occurs, and the transitional turbulence model is suggested at such Reynolds numbers [176, 178].

6.2.2.2 Model sensitivity study

The sensitivity studies were performed to obtain a reliable CFD oscillating aerofoil model, which will be applied in order to predict the dynamic aerodynamic force coefficients of the aerofoil and compare the findings with the experimental data. For this reason, the domain size, number of nodes around the aerofoil, and time step size studies have been carried out.

6.2.2.2.1 Domain size

The flow around the single aerofoil is modelled by a rectangular-shaped computational domain. The created computation domain is divided into two regions, namely a circular subdomain and a rectangular stationary domain. These two regions are connected using the interface boundary condition in order to ensure that the continuity in the flow field is achieved. The velocity inlet boundary condition is placed on the left side of the computational domain while the pressure outlet is applied to the right side of the computational domain, and the aerofoil is treated as a stationary wall with no-slip boundary. Figure 6.3

presents the computational domain used for the domain size sensitivity study. As indicated in the figure, A is the distance between the velocity inlet and the centre of the aerofoil, B is the distance between the centre of the aerofoil and the pressure outlet, C is the distance between two symmetry boundaries, and D is the radius of the small circular subdomain that is located at the vicinity of the aerofoil in order to enable easier variation of the angle of attack.
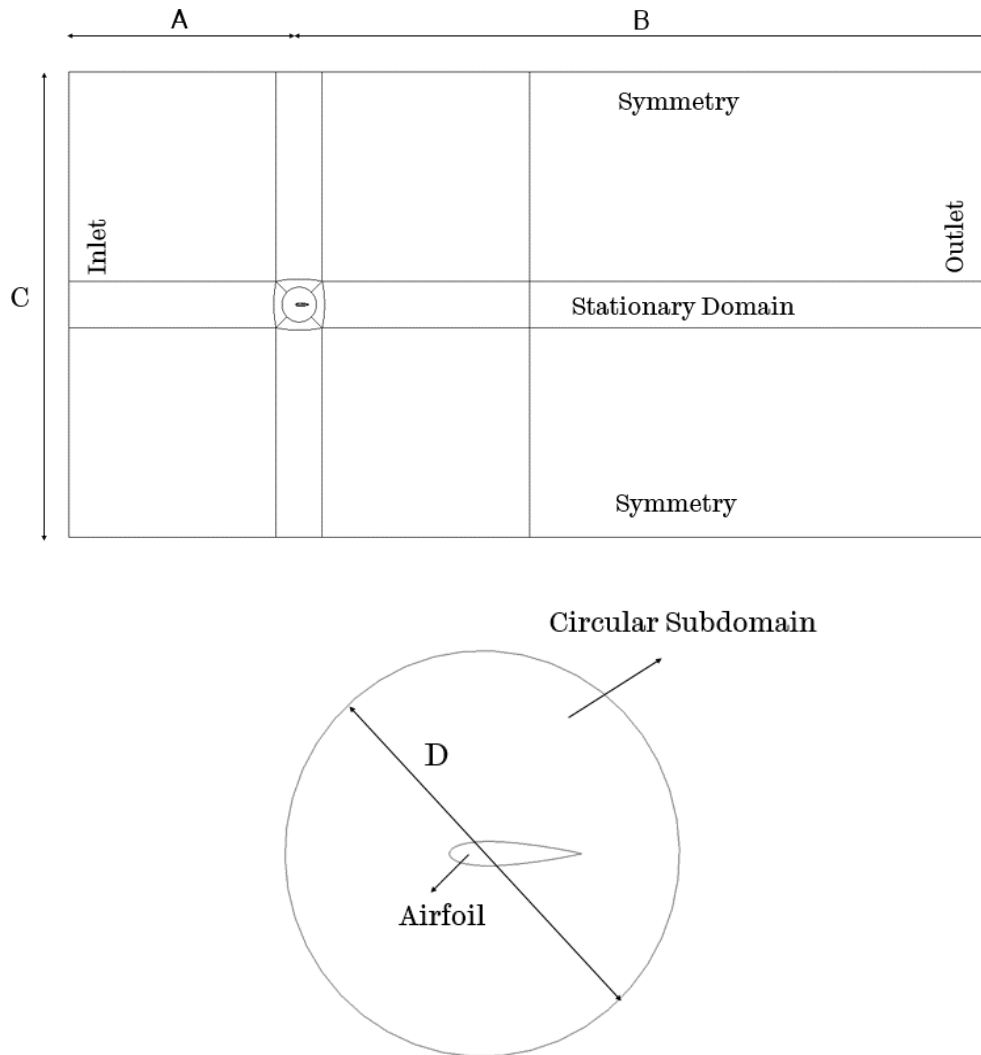
Figure 6.3. The schematic of the domain created for the computations.

The domain size sensitivity study is conducted in order to ensure that the changing on the domain size of the computational domain does not affect the predicted aerofoil forces. For this reason, five different domain size cases,

namely Domain 1, Domain 2, Domain 3, Domain 4, and Domain 5, have been created in ANSYS Design Modeller, and the values of each case are illustrated in Table 6.2. The values of Domain 1 have been selected as relatively small values, and then these values have been proportionally increased for other cases in order to find optimum values for the computational domain.

Table 6.2. Computational domain sizes for 2D CFD oscillating aerofoil validation study.

Name	Values			
	A	**B**	**C**	**D**
Domain 1	5c	15c	10c	3c
Domain 2	10c	30c	20c	3c
Domain 3	15c	45c	30c	3c
Domain 4	20c	60c	40c	3c
Domain 5	25c	75c	50c	3c

Figure 6.4 shows the predicted lift coefficient as a function of the angle of attack of the aerofoil for the domain size study. As can be seen in the figure that the changes in the domain size affect the obtained results. However, increasing the domain size beyond Domain 4 has very little effect on the results. Therefore, the dimension of Domain 4 can be selected to ensure domain independence results. The selected domain is extended 20 chords length upstream, above, and below the pitching position of the aerofoil (1/4c), and this appears to be enough to avoid the effect of the side boundaries of the computational domain. It is also extended 60 chords length downstream in order to ensure that the pressure outlet is as close to a uniform atmospheric pressure as possible.
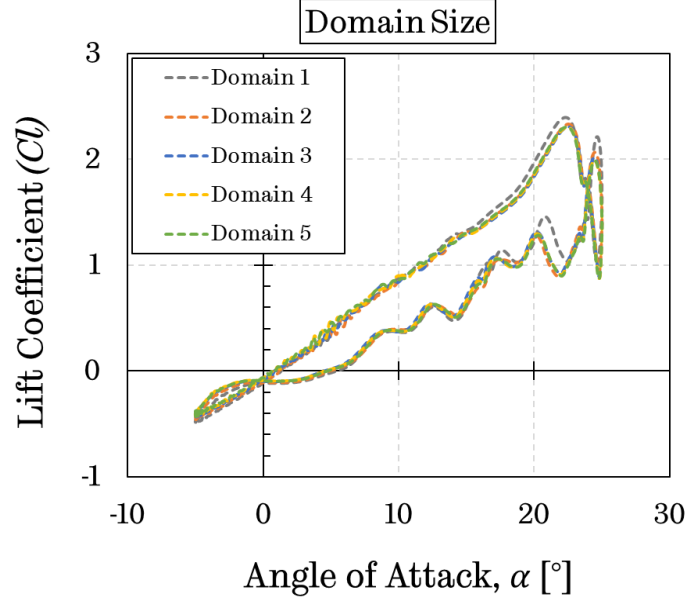
Figure 6.4. The lift coefficient as a function of the angle of attack of the aerofoil for the domain size study.

6.2.2.2.2 Meshing topology and independency

One of the most critical parts of the CFD simulations is to create a proper mesh in order to obtain accurate results. Therefore, a hybrid mesh, which consists of a structured mesh used for both around the aerofoil and in the far fields, while an unstructured mesh is used for the rotating domain, is employed as the most appropriate mesh type in this study. The reason for choosing the hybrid mesh is since the hybrid mesh provides a flexible approach and reduces the number of mesh elements in the computational domain [180]. The computational domain is discretised into small control volumes. In order to allow the turbulence model to predict the performance, the literature recommends that the boundary layer with at least 10 layers of cells should be employed in order to ensure sufficient boundary layer modelling [153]. However, in the present study, the mesh inflation with 40 layers of cells having the first cell height of about 6.5×10^{-5} has been used to obtain a y^+ value less than 1. Maintaining these values allows applying the enhanced wall treatment turbulence models, such as $k - \epsilon$ and $k - \omega$ turbulence models [152].

Figure 6.5 illustrates the computational grid for the oscillating aerofoil. A hybrid mesh is selected in this present study by applying a structured mesh around the aerofoil, which provides more accurate predictions for the flow near the aerofoil boundary layer, and stationary domain while an unstructured mesh for the circular subdomain due to its simplicity.
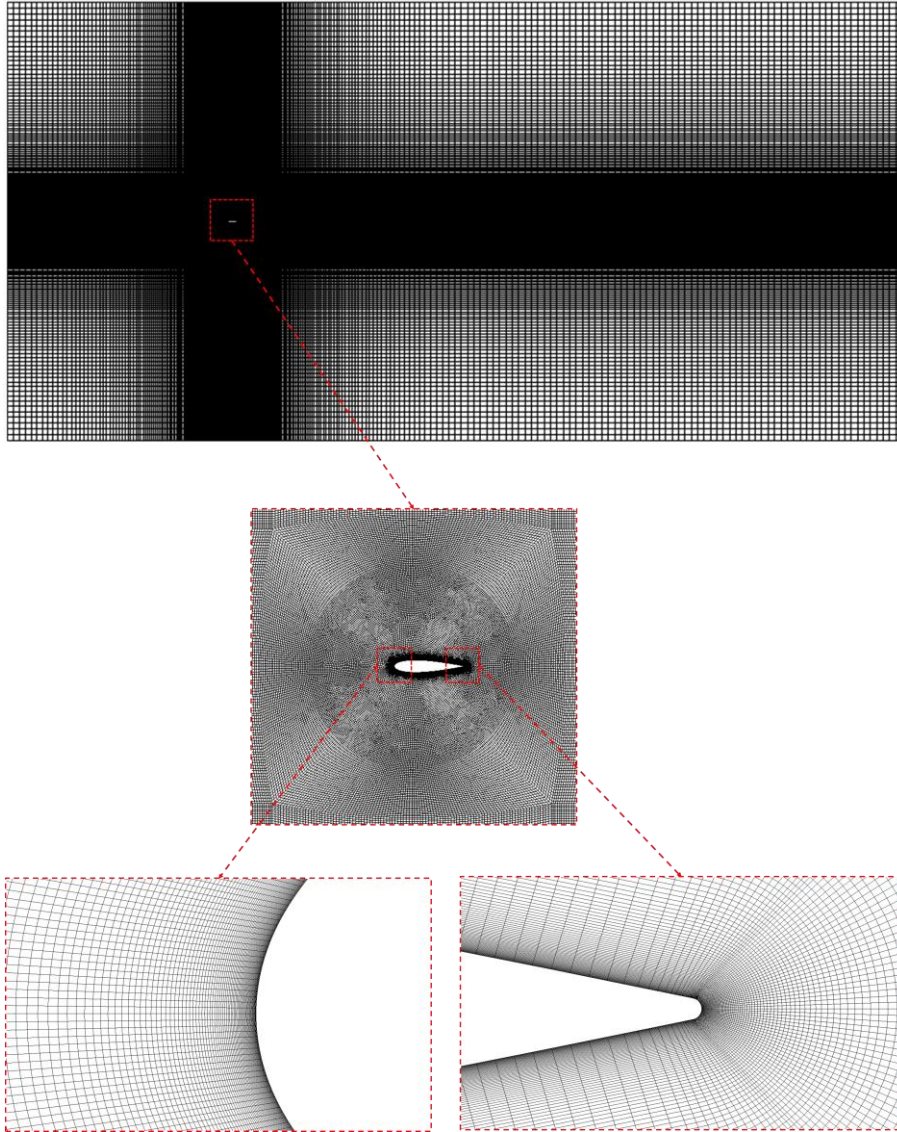
Figure 6.5. The grid structure of the computational domain, circular subdomain, and aerofoil surface.

Five different number of nodes around the aerofoil, as shown in Table 6.3, namely Node 1, Node 2, Node 3, Node 4, and Node 5, which have 150, 300, 500, 750,

and 1000 nodes, respectively, have been created by using the ANSYS Meshing Module and examined in order to obtain grid independence results. The comparison of the predicted lift force coefficients as a function of the angle of attack for the different number of nodes around the aerofoil has been presented in Figure 6.6. The figure shows that no significant difference was obtained in the lift force coefficients observed between Node 4 and Node 5 and therefore, Node 4 has been chosen in terms of the accuracy and computational time for the future simulations. The selected number of nodes for the aerofoil surface has 750 nodes that are properly clustered at the leading and trailing edges of the aerofoil where high gradients in the pressure and flow are expected. The final mesh consists of approximately 191,000 cells, as shown in Figure 6.5.

Table 6.3. The number of nodes around the investigated aerofoil.

	Values				
	Node 1	**Node 2**	**Node 3**	**Node 4**	**Node 5**
Number of Nodes	150	300	500	750	1000
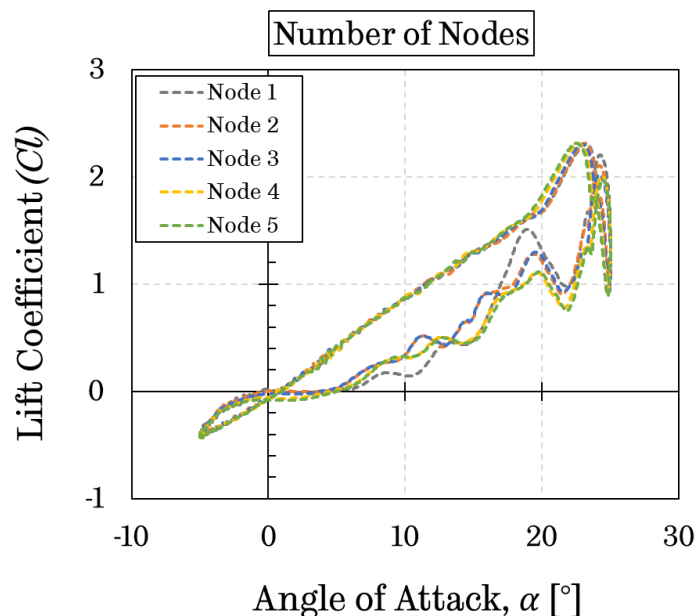
Figure 6.6. The lift coefficient as a function of the angle of attack of the aerofoil for the number of nodes study.

6.2.2.2.3 Time step size study

In order to identify an appropriate time step size, a time step size sensitivity study has been carried out with a non-dimensional time constant ($\tau = t/T$) of 0.001, 0.0005, and 0.00025. The lift force coefficients computed from the simulations on the three different time steps as a function of the angle of attack have been presented in Figure 6.7. The figure shows that similar lift force coefficients were obtained for all the time step investigated and thus, $\tau = 0.005$ has been selected for the further simulations in order to reduce the computational time.
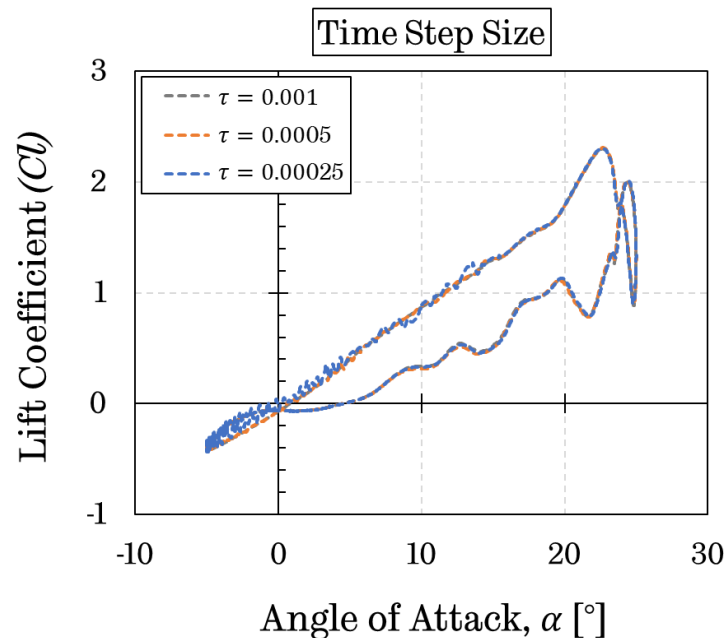
Figure 6.7. The lift coefficient as a function of the angle of attack of the aerofoil for the time step size study.

6.2.2.3 Model validation

Two cases have been selected to validate the present numerical model. Firstly, the prediction accuracy of the present CFD oscillating model has been examined by comparing against the experimental test conducted by Lee and Gerontakos [168], and other numerical studies performed by Gharali et al. [178] and Karbasian et al. [179], and a comparison among these four simulations in terms

of the force coefficients is illustrated in Figure 6.8. The current CFD result has a good agreement with the experimental data and the other CFD simulation results. It can be observed that in the upstroke part of the motion, within the low and medium range of the angles of attack, $0° \leq \alpha \leq 20°$, the current CFD results for the aerodynamic force coefficients agree well with the experimental data. However, at the high angles of attack, $20° \leq \alpha \leq 25°$ where the leading edge vortex (LEV) has been released, the much larger deviation in Cl and Cd between the current CFD results and the experimental data has been observed. This may be due to the limited accuracy of the numerical model to capture the complicated flow phenomena, such as the deep stall. However, the peak Cl observed in the experimental study was not obtained by any of the numerical simulations.

In the downstroke part of the motion, the current lift coefficient curve is much closer to the experimental lift curve compared to the other numerical results. In addition, there are several fluctuations observed during the downstroke motion, which may be due to the reattachment of the flow to the aerofoil surface. In terms of the drag force coefficient, there is generally a less satisfactory agreement between the numerical simulations and the experimental data, particularly when $\alpha \leq 16°$. This is due to the persistent flow separations at high angles of attack, resulting in difficulties to accurately model the viscous effects adjacent to the aerofoil surface when using RANS models [177].
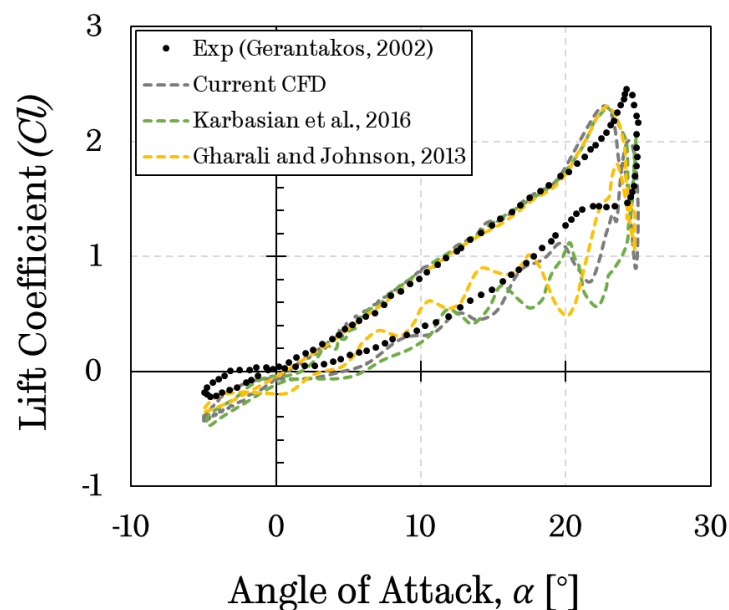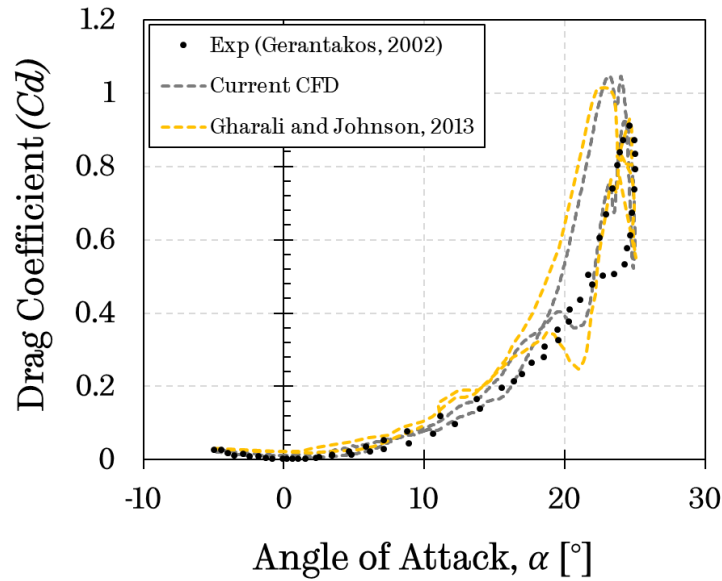
Figure 6.8. The lift and drag coefficients of the NACA0012 aerofoil as a function of the angle of attack for the current CFD model and the comparison with the experimental study and other numerical studies at Re=1.35×10^5.

Secondly, to illustrate the accuracy of the present numerical model, a second validation study has been carried out by employing a NACA0015 aerofoil due to the existence of the experimental data [181] with the same oscillating motion as the previous experimental data and the operating conditions are shown in Table 6.4. The prediction of the chordwise force coefficient as a function of the angle of attack and comparison with the experimental and the other numerical data have been illustrated in Figure 6.9. It is believed that this second validation result will provide the advantages of the comparison in terms of the chordwise force coefficient. The excellent agreement has been obtained in the prediction of the peak chordwise force coefficient with both the experimental and other numerical results.

Table 6.4. Validation case parameters

Aerofoil	NACA0015
Chord	0.15m
V_∞	19.48m/s
Reynolds number	200,000
Pitching motion	$\alpha = 10° + 15°\sin(\omega t)$
ω	25.97 rad/s
Reduced frequency (k)	0.1
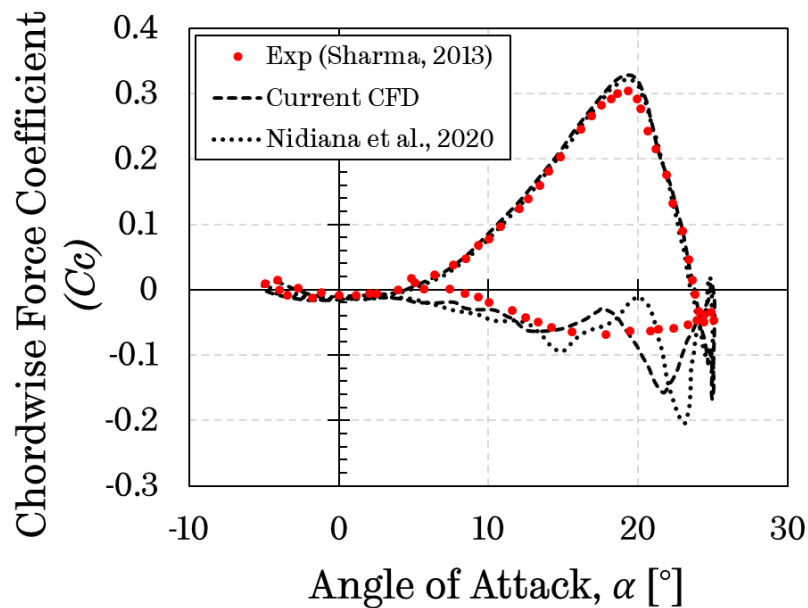
Figure 6.9. The chordwise force coefficient of the NACA0018 aerofoil as a function of the angle of attack for the current CFD model and the comparison with the experimental study and other numerical studies at Re=2×10^5.

In view of the overall agreement with the experimental data and the numerical results, the present CFD model, since it captures the chordwise force coefficient with an excellent agreement, is deemed to be sufficiently accurate enough to investigate the dynamic performance of the J-shaped aerofoil by comparing its conventional profile with regards to the aerodynamic forces and the unsteady flow fields.

An example of the unsteady lift force coefficient under the dynamic stall for the validated oscillating aerofoil and the flow structures developed over the aerofoil at different angles of attack have been illustrated in Figure 6.10. This section aims to provide a general understanding of the dynamic stall process and better explain the flow structures generated over the validated oscillating NACA0012 aerofoil using the quantitative visualisation. Over the initial steps of the upstroke motion, $10°\uparrow<\alpha<19.37°\uparrow$ (Figure 6.10 (1)-(3)), the entire suction side of the aerofoil is characterised as an attached shear layer without flow separation. However, the thickness of the shear layer at the trailing edge increases and the lift force coefficient increases linearly with the increasing angle of attack. At the pitch angle, $\alpha=19.37°\uparrow$ (Figure 6.10 (3)), the lift coefficient starts to deviate from its linear attached trend and the leading edge vortex (LEV) starts to develop and this extends over almost half of the suction side of the aerofoil. This stage of the oscillating motion is known as the stall-onset angle, which represents the stall inception process. The increase in the angle of attack from $19.37°\uparrow$ to $22.66°\uparrow$ induces the leading edge vortex (LEV) to grow in size and to extend over almost the entire suction side of the aerofoil, as shown in Figure 6.10 (4). At this stage, due to the vortex moves downstream throughout the chord length of the aerofoil, the lift coefficient still increases and reaches its maximum value and then, stalls, this point is called lift stall. During the remaining upstroke motion (Figure 6.10 (5)), the aerofoil experiences the deep dynamic stall condition, where the capability of the lift force generation dramatically decreases. The leading edge vortex (LEV) starts to move away from the aerofoil surface and a trailing edge vortex (TEV) that features a counter-clockwise rotation has been generated. When the aerofoil starts to pitch down (Figure 6.10 (6)), a second peak in the lift coefficient is observed. At this stage, the primary vortex formed at the leading edge is shed into the wake, and the secondary vortex is formed over the suction side of the aerofoil surface. Afterwards, the secondary leading edge vortex (LEV) is subsequently shed into the wake again and a secondary trailing edge vortex (TEV) is formed at $\alpha=21.73°\downarrow$ (Figure 6.10 (7)). Once the pitch angle is further reduced, the flow starts to reattach over the aerofoil surface. At $\alpha=0°\downarrow$ (Figure 6.10

(9)), the separated boundary layer is attached to the aerofoil surface until $x/c \approx 0.85$. At the negative angle of attack region (At α=-5°↓, (Figure 6.10 (10))), the chaotic flow phenomenon is disappeared from the upper surface of the aerofoil.
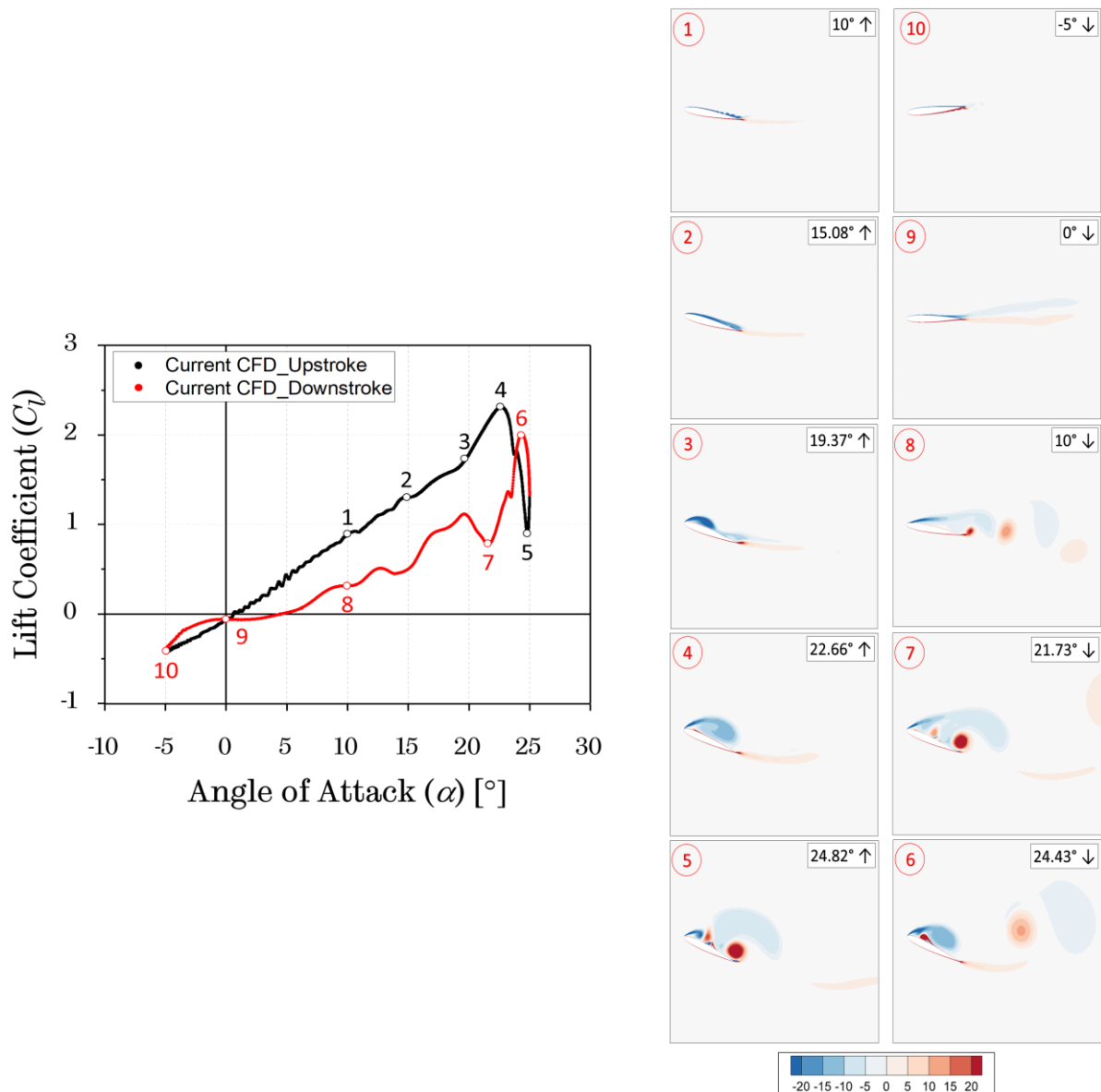
Figure 6.10. Lift coefficient as a function of the angle of attack and the contours of the normalised z-vorticity ($w_z c / V_\infty$) of the flow over the NACA0012 aerofoil during the different complete pitching motions.

6.2.3 Darrieus motion

6.2.3.1 Effect of the aerofoil thickness

In this section, the influence of the aerofoil's thickness on the dynamic stall behaviour has been investigated during the Darrieus oscillating motion, which is described by using Eq. 6.2, under the operating conditions of the Reynolds number $Re = 0.72 \times 10^5$, the tip speed ratio λ=2.5 and $\beta = 0°$. Two different aerofoils have been adopted, namely the NACA0012 and NACA0018, and their J-shaped profiles with several different opening ratios. The flow conditions and the settings in the numerical simulations are the same for all the numerical cases investigated. Figure 6.11 shows a comparison of the aerodynamic force trends of the NACA0012 and NACA0018 aerofoils and their J-shaped profiles undergoing the Darrieus motion. The findings show that the increase in the opening ratio over the aerofoil surface indicates an increase in the aerodynamic performance, particularly concerning the chordwise force coefficient, in the positive angles of attack region, which corresponds to the upstream part of the turbine (see Figure 6.11 (c) and (f)). On the contrary, a reduction in the chordwise force coefficient with the increase in the opening ratio has been observed in the negative angles of attack region, which refers to the downstream part of the turbine (see Figure 6.11 (c) and (f)). Although no significant differences are observed during the negative angles of attack motion in the lift force coefficient trends, the J-shaped profile with a 90% opening ratio produces a higher drag force compared to the conventional aerofoil and other J-shaped profiles with smaller opening ratios, particularly during the upstroke motion in the negative angles of attack, where the opening section is located on the suction side of the aerofoil. This is the reason why the performance decreases with the increase in the opening ratio in the negative angles of attack region.
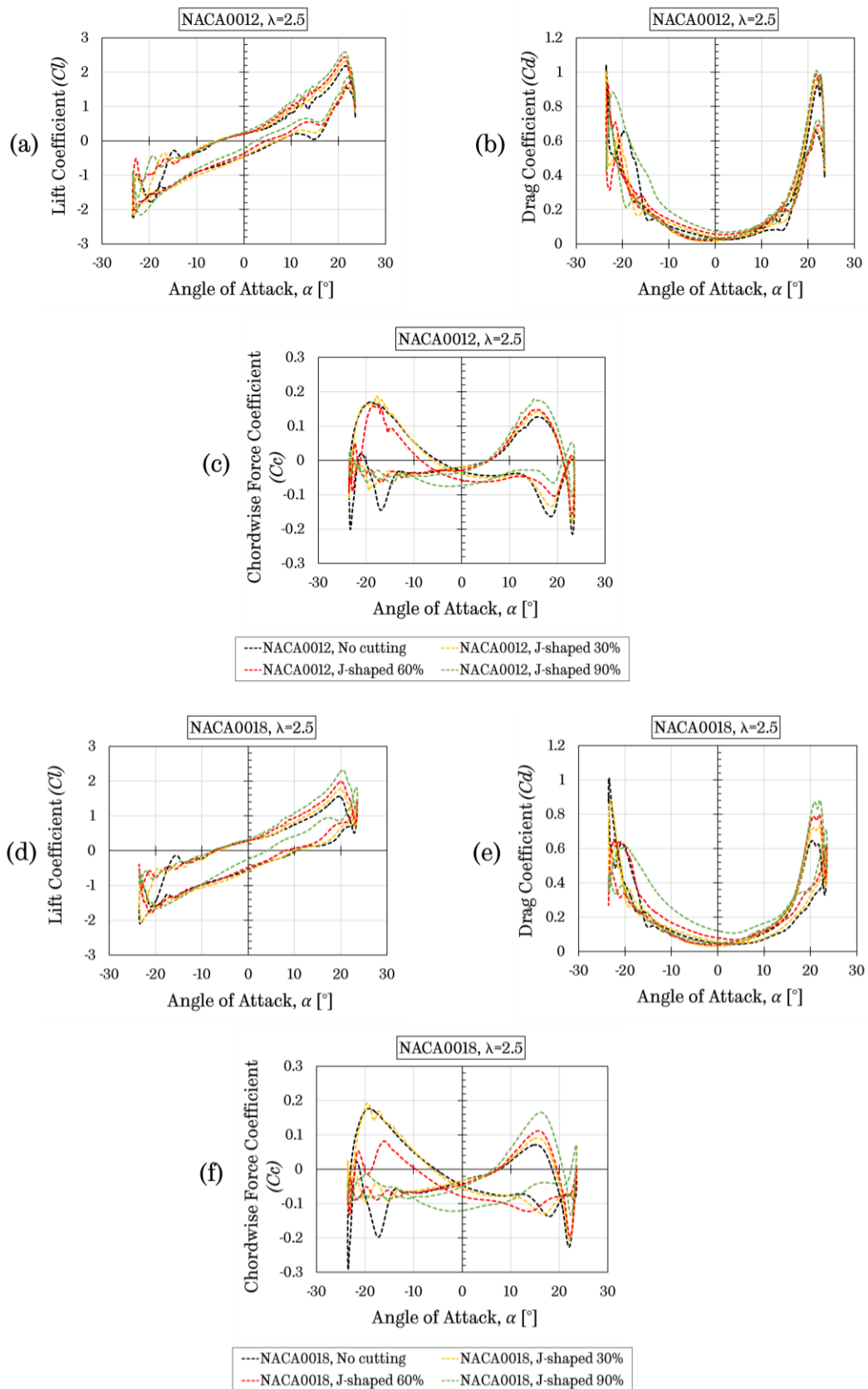
Figure 6.11. The comparison of the aerodynamic force trends of the NACA0012 and NACA0018 aerofoils and their J-shaped profiles undergoing the Darrieus motion.

Furthermore, Figure 6.12 shows a comparison of the aerofoils investigated in terms of the different opening ratios as a function of the angle of attack. It can be observed in the figure that there is no significant difference on the chordwise force coefficient observed in the negative angles of attack region, while the difference is much clearer in the positive angles of attack region; however, this difference decreases with the increase in the opening ratio. For instance, the peak chordwise force coefficient of the NACA0012 aerofoil with no cutting is obtained as 0.127 at α =16.06° while that one is 0.0717 at α =15.07° for NACA0018 aerofoil with no cutting. However, the peak chordwise force coefficient of the NACA0012 aerofoil with a 90% opening is found to be 0.1745 at α =16.33° while that one is 0.165 at α =16.19° for the NACA0018 aerofoil with a 90% opening ratio. This may be also caused by the flow separation phenomenon since the flow around the thicker aerofoil and its J-shaped profile separates earlier than the thinner aerofoil and its J-shaped profiles as the angle of attack increases.

To summarise, the NACA0012 and its J-shaped profiles show a better aerodynamic performance than that of NACA0018 and its J-shaped profiles at the positive angles of attack region. The reason for this may be that the thinner airfoils have a higher performance at relatively higher tip speed ratios while the thicker aerofoils have a higher performance at lower tip speed ratios [123]. Therefore, thicker aerofoils are generally preferred in VAWTs applications to improve the starting torque at low λ values [182]. However, since the wake effect due to the interaction of the blades and shaft was not taken into account in the Darrieus oscillating motions, the downstream part, which refers to the negative angles of attack region in the Darrieus motion case, appears to be much more complicated in obtaining a reliable conclusion.
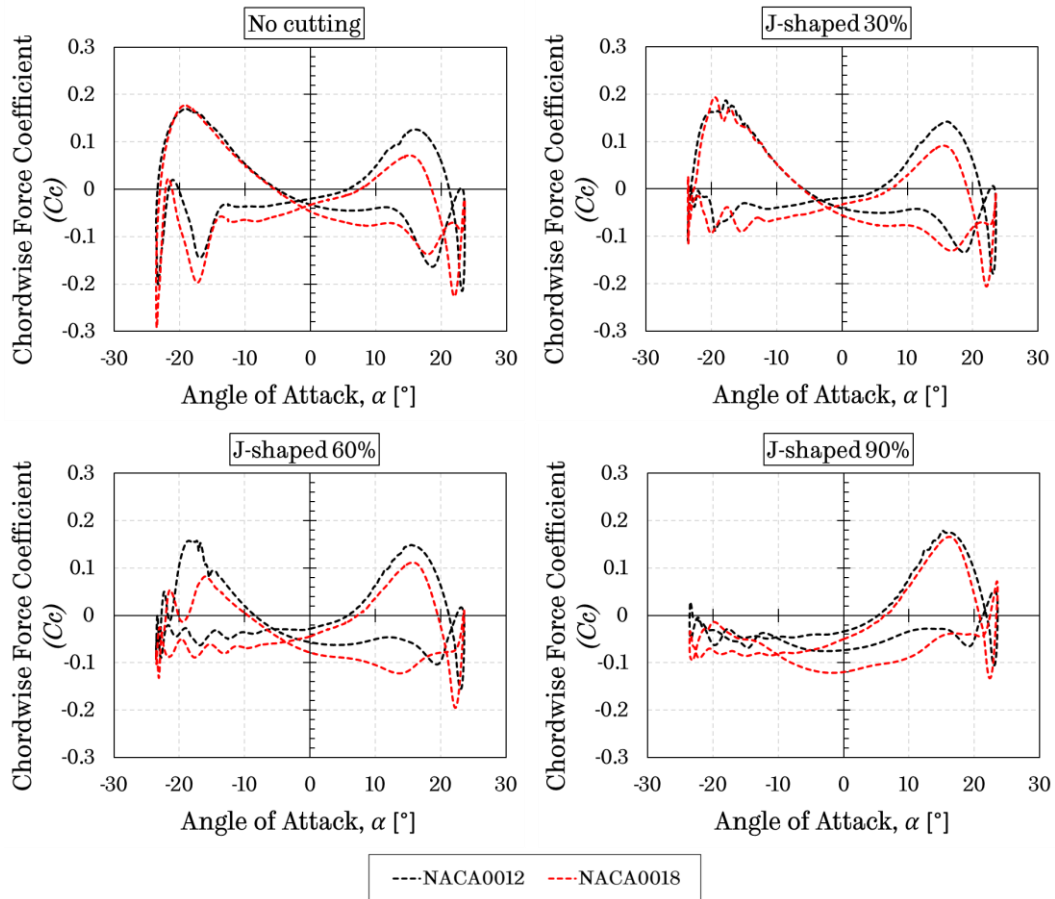
Figure 6.12. The chordwise force coefficients as a function of the angle of attack for NACA0012, NACA0018, and their J-shaped profiles.

6.2.3.2 Influence of the λ at constant Reynolds number

The tip speed ratio plays a crucial role for the VAWT operation. Therefore, in this section, the influence of the tip speed ratio on the dynamic performance, such as the maximum chordwise force coefficient, stall-onset angle, and maximum angle of oscillation, has been examined while keeping the oncoming relative wind speed the same. The tip speed ratios examined in the present study are 2, 2.5, and 3.5 as they are usually identified to be small (λ=2) enough for higher possibility of the dynamic stall occurrence and relatively high (λ=3.5) enough to reduce the effect of the dynamic stall. The operating parameters applied to this investigation are (1) Reynolds number is kept constant as 72.000 and (2) aerofoils

tested are NACA0018 and its J-shaped profile with different values of the opening, namely 30%, 60%, and 90%.

Figure 6.13 illustrates the aerodynamic force coefficients, such as lift, drag, and chordwise force coefficients, as a function of the angle of attack for the tip speed ratios of 2, 2.5, and 3.5, respectively. As can be seen from the figure, the aerofoil performance in terms of the chordwise force coefficient increases with the increase in the opening ratio at the given tip speed ratios in the positive angles of attack region. However, during the negative angle of attack motion, the J-shaped profile with an increase in the opening ratio decreases the performance. It is also observed that, even though at low tip speed ratio, such as λ=2, the J-shaped profile with a larger opening ratio can produce the positive chordwise force coefficient at some oscillating positions in the negative angles of attack region, this situation is getting worse with the increase in the λ. This situation causes a significant reduction in the overall torque performance at high λ values when the J-shaped profile is used.

Nevertheless, Figure 6.13 also quantifies the increase in the lift coefficient when using an aerofoil with a higher opening in the positive angle of attack motion for all tip speed ratios. However, the aerofoil with no cutting produces a slightly higher lift force compared to J-shaped aerofoils in the negative angle of attack motion. In addition, one of the most interesting findings is that the difference between the aerofoils investigated in terms of the lift force coefficient decreases with the increase in the tip speed ratio, especially during the negative angle of attack motion. However, the J-shaped profile with a 90% opening always produces a higher drag force coefficient at all the tip speed ratios investigated, particularly during the upstroke motion, where the opening is located on the suction side of the aerofoil, in the negative angles of attack region. The reason for this situation will be discussed in Section 6.2.3.6 using the flow field generated over the aerofoils.

(a)

NACA0018, λ=2

(b)

NACA0018, λ=2

(c)

NACA0018, λ=2

----NACA0018, No cutting   NACA0018, J-shaped 30%
----NACA0018, J-shaped 60%   NACA0018, J-shaped 90%

(d)

NACA0018, λ=2.5

(e)

NACA0018, λ=2.5

(f)

NACA0018, λ=2.5

Secondary
Vortex

----NACA0018, No cutting   NACA0018, J-shaped 30%
----NACA0018, J-shaped 60%   NACA0018, J-shaped 90%
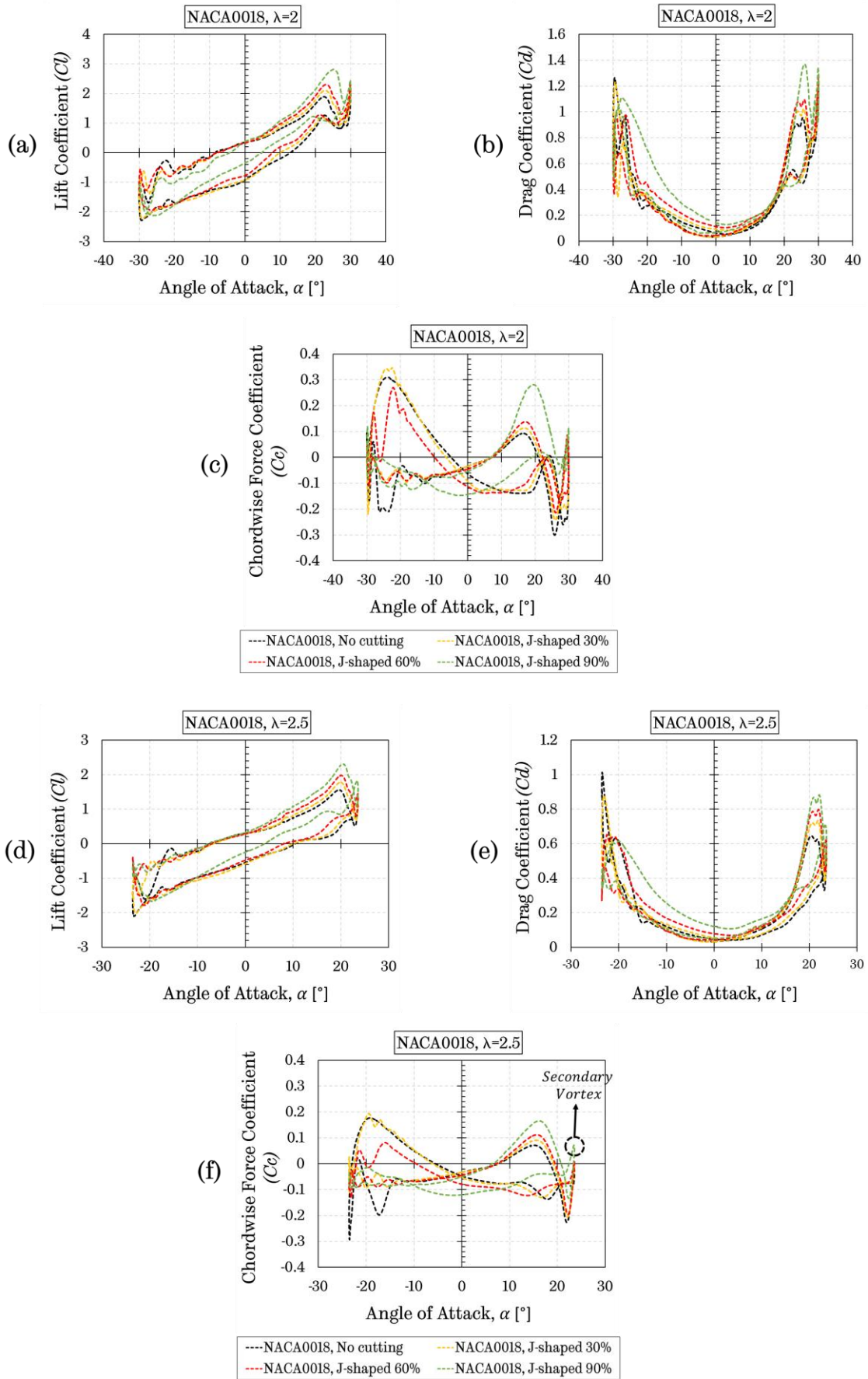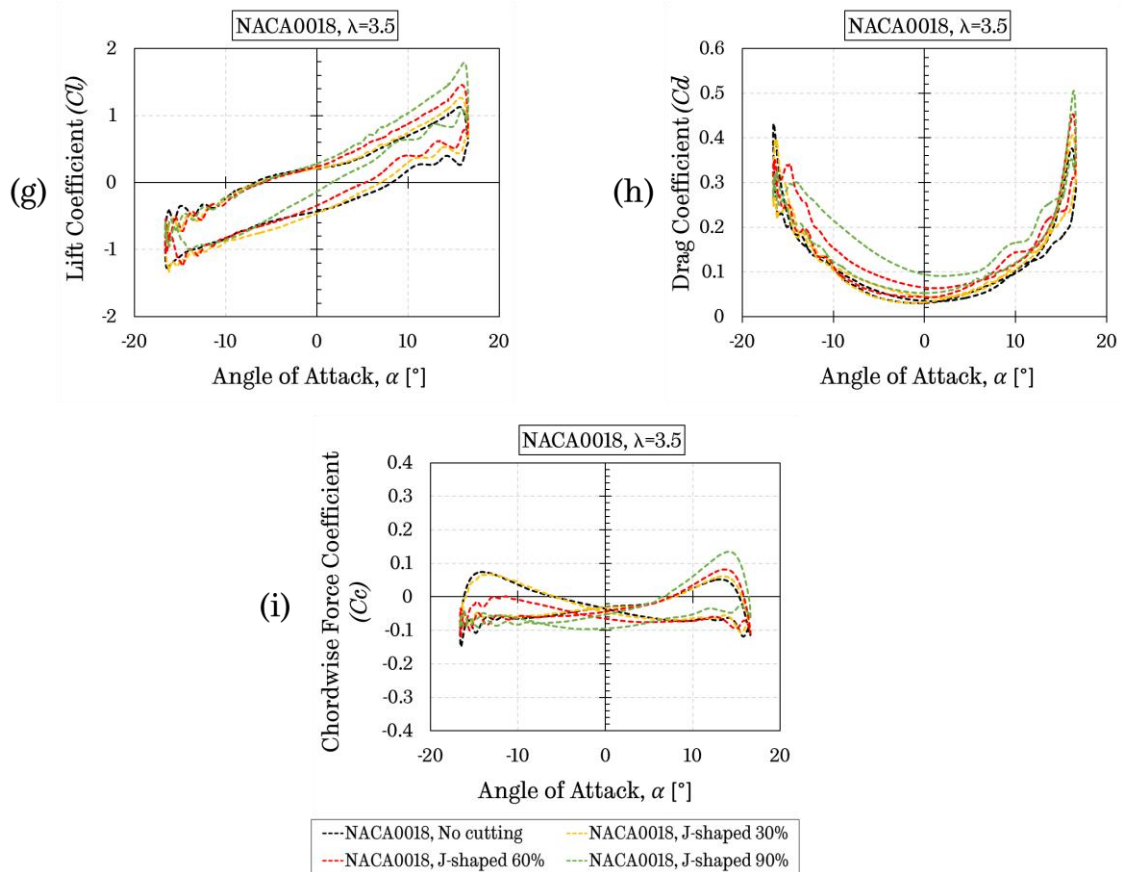
Figure 6.13. The aerodynamic force coefficients as a function of the angle of attack for the tip speed ratio of 2, 2.5, and 3.5 undergoing the Darrieus motion.

Figure 6.14 illustrates the chordwise force coefficients as a function of the angle of attack for the NACA0018 and its J-shaped profile in terms of the different tip speed ratios. The influence of the tip speed ratio on the dynamic performance of the J-shaped aerofoil and its conventional profile undergoing the Darrieus motion has shown that the stall-onset angle increases with a decrease in the tip speed ratio. For example, for the tip speed ratio investigated with the value of the 2, the stall-onset angles of the aerofoils tested with no cutting, 30%, 60%, and 90% opening ratios have been found as 16.25°, 16.77°, 17.09°, and 19.52°, respectively. For the tip speed ratio of 2.5, the stall-onset angels of these aerofoils were 15.07°, 15.54°, 15.71°, and 16.19°, respectively. Additionally, for the highest tip speed ratio (λ=3.5) investigated, the stall-onset angles of these aerofoils have been obtained as 13.18°, 13.5°, 13.72°, and 14.18°, respectively. The results show that with

the decrease in the tip speed ratio, the delay in the stall-onset angle increases for each opening ratio of J-shaped profile, particularly in the positive angles of attack region, which corresponds to the upstream part of the turbine.
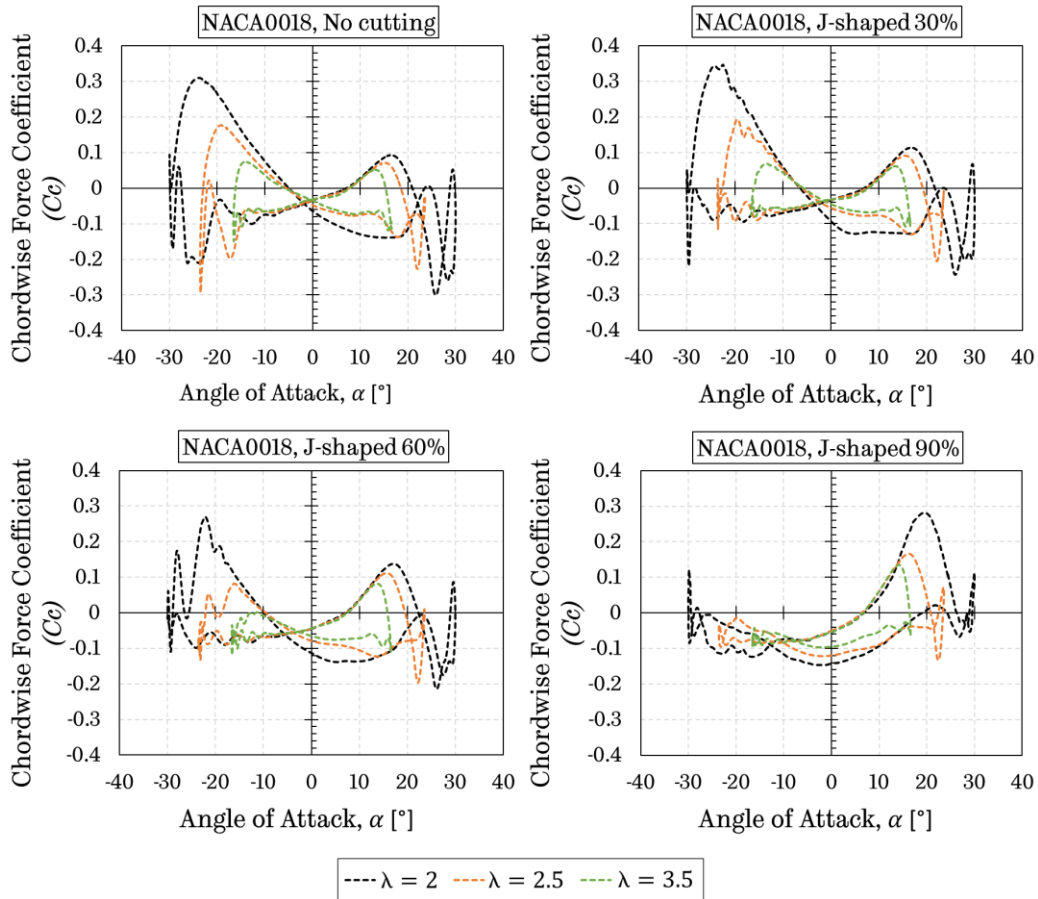
Figure 6.14. The chordwise force coefficients as a function of the angle of attack for the NACA0018 and its J-shaped profiles in terms of the different tip speed ratios.

Furthermore, in Figure 6.15, the maximum chordwise force coefficients obtained in the positive angles of attack region and the stall-onset angles as a function of the opening ratio over the aerofoil surface in terms of the different tip speed ratios are illustrated. As can be observed in the figure, the maximum chordwise force coefficient increases with a decrease in the tip speed ratios investigated. Furthermore, the more obvious difference in the maximum chordwise force coefficient is obtained with the J-shaped profile with a 90% opening ratio at λ=2. At this tip speed ratio, the J-shaped profile with a 90%

opening ratio produces the much higher chordwise force coefficient compared to other aerofoil profiles. This could be an important indication that the J-shaped aerofoil with the increase in the opening ratio may enhance the self-starting capability due to the higher performance at the lower tip speed ratios. However, at higher tip speed ratios, such as λ=3.5, the J-shaped aerofoil with a higher opening ratio decreases the overall performance due to the production of the higher drag force coefficient in the negative angles of attack region.
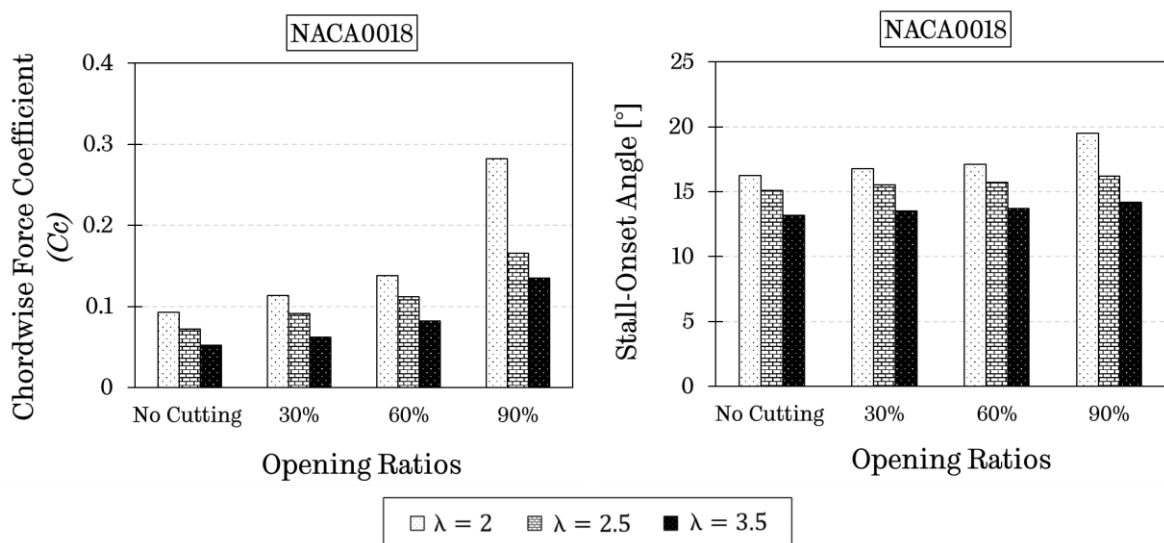
Figure 6.15. The maximum chordwise force coefficient in the positive angles of attack region and the stall-onset angle as a function of the opening ratio over the aerofoil surface in terms of the different tip speed ratios.

The tip speed ratio also significantly affects the maximum angle of the oscillation of the aerofoil during the Darrieus motion. The larger is the difference between the stall-onset angle, where the maximum chordwise force coefficient is obtained, and the maximum angle of oscillation, and then the secondary vortices most likely occur. It is important to note that the secondary vortex is due to the induction of a trailing edge vortex, in particular at the high angles of attack region, also known as in the deep stall region.

In order to indicate the effect of the tip speed ratio on the secondary vortex generation, the J-shaped profile with a 90% opening has been investigated at the tip speed ratios of λ=2.5 and λ=3.5. For the tip speed ratio of λ=2.5, the difference between the stall-onset angle and the maximum angle of oscillation is 7.38° while this difference is 2.42° for the tip speed ratio λ=3.5. Therefore, the bigger difference between these two angles at λ=2.5 allows releasing the primary vortex formed at the leading edge of the aerofoil into the wake as a secondary vortex.

Figure 6.16 illustrates the normalised x-velocity (V_x/V_∞) and z-vorticity ($w_z c/V_\infty$) contours for the oscillating J-shaped aerofoil with a 90% opening at λ=2.5 and λ=3.5. The angles of attack selected to analyse the secondary vortex generations at λ=2.5 are $\alpha = 20.45°$ and $\alpha = 23.48°$, which are corresponding to the angles where the maximum lift force coefficient and secondary peak chordwise force coefficient are obtained, respectively. In addition to this, for λ=3.5, the angles of attack selected are $\alpha = 16.21°$ and $\alpha = 16.6°$, which corresponds to the angles where the maximum lift force coefficient is obtained and the maximum angle of oscillation is achieved, respectively. In order to illustrate the secondary vortex generation over the aerofoil that caused the secondary peak chordwise force coefficient, the normalized z-vorticity contours for λ=2.5 at $\alpha = 23.48°$ in a comparison with that for λ=3.5 at $\alpha = 16.6°$ have been presented in Figure 6.16. As it can be seen from the figure, a formation of the secondary vortex can be observed only in the normalized x-velocity contour of the tip speed ratio λ=2.5, while no indication of a secondary vortex has been observed at λ=3.5. This is substantially due to the large difference between the stall-onset angle and the maximum angle of oscillation obtained in a lower tip speed ratio of λ=2.5 investigated, which results in a deeper stall condition. Furthermore, the secondary vortex obtained at λ=2.5 can be also observed in the chordwise force coefficient (see Figure 6.13 (f)).
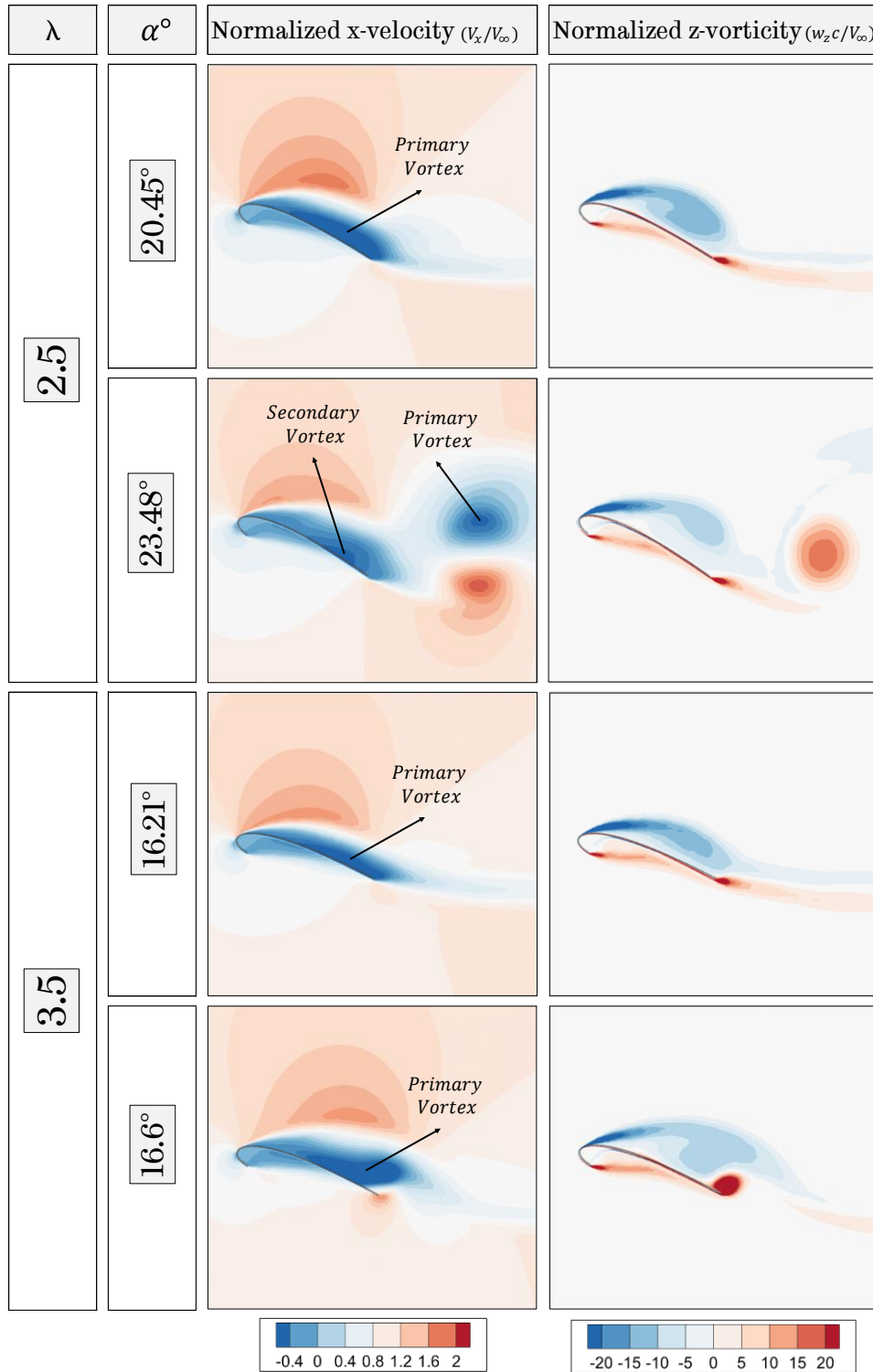
Figure 6.16. The normalised x-velocity and z-vorticity contours for the oscillating J-shaped aerofoil with a 90% opening at λ=2.5 and λ=3.5.

6.2.3.3 Reynolds number effect at constant λ

In this section, the effect of increasing the Reynolds numbers on the dynamic stall performance of the oscillating aerofoils is analysed by considering the Reynolds numbers of Re=0.4×10^5, 0.72×10^5 and 1×10^5, which are appropriate to the urban applications of the H-type VAWTs and this range of the Reynolds number make a contribution towards a much better understanding of the flow physics of the dynamic stall phenomena to assist in the design of the J-shaped aerofoil for the H-type VAWT applications [173, 174, 175]. The operating parameters applied to this investigation are (1) tip speed ratio is kept constant as λ=2.5 and (2) aerofoils tested are NACA0018 and its J-shaped profile with different values of the opening, namely 30%, 60%, and 90%.

The effect of the increased Reynolds number on the aerofoil's aerodynamic performance undergoing Darrieus motion for the NACA0018 aerofoil and its J-shaped profiles has been illustrated in Figure 6.17. As can be seen in the figure that the level of the unsteadiness in terms of the aerodynamic coefficients is significantly decreased with the increase in the Reynolds number for all the aerofoils investigated with the reduced secondary vortex evident. Furthermore, the increase in the Reynolds number increases the maximum chordwise force coefficient (see Figure 6.17 (c), (f), and (i), particularly during the positive angle of attack motion, which may result in the alleviation of the undesired effects of the dynamic stall for small-scale VAWTs.

Differently from the effect of the tip speed ratio on the lift force coefficient in the negative angle of attack region, with the increase in the Reynolds number, no significant difference has been observed on the lift coefficient during the negative angle of attack motion. However, a considerable drag generation has taken place with the increase in the opening ratio during the upstroke motion in the negative angles of attack region for all the cases studied (see Figure 6.17 (b), (e), and (h).

Additionally, it is also interesting to observe that with the increase in the opening ratio, the difference on the stall-onset angle becomes clearer at the lower Reynolds number investigated. For example, at Reynolds number of 40,000, the stall-onset angle for the NACA0018 with no cutting is $\alpha =10.73°$, while it is $\alpha =13.93°$ for NACA0018 with 90% opening ratio; however, at Reynolds number of 100,000, stall-onset angle is found as $\alpha =18°$ for NACA0018 with no cutting, while it is $\alpha =18.5°$ for NACA0018 with a 90% opening ratio (see Figure 6.17 (c), (f), and (i)).
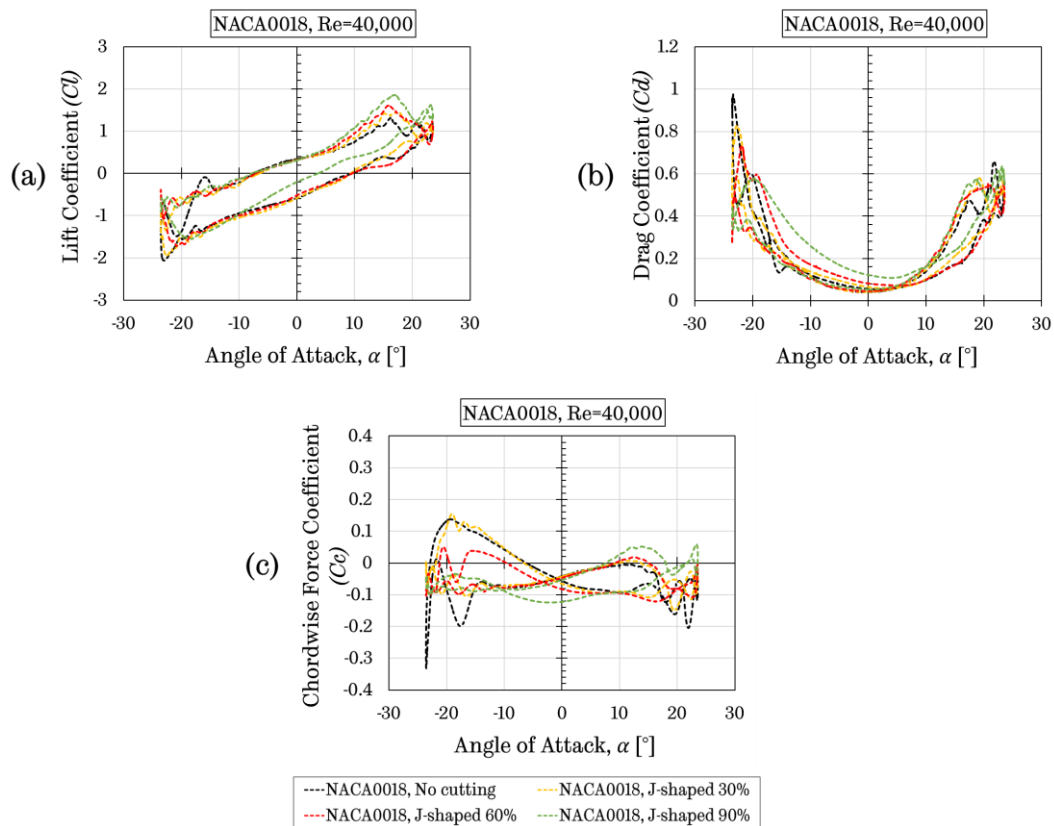
Figure 6.17. The chordwise force coefficients as a function of the angle of attack for the NACA0018 and its J-shaped profiles in terms of the different Reynolds numbers.

Furthermore, Figure 6.18 reorganised the plots in Figure 6.17 in order to show more clearly the effect of the Reynolds numbers on the chordwise force coefficients of each of the NACA0018 and its J-shaped profiles. It is apparent that the influence of the increasing Reynolds number results in a delay of the dynamic stall to higher angles of attack and subsequently a higher maximum chordwise force coefficient is attained for all the aerofoils investigated.
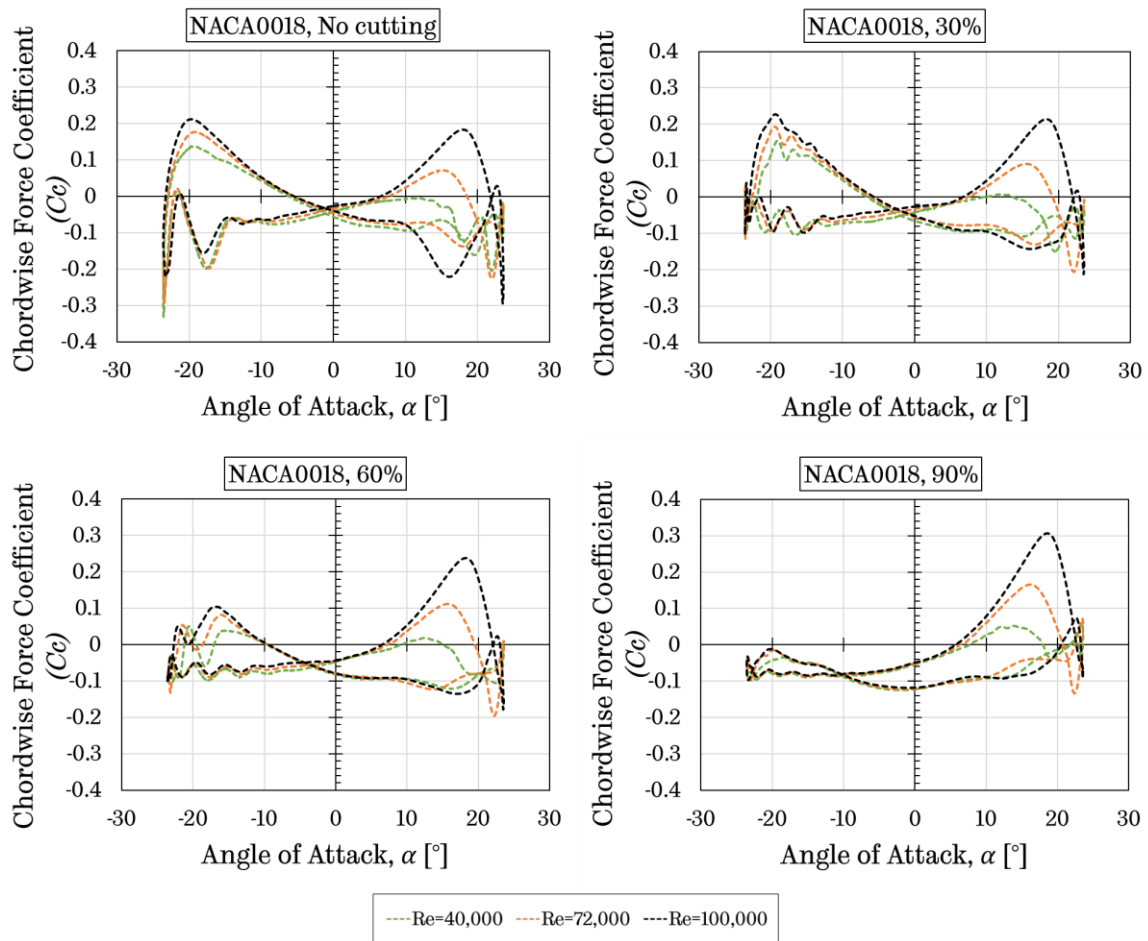
Figure 6.18. The chordwise force coefficients of the NACA0018 and its J-shaped profiles as a function of the angle of attack for different Reynolds numbers.

Furthermore, in Figure 6.19, the maximum chordwise force coefficient obtained in the positive angles of attack region and the stall-onset angle as a function of the opening ratio over the aerofoil surface in terms of the different Reynolds numbers are illustrated. As can be seen in the figure that, the maximum chordwise force coefficient in the positive angles of attack regions

increases with the increase in the Reynolds number. Among all the aerofoils tested, the J-shaped profile with a 90% opening ratio illustrates a better chordwise force coefficient generation at all Reynolds numbers investigated. Moreover, it is also found that the J-shaped profile with a 90% opening ratio has a further delay on the stall-onset angle compared to the conventional aerofoil at the lowest Reynolds number tested. However, with the increase in the Reynolds number, the difference between the stall-onset angle of the conventional aerofoil and its J-shaped profiles reduces. Indeed, in terms of the H-type VAWT aerodynamic efficiency and the self-starting ability, a significant increase in the maximum chordwise force coefficient and a further delay on the stall-onset angle will provide a benefit to the turbine.
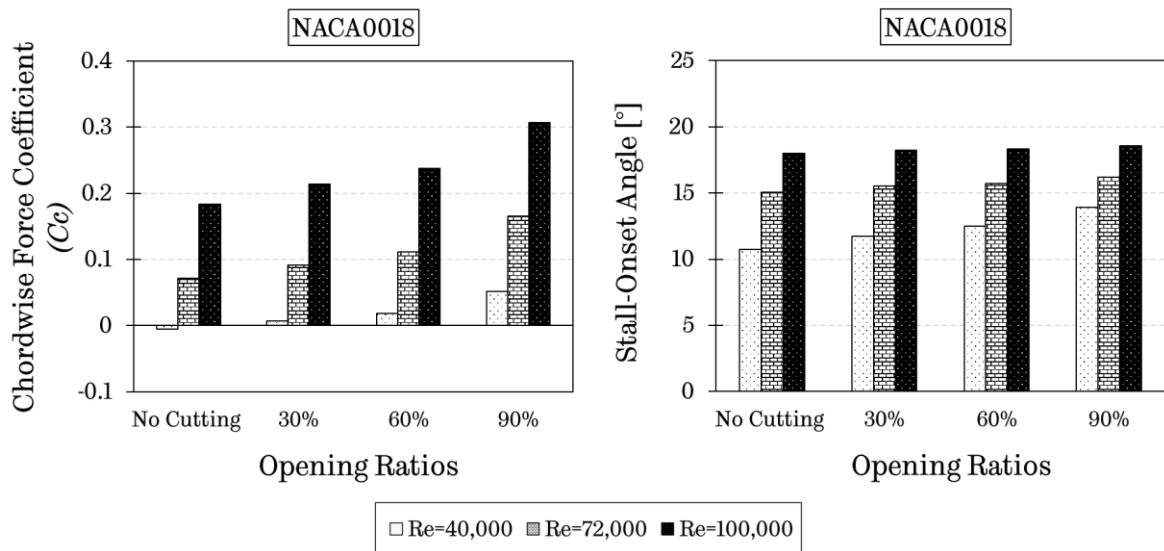
Figure 6.19. The maximum chordwise force coefficient in the positive angles of attack region and the stall-onset angle as a function of the opening ratio over the aerofoil surface in terms of the different Reynolds numbers.

6.2.3.4 Effect of pitch angle (β) at constant Reynolds number

In the present study, seven different pitch angles (β), namely $\beta = -8°, -4°, -2°, 0°, 2°, 4°,$ and $8°$, were selected to analyse the effect of the positively and negatively pitched J-shaped aerofoils on the aerodynamic performance, in particular dynamic stall aspects, compared to its conventional profile.

For the simplicity of the presentation, only three pitch angle cases, namely the pitch angles of $\beta = -8°, 0°,$ and $8°$ have been chosen for the comparison. In Figure 6.20, the chordwise force coefficient as a function of the angle of attack for the NACA0018 aerofoil and its J-shaped aerofoils concerning three different pitch angles have been illustrated. The reason to present the findings in the figure of the chordwise force coefficient is to evaluate the stall onset angle when the various pitch angle values are applied to the J-shaped profile. In addition, the chordwise force coefficients for the different pitch angles corresponding to the upstroke motion of the aerofoil are also presented in Figure 6.20. As can be seen from the figures, the maximum chordwise force coefficient increases with the increase in the opening ratio, particularly in the positive angles of attack region, regardless of the value of the pitch angle. However, varying the pitch angle results in an increase in the stall-onset angle if the pitch angle increases the maximum angle of attack. For instance, the stall-onset angle with $\beta = 8°$ is found as 14.19° for the J-shaped profile with a 90% opening and when using $\beta = -8°$ is found as 17.11°. The maximum angle of attacks are found to be 15.57° and 31.57° for pitch angles $\beta = 8°$ and $\beta = -8°$, respectively. These maximum angles of attack have been calculated for the corresponding pitch angles based on a tip speed ratio of $\lambda = 2.5$.
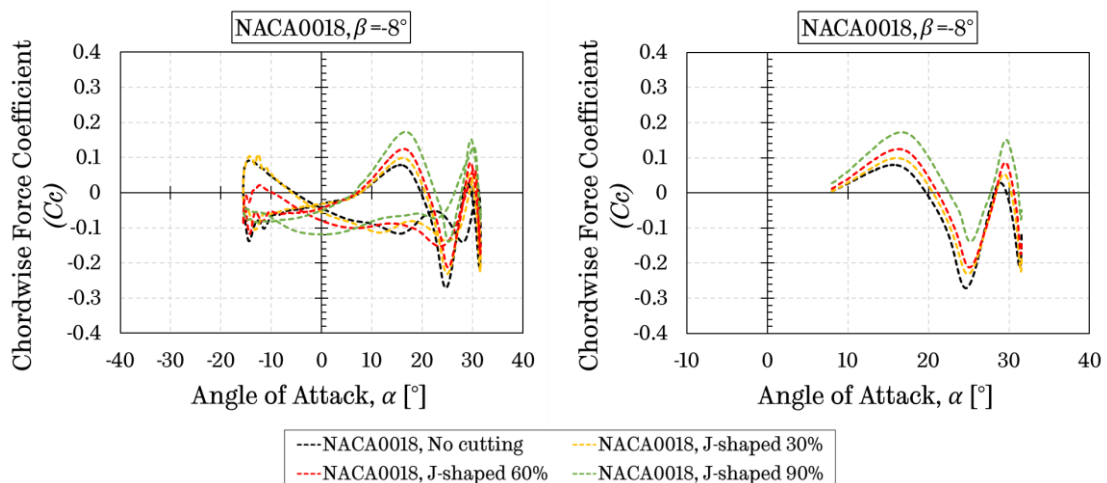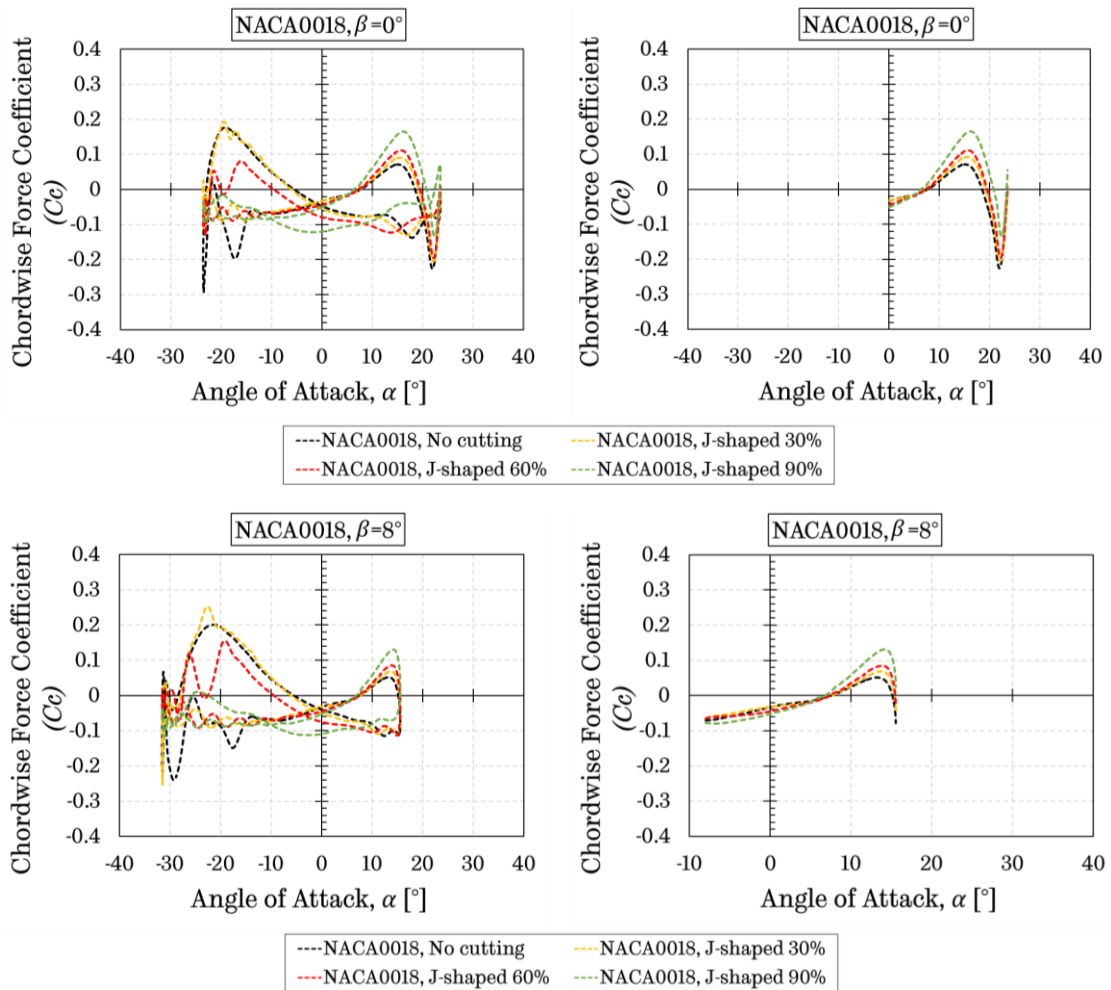
Figure 6.20. The chordwise force coefficient as a function of the angle of attack for NACA0018 aerofoil and its J-shaped aerofoils concerning pitch angles $\beta = -8°, 0°,$ and $8°$.

Furthermore, Figure 6.21 indicates the chordwise force coefficients as a function of the angle of attack for the NACA0018 and its J-shaped profiles with the opening ratios concerning the different values of the pitch angle. It is interesting to observe that no indication of the secondary vortex is obtained for the most positive pitch angle ($\beta = 8°$). However, with the most negative pitch angle ($\beta = -8°$), despite experiencing a larger stall-onset angle, the maximum angle of attack reached by the aerofoil at the end of the upstroke motion will be higher, which results in a secondary peak in the chordwise force coefficient. The secondary peak vortices observed in the chordwise force coefficient causes the largest severity in the deep stall conditions. In addition, it can be observed that

the magnitude of the secondary vortices of the negative pitch angles increases with the increase in the opening ratio.
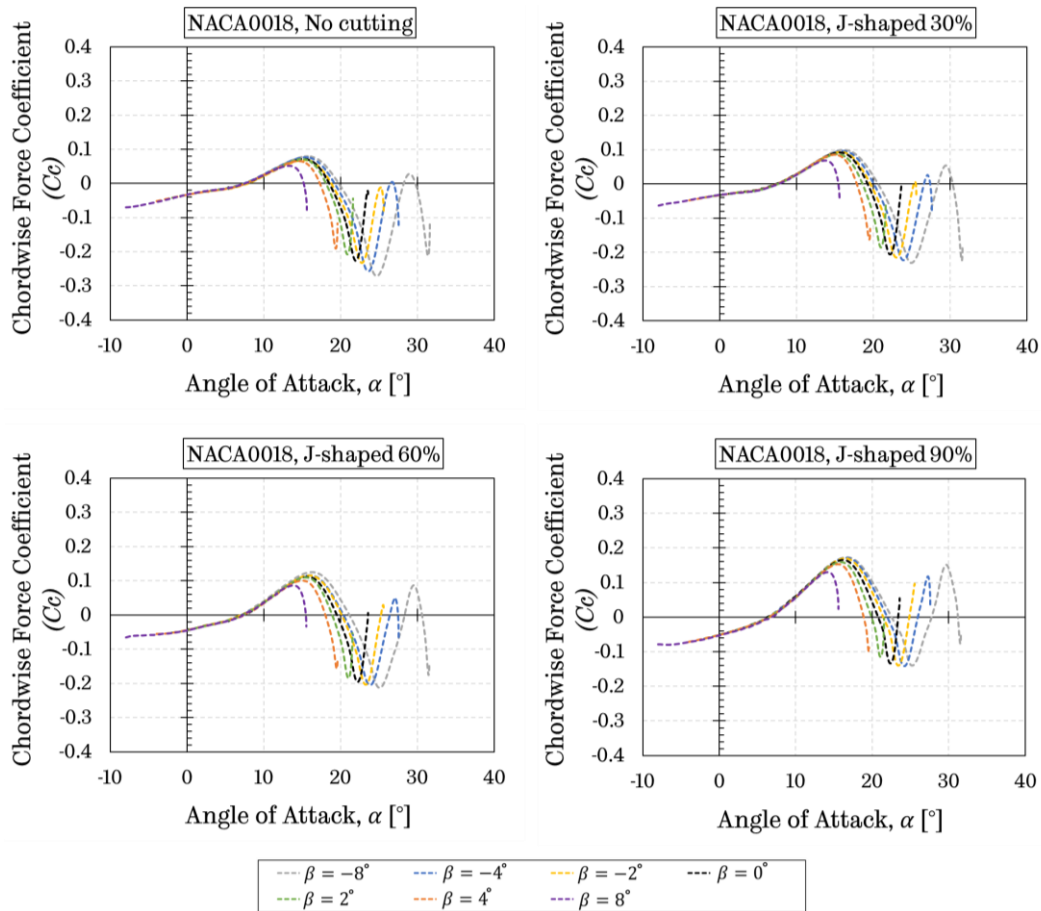
Figure 6.21. The chordwise force coefficients as a function of the angle of attack for the NACA0018 and its J-shaped profiles with the opening ratios concerning the different values of the pitch angle.

Consequently, the pitch angle has demonstrated to have one of the most significant impacts in delaying the stall-onset angle to a larger angle of attack. Figure 6.22 shows a summary of the effect of the pitch angle on the maximum chordwise force coefficient in the positive angles of attack region and the stall-onset angle as a function of the conventional aerofoil and its J-shaped profiles concerning the different values of the pitch angles. The results indicate that with the increase in the opening ratio, the maximum chordwise force coefficient increases; however, it decreases with the most positive pitch angles of attack. Among all aerofoils investigated, the J-shaped profile with a 90% opening ratio

indicates better aerodynamic performance in terms of the peak chordwise force coefficient. In addition, it is clear that the value of the pitch angle that decreases from positive to negative, the stall-onset angle is delayed to a larger angle of attack, regardless of the aerofoil investigated.
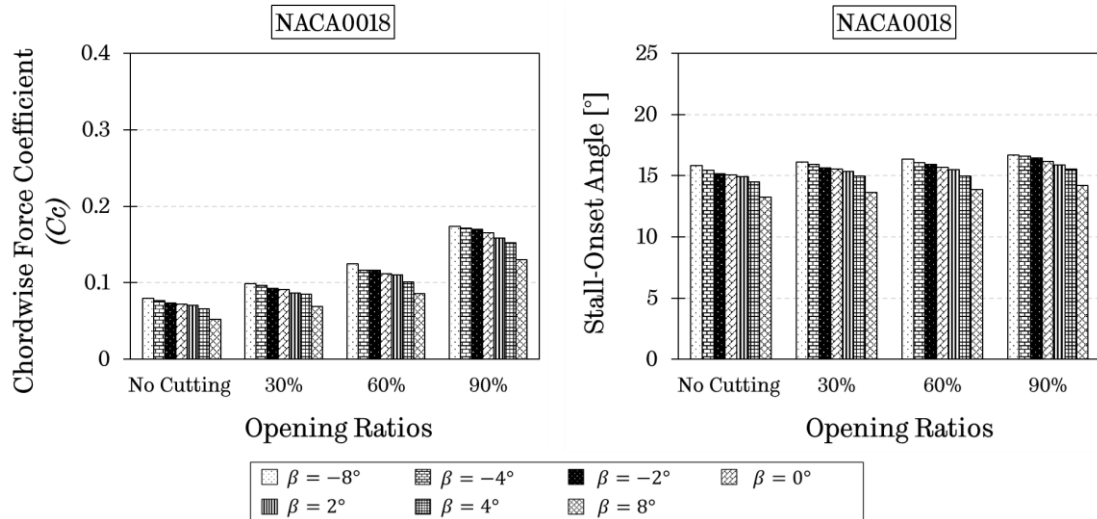
Figure 6.22. The maximum chordwise force coefficient in the positive angles of attack region and the stall-onset angle as a function of the opening ratio over the aerofoil surface in terms of the different values of the pitch angle.

6.2.3.5 Influence of the relative velocity on the stall-onset angle

The investigations have been carried out using the constant relative velocity in the previous sections. However, in this section, the constantly varying relative velocity described in Section 6.2.1 has been employed in the simulations to observe its impact on the stall-onset angle and to compare the difference on the stall-onset angle when using the constant-average relative velocity. In the VAWT simulations, the average relative velocity, which is generally expressed as wR or λV_{∞}, is frequently employed in order to simplify the analysis. Therefore, it is interesting to evaluate its effect on the J-shaped aerofoil aerodynamic behaviour in comparison with its conventional profile. The operating parameters employed in this investigation are the tip speed ratio of $\lambda=2.5$ and average Reynolds number of 72,000.

In Figure 6.23, the chordwise force coefficient as a function of the angle of attacks for the NACA0018 and its J-shaped profiles concerning the variable and constant relative velocities has been illustrated. The findings of the present investigation have shown that, in the positive angles of attack region, the stall-onset is not considerably influenced when the variable relative velocity is employed. On the contrary, in the negative angles of attack region, the prediction of the stall-onset angle using the variable relative velocity may have a significant effect. However, it is interestingly observed that the effect of the variable relative velocity in the negative angles of attack decreases with the increase in the opening ratio.
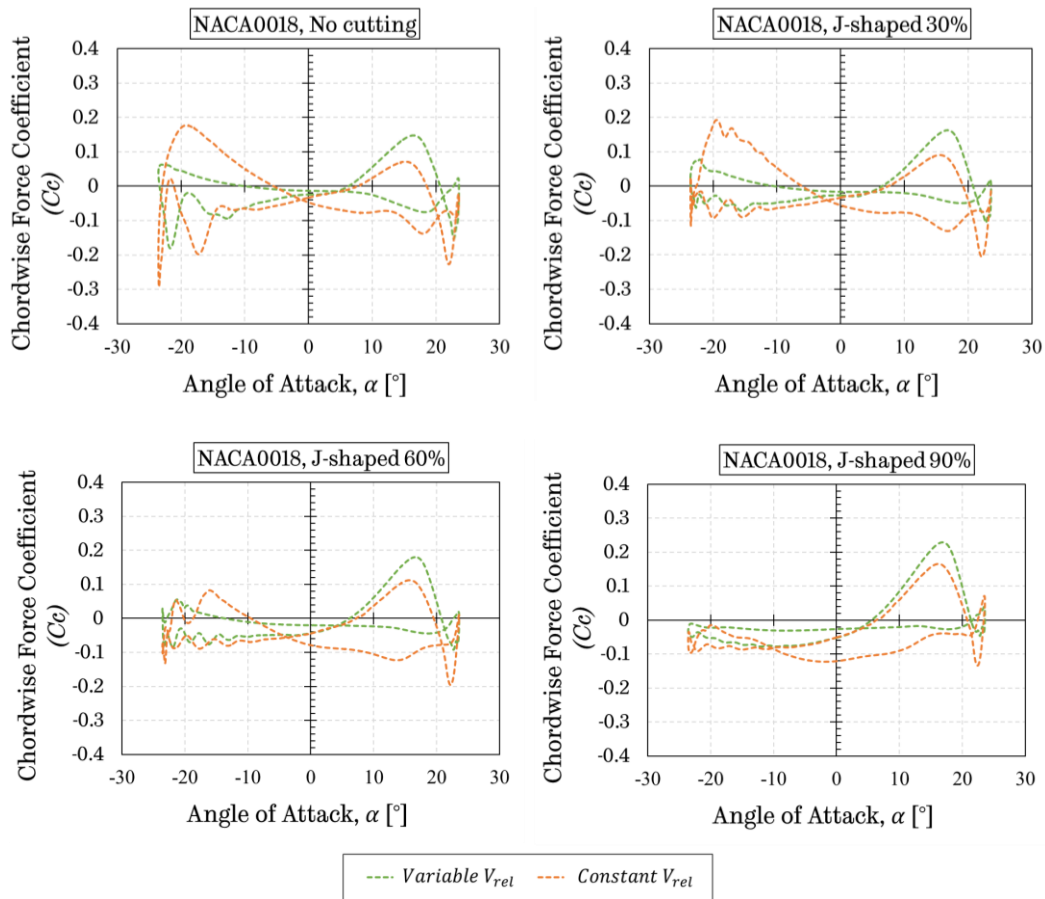
Figure 6.23. The chordwise force coefficient as a function of the angle of attacks for the NACA0018 and its J-shaped profiles concerning the variable and constant relative velocities at λ=2.5.

6.2.3.6 Flow visualization over the conventional aerofoil and its J-shaped profile with a 90% opening ratio

The flow field generated over the conventional aerofoil, NACA018, and its J-shaped profile with a 90% opening is visualized, thus allowing the qualitative comparison of the aerodynamics of the two aerofoils over the entire Darrieus motion cycle under the operating conditions of λ=2.5 and Re=72.000 with $\beta = 0°$. The reason why these two aerofoils have been selected is to illustrate the distinct difference between the conventional aerofoil and its J-shaped profile in terms of the flow structures generated over the aerofoils.

The dynamic stall process can be explained for the conventional aerofoil and its J-shaped profile with a 90% opening at twelve different characteristics of instantaneous angles of attack corresponding to the major flow features undergoing the Darrieus motion, as shown in the Figure 6.24. It is also important to note that the signs "↑" and "↓" are implied the aerofoil upstroke and downstroke motions, respectively.
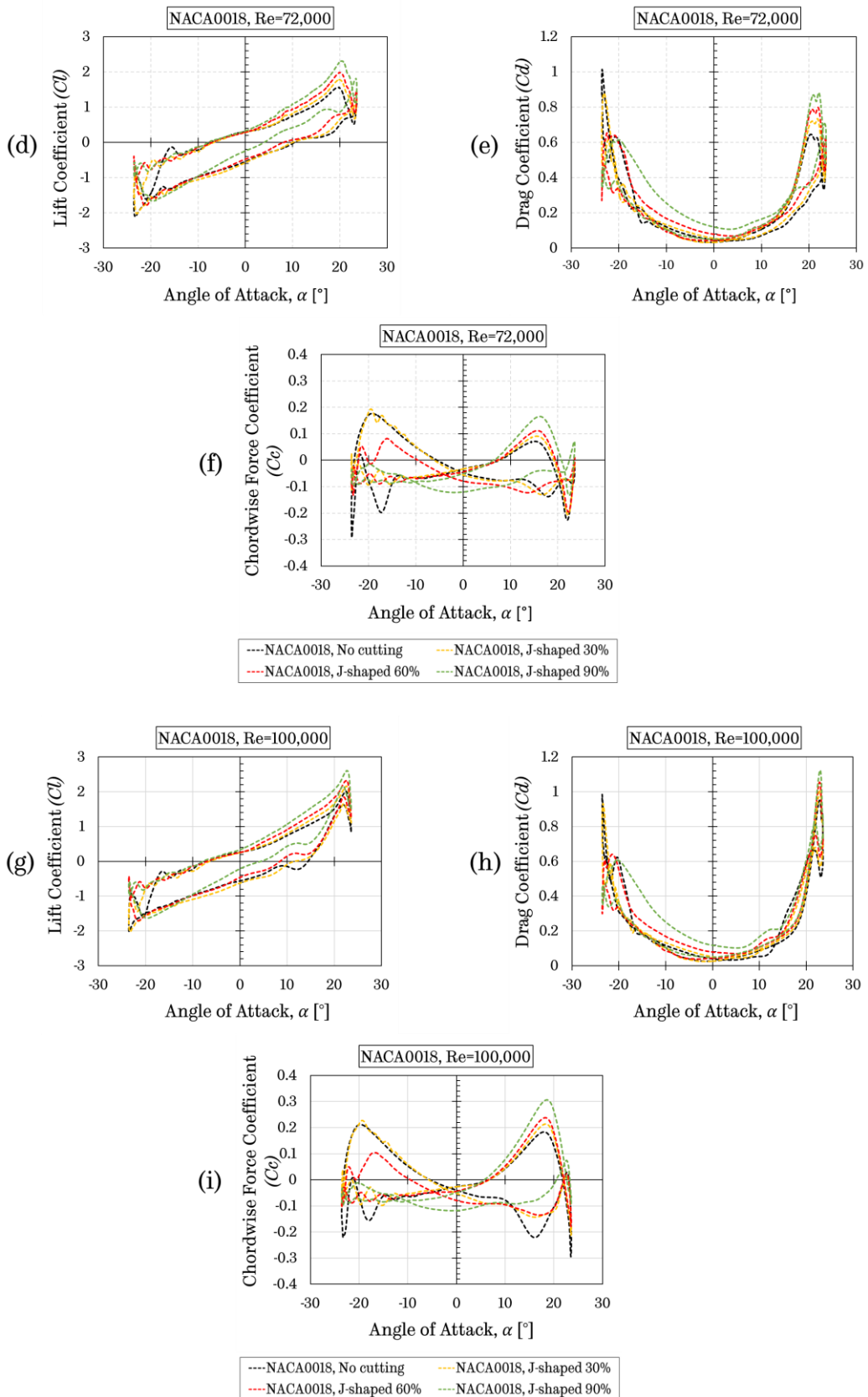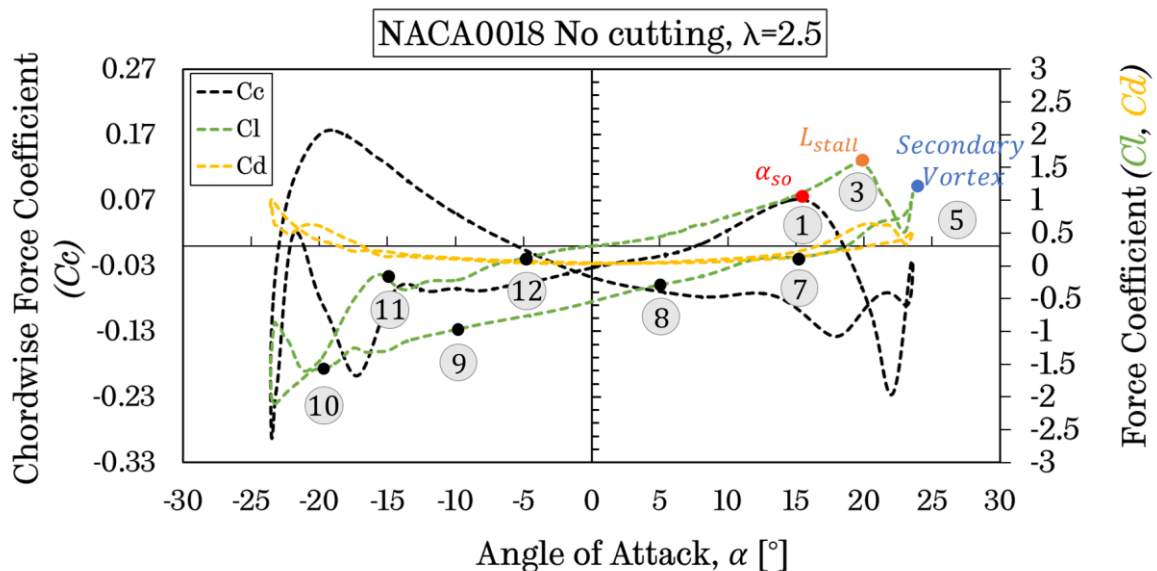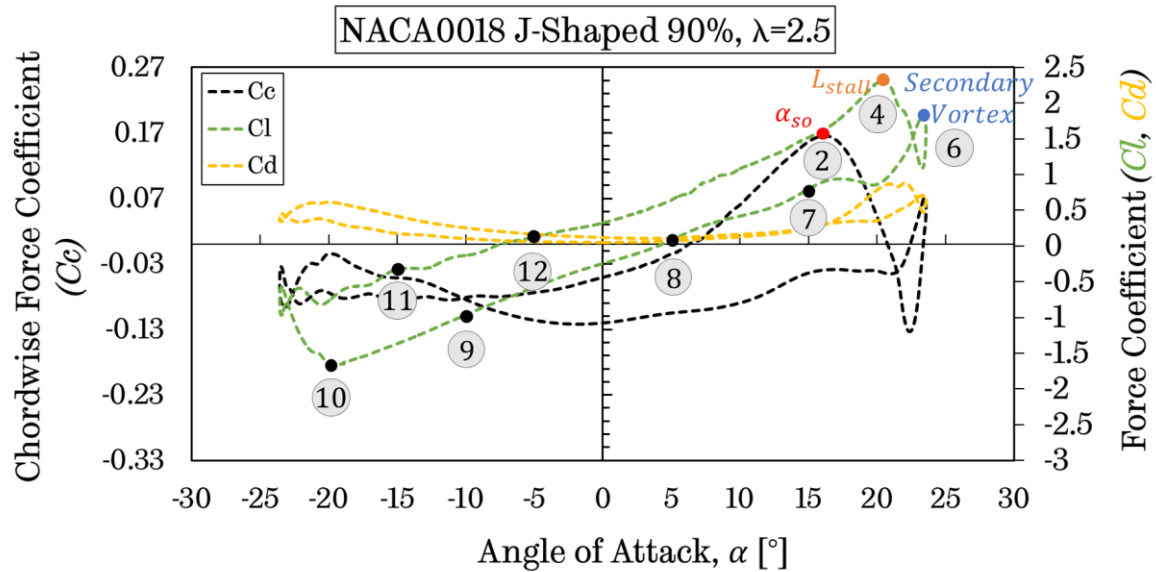
Figure 6.24. The chordwise force coefficient as a function of the angle of attacks for the NACA0018 and its J-shaped profiles with a 90% opening ratio concerning the major flow features undergoing the Darrieus motion.

This Darrieus motion is divided into two stages, the motion in positive angles of attack and negative angles of attack regions. The flow is visualized in Figure 6.25 - Figure 6.30 (a-b) using the contours of instantaneous normalized z-vorticity $(w_z c/V_\infty)$ (*upper contours*), and normalized x-velocity component (V_x/V_∞) (*lower contours*). In addition, the pressure distribution over the aerofoil surfaces was plotted in Figure 6.25 - Figure 6.30 (c) on the right.

At $\alpha = 15.1° \uparrow$ and $\alpha = 16.25° \uparrow$ (see Figure 6.25 (a) and (b)) during the upstroke motion in the positive angles of attack region, compared to the J-shaped aerofoil, thicker and further away vortices are observed over the suction side of the conventional aerofoil, which indicates the early stall-inception is taken place over the conventional aerofoil. In addition, a noticeable difference between the conventional and J-shaped aerofoils can be observed in the non-dimensional x-velocity contours. Further, it can be seen that at the suction side, a higher-scale velocity profile can be observed over the J-shaped aerofoil resulting in a lower pressure generation, while a lower-scale of the velocity profile is generated over the pressure side of the J-shaped aerofoil resulting in a greater pressure

generation compared to the conventional aerofoil. This higher-pressure difference between the suction and pressure side of the J-shaped profile exhibits an encouraging contribution to the overall lifting capacity of J-shaped aerofoil.
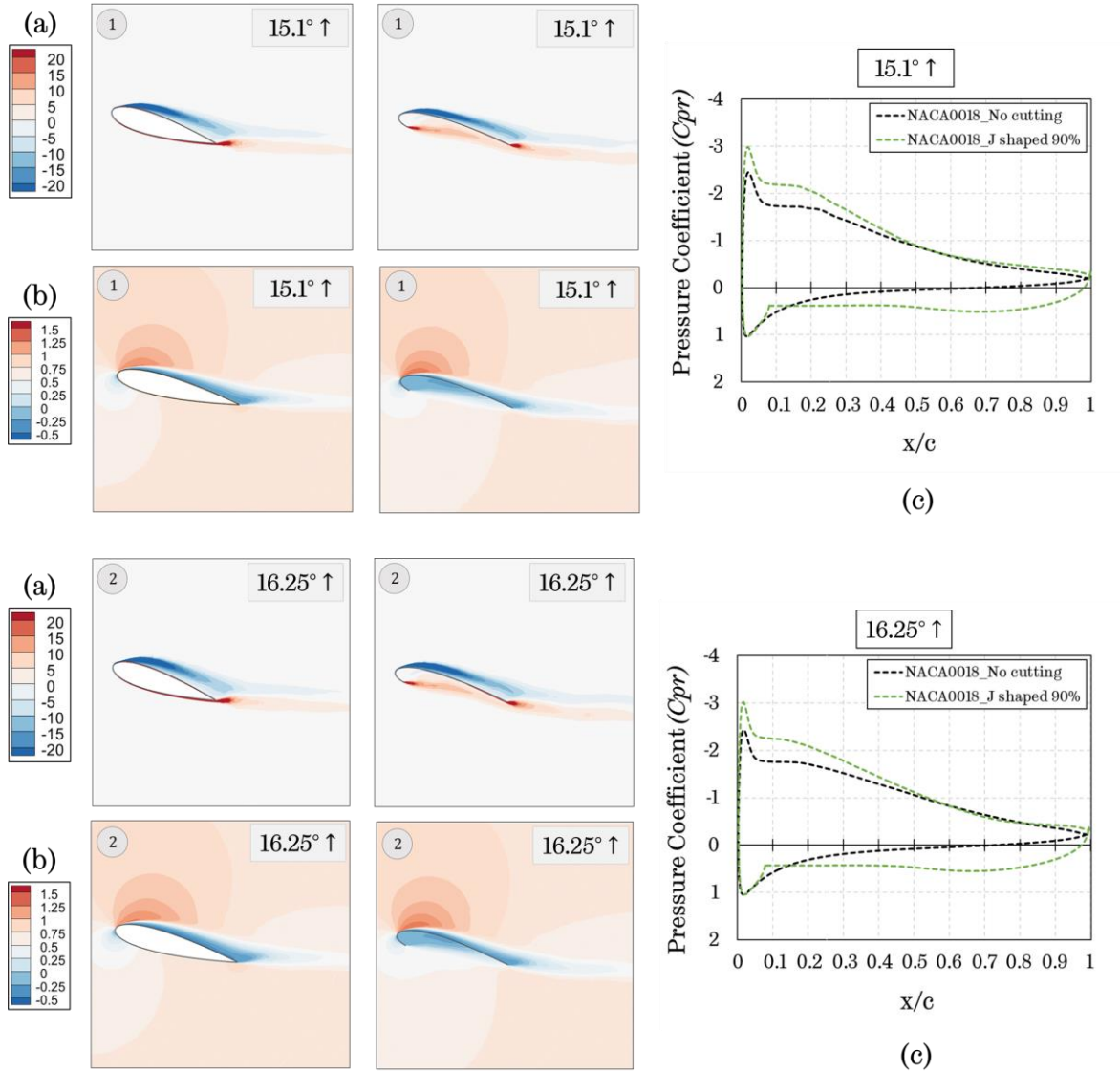
Figure 6.25. The contours of the (a) normalized z-vorticity ($w_z c/V_\infty$) and (b) normalized x-velocity (V_x/V_∞) of the flow over the conventional aerofoil and the J-shaped aerofoil with a 90% opening and (c) pressure distribution over both aerofoils at angles of attack $\alpha = 15.1°$ ↑ and $\alpha = 16.25°$ ↑.

The stall-onset provokes a lift overshoot for both aerofoils starting at $\alpha = 15.1°$ ↑ and $\alpha = 16.25°$ ↑ for the conventional aerofoil and its J-shaped profile, respectively. During the stage of the higher lift force generation ($\alpha = 19.6°$ ↑

and $\alpha = 20.45° \uparrow$, see Figure 6.26 (a) and (b)), the J-shaped aerofoil produces greater lift when compared to the conventional aerofoil. The difference in the generation of the lift force between two aerofoils is due to the leading edge vortex (LEV) remaining closer to the suction side of the J-shaped aerofoil in comparison with a quicker detachment of leading edge vortex from the conventional aerofoil. Being the leading edge vortex is further away from the suction side of the aerofoil results in a weaker leading edge vortex, which is easily shedding into the wake. Consequently, the dynamic stall angle of the J-shaped aerofoil is 20.45°, while it is 19.6° for the conventional aerofoil. It is clear that the J-shaped aerofoil delays the shedding of the leading edge vortex and this results in a further increment in lift coefficient. The maximum lift coefficient values can be quantified with Figure 6.24 showing that the J-shaped aerofoil has its peak at $Cl = 2.3$ while the peak of the conventional aerofoil is $Cl = 1.56$, so the J-shaped aerofoil produces approximately 30% more maximum lift than the conventional aerofoil. Furthermore, at $\alpha = 19.6° \uparrow$ and $\alpha = 20.45° \uparrow$, (see Figure 6.26 (c)) secondary low-pressure peak, which is observed at approx. 0.6<x/c<0.7, illustrates a possible beginning of the secondary vortex formation.
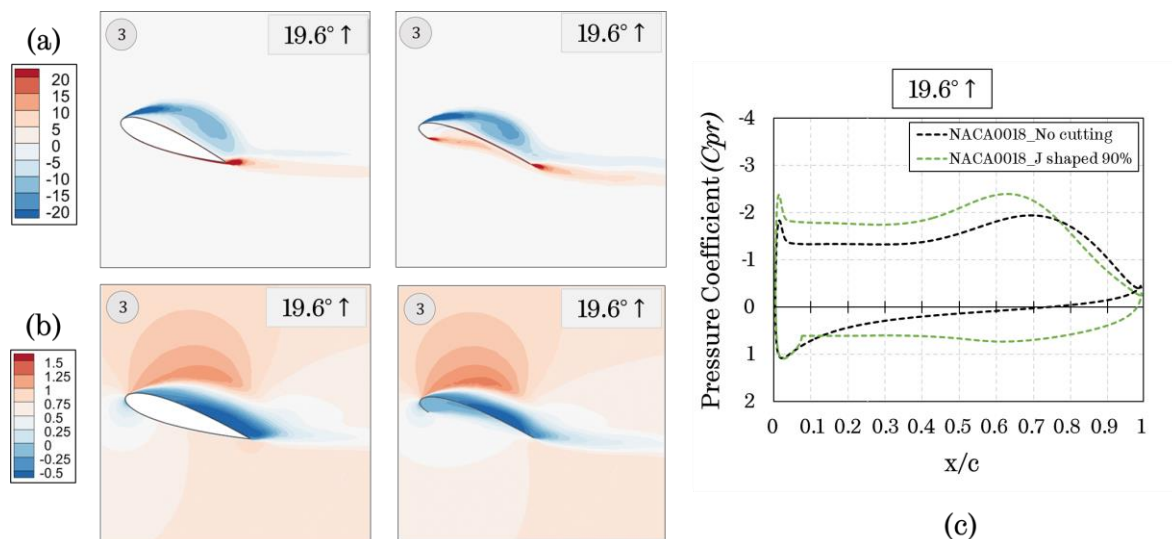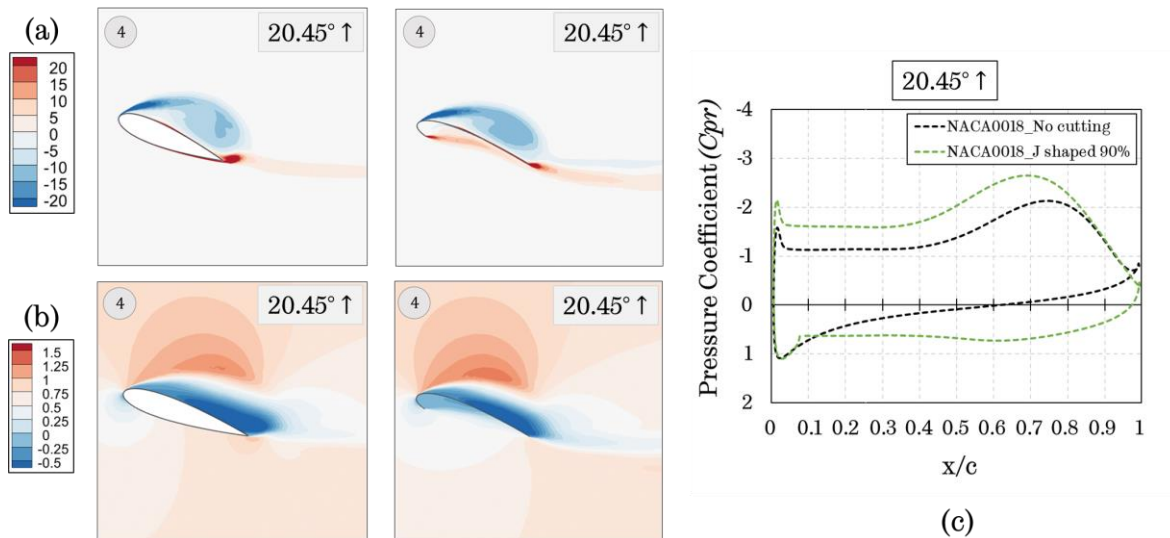
Figure 6.26. The contours of the (a) normalized z-vorticity ($w_z c/V_\infty$) and (b) normalized x-velocity (V_x/V_∞) of the flow over the conventional aerofoil and the J-shaped aerofoil with a 90% opening and (c) pressure distribution over both aerofoils at angles of attack $\alpha = 19.6°\uparrow$ and $\alpha = 20.45°\uparrow$.

During the post-stall region, where the angle of attack ($\alpha = 23.58°\uparrow$ and $\alpha = 23.48°\uparrow$, see Figure 6.27 (a) and (b)), exceeds the dynamic stall angle, the secondary vortices occur and the deep stall conditions are observed in both aerofoils. In this region, the flow is characterized by the shedding of the leading edge vortex and this causes a sudden decrease in the lift, drag, and chordwise force coefficients. The coefficients show very similar patterns for both aerofoils during the post-stall region. However, the J-shaped aerofoil produces more lift compared to the conventional aerofoil due to larger pressure difference observed between the suction and pressure sides of the aerofoil (see Figure 6.27 (c)).
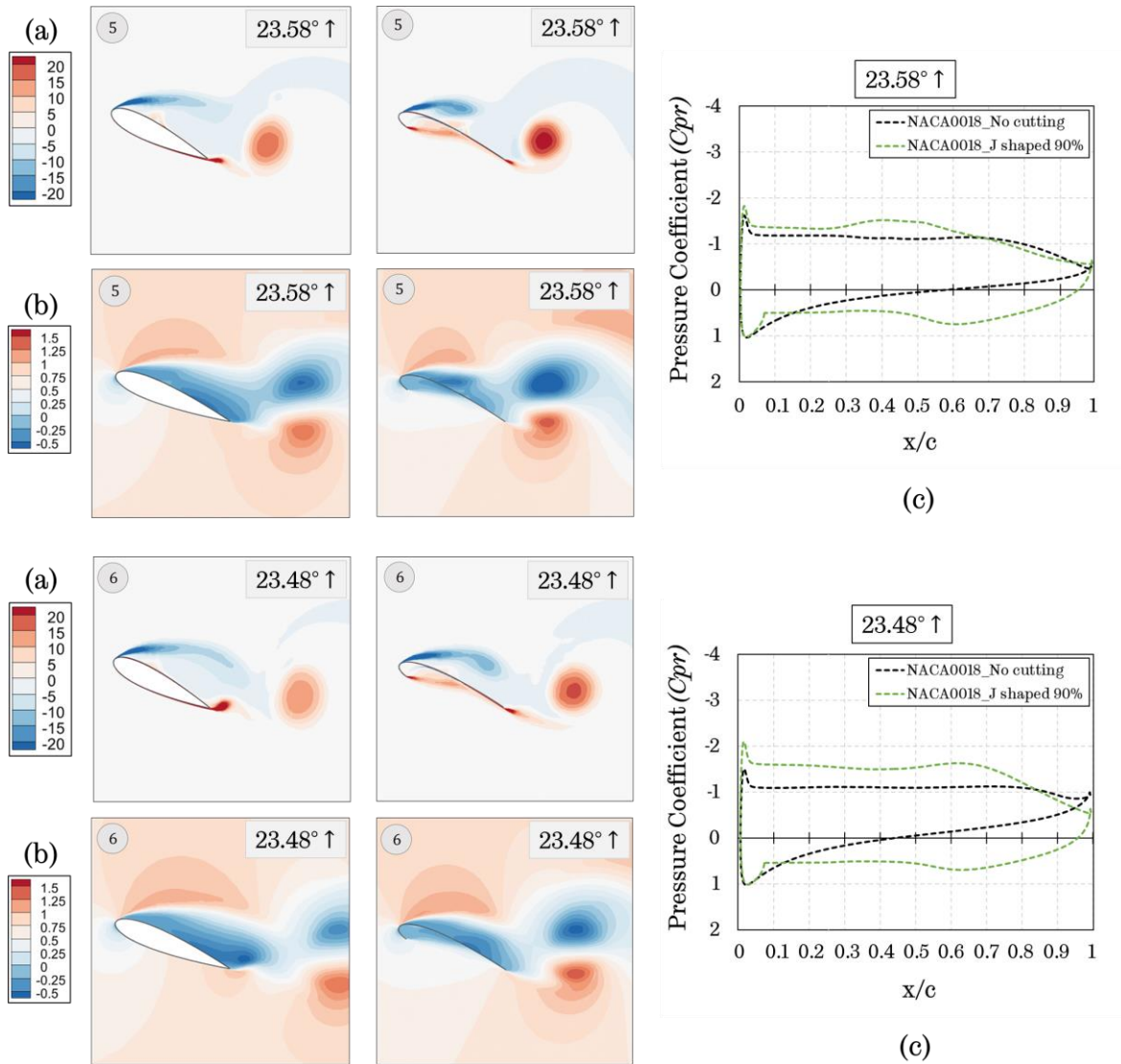
Figure 6.27. The contours of the (a) normalized z-vorticity ($w_z c/V_\infty$) and (b) normalized x-velocity (V_x/V_∞) of the flow over the conventional aerofoil and the J-shaped aerofoil with a 90% opening and (c) pressure distribution over both aerofoils at angles of attack $\alpha = 23.58°$ ↑ and $\alpha = 23.48°$ ↑.

During the downstroke motion in the positive angles of attack region ($\alpha = 15°$ ↓ and $\alpha = 5°$ ↓, see Figure 6.28 (a) and (b)), the flow starts to reattach from the front side to rear side of the aerofoil. The flow is characterized by the shear layer forming at the leading edge and expanding along the suction side of the aerofoil while the angle of attack is decreasing. At $\alpha = 15°$ ↓, there is no significant difference observed in the trend of the pressure coefficient of the conventional

aerofoil, especially at the position of 0.3<x/c, which results in a lift coefficient generated closed to zero. However, the J-shaped aerofoil produces a much higher lift coefficient since the pressure difference between the suction and pressure side of the aerofoil surface is greater than that of the conventional aerofoil. As the angle of attack decreases to 5°, a large portion of the flow over the suction side of the aerofoils become attached along the chord length; however, the only a mild pressure gradient is experienced by the suction and pressure sides of both aerofoils, which causes a reduction in the lift production.
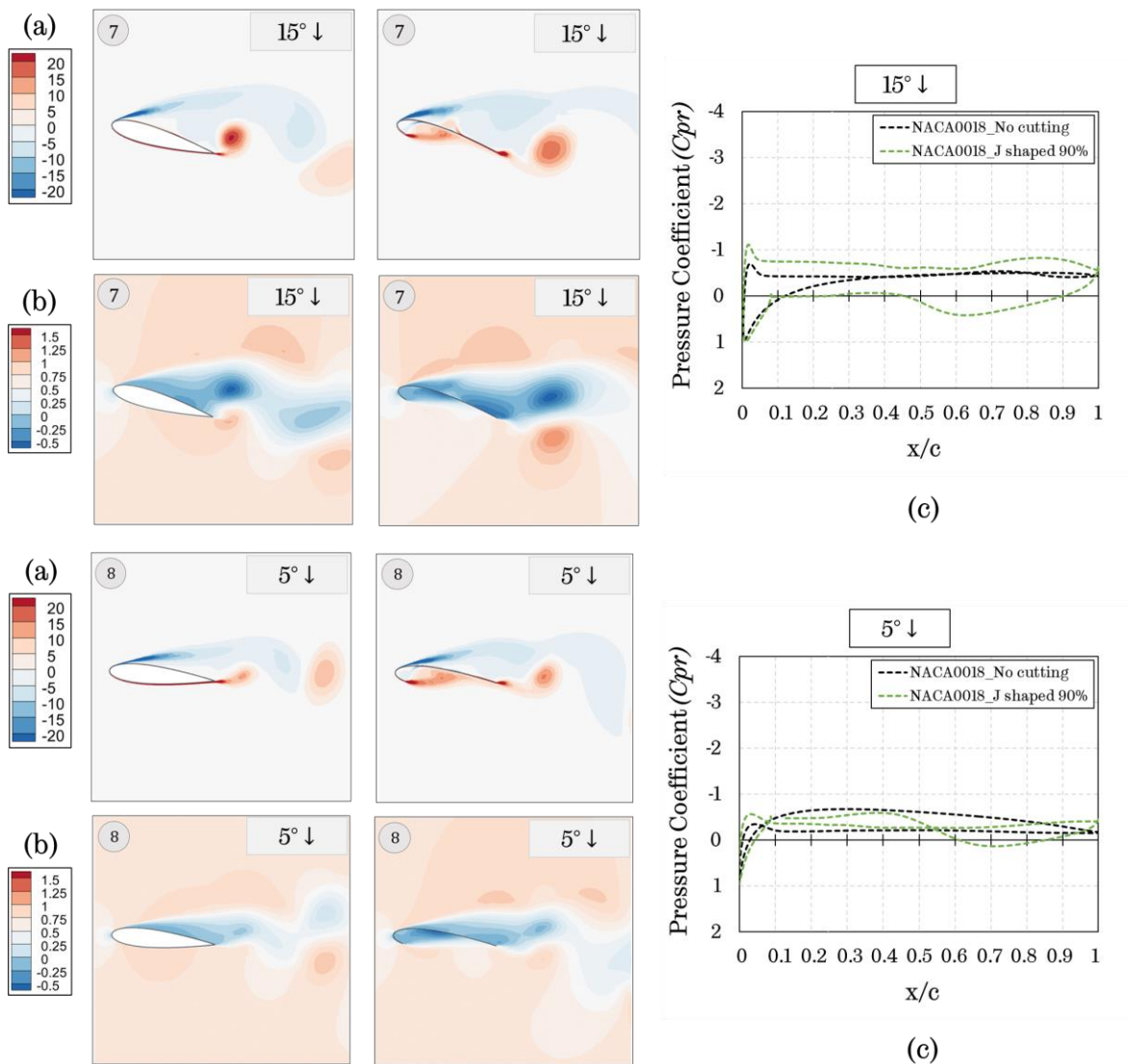
Figure 6.28. The contours of the (a) normalized z-vorticity ($w_z c/V_\infty$) and (b) normalized x-velocity (V_x/V_∞) of the flow over the conventional aerofoil and the J-shaped aerofoil with a 90% opening and (c) pressure distribution over both aerofoils at angles of attack $\alpha = 15° \downarrow$ and $\alpha = 5° \downarrow$.

At $\alpha = -10° \downarrow$ and $\alpha = -19.25° \downarrow$, (see Figure 6.29 (a) and (b) , concerning the pressure side, two aerofoils produce similar trends of the pressure coefficient; however, as can be seen from the x-velocity contours, at $\alpha = -10° \downarrow$, the conventional aerofoil has lower velocity magnitude at the position of x/c<0.3 and x/c>0.8 while the J-shaped aerofoil has lower velocity magnitude at the position of 0.3<x/c<0.8 over the suction side. Furthermore, at $\alpha = -19.25° \downarrow$, the conventional aerofoil has a lower velocity magnitude at the position for x/c<0.4 while the J-shaped aerofoil has a lower velocity magnitude at the position for 0.4<x/c over the suction side. Therefore, the two aerofoils generate approximately the same amount of lift force. However, the J-shaped aerofoil produces a greater drag for 0>AoA>-21 during the downstroke motion in the negative angles of attack region, which results in a significant reduction in the chordwise force coefficient.
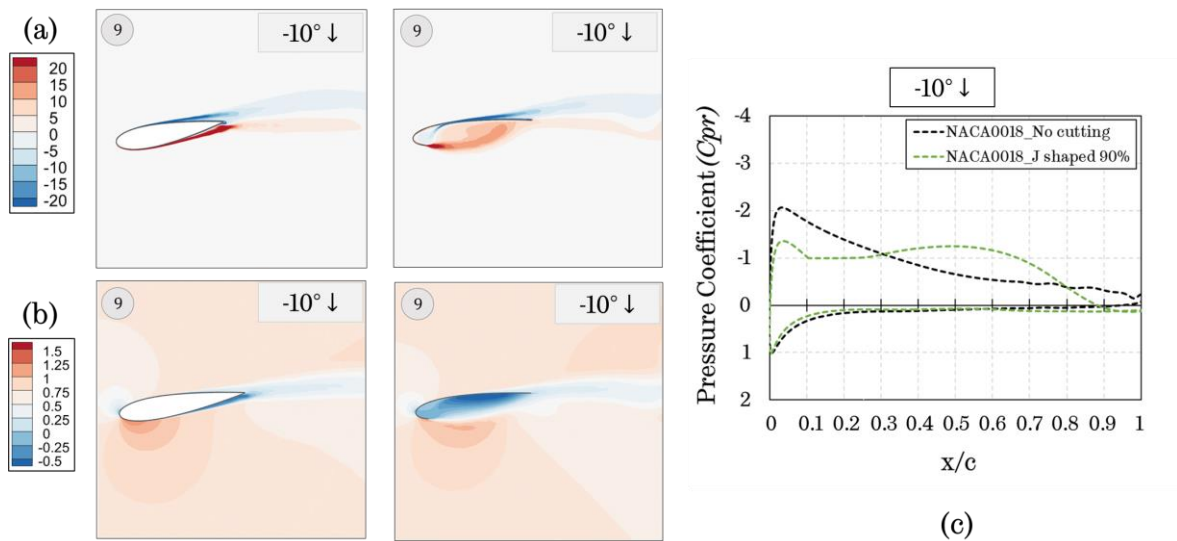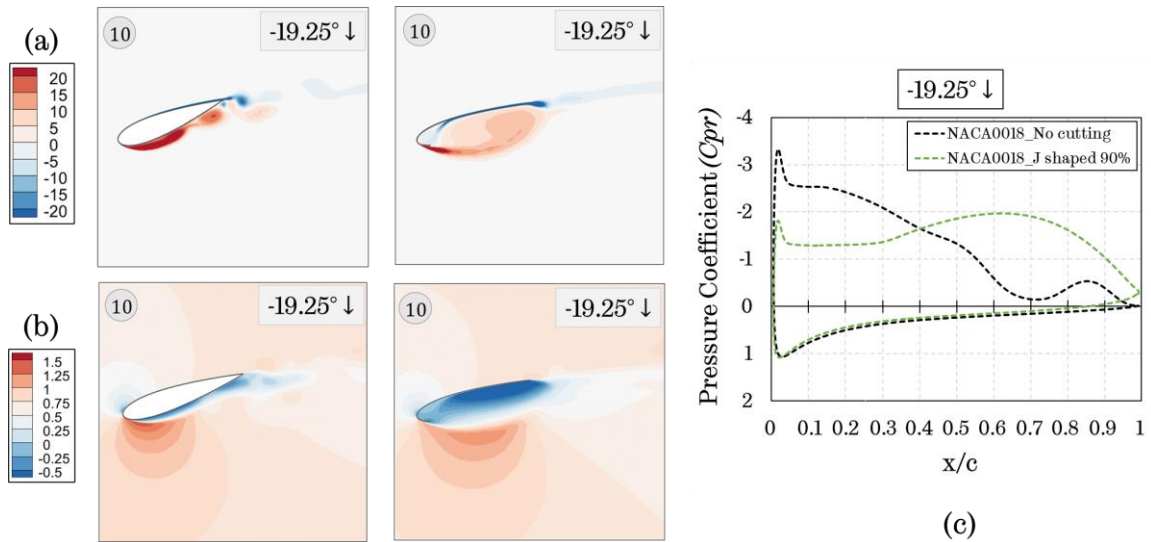
Figure 6.29. The contours of the (a) normalized z-vorticity ($w_z c/V_\infty$) and (b) normalized x-velocity (V_x/V_∞) of the flow over the conventional aerofoil and the J-shaped aerofoil with a 90% opening and (c) pressure distribution over both aerofoils at angles of attack $\alpha = -10°\downarrow$ and $\alpha = -19.25°\downarrow$.

During the upstroke motion in the negative angles of attack region ($\alpha = -15°\uparrow$ and $\alpha = -5°\uparrow$, see Figure 30 (a) and (b)), the trends of the pressure coefficient distributions of both aerofoils show similar behaviour. When looking at the x-velocity contours, both aerofoils produce similar flow characteristics, which results in a similar lift coefficient generation. Since the magnitude of the pressure distribution over the suction side is much greater than that of the pressure side of both aerofoils, the negative lift coefficient is generated by both aerofoils at these angles of attack.
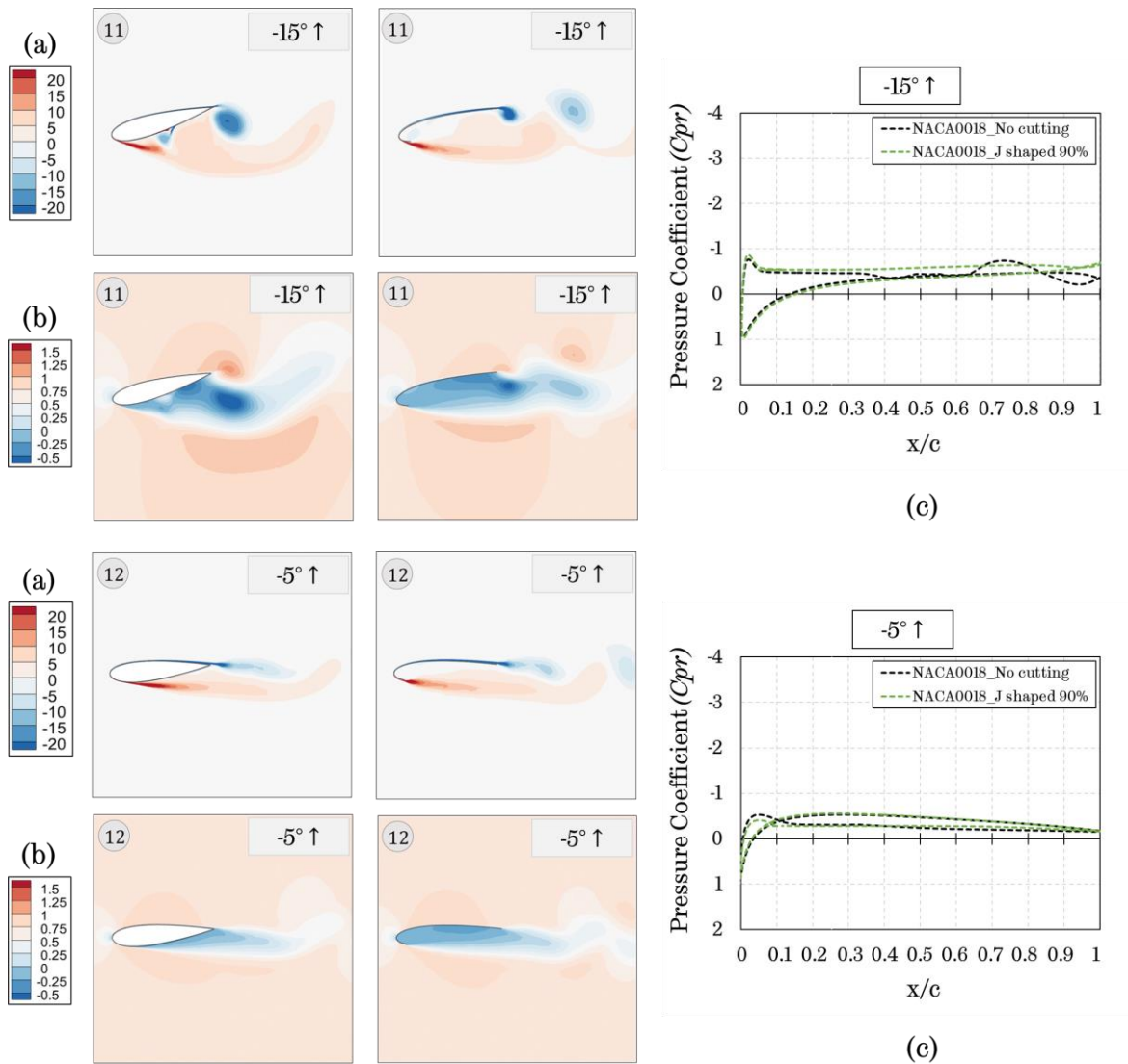
Figure 6.30. The contours of the (a) normalized z-vorticity ($w_z c/V_\infty$) and (b) normalized x-velocity (V_x/V_∞) of the flow over the conventional aerofoil and the J-shaped aerofoil with a 90% opening and (c) pressure distribution over both aerofoils at angles of attack $\alpha = -15°\uparrow$ and $\alpha = -5°\uparrow$.

The discussion is further confirmed using the contours of the velocity vector, velocity streamlines, velocity magnitude, and total pressure as illustrated in Figure 6.31 and Figure 6.32 for the conventional and its J-shaped aerofoils at angles of attack $\alpha = -15°\uparrow$ and $\alpha = -5°\uparrow$ in order to analyse the flow structures over the aerofoils investigated.

It is known that the friction drag and pressure drag play a crucial role over the aerofoil at different angles of attack. From the standpoint of the small angles of attack, the only mild adverse pressure gradient is experienced at the boundary layers on the suction and pressure side of an aerofoil, and it remains attached along almost the entire chord length. The wake is very small and inside the boundary layer, drag is dominated by the viscous friction. On the other hand, the magnitude of the adverse pressure gradients on the aerofoil surface increases with the increase in the angle of attack. Particularly, strong adverse pressure gradient may occur close to the leading edge on the suction side of the aerofoil and this may be adequately strong to separate the flow over the aerofoil surface. Consequently, the size of the wake will increase due to this separation and the pressure losses occur in the wake as a result of the eddy formation. Thus, pressure drag increases. It would be said that if a larger portion of the flow over the suction side of the aerofoil is separated at the higher angles of attack, the aerofoil can be considered to be stalled. Under these circumstances, the pressure drag is much greater than the viscous drag. According to this explanation, the contours of the pressure show that as the angle of attack increases from -5°↑ to -15°↑ in the negative angle of attack region during the upstroke motion, the pressure over the suction side of the aerofoils increases, which results in a greater drag production. Additionally, in comparison, the magnitude of the pressure over the suction side of the J-shaped aerofoil is much greater than that of the conventional aerofoil when the angle of attack decreases to -5°. This is the reason why the J-shaped aerofoil produces a much higher drag at the negative angle of attack region, especially during the upstroke motion.
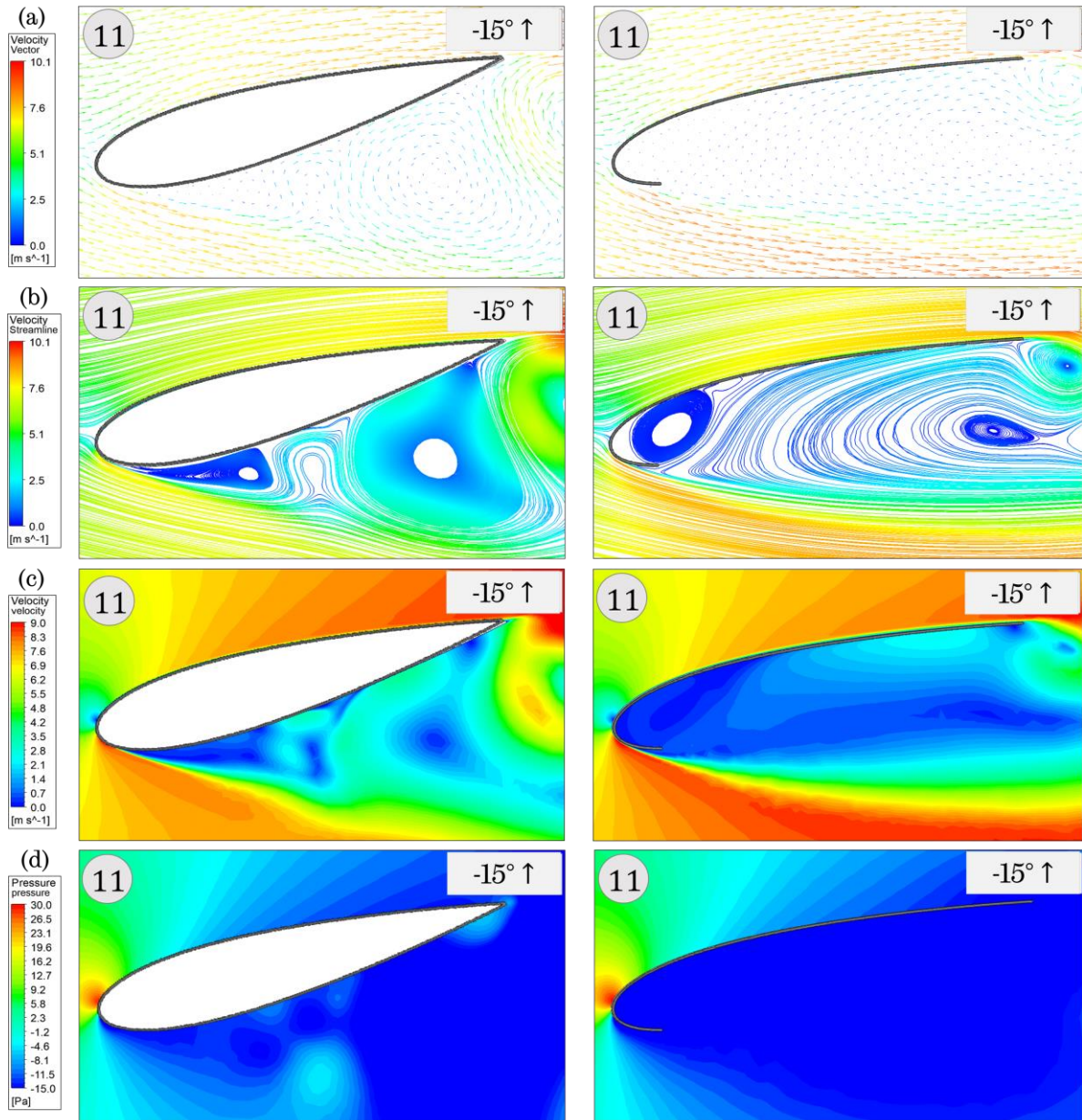
Figure 6.31. The contours of the (a) velocity vector, (b) velocity streamlines, (c) velocity magnitude, and (d) pressure of the flow over the conventional aerofoil and the J-shaped aerofoil with a 90% opening at the angle of attack $\alpha = -15°$ ↑.
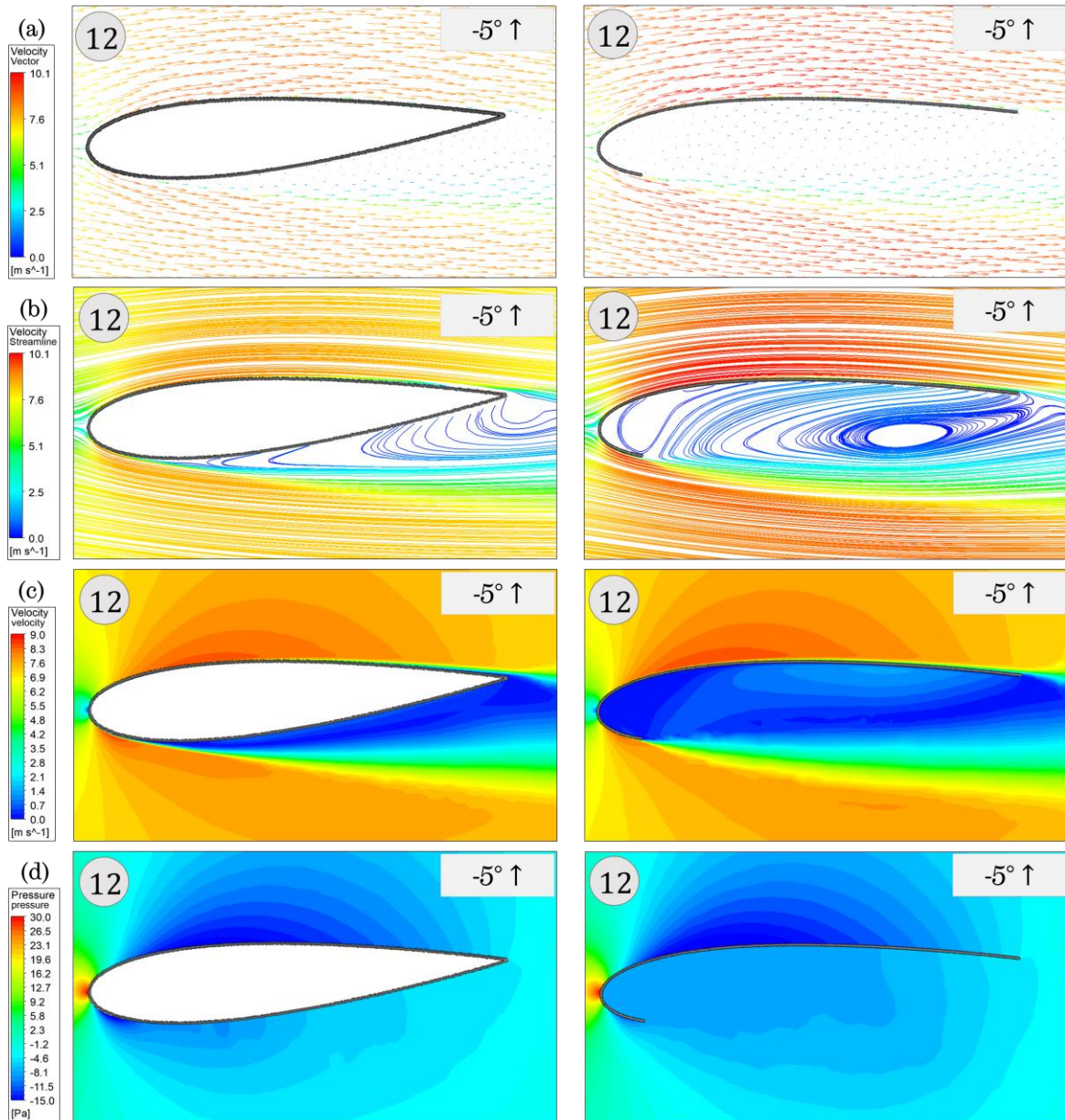
Figure 6.32. The contours of the (a) velocity vector, (b) velocity streamlines, (c) velocity magnitude, and (d) pressure of the flow over the conventional aerofoil and the J-shaped aerofoil with a 90% opening at the angle of attack $\alpha = -5° \uparrow$.

Comparison between the conventional aerofoil and its J-shaped profile quantifies the increase in the lift when using a J-shaped aerofoil, especially in the positive angles of attack region. Due to the majority of the torque generation occur in the upstream part of the VAWT, which corresponds to the positive angles of attack in the Darrieus motion, the greater lift force coefficient

generation of the J-shaped profile in the positive angles of attack region is an important finding and beneficial for the H-type VAWT in order to obtain higher performance. However, the current findings show that the J-shaped aerofoil not only exhibits a larger peak value of the lift coefficient but also produces a greater drag coefficient when compared to the conventional aerofoil, especially during the upstroke motion in the negative angles of attack region where the opening section is located in the suction side of the aerofoil. The increase in the lift force coefficient is accompanied by an increase in the drag force coefficient in the negative angles of attack region, which corresponds to the downstream part of the VAWT, which may be detrimental to the turbine performance. Therefore, the J-shaped aerofoil produces more drag, which is the reason why the overall performance of the turbine in the negative angles of attack region decreases, especially at higher tip speed ratios.

6.3　Static performance

In order to provide a further investigation on the understanding of the aerodynamic characteristics of the J-shaped aerofoil profiles, in addition to the oscillating motion, the static behaviours of the J-shaped aerofoils are also analysed in this section. The objective of the present study is to analyse aerodynamic behaviour of the J-shaped aerofoil in comparison with its conventional profile at the different angles of attack in terms of static stall angle and static pressure distribution over the suction and pressure sides. For this purpose, the aerodynamic characteristics of the conventional aerofoil and its J-shaped profile with 30%, 60%, and 90% opening ratios have been analysed in terms of the static lift and drag coefficients. In addition, the visualization of the flow and the pressure distributions generated over the aerofoils investigated have been presented in order to provide a further qualitative comparison of the aerodynamic characteristics of the conventional aerofoil and its J-shaped profile at both positive and negative angles of attack region.

6.3.1   2D CFD static aerofoil study

6.3.1.1   Model description

Due to the interest in analysing the static performance for the conventional aerofoil and its J-shaped profiles with different opening ratios, static aerofoil simulations have been conducted using the same domain and mesh features as those used in the oscillating aerofoil simulations. The number of iterations employed to the static aerofoil simulations was 10000 in order to achieve a full stabilization of the lift force coefficient, and then the static stall for the conventional aerofoil and the J-shaped profiles have been obtained. In addition, the Reynolds number used in the present investigation is Re=0.72×10^5, which provides a fair comparison of the performance of the aerofoils investigated with the previously analysed dynamic performance.

6.3.1.2   Model validation

Before starting to investigate the static performance of the conventional aerofoil and its J-shaped profiles, the 2D CFD static aerofoil model employed the same computational setting as the oscillating aerofoil model have been validated against an experimental study conducted by Gerakopulos et al. [183] under the static aerofoil conditions in order to illustrate the reliability of the present numerical model for the static conditions.

The NACA0018 aerofoil profile was used for the validation studies at Reynolds number of 120,000. The main reason of selecting this experimental study is due to the lack of the experimental studies in the literature at such low Reynolds number and this Reynolds number appears to be consistent with that used in the oscillating aerofoil validation study.

Figure 6.33 shows a comparison between the current 2D CFD lift coefficient prediction using the SST $k - \omega$ turbulence model with the intermittency function with the experimental study conducted by [183]. As it can be seen from the figure, the CFD prediction using the SST $k - \omega$ turbulence model with the intermittency function match closely with the experimental measurements at

the low angle of attacks $\alpha < 6°$, showing a linear increase of the lift coefficient with the increase in the angle of attack. However, for $6° < \alpha < 16°$ the 2D CFD model under-predicts the lift coefficient. It should also be pointed out that the prediction of the static stall angle is also successfully captured when using the present CFD model as it is measured in the experimental study by Gerakopulos et al. [183]. Therefore, the SST $k - \omega$ turbulence model with the intermittency function can also be used with confidence for the present investigation as it has been used in the oscillating aerofoil simulations.
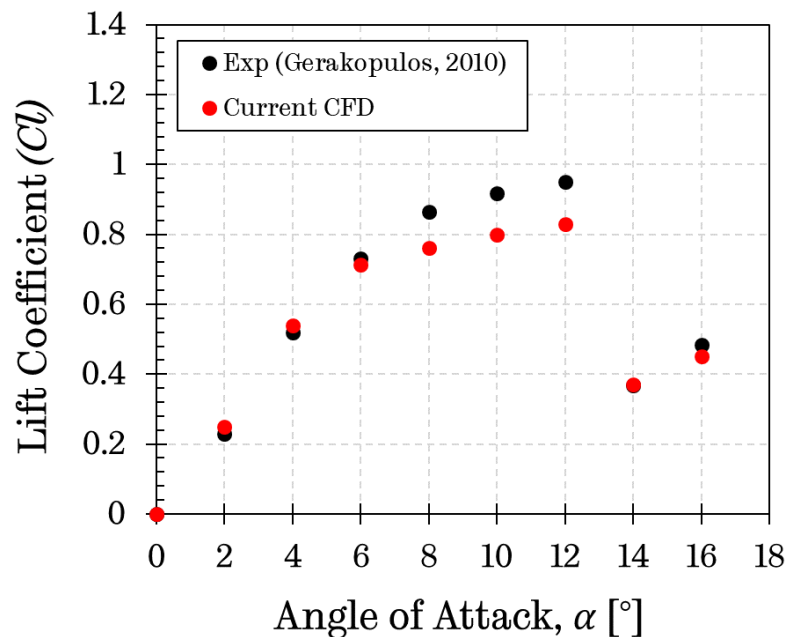
Figure 6.33. CFD static lift coefficient prediction compared with the experimental data [183].

Furthermore, Figure 6.34 illustrates the surface pressure coefficient of the aerofoil at the angle of attack between 0° and 16°. At the low Reynolds number of 120,000, the laminar boundary layer on the aerofoil upper surface undergoes the laminar to turbulent transition, which results in the flow reattachment closing the recirculation flow into a laminar separation bubble. As it can be seen from the figure, the current CFD model with the SST $k - \omega$ with the intermittency turbulence model successfully captured this laminar separation bubble phenomenon.

The separation bubble location moves from the trailing edge to the leading edge of the aerofoil due to the increase in the angle of attack, and the length of the separation bubble is reduced. The current result is consistent with the findings by [183]. When the aerofoil stalls at 14°, the laminar separation bubble bursts, which results in a full leading-edge stall behaviour by a sudden and significant drop in the lift coefficient and the highest value of the suction pressure coefficient, as seen in Figure 6.34.
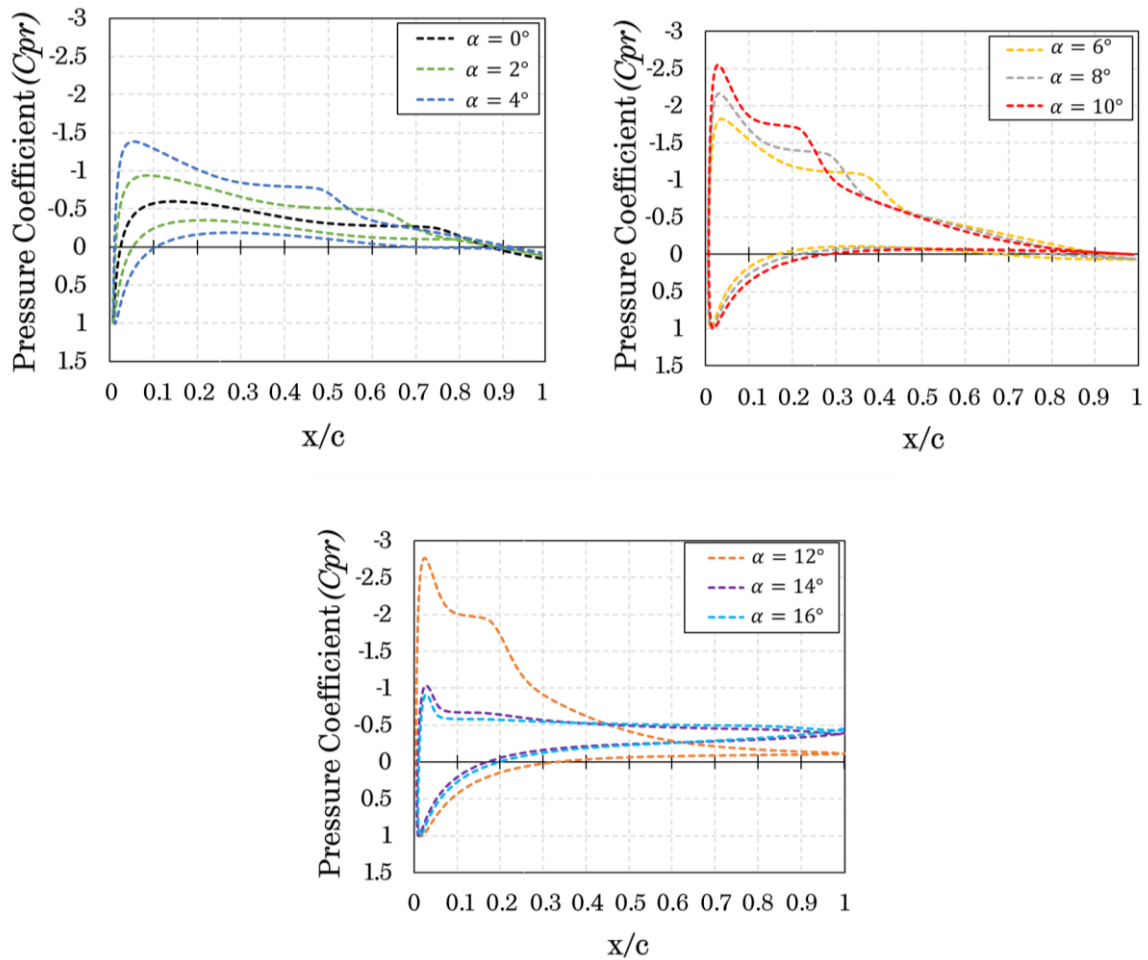
Figure 6.34. Surface pressure coefficient of the aerofoil at various angles of attack predicted by the CFD model with the SST $k - \omega$ turbulence model with the intermittency function.

In addition, the laminar separation bubble phenomenon can be observed in the velocity streamlines around the aerofoil. Figure 6.35 illustrates the

streamlines in the vicinity of the NACA0018 aerofoil at the angle of attack between 0° and 16°. As it can be seen from the figure, when $\alpha = 0°$, the location of the separation bubble is close to the trailing edge of the aerofoil; however, with the increasing of the angle of attacks, it moves towards the leading edge of the aerofoil. Furthermore, the length of the bubbles become shorter while the angle of attack increases. In addition, a full leading edge stall occurs when the angle of attack reaches 14°.
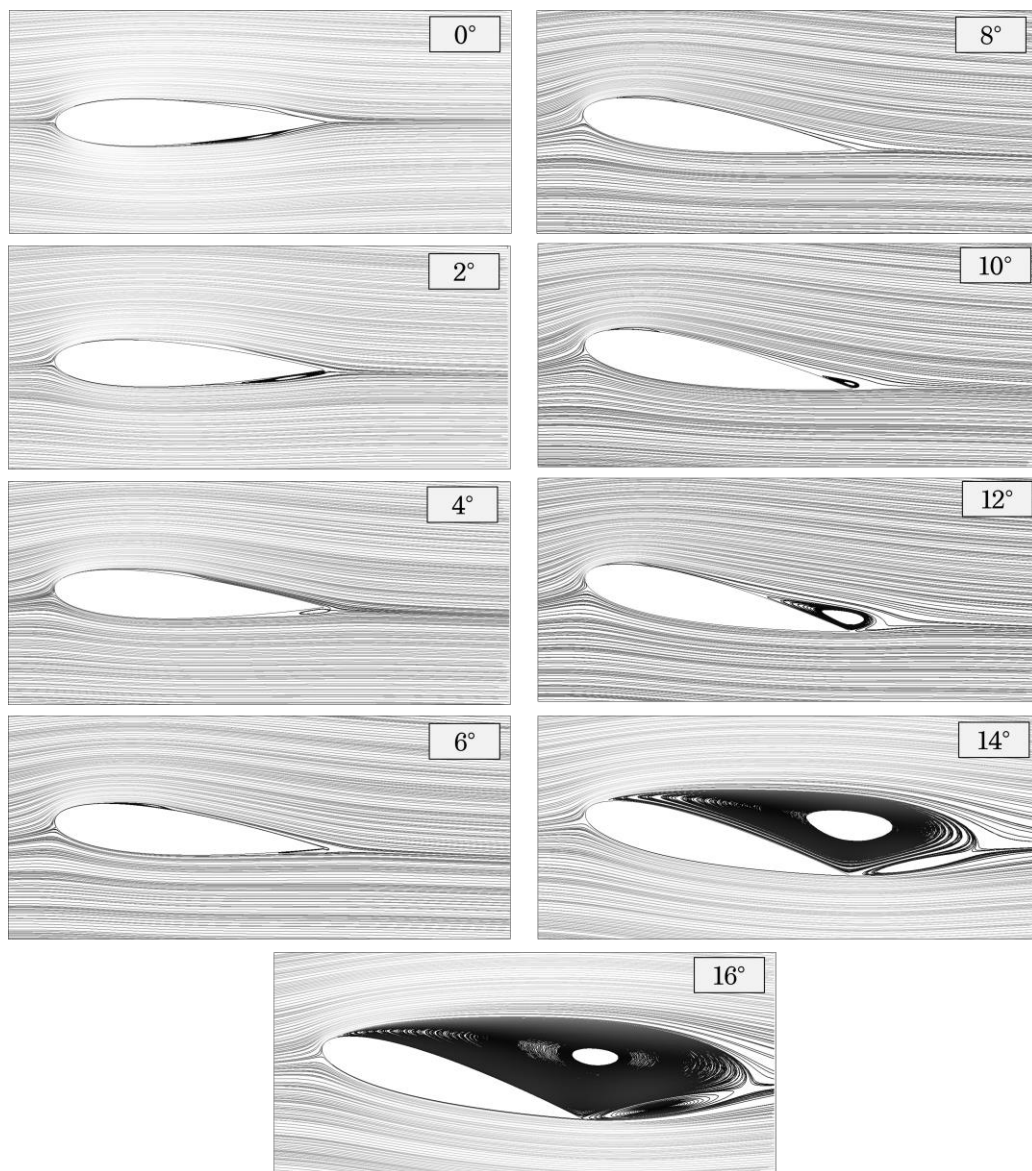
Figure 6.35. Streamlines in the vicinity of the NACA0018 aerofoil at an angle of attack between 0° and 16°.

In order for further validation of the current CFD model, the same methodology used by Gerakopulos [183] to measure the laminar separation bubble and reattachment locations has been applied in the present study in order to compare the findings. Detailed information on the estimation of these crucial phenomena can be found in [183].

According to the above explanation, the location of the laminar separation bubble and reattachment has been estimated and illustrated in Figure 6.36. As can be seen from the figure, the location of these phenomena has been successfully captured. Moreover, Figure 6.36 also illustrates two distinct regions for both the separation (S) and reattachment (R), which are referred to as Zone I and Zone II. Zone I is represented by a nearly linear reduction in the separation and reattachment locations at the angle of attack between 0° and 6°, whereas Zone II is associated with a more gradual linear reduction of the separation and reattachment locations from $\alpha = 8°$ to the stall angle. This rate of change in the separation and reattachment locations with the change of the angle of attack may be due to the slope change in the lift coefficient as shown in Figure 6.33.
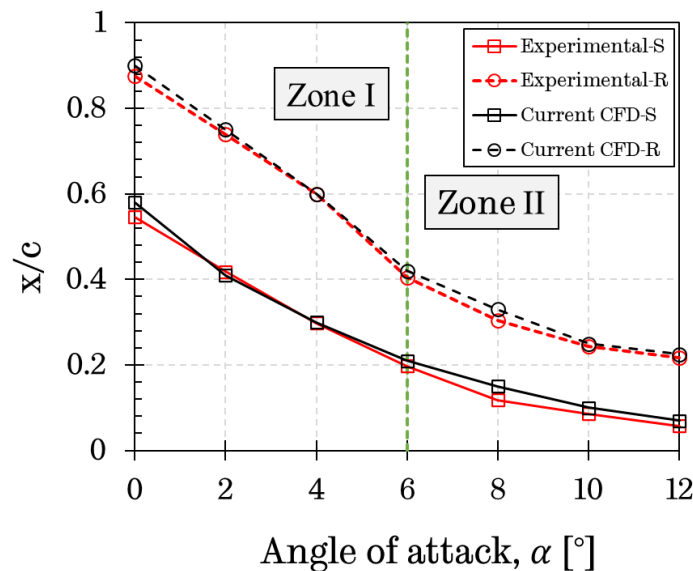
Figure 6.36. The separation and reattachment locations of the laminar separation bubble as a function of the angle of attack predicted by the current CFD model compared with the experimental data [183] at a Reynolds number of 120,000. S and R are the locations of the separation and reattachment, respectively.

Based on the validation study performed in this section, the following conclusions can be listed:

- The CFD aerofoil model when using the SST $k - \omega$ turbulence model with intermittency function is able to provide a reasonably good prediction for the aerofoil static lift coefficients at the low angle of attacks. The predicted CFD results show that there is a sudden aerofoil stall, which results in a sudden reduction in the static lift coefficient.

- The present CFD aerofoil model successfully captures the static stall angle at $\alpha = 14°$, which is in agreement with the experimental data.

- The SST $k - \omega$ turbulence model with the intermittency function is able to capture the laminar separation bubble phenomena that appears at the upper surface of the aerofoil at the relatively low Reynolds numbers. The locations of the laminar separation bubbles and reattachment have closely matched those measured by the experimental study [183]. Moreover, this phenomenon can be observed in the velocity streamline contours.

- The current CFD results also show two distinct static lift coefficient slope regions, which are linked to the rate of the advancement of the bubble separation and reattachment locations.

6.3.2 Characteristics of the static lift and drag force coefficient of the conventional aerofoil and its J-shaped profiles

The conventional aerofoil and its J-shaped profile with 30%, 60%, and 90% opening ratios have been compared at Re=72,000 in terms of the static lift and drag force coefficients. Figure 6.37 shows the static lift and drag coefficients as a function of the angle of attack for the J-shaped aerofoils in comparison with the representative conventional aerofoil NACA0018.
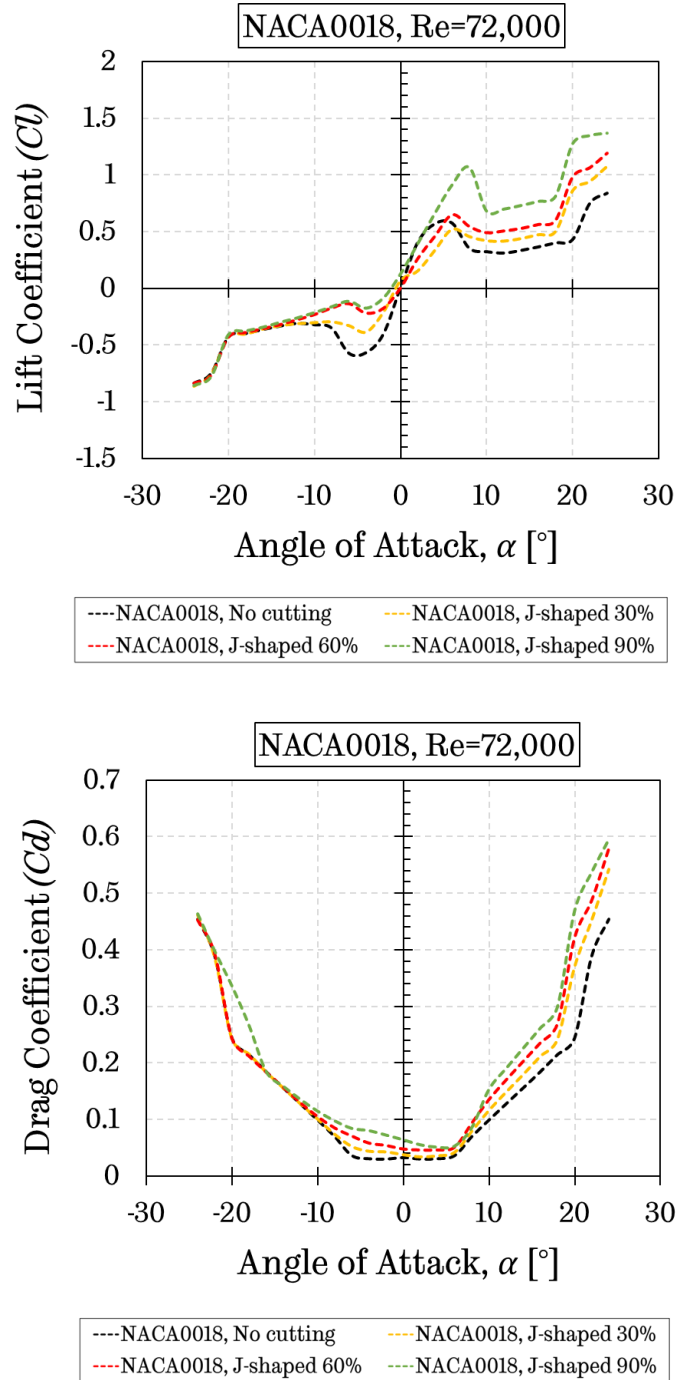
Figure 6.37. Static lift and drag force coefficients as a function of the angle of attack for static performance comparison of the conventional aerofoil and the J-shaped profiles at Re=72,000.

As can be seen from the figure that in the positive angles of attack region, the J-shaped profile with a 90% opening ratio has a better aerodynamic performance

in terms of the static lift force coefficient along all the angles of attack investigated. However, interestingly the conventional aerofoil exhibits a larger static lift force coefficient compared to the J-shaped aerofoils with 30% and 60% opening ratios at the angles of attack between $0° < \alpha < 6°$. After the angle of attack of $\alpha = 6°$, the static lift force coefficient increases with the increase in the opening ratio on the aerofoil surface. In addition, the delay in the static stall angle is also observed when the opening ratio increases, particularly it is very clear when the conventional aerofoil is compared with the J-shaped aerofoil with a 90% opening ratio. For instance, the static stall angle obtained for the conventional aerofoil is $a_{ss} = 6°$ with a value of peak static lift force coefficient of Cl=0.572; while that of $a_{ss} = 8°$ for the J-shaped profile with a 90% opening ratio with a value of peak static lift force coefficient of Cl=1.06.

On the contrary, in the negative angles of attack region, the conventional aerofoil exhibits a better aerodynamic performance concerning the static lift force coefficient compared to the J-shaped profiles, especially at the angle of attack between $-12° < \alpha < 0°$. In this range of the angle of attack, the performance reduces with the increase in the opening ratio. However, with the further increase in the angle of attack, there is no noticeable difference between the lift force coefficients generated by the aerofoils investigated has been observed.

On the other hand, in the positive angles of attack region, the J-shaped aerofoils with the different opening ratios produce a much higher static drag force coefficient compared to the conventional aerofoil. Furthermore, the static drag force increases with the increase in the opening ratio. Even though all aerofoils investigated produce similar drag force coefficients at some negative angles of attack, generally J-shaped profile with the biggest opening ratio investigated produces a larger drag force coefficient.

Although the increment on the static lift force and a further delay on the static stall angle has been obtained with the use of the J-shaped profile, especially in the positive angles of attack region, a higher drag generation may result in a

reduction on the turbine overall performance, particularly at higher tip speed ratios. Overall, the findings observed in the static J-shaped profile performance in comparison with the conventional aerofoil are consistent with those of the dynamic performance.

6.3.3 Flow visualization and pressure distribution over the conventional aerofoil and its J-shaped profile with a 90% opening ratio

In the present section, the numerically simulated development of the flow structures over the stationary conventional aerofoil and its J-shaped profile with a 90% opening ratio is presented at eight static pitch angles (-12°, -8°, -6°, -2°, 2°, 6°, 8°, and 12°) in order to allow a qualitative comparison of the aerodynamics of the two aerofoils investigated. The evaluation of the flow structures is described using the contours of the normalized z-vorticity ($w_z c/V_\infty$) (*upper contours*) and velocity streamlines (*lower contours*) in Figures 6.38 - Figures 6.42 (a-b). Furthermore, the surface pressure distributions of the conventional aerofoil and the J-shaped aerofoil has been plotted Figures 6.38 - Figures 6.42 (c) and discussed in order to assist in further understanding of the flow behaviour over the aerofoils.

At $\alpha = 2°$ (see Figures 6.38 (a) and (b)), the flow around both aerofoils show a similar structure, especially at the suction side of the aerofoils and the flow remains fully attached to both aerofoil's surfaces. Therefore, no significant difference observed in the pressure distribution on the suction side between the conventional aerofoil and its J-shaped profile, as shown in Figure 6.38 (c). However, the pressure on the pressure side of the J-shaped aerofoil is very different from that of the conventional aerofoil, especially at $0.1 < x/c < 0.3$ and $0.75 < x/c < 1$. It is higher than that of the conventional aerofoil. On the other hand, the conventional aerofoil has a higher pressure coefficient than that of the J-shaped aerofoil at $0.35 < x/c < 0.7$. This situation leads to an overall slightly greater static lift force generated by the J-shaped aerofoil at this angle of attack.
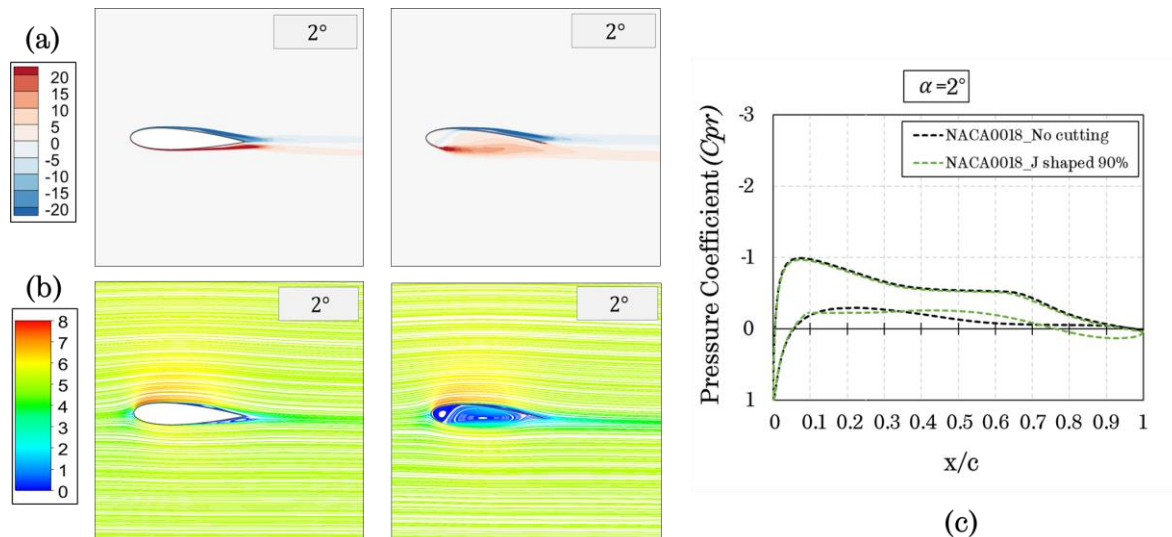
Figure 6.38. The contours of the (a) normalized z-vorticity ($w_z c/V_\infty$) and (b) velocity streamlines of the flow over the conventional aerofoil and the J-shaped aerofoil with a 90% opening and (c) pressure distribution over both aerofoils at angles of attack $\alpha = 2°$.

As the angle of attack increases further to $\alpha = 6°$, where the conventional aerofoil experiences the static stall angle, the flow over the conventional aerofoil surface has started to develop a rear-to-front flow slightly which is shortening the laminar shear layer on the suction side, while the flow is still attached to the J-shaped aerofoil's surface (see Figure 6.39 (a)). Furthermore, for both aerofoils, the length of the bubbles become shorter while the angle of attack increases from $\alpha = 2°$ to $\alpha = 6°$. Additionally, a remarkable difference in the velocity contours and pressure distributions between the aerofoils investigated has been observed at $0 < x/c < 0.44$ on the suction sides and $0.1 < x/c < 1$ on the pressure sides (see Figures 6.39 (b) and (c)). Compared to the conventional aerofoil, the overall pressure on the pressure side of the J-shaped aerofoil is higher, particularly toward the trailing edge of the aerofoils, where a much lower velocity magnitude is achieved for the J-shaped profile. On the other hand, as can be seen in the velocity streamline contours, the velocity magnitude over the suction side of the J-shaped aerofoil is much higher than that of the conventional aerofoil, especially at $0 < x/c < 0.44$. Therefore, the J-shaped profile with a 90% opening ratio has a larger negative pressure on the suction side than that of the

conventional aerofoil. Consequently, compared to the conventional aerofoil, the J-shaped profile produces a much greater static lift force due to the higher-pressure difference obtained between the suction and pressure sides.
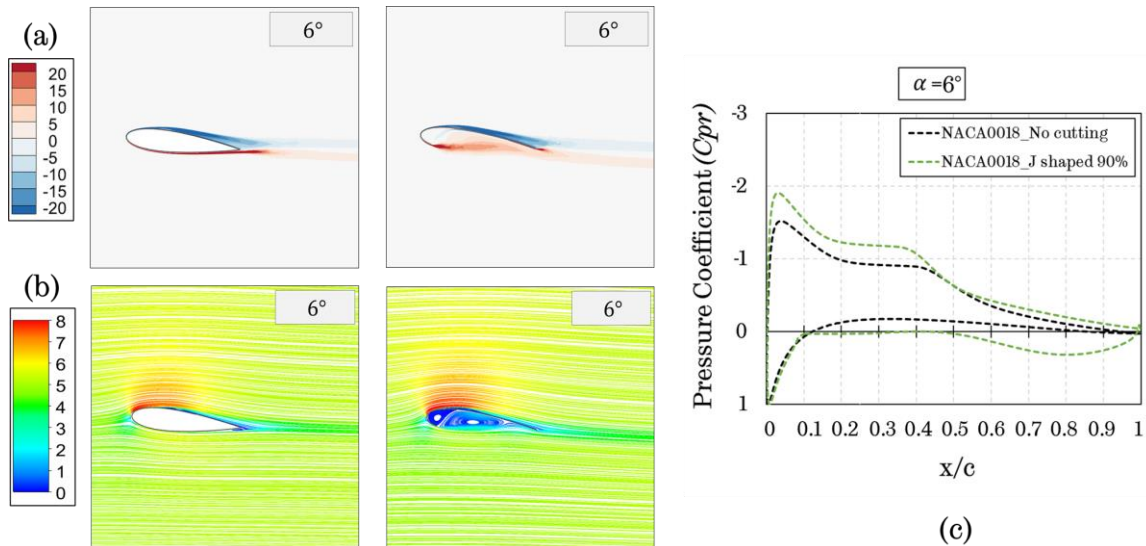
Figure 6.39. The contours of the (a) normalized z-vorticity ($w_z c/V_\infty$) and (b) velocity streamlines of the flow over the conventional aerofoil and the J-shaped aerofoil with a 90% opening and (c) pressure distribution over both aerofoils at angles of attack $\alpha = 6°$.

At $\alpha = 8°$ (see Figure 6.40), where the J-shaped profile experiences the static stall angle, the vorticity layer on the suction side of the conventional aerofoil is detached from the trailing edge which can be observed from Figure 6.40 (b) and the bubble bursts which results in a full leading-edge stall featured by a sudden and dramatic drop in the suction pressure peak and the static lift force coefficient of the conventional aerofoil. On the other hand, for the J-shaped aerofoil, the leading edge vortex (LEV) is still attached but it is close to being shed. Concerning the pressure distributions over the aerofoils, the J-shaped profile has the highest negative peak pressure on the suction side compared to the conventional aerofoil. Furthermore, along the all pressure side, the J-shaped profile produces a higher positive pressure due to a low velocity zone generated in the opening section. Therefore, the biggest difference in the static lift force coefficient between the aerofoils generated has been achieved at the angle of attack $\alpha = 8°$.
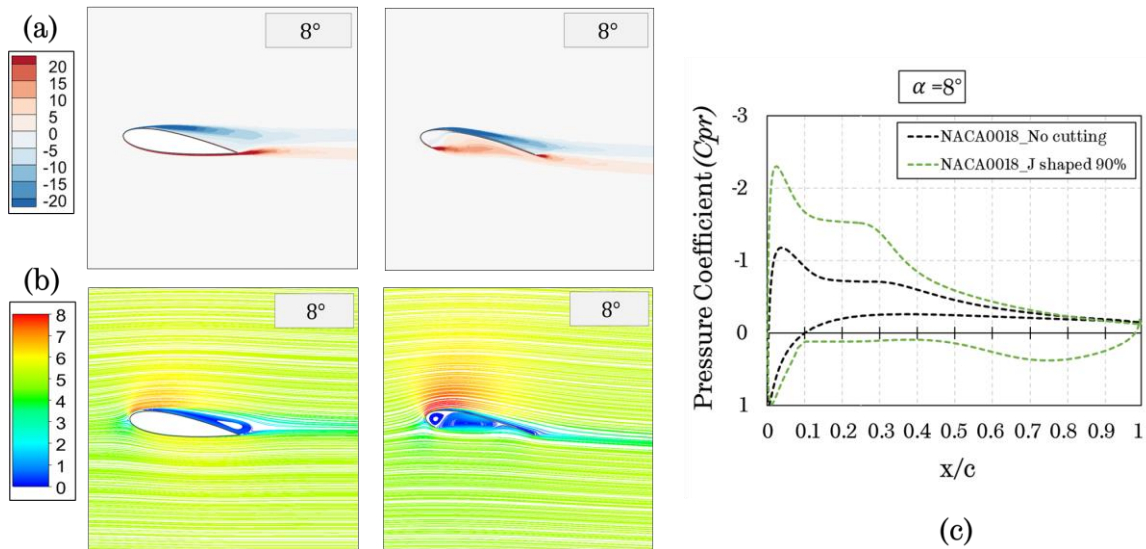
Figure 6.40. The contours of the (a) normalized z-vorticity ($w_z c/V_\infty$) and (b) velocity streamlines of the flow over the conventional aerofoil and the J-shaped aerofoil with a 90% opening and (c) pressure distribution over both aerofoils at angles of attack $\alpha = 8°$.

At $\alpha = 12°$ (see Figure 6.41), the flow is fully separated from the suction side on both the aerofoil surfaces and approximately the same pressure distribution can be obtained over the suction sides. However, a noticeable difference in the flow field and the pressure distribution over the pressure side of the two aerofoils investigated are observed. Along all of the pressure side, the J-shaped profile has a lower velocity magnitude compared to the conventional aerofoil, which results in a higher-pressure difference between these aerofoils surfaces. Therefore, in the fully-stall region, the J-shaped profile produces a greater static lift force coefficient compared to the conventional aerofoil at this angle of attack.
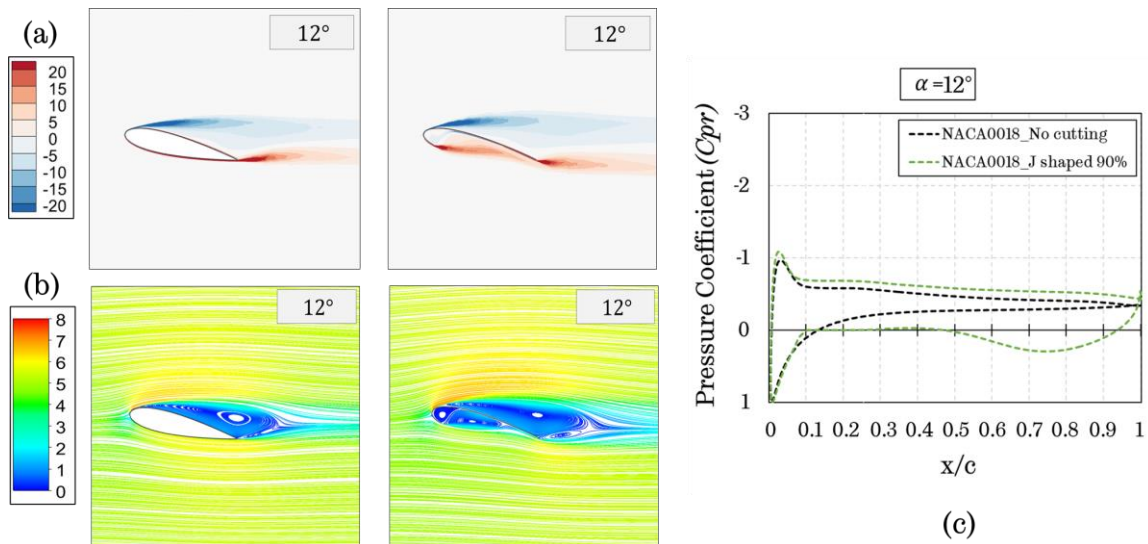
Figure 6.41. The contours of the (a) normalized z-vorticity ($w_z c/V_\infty$) and (b) velocity streamlines of the flow over the conventional aerofoil and the J-shaped aerofoil with a 90% opening and (c) pressure distribution over both aerofoils at angles of attack $\alpha = 12°$.

In terms of the negative angles of attack region, as it can be seen from the Figure 6.37 that the conventional aerofoil produces a much greater static lift force coefficient compared to the J-shaped profile with a 90% opening ratio, except at higher negative angles of attack. The flow field generated around the J-shaped profile, such as the vortex structures, on the pressure side is qualitatively similar to that around the conventional aerofoil, as shown in Figure 6.42 (a). Therefore, the aerofoils have approximately the same pressure level on the pressure side (see Figure 6.42 (c)). On the other hand, when the angle of attack of the aerofoils investigated is in the negative region, the opening section over the J-shaped aerofoil is located on the suction side. Even at the smaller negative angle of attack ($\alpha = -2°$), the flow over the suction side of the J-shaped aerofoil is fully separated compared to the conventional aerofoil. Therefore, there is no significantly increment observed on the peak negative pressure of the J-shaped aerofoil with the increase in the negative angles of attack. Consequently, a higher difference in the static lift fore coefficient between the conventional and its J-shaped profile can be obtained at the negative angles of attack region. As a result, the negative peak pressure generated on the suction side of the conventional

aerofoil is much greater than that of the conventional aerofoil at all the angles of attack examined.
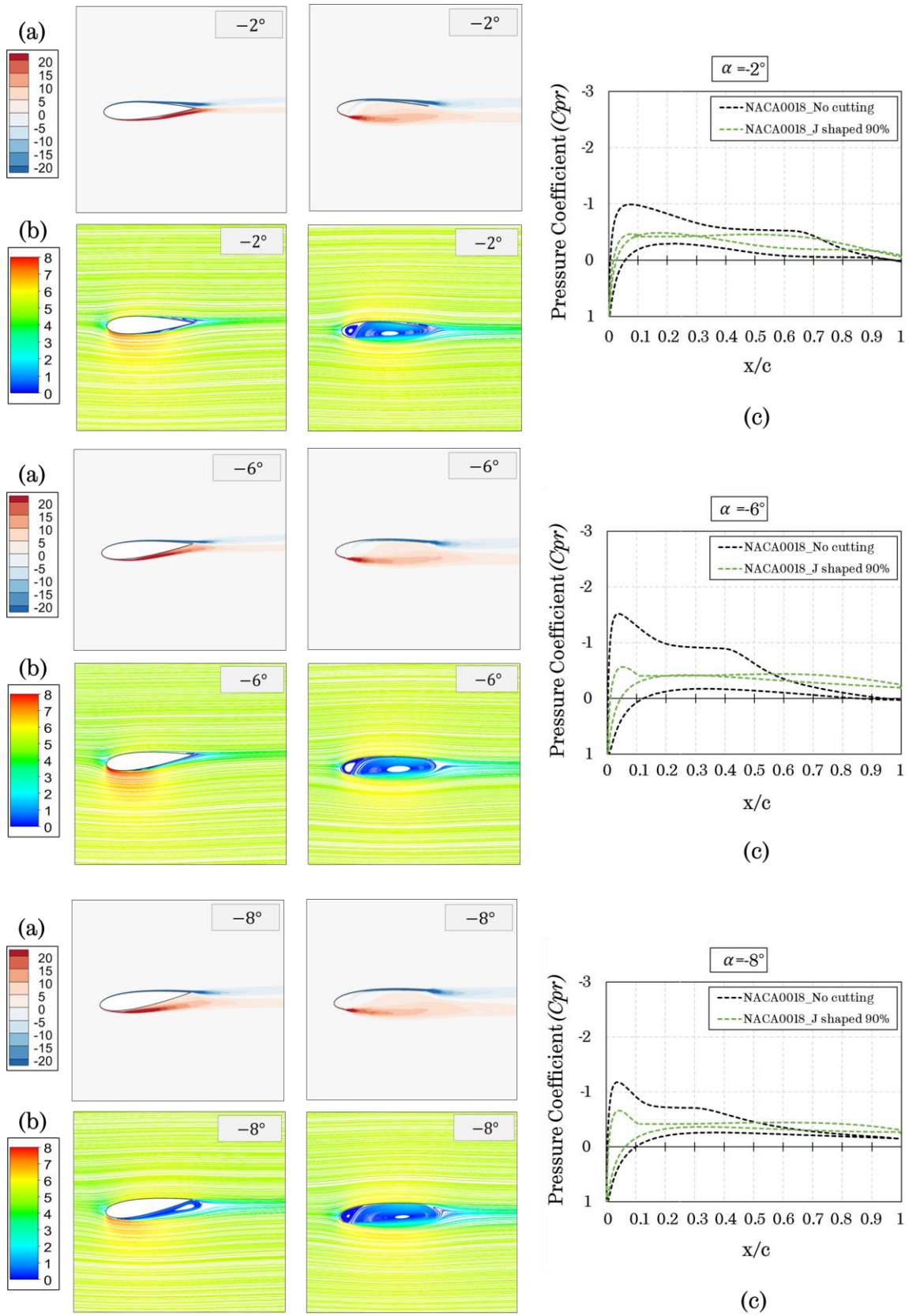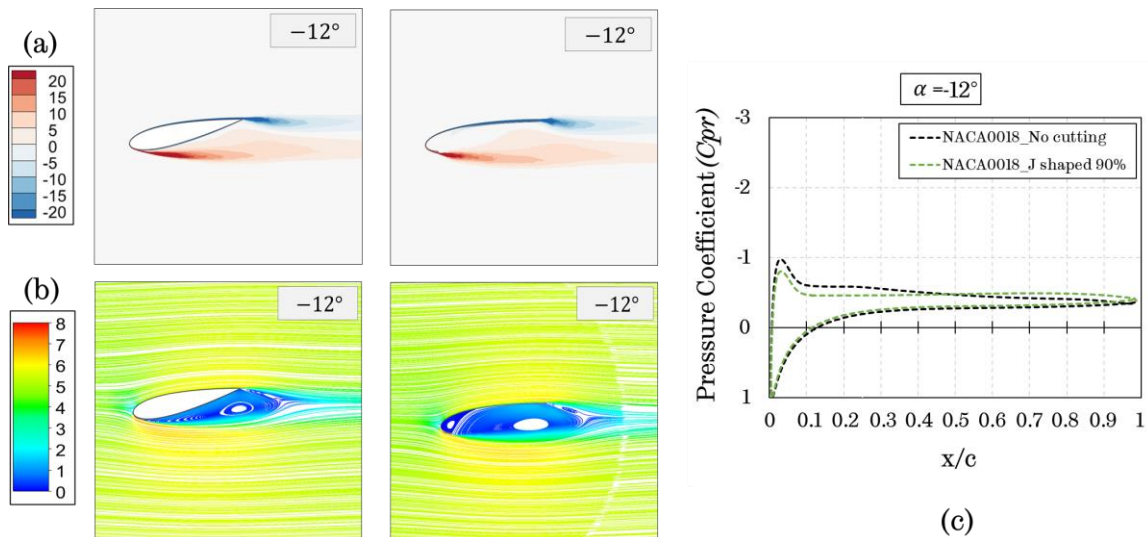
Figure 6.42. The contours of the (a) normalized z-vorticity ($w_z c/V_\infty$) and (b) velocity streamlines of the flow over the conventional aerofoil and the J-shaped aerofoil with a 90% opening and (c) pressure distribution over both aerofoils at angles of attack $\alpha = -2°, -6°, -8°,$ and $-12°$.

6.4 Conclusion

In this chapter, the dynamic and static performance characteristics of the conventional aerofoil and its J-shaped profiles with 30%, 60%, and 90% opening ratios have been investigated. Firstly, the Darrieus pitching motion has been employed in the simulations in order to account for the aerodynamic behaviour of the J-shaped aerofoil in comparison with its conventional profile NACA0018 by considering the crucial parameters such as aerofoil thickness, tip speed ratio, Reynolds number, pitch angle, and the constantly changing relative velocity. Furthermore, qualitative and quantitative comparisons have been conducted for conventional aerofoil and its J-shaped profiles from an aerodynamic point of view. Secondly, the stationary conventional aerofoil and its J-shaped profiles have been investigated under the same numerical characteristics as those employed in the dynamic aerofoil simulations in order to evaluate the static performance of the aerofoils examined.

Conclusions can be drawn as follows:

- Regardless of the fact that the simulation has been carried out under the dynamic or static conditions, the simulation results reveal that a much greater lift force coefficients of the aerofoils investigated increases with the increase in the opening ratio on the aerofoil surface in the positive angles of attack region.

- Additionally, the dynamic and static stall angles are further delayed in the positive angles of attack region when the opening ratio increases, which may result in a more torque generation in a wider azimuthal position in a complete turbine rotation, especially in the upstream part. However, in terms of the negative angles of attack, the conventional aerofoil shows a much better performance compared to the J-shaped aerofoils.

- Due to the majority of the torque generation during the upstream part of the VAWT, the greater lift force coefficient generation of the J-shaped profile in the positive angles of attack region may enhance the turbine torque generation at low tip speed ratios, which assists turbine to self-start.

- The NACA0012 and its J-shaped profiles show a better aerodynamic performance than that of NACA0018 and its J-shaped profiles at the positive angles of attack region at high λ values. The reason for this may be that the thinner airfoils have a higher performance at relatively higher tip speed ratios while the thicker aerofoils have a higher performance at lower tip speed ratios. Therefore, the thicker aerofoil may be preferred for the H-type VAWT applications for self-start.

- The findings show that the tip speed ratio and the pitch angle significantly affect the maximum angle of oscillation of the aerofoils and the magnitude of the stall-onset angle. With the decrease in the tip speed ratio, the higher delay in the stall-onset angle is observed for each opening ratio of the J-shaped profile, particularly in the positive angles of attack region, which may result in an enhancement of the self-starting capability of the H-type VAWTs.

- The J-shaped profile with a 90% opening ratio has a further delay on the stall-onset angle compared to the conventional aerofoil at the lowest Reynolds number investigated. Among all the aerofoils investigated, the J-shaped profile

with a 90% opening ratio indicates better aerodynamic performance in terms of the peak chordwise force coefficient at low λ values.

• Furthermore, it is clear that the value of the pitch angle decreasing from positive to negative, the stall-onset angle is delayed to a larger angle of attack, regardless of the aerofoils investigated. However, since the aerofoils experience a deep stall condition at the high angles of attack with the increase in the negative pitch angle, this may cause an overall performance reduction for the turbine with the utilisation of the higher values of the negative pitch angle.

• In the positive angles of attack region, the stall-onset is not considerably influenced when the variable relative velocity is employed. On the contrary, in the negative angles of attack region, the prediction of the stall-onset angle considering the variable relative velocity may have a significant effect. However, it is interestingly observed that the effect of the variable relative velocity in the negative angles of attack decreases with the increase in the opening ratio.

• The torque that an aerofoil generates depends on the available lift force, i.e. if the aerofoil has a higher lift coefficient, then more torque is expected to be generated, which consequently increases the performance of the turbine, particularly at low tip speed ratios. The effect of the operating parameters investigated in terms of the dynamic performance of the oscillating aerofoil undergoing the Darrieus motion shows that the J-shaped aerofoil with a 90% opening ratio indicates its superior in the positive angles of attacks, where about 90 or 95% of the torque of a typical VAWT is generated, but also higher drag.

• The J-shaped aerofoil not only exhibits a larger peak value of the lift coefficient but also produces a greater drag coefficient in comparison with the conventional aerofoil, especially during the upstroke motion in the negative angles of attack region where the opening section is located on the suction side of the aerofoil. Therefore, the overall performance of the J-shaped aerofoils in turbine applications, in terms of the downstream part generally decreases with the increase in the opening ratio and this may be as a result of the lift decrease being accompanied by an increase in the drag in the negative angles of attack regions.

- Furthermore, the comparison between the characteristics of the dynamic and static conditions clearly illustrates that when an aerofoil is under the oscillating motion, the dynamic stall angle can be considerably delayed beyond the static stall angle. Therefore, the static aerofoil data appears to be not suitable for evaluating the performance of the J-shaped aerofoil when it is employed to the turbine application.

Chapter 7

Evaluation of the effect of J-shaped aerofoil on H-type VAWT self-starting capability

7.1   Introduction

As discussed in Section 2.3.2, although a limited number of researches has been conducted in order to investigate the effect of the J-shaped profile on the turbine self-starting behaviour, none of these studies considered the turbine dynamic self-starting characteristics based on turbine time-varying start-up data. In the previous studies existing in the literature, the self-starting performance of the H-type VAWT with the J-shaped aerofoil has been evaluated based on the calculated torque and power coefficients at the individual low tip speed ratios, which only implies whether the turbine may self-start or not and never provides a full understanding of the effect of the J-shaped profiles on the

turbine self-starting. Furthermore, the effect of the J-shaped aerofoil on the turbine self-starting behaviour is not fully understood due to the inconsistency results obtained in the previous studies. Therefore, the novelty of the present study is not only providing a further understanding of the self-starting capability of the J-shaped aerofoils but also investigating of how the different design parameters affect the self-starting performance of the turbine with the J-shaped aerofoil in comparison with the conventional aerofoil.

The main objectives of the current chapter are as follows:

- Investigate the effect of the openings located on the aerofoil outer and inner surfaces on the self-start of the turbine.
- The influence of the J-shaped aerofoil with the different opening rations on the turbine torque generation considering the low and high tip speed ratios.
- Provide an in-depth understanding of the lift and drag contributions of the J-shaped aerofoil to the torque generation at different tip speed ratios.
- Evaluation of the various aerofoil profiles with and without an opening for the dynamic start-up performance of the turbine.
- Investigate the effect of the pitch angle on the turbine self-starting behaviour using the J-shaped aerofoils in comparison with the conventional aerofoil.
- Investigation on the self-starting characteristics of the turbine with a J-shaped profile considering the resistance.

This chapter is structured as follows: Section 7.2 aims to investigate the effect of the wind speeds on the turbine self-starting behaviour and define the problematic case to use for investigations. Section 7.3 presents the effects of the different opening ratios on the turbine overall performance, in terms of the torque generation and turbine dynamic self-starting characteristics. In Section 7.4, a number of different aerofoils and their J-shaped profiles have been investigated in terms of the self-starting characteristics. Section 7.5 illustrates the influence of the positive and negative pitch angles on the turbine self-

starting behaviour. Finally, in Section 7.6, the resistance, which has been selected based on the bearing resistance typically employed in small-scale H-type VAWTs, has been considered in the dynamic start-up simulations.

7.2   The effect of the wind speeds on the torque generation and the self-starting

In this section, the turbine net torque generation and the dynamic start-up performance are examined using different freestream wind speeds, namely $V_\infty = 4, 5, 6m/s$. As mentioned in Chapter 5, the research turbine used in this thesis is able to escape the plateau stage and reach its steady-state operating condition under the free wind speed of $V_\infty = 6m/s$. The present section has been designed to assess the turbine net torque generation at different λ values and if the turbine will be able to self-start under wind speeds lower than $6\ m/s$, i.e. 4 and $5m/s$. The model setups are the same as detailed in Chapter 5.

Firstly, the turbine performance has been analysed at eight constant tip speed ratios in terms of the generated net torque. Figure 7.1 illustrates the turbine torque coefficient as a function of the tip speed ratio for different wind speeds. There are two distinct regions observed in this figure: (i) with the free wind speed lower than $6m/s$, the turbine generates a net negative torque region at low tip speed ratios, known as "the dead band" [12]. This negative torque region may prevent the turbine speed up and escape from the plateau stage unless this dead band is sufficiently small and the turbine can gain enough momentum to break through the plateau stage. Therefore, it can be expected that the turbine under the wind speed $4m/s$ and $5m/s$ may fail to self-start. (ii) At the optimum tip speed ratio, where the turbine produces the higher torque, the magnitude of the torque generated increases with the increase in the wind speed.
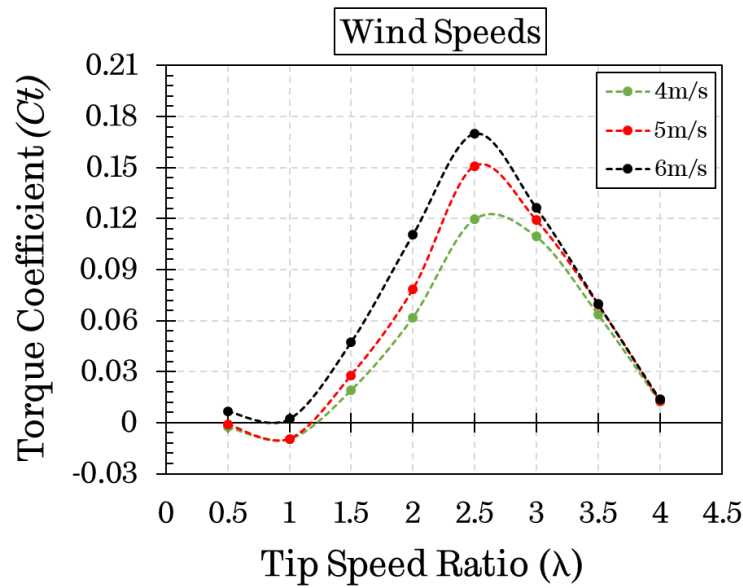
Figure 7.1. Turbine torque coefficient as a function of the tip speed ratio considering different free wind speeds of $V_\infty = 4, 5, 6 m/s$.

Secondly, a further study has been conducted by investigating the turbine dynamic start-up behaviour under different free wind speeds as shown in Figure 7.2. As it can be seen in the figure, the turbine can only self-start under a free wind speed of $6m/s$. This finding supports the results obtained in the turbine torque coefficient versus tip speed ratio curve (see Figure 7.1), which showed no dead band under the free wind speed of $6m/s$. At a wind speed lower than $6m/s$, a J-shaped aerofoil may be employed to enable the turbine to self-start, and this will be discussed in the next section.
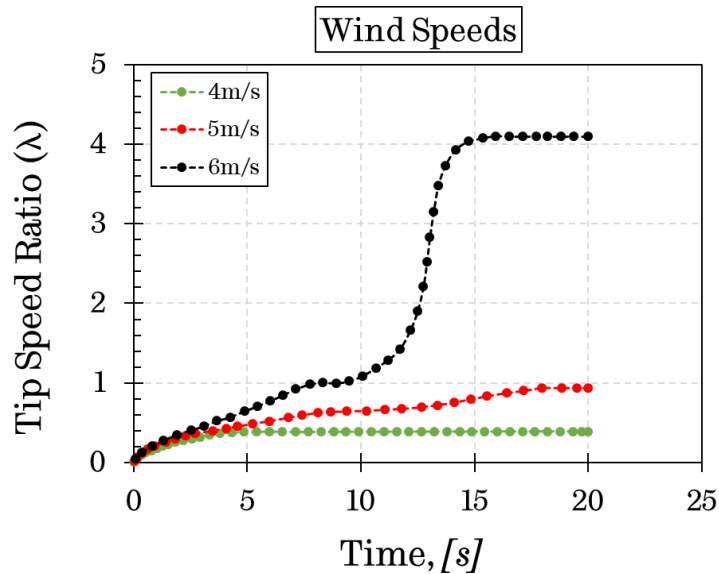
Figure 7.2. Turbine torque coefficient as a function of the tip speed ratio considering different free wind speeds of $V_\infty = 4, 5, 6 m/s$.

7.3   Evaluation of the J-shaped profile for self-starting

The present section has been designed to evaluate the turbine with the J-shaped aerofoils with different numbers of the opening ratios, in terms of the performance at low and high tip speed ratios and the dynamic start-up behaviour. The same turbine was studied, i.e. with a conventional aerofoil NACA0018, the turbine radius of $R = 0.375m$ and the blade chord length of $c = 0.083m$. Six opening ratios, 10%, 20%, 30%, 40%, 60%, and 90%, located at the outer and inner surface of the aerofoil have been investigated. The schematic of the turbine with the original NACA0018 aerofoil profile (no cutting) and the aerofoils with six different opening ratios (OR) are investigated when the openings are located at the outer surface have been illustrated in Figure 7.3.
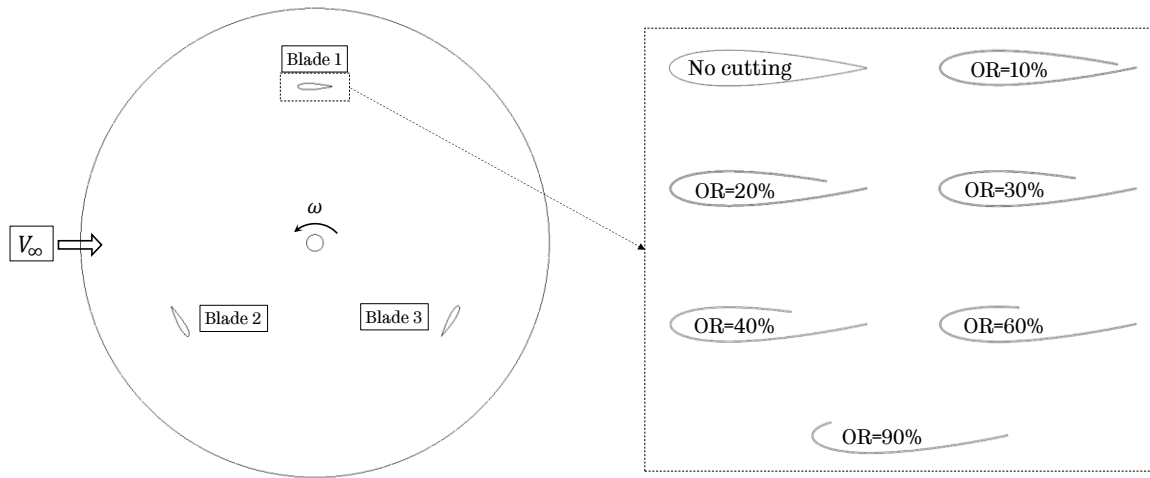
Figure 7.3. The schematic of the turbine and the aerofoils with six different opening ratios, namely 10%, 20%, 30%, 40%, 60%, and 90%.

7.3.1 The effect of the opening ratio on the turbine dynamic start-up behaviour considering the inner and outer openings

In this part of the study, the effect of the opening location on the turbine dynamic start-up behaviour have been investigated for the J-shaped aerofoils with the different opening ratios. Firstly, the J-shaped aerofoil with the openings located at the outer surface has been taken into account. Figure 7.4 shows the turbine tip speed ratio as a function of the time for the turbine with the J-shaped aerofoil with different opening ratios considering the openings located at the outer surface. As can be seen in the figure, with the increase in the opening ratio, the start-up time reduces, while the tip speed ratio at the final steady-state decreases. However, the turbine with the original aerofoil profile and the J-shaped aerofoil with a 10% opening ratio cannot escape the plateau stage and fail to start. It is believed that the reason that caused this situation is due to the negative torque generation at the critical tip speed ratio range, which is the tip speed ratio is less than 1.
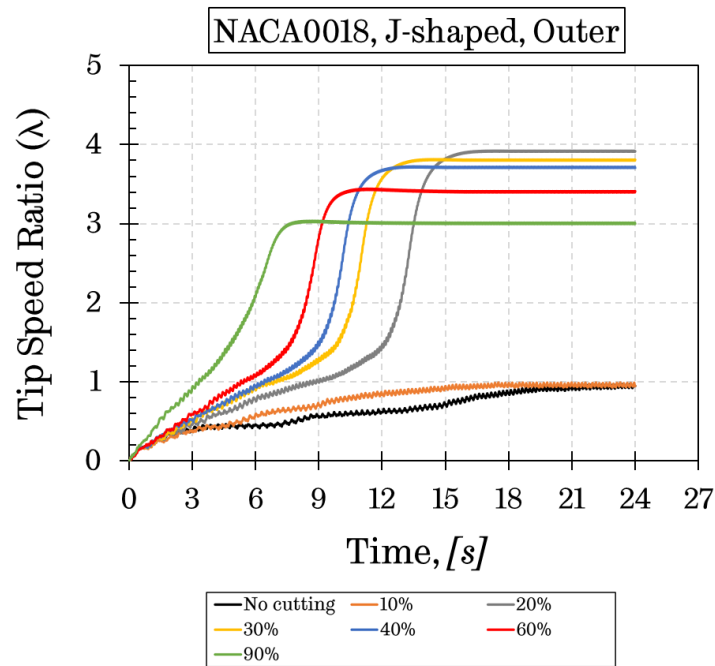
Figure 7.4. The tip speed ratio as a function of the time for the turbine with J-shaped aerofoils with different openings located at the outer surface.

Furthermore, in order to fully understand the effect of the opening ratio on the turbine dynamic start-up behaviour, the J-shaped aerofoils with the openings located at the inner surface have been also investigated. Figure 7.5 presents the tip speed ratio as a function of the time for the turbine with J-shaped aerofoils with different openings located at the inner surface. Clearly, the turbine with the J-shaped aerofoil with the larger and smaller openings do not provide the self-starting ability, but the opening ratios of 30-40% do assist the turbine to self-start and they reach the same final speed as when the opening is in the outer side but take a much longer time.

It can be concluded that the turbine with the J-shaped aerofoil with the openings located at the inner surface does not appear to bring any benefit and makes the choice of the inner profiles unreasonable compared with the outer surface. For this reason, the J-shaped aerofoil with the openings located at the outer surface will be employed to the further investigations.
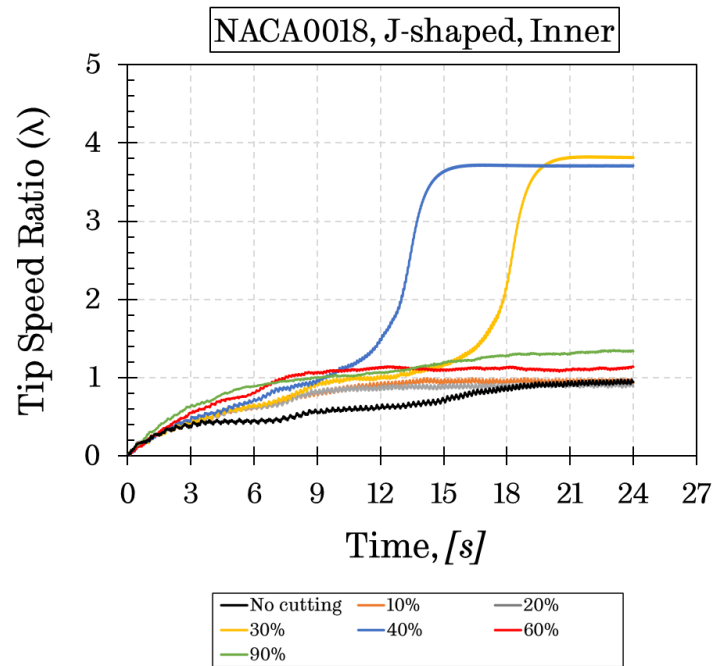
Figure 7.5. The tip speed ratio as a function of the time for the turbine with J-shaped aerofoils with different openings located at the inner surface.

7.3.2 The effect of the opening ratios on the turbine torque generation

The turbine torque coefficient at several tip speed ratios considering the different openings has been analysed under the free wind speed of $5m/s$ for the outer surface opening. For this purpose, four λ values, such as λ=0.5, λ=1, λ=2.5, and λ=3.5, which are corresponding the high λ and low λ, have been selected in order to demonstrate the effect of the J-shaped aerofoils at the different operating conditions. The instantaneous torque coefficients obtained at the selected λ values have been presented in Figure 7.6 as a function of the tip speed ratio. The figure illustrates that the J-shaped aerofoil with different opening ratios shows different aerodynamic characteristics at low and relatively high λ regions. Therefore, in order to provide a comprehensive understanding of the influence of the J-shaped profile with different opening ratios on the turbine torque generation, the low and high λ regions should be evaluated separately.
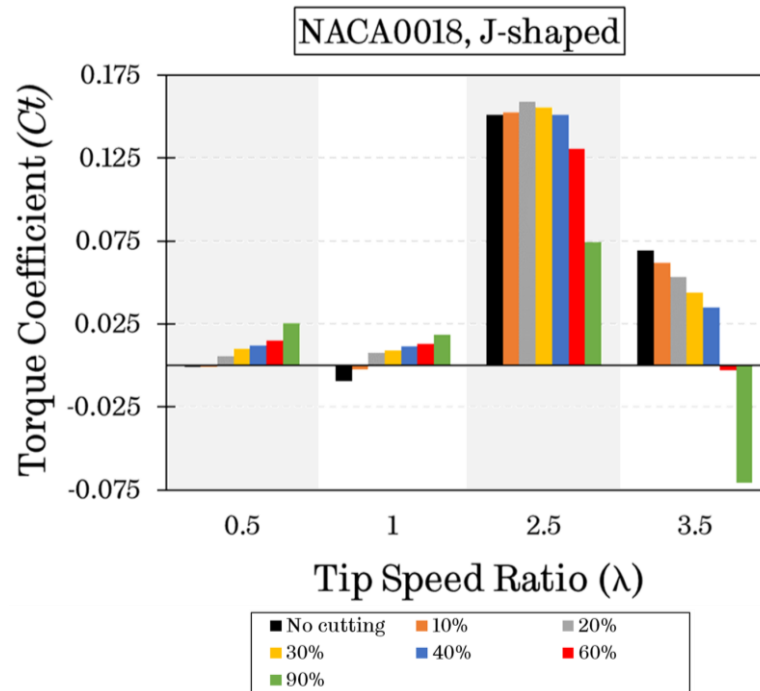
Figure 7.6. The instantaneous torque coefficient as a function of the tip speed ratio considering the different opening ratios.

At the low λ region in which λ = 0.5 and λ = 1, as it can be seen in the figure that the turbine with the original aerofoil (no cutting) and 10% opening ratio produces negative torque, which results in failing to self-start. On the other hand, the generated torque increases with the increase in the opening ratio, but the one with a 90% opening ratio has a noticeably larger amplitude at both tip speed ratios, which is beneficial to the turbine self-starting capability. It is also observed that increasing the torque coefficients at the low tip speed ratios are not linear with respect to the increasing in the opening ratios.

Further investigation on the variation on the instantaneous torque coefficient of a single blade as a function of the azimuthal angles, with different opening ratios when λ = 0.5 and λ = 1 have been plotted in Figure 7.7. This investigation gives more specific information on the effect of the opening ratios regarding the upstream and downstream part of the turbine to further understand the instantaneous torque loss caused by the opening. Although there is no obvious

difference observed between the J-shaped aerofoils with different openings in the downstream part (180° < θ < 360°) of the turbine, the instantaneous torque coefficient appears to be increasing with the increase in the opening ratio in the upstream part (0° < θ < 180°) of the turbine at both tip speed ratios investigated. That is the reason why the turbine with the J-shaped aerofoil with a larger opening ratio produces a much greater torque than the turbine with the smaller opening ratios at these tip speed ratios (see Figure 7.6).
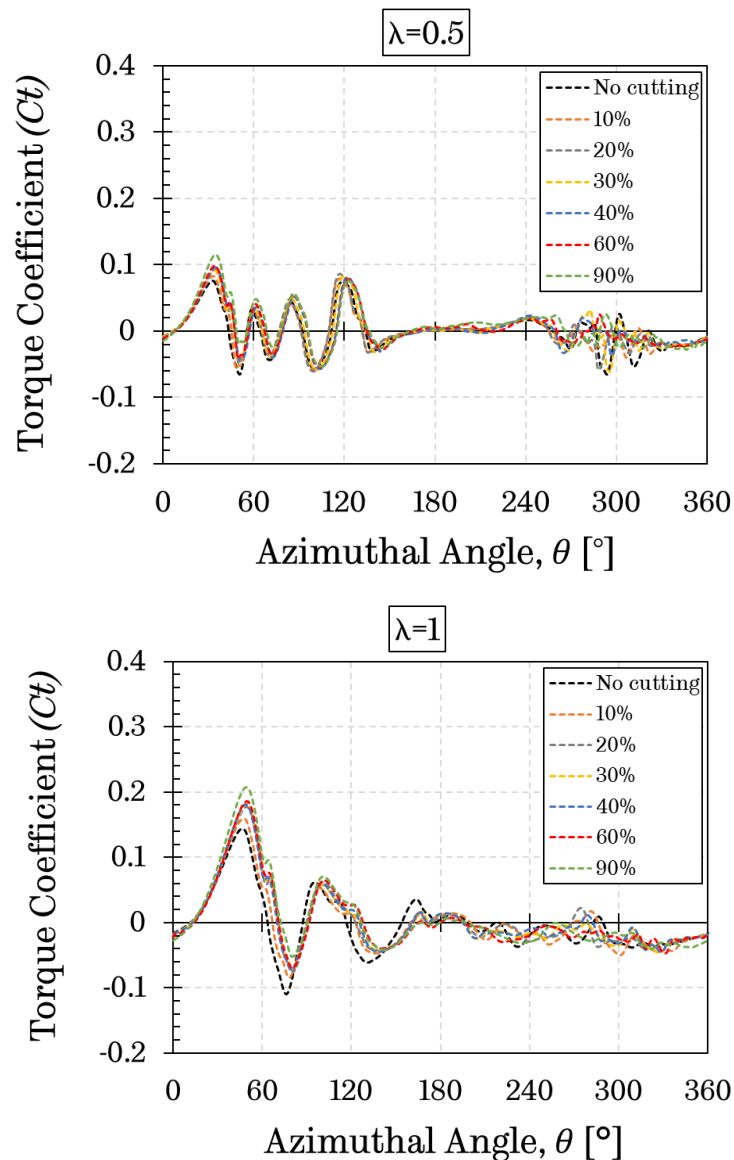
Figure 7.7. The blade instantaneous torque coefficient as a function of the azimuthal angle considering the different opening ratios at λ = 0.5 and λ = 1.

Furthermore, at the relatively high λ region in which $\lambda = 2.5$ and $\lambda = 3.5$ (see Figure 7.6), the J-shaped aerofoil demonstrates different aerodynamic behaviour. At $\lambda = 3.5$, the turbine torque coefficient gradually decreases with the increase in the opening ratios. The results of this investigation show that although the increasing opening ratio increases the possibility of the turbine self-starting, due to the generated high torque at the low tip speed ratios, it may cause a large penalty on the generated torque at the high tip speed ratios. On the other hand, at the optimum tip speed ratio of $\lambda = 2.5$, where the turbine generates a highest torque, the turbine with the J-shaped aerofoil with a 20% opening ratio generates the highest torque coefficient compared to the other cases. The reason behind this situation might be explained by looking at the aerodynamic behaviour of the turbines investigated. Therefore, a comparison between the different opening ratios in terms of the lift and drag coefficients has been presented in Figure 7.8 at the tip speed ratio of $\lambda = 2.5$. As it can be seen in the figure, even though there is no significant difference observed in the downstream part of the turbine, except the 90% opening ratio, the lift coefficient increases with the increase in the opening ratios in the upstream part of the turbine. On the other hand, it is clear that the drag coefficient increases with the increase in the opening ratios in both the upstream and downstream part of the turbine, which causes a significant reduction on the overall performance. The findings observed in this study appear to be consistent with those in Section 6.2.3.2 that have examined the effect of the opening ratios at the tip speed ratio of $\lambda = 2.5$ under the Darrieus motion.
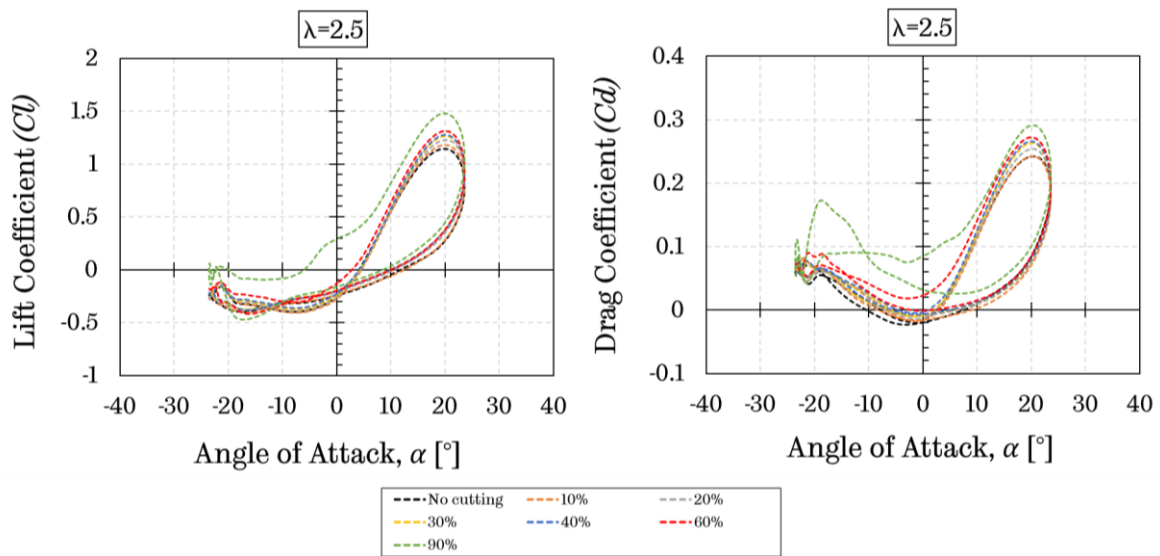
Figure 7.8. The lift and drag coefficient as a function of angle of attack considering the different opening ratios at λ = 2.5.

A further comparison between the J-shaped aerofoil with the original profile and a 20% opening ratio in terms of the lift and drag force coefficients has been presented separately in Figure 7.9 in order to better understand why the turbine with J-shaped aerofoil with a 20% opening ratio produces a higher torque coefficient compared to the original profile. As it can be seen in the figure, although both aerofoils exhibit a similar pattern in the lift coefficient in the downstream part of the turbine, the J-shaped aerofoil with 20% opening ratio generates a greater lift force coefficient than that of the original profile at almost all the angles of attacks in the upstream part of the turbine. On the other hand, regarding the drag force coefficient in the positive angles of attack region, the J-shaped aerofoil procures a higher drag in the region where the angle of attack increases from to 0° to the maximum angle of attack (23.57°) while the original profile generates a higher drag in the region where the angle of attack decreases from the maximum angle of attack (23.57°) to 0°. This leads to a similar drag force generation in the upstream part of the turbine. This is the reason why the turbine with J-shaped profile with a 20% opening ratio produces a slightly higher torque coefficient compared to the original aerofoil profile at the λ = 2.5.
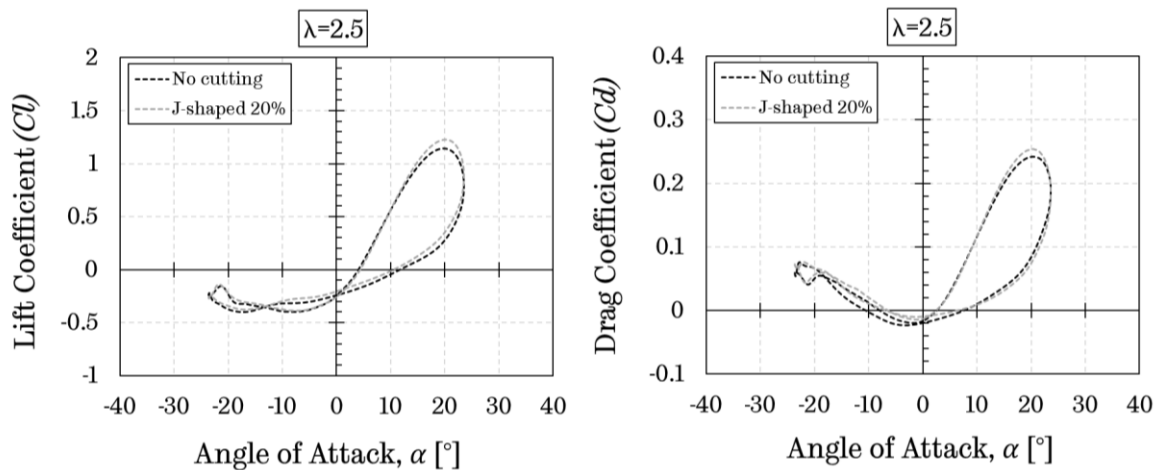
Figure 7.9. Comparison between the J-shaped aerofoil with the original profile (no cutting) and a 20% opening ratio in terms of the lift and drag force coefficients at λ = 2.5.

To further explore the loss of overall performance at the high tip speed ratios when the J-shaped aerofoils are employed, the blade instantaneous torque coefficients as a function of the azimuthal angles for the aerofoils investigated at λ = 2.5 and λ = 3.5 have been illustrated in Figure 7.10. At the tip speed ratio of λ = 2.5, although the magnitude of the instantaneous torque coefficient increases with the increase in the opening ratio in the upstream part of the turbine, the loss of the instantaneous torque coefficient significantly increases along the entire downstream part of the turbine when the opening ratio increases. However, at the tip speed ratio of λ = 3.5, the difference on the instantaneous torque coefficients generated by the aerofoils investigated in the upstream part of the turbine decreased, but the J-shaped aerofoil with a 90% opening still produces a much greater torque coefficient at the azimuthal position between 60° and 150°. Conversely, regarding the downstream part of the turbine, the blade instantaneous torque coefficient significantly decreases with the increase in the opening ratio. Therefore, this is the reason why the turbine with the original aerofoil profile is able to produce a much greater torque at the high tip speed ratio regions.
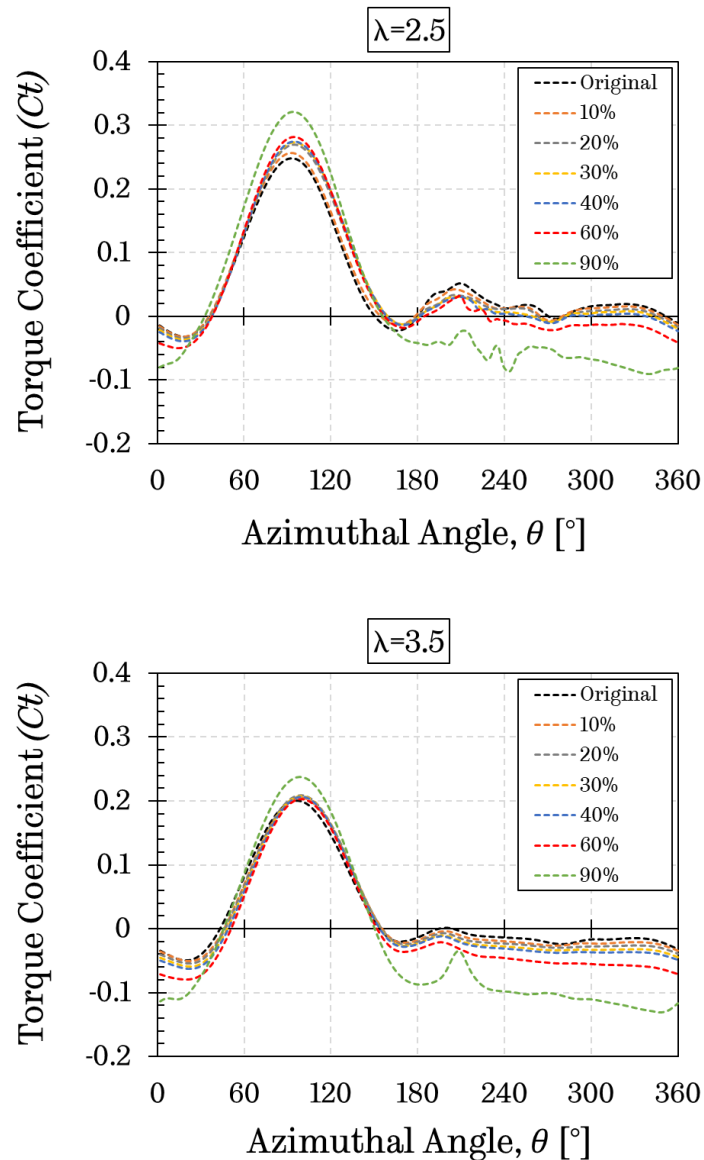
Figure 7.10. The blade instantaneous torque coefficient as a function of the azimuthal angle considering the different opening ratios at λ = 2.5 and λ = 3.5.

7.3.3 The lift and drag of the J-shaped aerofoil with a 90% opening ratio and the original aerofoil

The contribution of the lift and drag coefficients to the turbine torque coefficient for different tip speed ratios, such as 0.5, 1, 2.5, and 3.5, have been analysed. As discuses in Chapter 5, although the H-type VAWTs are known as the lift-driven machines, the drag force might have a positive impact on the turbine

torque generation, at the tip speed ratio less than 1 when it coincides with the rotational direction of the turbine. The J-shaped aerofoil with different opening ratios is expected to contribute more positive drag to the torque generation compared to the original aerofoil profile. Therefore, in the present investigation, the original aerofoil profile (no cutting) and the J-shaped aerofoil with a 90% opening ratio have been selected due to the fact that the difference on the aerodynamic behaviour of these aerofoils is quite distinct.

Figure 7.11 demonstrates the lift and drag force contributions to the torque generation as a function of the azimuthal angles for the original aerofoil profile and the J-shaped aerofoil with a 90% opening ratio at $\lambda = 0.5$ and $\lambda = 1$. At the tip speed ratio of $\lambda = 0.5$, as can be observed in the figure, the turbine is not only driven by the lift force, but the drag force also contributes to the turbine torque generation in some azimuthal angles of the complete revolution, especially between 120° and 240°. In most of the azimuthal angles of the upstream part of the turbine, the positive lift contribution obtained from the J-shaped aerofoil with a 90% opening ratio is more significant than that of the original aerofoil profile, while the region of the positive drag contribution obtained from the J-shaped aerofoil with a 90% opening ratio is higher than that of the original aerofoil profile. This situation leads to a much more positive net torque generation from the turbine with the J-shaped profile with a 90% opening ratio (see Figure 7.6).

The positive contribution of the drag force decreases while the tip speed ratio is approaching to 1. However, at the tip speed ratio of $\lambda = 1$, the J-shaped aerofoil with a 90% opening ratio still produce a higher positive lift force contribution in most of the azimuthal angles compared to the original aerofoil profile, while the negative drag force contributions appear to be similar for both aerofoils. That is the reason why the turbine with the J-shaped aerofoil with a 90% opening ratio generates a higher average turbine torque (see Figure 7.6), which is beneficial to the turbine self-starting capability.
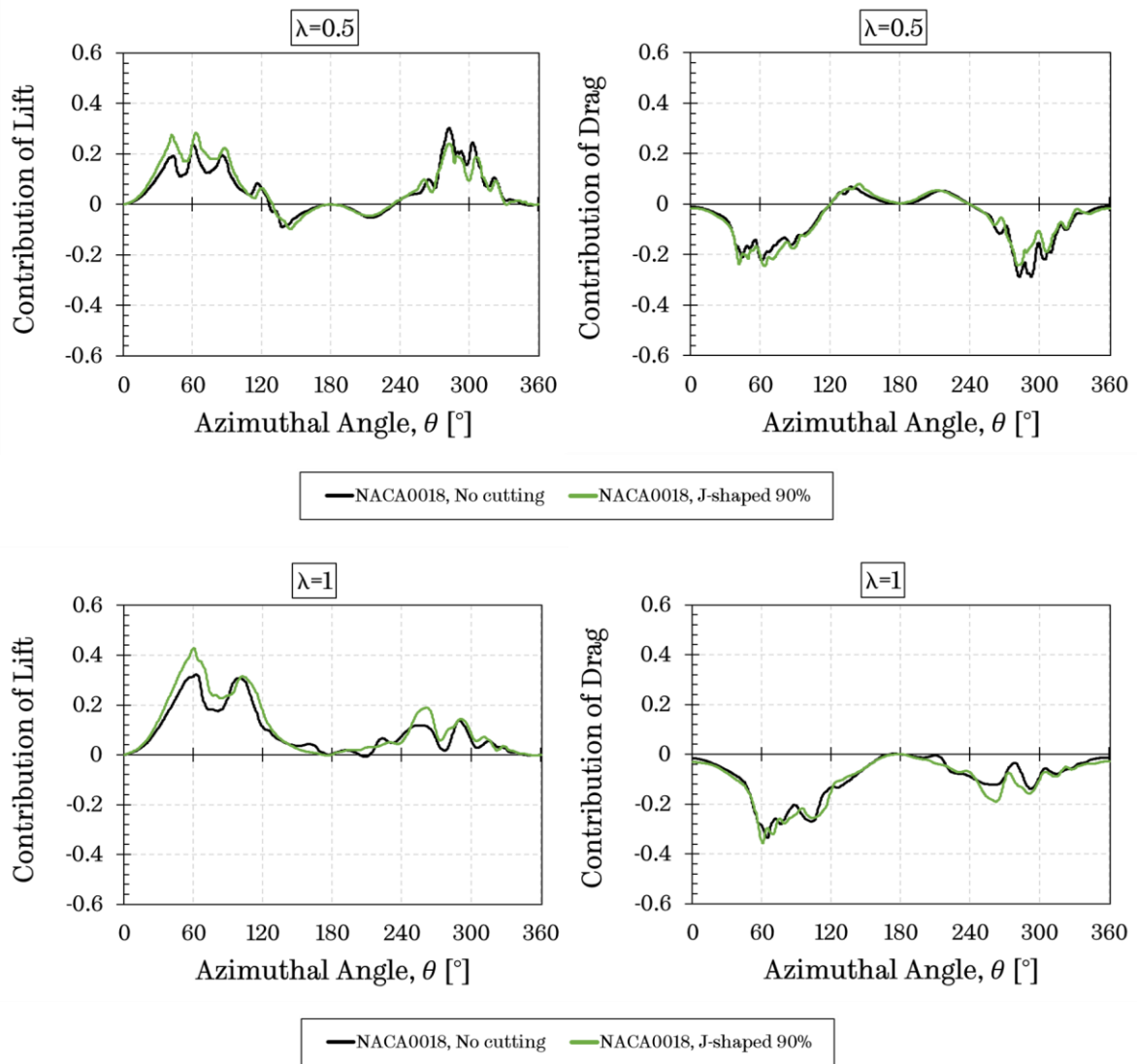
Figure 7.11. The contribution of the lift and drag to the torque generation as a function of blade azimuthal angle for the original aerofoil profile and the J-shaped aerofoil with a 90% opening ratio at λ = 0.5 and λ = 1.

The contributions of the lift and drag forces of the original aerofoil profile and the J-shaped aerofoil with a 90% opening ratio at λ = 2.5 and λ = 3.5 have been plotted in Figure 7.12. As can be observed in the figure, the J-shaped profile with a 90% opening ratio provides a much greater positive lift contribution in the upstream part of the turbine, while the positive lift contribution of the original aerofoil profile is more significant in most of the azimuthal angles of the

downstream part of the turbine at both tip speed ratios. In addition, regarding the negative drag contribution, the J-shaped aerofoil with a 90% opening ratio always produces a much greater negative drag contribution to the torque generation at both tip speed ratios. This situation results in a lower overall performance of the turbine with the J-shaped aerofoil with a 90% opening ratio compared to the original aerofoil profile at high tip speed ratios.
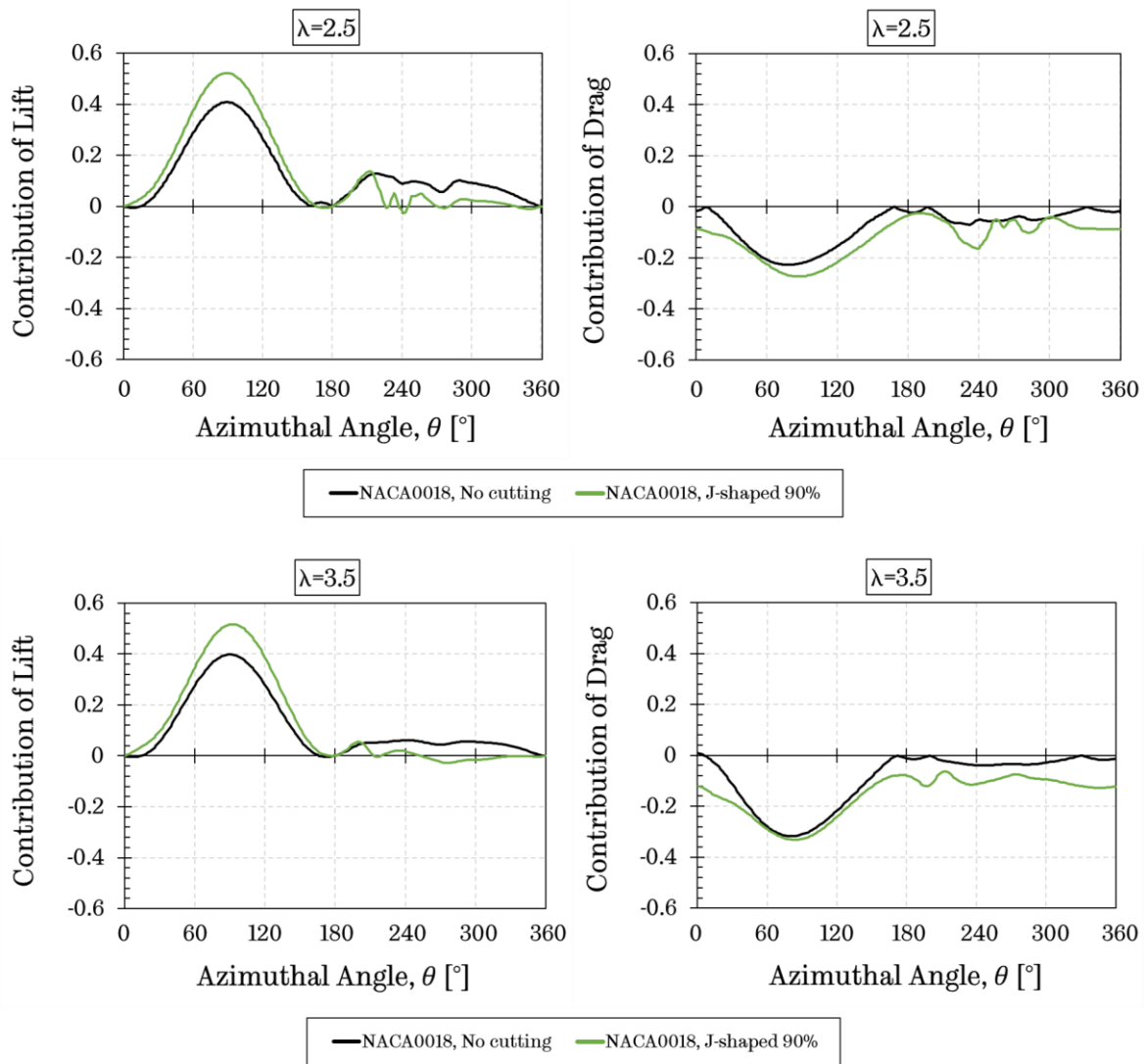
Figure 7.12. The contribution of the lift and drag to the torque generation as a function of blade azimuthal angle for the original aerofoil profile and the J-shaped aerofoil with a 90% opening ratio at λ = 2.5 and λ = 3.5.

7.4   The influence of the aerofoil profile on the turbine self-starting

According to the review of the literature conducted in Chapter 2, four typical aerofoils generally used for H-type VAWT and their J-shaped profiles with different opening ratios have been investigated and compared in terms of the dynamic start-up behaviour in this chapter. The aerofoil profiles investigated are as follows:

- NACA0012 and NACA0018 are the typical symmetrical NACA00xx series aerofoils and most widely used profiles for the H-type VAWT applications [182, 184, 185]. The purpose of choosing these two different profiles is to observe the effect of the aerofoil thickness with and without openings on the turbine self-starting behaviour.

- NACA2518 and NACA4518 are the cambered series of the NACA0018 aerofoil, which have the maximum camber of 2% and 4%, respectively, at 50% of the chord. As suggested by Kirke and Lazauskas [186] the cambered aerofoils may be able to demonstrate a better turbine performance, especially during the start-up period.

- Additionally, in order to fully investigate the influence of the cambered aerofoils on the turbine self-starting, the reversed version of these cambered aerofoils have been employed to the turbine blades considering the different opening ratios.

All investigations and comparisons have been performed by using the selected aerofoils with no cutting, 30%, 60%, and 90% opening ratios applied to the aerofoil's outer surface. Additionally, the concave side is the outer side of the NACA2518 and NACA4518, while that of the inner side for their reversed versions. The rotor radius and chord length have been chosen as $R = 0.375m$ and $c = 0.083m$, respectively, and the upstream free wind speed was $V_\infty = 5m/s$.

Figure 7.13 (a) shows the tip speed ratio as a function of the time for the thinner aerofoil NACA0012 considering the different opening ratios. As can be

seen in the figure, NACA0012 aerofoil with no cutting, 30%, and 60% opening ratios have given the worse self-starting performance; only the aerofoil with the highest opening ratio, OR = 90%, tested is able to escape the plateau stage and reach the final steady-state condition. Furthermore, the NACA0018 J-shaped profile with the 30%, 60%, and 90% opening ratios demonstrate fully self-start characteristics. Although the start-up time decreases with the increase in the opening ratio, the final tip speed ratio in the steady-state condition decreases with the increase in the opening ratio (see Figure 7.13 (b)). The findings reveal that the thicker aerofoil NACA0018 with even a shorter opening ratio, such as 30%, is able to self-start compared to the relatively thinner aerofoil NACA0012. It is also important to note that even though NACA0012 J-shaped aerofoil with a 90% opening ratio demonstrates a slower start-up characteristic compared to the NACA0018 aerofoil with a 90% opening ratio, its final tip speed ratio in the steady-state condition is much greater than that of the NACA0018 aerofoil. Nevertheless, the results indicate that the blade operating with the thicker aerofoil provides a much better self-starting characteristic with a wider range of the opening ratio at a tested wind speed of $5 m/s$.
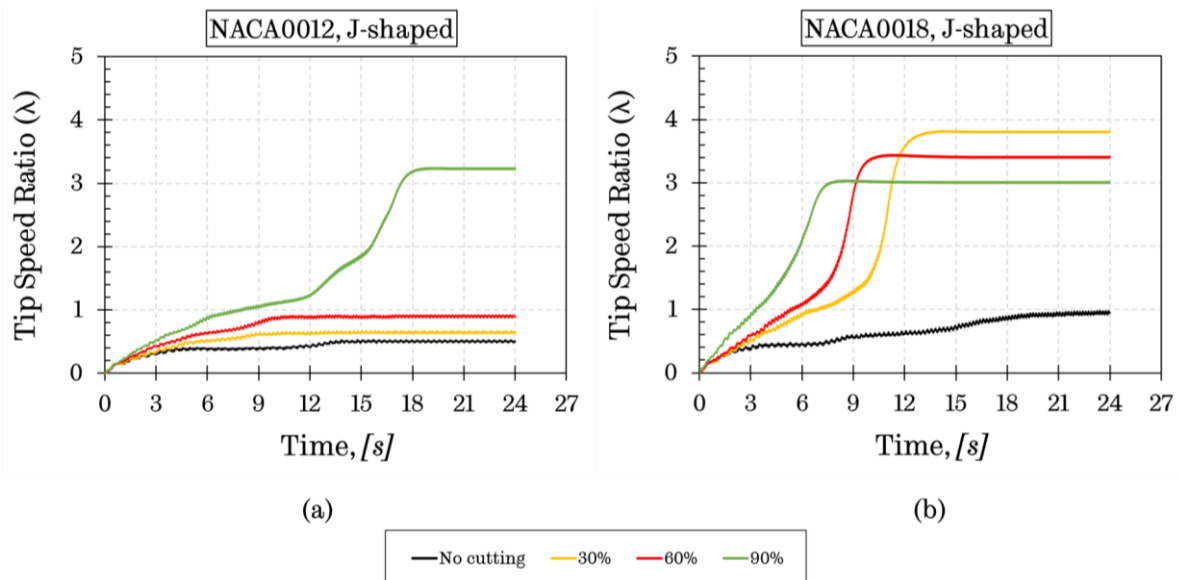
Figure 7. 13. The tip speed ratio as a function of the time for NACA0012, NACA0018 and their J-shaped aerofoils considering different opening ratios.

Figure 7.14 shows the tip speed ratio as a function of the time for the cambered aerofoil NACA2518 and its reversed version considering the different opening ratios. Figure 7.14(a) illustrates the turbine with NACA2518 J-shaped profile with 60% and 90% opening ratios can self-start but the turbine with NACA2518 J-shaped profile with no cutting and 30% opening ratio fails to self-start. Furthermore, regarding its reversed version, the turbine with NACA2518 reversed aerofoil has also the self-starting capability even with a 30% opening ratio (see Figure 7.14 (b)). With regards to the turbine's final tip speed ratio in the steady-state condition, the turbine with original NACA2518 and its reversed version having the opening ratio of 60% and 90% reach the steady-state condition at almost the same final tip speed ratios. However, although the start-up time of the turbine with NACA2518 reversed with a 90% opening ratio is much longer than that of the original NACA2518, NACA2518 reversed aerofoil has a higher final tip speed ratio.
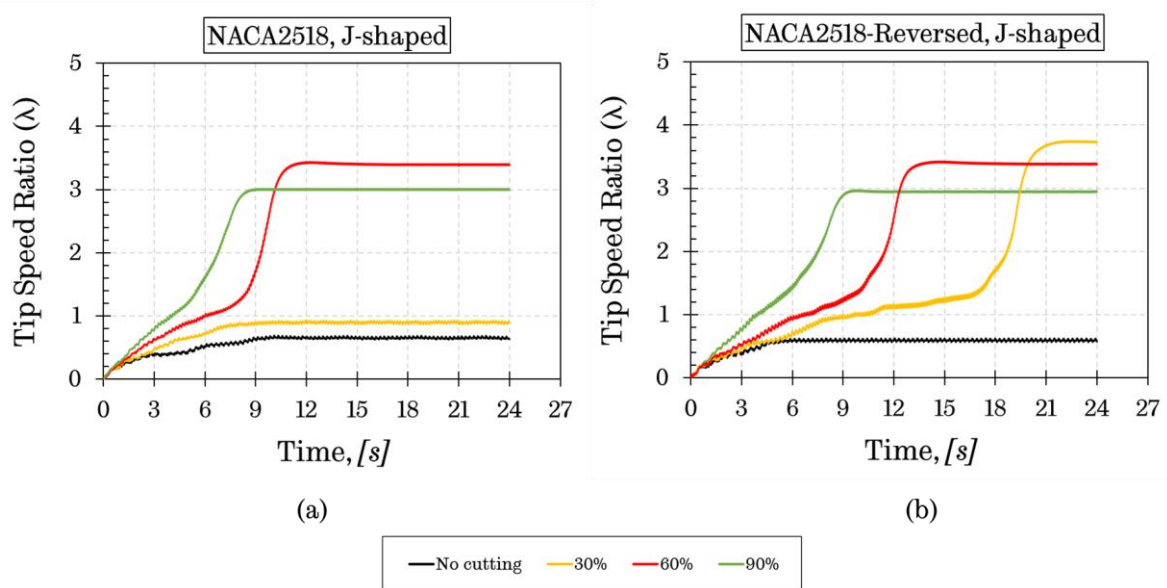
Figure 7.14. The tip speed ratio as a function of the time for NACA2518, NACA2518-reversed and their J-shaped aerofoils considering different opening ratios.

Finally, the relatively high cambered aerofoil NACA4518 and its reversed version have been investigated and compared in Figure 7.15. As it can be seen in Figure 7.15 (a), the use of the highly cambered aerofoil NACA4518 with the different values of the opening ratios, does not exhibit a remarkable self-starting characteristic, except the highest opening ratio, 90%, compared to the other opening ratios. On the other hand, its reversed version with 60% and 90% opening ratios are still able to escape the plateau stage and reach to their steady-state conditions (see Figure 7.15 (b)).
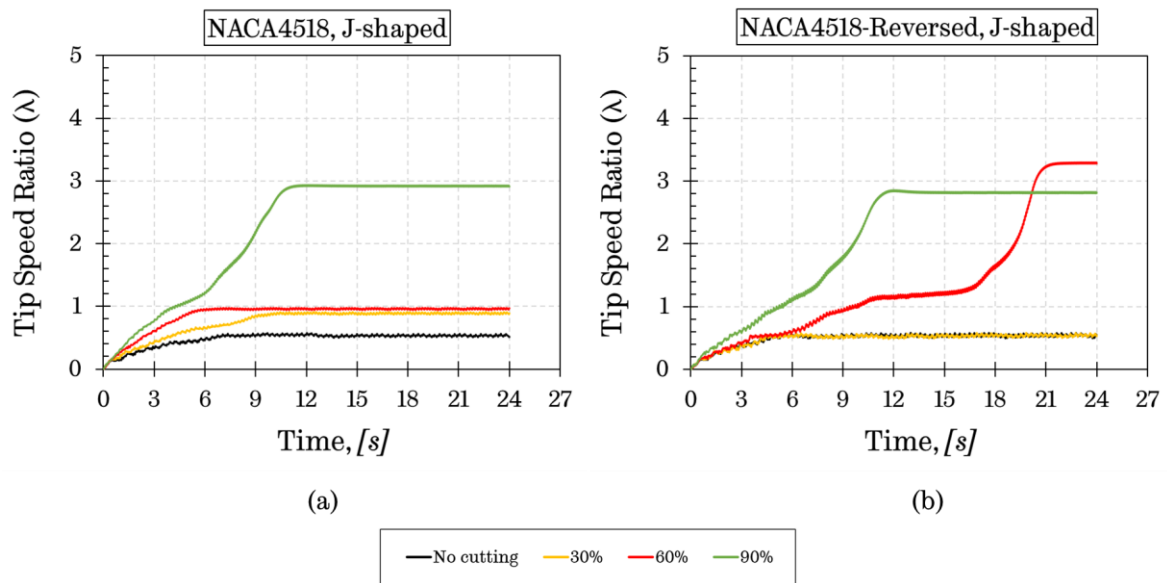
Figure 7.15. The tip speed ratio as a function of the time for NACA4518, NACA4518-reversed and their J-shaped aerofoils considering different opening ratios.
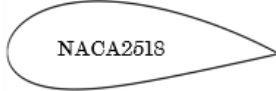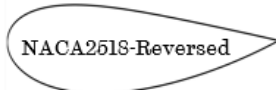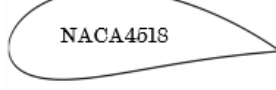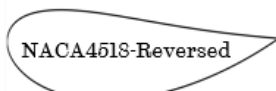
In conclusion, the results obtained from the analyses of the effect of the aerofoil profile with and without an opening on the turbine dynamic start-up behaviour are summarised in Table 7.1. As it can be seen in the table, NACA0012, NACA4518 and their J-shaped profiles do not appear to bring a significant benefit compared to the NACA0018 aerofoil and its J-shaped profiles. The results of this investigation also show that the turbine with all the aerofoil profiles investigated with a 90% opening ratio can escape the plateau stage and reach its

steady-state condition; however, the original aerofoils, which have no cutting on the surface, cannot self-start at the tested upstream wind speed of $5m/s$.

The findings of the current study also suggest that even though the thinner aerofoil NACA0012 can exhibit a higher final tip speed ratio at the steady-state condition when a 30% opening ratio is applied, the thicker aerofoil NACA0018 provides a better self-starting characteristic with a wider range of the opening ratio compared to the thinner aerofoil NACA0012. These results are consistent with those of the other studies and suggest that the thicker aerofoils are able to enhance the turbine performance, in particular at the low λ values, which may lead to improve the self-starting capability [123, 128, 182].

The most obvious finding to emerge from this study was that the reversed versions of the cambered aerofoils investigated demonstrate a better self-starting capability compared to their original profiles. However, in comparison with the thicker aerofoil NACA0018 and its J-shaped profiles, the original and reversed cambered aerofoils do not show any improvement on the self-starting capability in terms of the start-up time and final tip speed ratio. An opposite conclusion to that drawn by Kirke and Lazauskas [186] has been obtained in the current study, who claimed that the turbine with the cambered blade can self-start easily according to their calculations based on the Blade Element Momentum (BEM) studies. The reason for the discrepancy between the current findings and that of by Kirke and Lazauskas [186] may be due to the fact that the lack of the high quality of the aerodynamic data could have had an effect on their findings since the BEM model is highly depended on the quality of the input aerodynamic force coefficients, such as lift and drag coefficients.

Table 7.1. The comparison of the self-starting capabilities of the aerofoils investigated in terms of the self-starting time and final tip speed ratio.

	Self-starting capability				Self-starting time (s)				Final λ			
	0%	30%	60%	90%	0%	30%	60%	90%	0%	30%	60%	90%
NACA0012	NO	NO	NO	YES	—	—	—	19.7	—	—	—	3.23
NACA0018	NO	YES	YES	YES	—	15.2	12.2	9.2	—	3.81	3.41	2.99
NACA2518	NO	NO	YES	YES	—	—	14.6	10.4	—	—	3.38	2.99
NACA2518-Reversed	NO	YES	YES	YES	—	23.4	16.02	12.03	—	3.73	3.37	2.95
NACA4518	NO	NO	NO	YES	—	—	—	12.55	—	—	—	2.91
NACA4518-Reversed	NO	NO	YES	YES	—	—	22.9	13.78	—	—	2.28	2.81

7.5   Turbine self-starting performance with different pitch angles

The active pitch control mechanism can enable the turbine blades to produce the optimum torque at the low tip speed ratio regions, which results in a better turbine power output and self-starting ability [187]. However, due to the fact that

the small-scale H-type VAWT has been considered in the present study, the active pitch control mechanism is not taken into account due to its complexity and economically unviable. Instead of the active pitch control, another alternative way to change the aerodynamics of the blades during a complete revolution by using the fixed pitch angles will be investigated numerically in order to observe the influence of fixed pitch angle on the turbine dynamic start-up behaviour.

The numerical investigations have been performed at the seven values of the fixed pitch angles, which are -8°, -4°, -2°, 0° (no pitch), 2°, 4° and 8°, and the definition of the pitch angle for the current investigation is shown in Figure 7.16. However, a detailed explanation of the pitch angle applied to the present thesis can be found in Section 2.2.3. The aerofoil profiles used in the present study are the conventional aerofoil NACA0018 and its J-shaped profiles with 30%, 60%, and 90% opening ratios with a rotor radius $R = 0.375m$ and blade chord length $c = 0.083m$. The upstream free wind speed was $V_\infty = 5m/s$. s
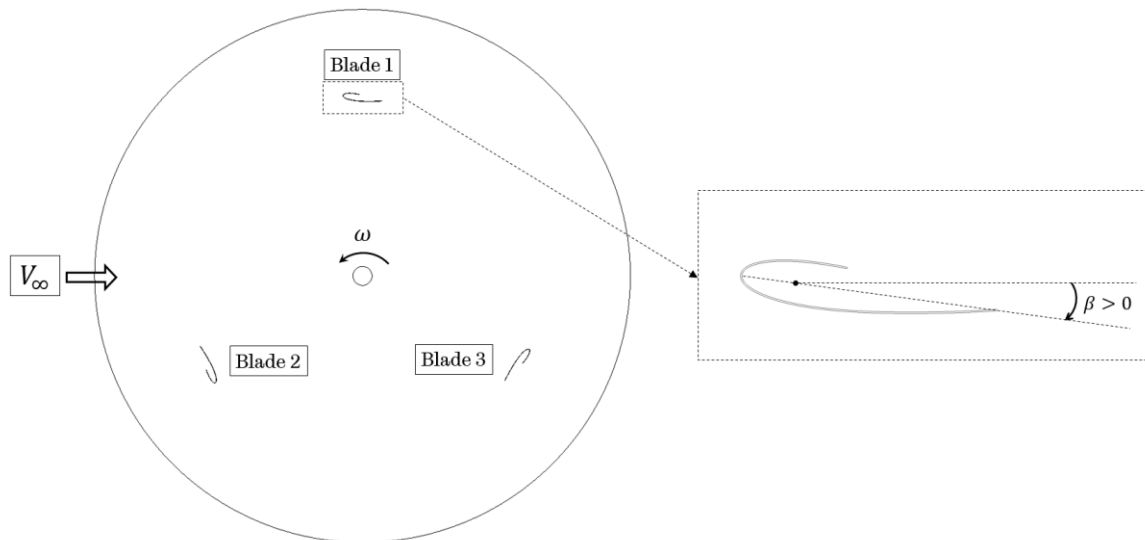
Figure 7.16. The definition of the pitch angle used in this thesis.

Figure 7.17 presents the tip speed ratio as a function of the time for the different values of the fixed pitch angles considering the conventional aerofoil NACA0018 and its J-shaped profiles with 30%, 60%, and 90% opening ratios.

Figure 7.17 (a) shows the effect of the different values of the fixed pitch angles on the turbine self-starting behaviour using the conventional aerofoil NACA0018. As it can be seen in the figure that the conventional aerofoil with all the fixed pitch angles investigated cannot assist the turbine to self-start and the value of the final tip speed ratio reduces with the most negative value of the pitch angle. At the opening ratio, $OR = 30\%$, (see Figure 7.17 (b)), the turbine with the blade pitch angles of $\beta = 2°$ and $\beta = 4°$ improve the turbine self-starting performance in terms of the turbine start-up time compared to pitch angle of $\beta = 0°$. However, the results reveal that a positively further increase in the pitch angle does not help the turbine to self-start if the 30% opening ratio is employed. Moreover, regarding the negative pitch angles, the self-starting behaviour is getting worse with all the negative pitch angles investigated. Concerning the J-shaped profile with 60% opening ratio (see Figure 7.17 (c)), the positive pitched blades are able to enhance the turbine self-starting capability compared to the negative pitched blades. In addition to this, although the turbine with the blade pitch angles of $\beta = 2°$ and $\beta = 4°$ reaches the steady-state condition at almost the same final tip speed ratio as the blade without a pitch angle, the blade with the blade pitch angles of $\beta = 4°$ shows a faster start-up time. However, the turbine with the most positive pitch angle ($\beta = 8°$) significantly degrades the turbine final tip speed ratio. At the opening ratio, $OR = 90\%$, the advantages and disadvantages of the pitch angle become much more obvious. As it can be seen in Figure 7.17 (d), the turbine self-starting time decreases with the changing the blade pitch angle from $\beta = 2°$ to $\beta = 8°$. Unlike the effect of the negative pitched angles on the turbine self-starting behaviour with 30% and 60% opening ratios, by employing a slightly negative pitched blade of $\beta = -2°$ also shows an improved self-starting performance in terms of the final tip speed ratio at the steady-state condition. However, with this slightly negative pitch angle, the turbine self-starts much later and a much slower turbine acceleration can be observed during the plateau stage.
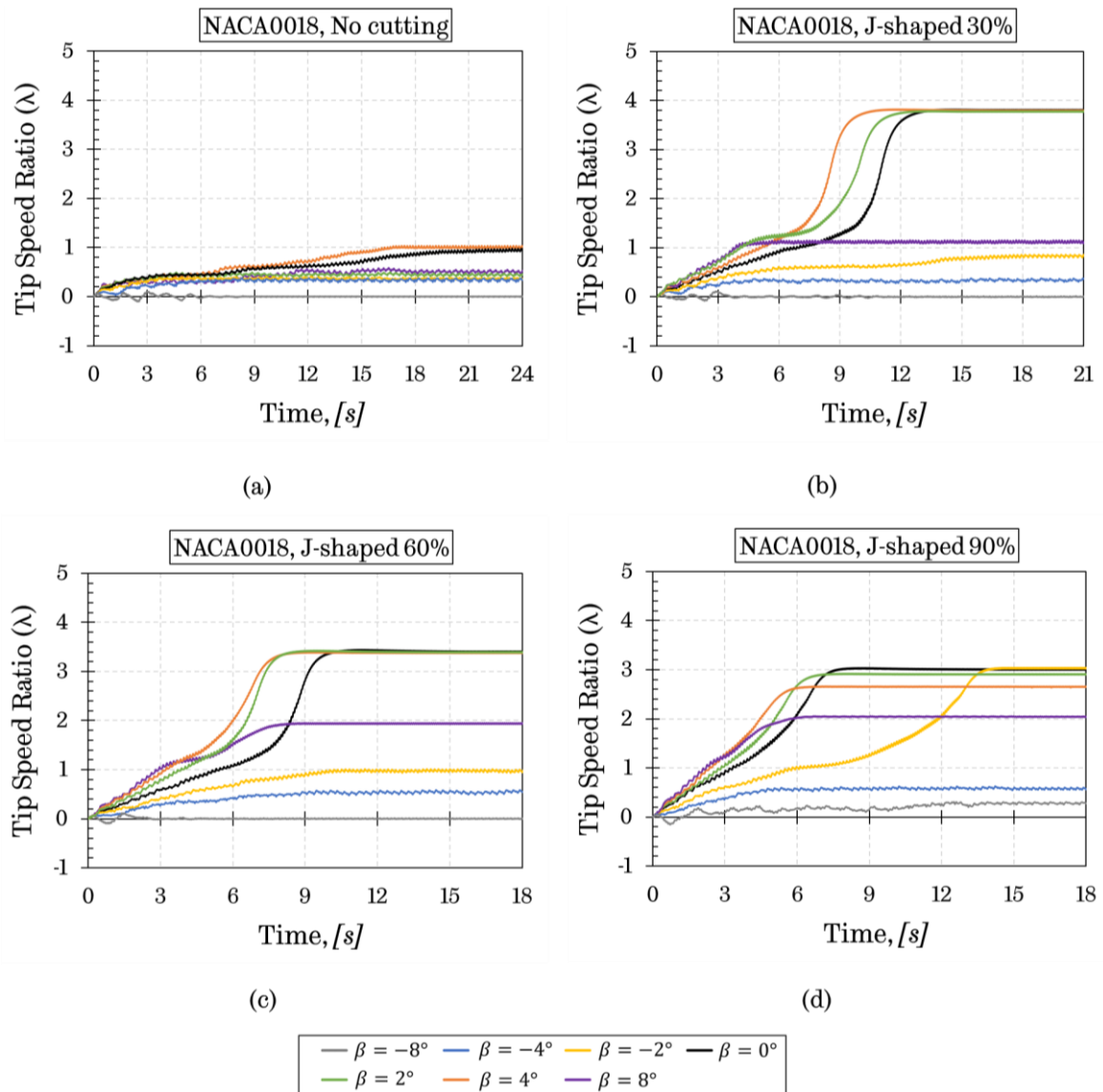
Figure 7.17. The tip speed ratio as a function of the time for the different values of the fixed-pitch angles considering the conventional aerofoil NACA0018 and its J-shaped profiles with 30%, 60%, and 90% opening ratios.

A further study has been conducted by looking at the blade instantaneous torque generation under the different pitch angles using the J-shaped aerofoil with 90% and 60% opening ratios at the tip speed ratio of $\lambda = 1.6$ and $\lambda = 3.38$, respectively. For the J-shaped aerofoil with a 90% opening ratio at $\lambda = 1.6$ (Figure 7.18), where the blade still experiences the dynamic stall, the peak torque coefficients for $\beta = 8°$, $\beta = 4°$, $\beta = 2°$, $\beta = 0°$, and $\beta = -2°$ have been obtained at

$\theta = 89.4°$, $\theta = 85.8°$, $\theta = 82.4°$, $\theta = 78°$, and $\theta = 75.7°$, respectively. The positive pitch angles successfully delay the stall and enable the blade to produce more torque for a greater portion of the azimuthal angle. However, the blade performance in the downstream part of the turbine significantly decreases by the large positive pitch angle. The pitch angle of $\beta = 8°$ produces a negative torque in the azimuthal angles between $\theta = 200°$ and $\theta = 360°$, which offsets the positive contribution of the blade in the upstream part of the turbine and may lead to lower torque generation at all the start-up stages. With regards to the negative pitch angle $\beta = -2°$, the stall occurs earlier than $\beta = 0°$ at $\theta = 75.7°$ as shown in Figure 7.18. Although the negative pitch angle yields better blade performance in the downstream part of the turbine, the much deteriorated torque generation has been obtained in the upstream part, which may result in a much slower turbine acceleration during the plateau stage (see Figure 7.17 (d)).
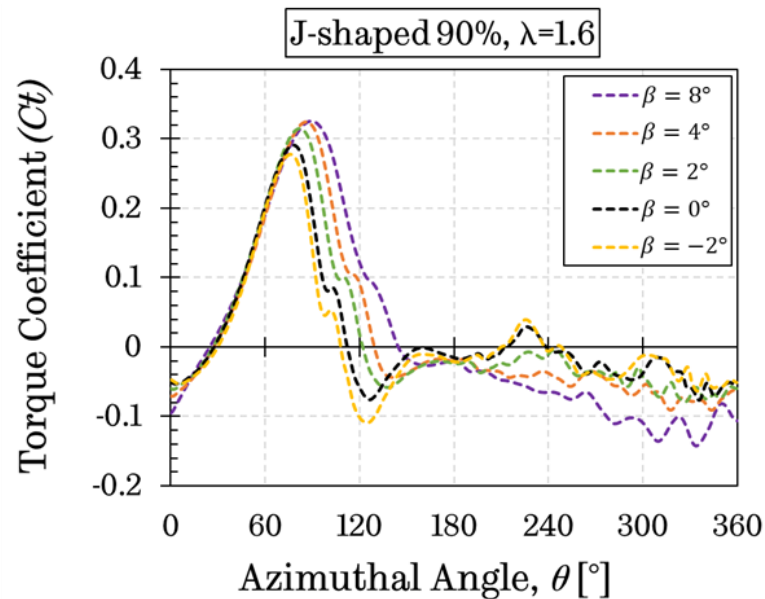
Figure 7.18. The blade instantaneous torque generation under the different pitch angles using the J-shaped aerofoil with 90% opening ratio at the tip speed ratio of $\lambda = 1.6$.

Furthermore, Figure 7.19 illustrates the instantaneous torque coefficient for the J-shaped aerofoil with a 60% opening ratio at $\lambda = 3.38$, where the blade no longer experiences stall. Compared to $\beta = 0°$, the positive pitch angle, such as

$\beta = 2°$ or $\beta = 4°$, increases the blade performance in the downstream part of the turbine; however, overall torque coefficients are almost the same due to the reduced performance in the upstream part of the turbine. Therefore, the turbine with $\beta = 4°, 2°,$ and $0°$ reaches the steady-state condition at almost the same final tip speed ratio (see Figure 7.17 (c)).
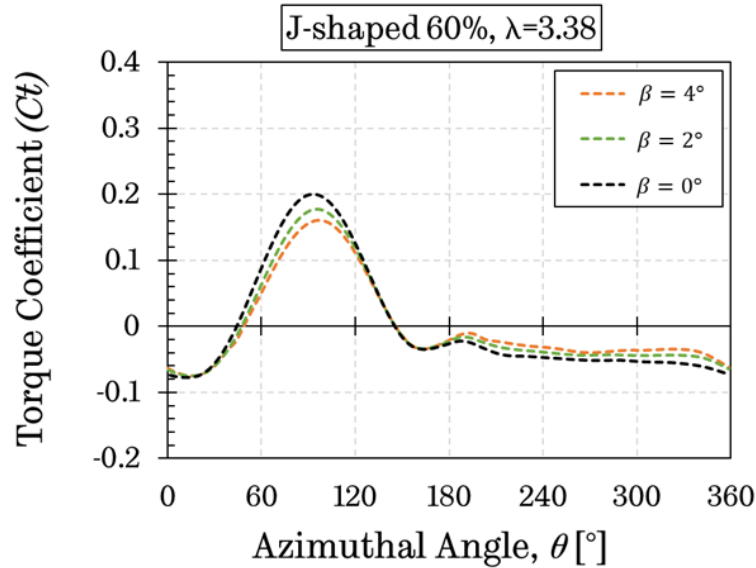
Figure 7.19. The blade instantaneous torque generation under the different pitch angles using the J-shaped aerofoil with 60% opening ratio at the tip speed ratio of $\lambda = 3.38$.

Since the majority portion of the torque is produced by the blade in the upstream part of the turbine, a positive pitched blade can delay the blade stall and assist the blade generates more torque over a greater portion of the upstream part of the turbine at the low λ values. This delayed stall is responsible for the improved turbine performance measured at the low λ values, which might be beneficial for the turbine to enhance the self-starting capability. However, the highly negative torque generation in the downstream part of the turbine may provide a negative contribution to the overall torque generation, which is not desirable for the turbine self-starting (e.g. $\beta = 8°$). With the increase in the tip speed ratio, the blade angle of attack variation is significantly reduced and above a critical tip speed ratio, the blade no longer experiences stall during

the complete turbine revolution. In terms of the relatively high tip speed ratios, a positive pitch angle decreases the blade angle of attack in the upstream region resulting in less torque produced. On the contrary, this positive pitch angle also increases the blade angle of attack in the downstream part of the turbine; therefore, the blade is able to capture the high possibility of the torque generated compared to the blade with no pitch.

In a conclusion, the findings in this section reveal that the pitch angle has a different effect depending on the J-shaped aerofoil with the different value of the opening ratios. Although the pitched J-shaped aerofoil has mixed effects on the turbine performance in different tip speed ratios, the J-shaped turbine with a slightly positive pitched blade ($\beta = 2°$) clearly illustrates a better start-up time in all cases investigated and a similar final tip speed ratio value at the steady-state condition compared to the $\beta = 0°$. On the contrary, the negative pitch angles do not bring any benefits with the J-shaped aerofoil, except the turbine with 90% opening ratio J-shaped aerofoil with a slightly negative pitch angle ($\beta = -2°$). In addition, a too large negative pitch angle, such as $\beta = -4°$ and $\beta = -8°$, prevents the turbine from self-starting in all the cases investigated.

7.6   The effect of mechanical resistance on the turbine start-up

The starting capability of an H-type VAWT (or rotor acceleration, a) can be mathematically expressed as follows;

$$a = \frac{T_w - T_{res}}{I}$$

(7.1)

where T_w is the aerodynamic torque generated by the wind turbine, T_{res} is the resistive torque generated by other components, such as the generator and the bearing system, and I is the turbine moment of inertia.

The equation shows that the acceleration can be improved by increasing the aerodynamic torque and decreasing the turbine moment of inertia with a constant resistive torque. In the previous sections, it has been proved that the

turbine with a J-shaped profile is able to enhance the aerodynamic torque generation, especially in the low tip speed ratios. However, it would have been more interesting and appropriate if the resistance had been implemented in the calculations. Therefore, the purpose of the current study is to determine the effect of the J-shaped profile with the different numbers of the opening ratios on the turbine dynamic start-up behaviour by considering the resistance in the calculations. In order to do this, similar to Chapter 4 and Chapter 5, a new UDF code, which includes the physical characteristics of the turbine, its moment of the inertia, and the resistance, has been written in the C language and implemented into the ANSYS Fluent solver under the dynamic mesh zone section. The details of the UDF code have been provided in the Appendix.

In the previous sections, the effect of the J-shaped aerofoil with different numbers of the opening ratio on the starting performance has been investigated based on the aerodynamic torque generated by the turbine tested. However, it is worth estimating and implementing the resistive torque, such as the bearing friction, to the current investigation in order to increase the quality and reliability of the influence of the J-shaped aerofoils on the turbine dynamic start-up behaviour. In order to do this, as discussed in Section 5.5, due to the lack of the information provided for the turbine, which has been selected according to the well-referenced configuration published by Rainbird [137], a bearing frictional coefficient of a typical bearing system that is generally employed to the vertical axis wind turbines has been considered in the present study. A detailed discussion on how the bearing frictional coefficient has been selected can be found in Section 5.5.

Figure 7.20 shows the tip speed ratio as a function of the time for the J-shaped aerofoil with a different number of the opening ratios considering the bearing frictional coefficient of $C_{fr} = 0.002$. The results obtained from this study indicate that when the bearing frictional coefficient is applied to the turbine, the J-shaped aerofoil turbine with 40%, 60%, and 90% opening ratios can still self-start;

however, the turbine with the opening ratios of 20% and 30% failed to self-start. As found in the Section 7.3.1, with the increase in the opening ratio, which is located at the outer surface of the aerofoil, the start-up time reduces while the final tip speed ratio decreases for the turbines that show the self-starting characteristic (e.g. the turbine with a J-shaped profile with 40%, 60%, and 90% opening ratios).
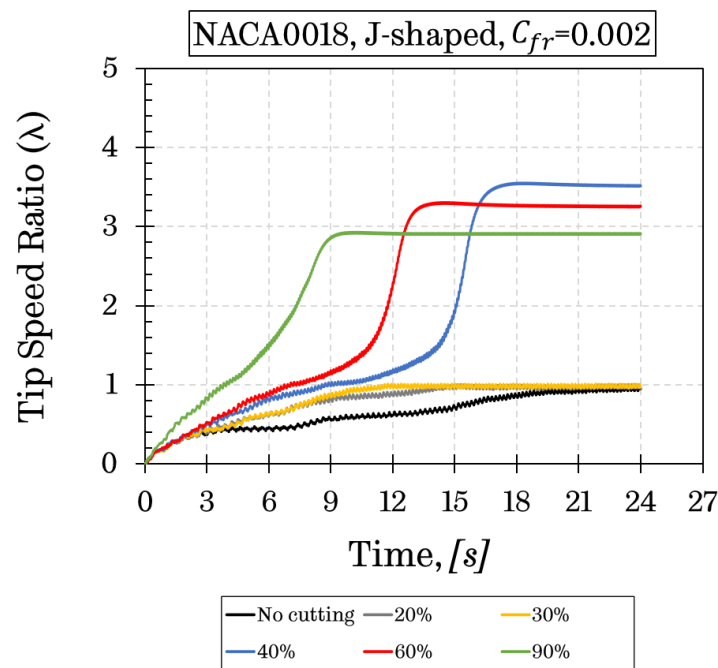
Figure 7.20. The tip speed ratio as a function of the time for the turbine with J-shaped aerofoils with a different number of opening ratios considering the bearing frictional coefficient of $C_{fr} = 0.002$.

Furthermore, a comparison between the J-shaped aerofoil turbine with and without the resistance in terms of the start-up time and final tip speed ratios has been illustrated in Figure 7.21. In this figure, the turbine with the opening ratios of 20% and 30% is not presented since they are not showing the self-starting characteristics. The figure demonstrates that the J-shaped turbine with resistance increases the start-up time while the final tip speed ratio in the steady-state condition decreases in all the opening ratios, which provide a self-starting

characteristic in both cases investigated. However, the discrepancy between the
J-shaped turbines with and without resistance decreases with the increase in the
opening ratio in terms of the start-up time and final tip speed ratio.
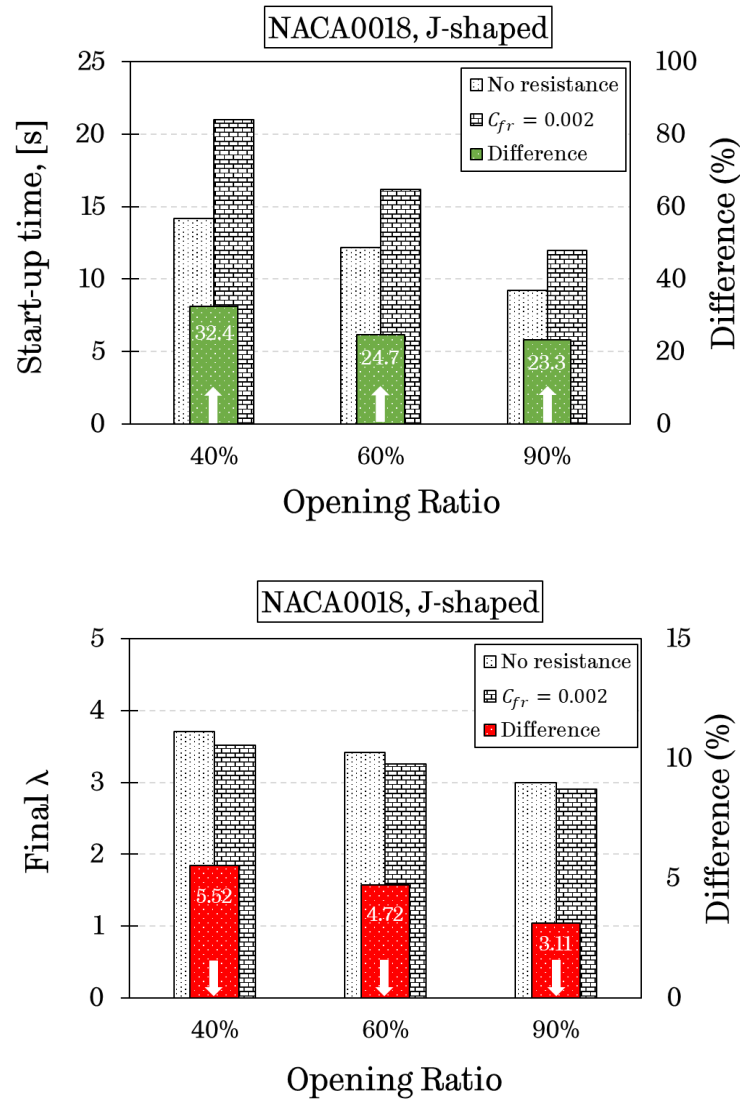
Figure 7.21. The comparison between the J-shaped aerofoil turbine with and without
resistance in terms of the start-up time and final tip speed ratios.

The investigations presented here strongly indicates that when a real-
situation based resistance is applied to the turbine with a J-shaped aerofoil
having different opening ratios, the range of the opening ratios, which enhances
the self-starting capability of the turbine, can be narrowed. For example,

although the J-shaped profile with a range of opening ratios between 20% and 90% can easily self-start the turbine without taking into account the resistance when the resistance is applied to the turbine, this range has been found to be between 40% and 90%. These findings provide a very important insight into advancing the knowledge of how the turbine with the J-shaped aerofoil having different numbers of the opening ratios affects the turbine dynamic start-up behaviour when considering the resistance.

7.7   Conclusion

A three bladed H-type VAWT with original aerofoils and their J-shaped profiles having a different number of the opening ratios have been investigated in this study in order to evaluate the effect of an aerofoil with and without openings on the surface in terms of the torque generation at low and high tip speed ratios and the dynamic start-up behaviour. In order to fill the gaps in the literature, this study has focused on the self-starting capability and the overall performance of the turbine with the J-shaped profiles, which have not been extensively studied in the past.

According to the numerical results obtained in the current study, several important conclusions can be drawn:

- The investigations presented here strongly recommended that although the torque coefficient versus tip speed ratio curve is able to provide an indication of the self-starting performance according to the torque generation at the low tip speed ratios, a further analysis, namely the turbine dynamic start-up curve, is required in order to fully understand the self-starting behaviour of the J-shaped aerofoils.

- The turbine with the J-shaped aerofoil having the openings located at the inner surface does not appear to bring any benefit and makes the choice of the inner profiles unreasonable compared with the outer surface.

- The effect of the J-shaped aerofoil with different opening ratios, which are located at the outer surface, may differ depending on the tip speed ratio. For instance, the largest opening ratio, which is the 90% in the present study, has a better performance at the low tip speed ratios, while the original aerofoil profile (no cutting) has the better performance at the higher tip speed ratio. Therefore, the selection of the optimum opening ratio completely depends on the purpose of the turbine. If a good self-starting performance is required, then the largest opening ratio should be preferred but there is a larger penalty at the higher tip speed ratios and this must be considered.

- The turbine with the original aerofoil profile and the J-shaped aerofoil with a 10% opening ratio is not able to accelerate and escape the plateau stage due to the negative torque generation at the critical range of the tip speed ratio (e.g. $0.5 < \lambda < 1.5$).

- Among the six different aerofoil profiles that have been investigated, the worst self-starting performance has been obtained by the thinner aerofoil NACA0012 and the highly cambered aerofoil NACA4518. However, the thicker aerofoil NACA0018 and cambered NACA218-reversed have been demonstrated to be a good choice for the H-type VAWT in terms of the self-starting characteristics. In addition, the reversed version of the cambered aerofoils investigated demonstrate a better self-starting capability compared to their original profiles.

- The turbine with the J-shaped aerofoil having a slightly positive pitch angle ($\beta = 2°$) clearly illustrates a better start-up capability in all cases investigated and a similar final tip speed ratio value at the steady-state condition compared to the $\beta = 0°$. However, the negative pitch angles do not bring any benefits to the H-type VAWT with the J-shaped aerofoil.

- This study has demonstrated, for the first time, that the turbine with and without resistance can reveal a different range of the opening ratios that enables the turbine to self-start. At first, a typical range of the bearing frictional coefficient (C_{fr}) starts from 0.0015 to 0.002 has been analysed in Chapter 5, and according to the real-situation-based value, $C_{fr} = 0.002$ has been selected for the

further investigations of the turbine having J-shaped aerofoil. Then, it has been found that although the J-shaped profile with a range of the opening ratios between 20% and 90% can easily self-start the turbine without taking into account the resistance. When the resistance is applied to the turbine, this range has been found to be between 40% and 90%. Therefore, the current findings shed much light on future studies related to the turbine with the J-shaped aerofoils.

Chapter 8

Novel hybrid blade design and its impact on turbine performance

8.1 Introduction

As discussed in Section 2.3.2, a wide range of solution strategies to overcome the self-starting problem of the H-type VAWTs have been employed. Among the several possible solutions, the Hybrid Darrieus and Savonius VAWT design appears to be one of the promising solutions, which combines a main lift-based Darrieus rotor and a smaller drag-based Savonius device to assist self-starting. However, the Hybrid VAWT design also has several challenges, such as new forms of the vortex shedding leading to high losses, the complexity of the system design increasing the costs, etc. Therefore, it is postulated that another method, which is called the Hybrid Blade design, would be an alternative solution to enhance the self-starting capability of the lift-based H-type VAWTs. As shown in Chapter 7, even though the turbine with the J-shaped aerofoil increases the self-starting capability due to the high torque generation at the low λ values, it also significantly decreases turbine efficiency at the high λ values. Therefore, the main objective of the hybrid blade design is not only increasing the torque

generation at the low λ values, also to maintain the continuation of high torque production at the relatively high λ values due to the utilisation of the conventional aerofoil profiles.

For this purpose, this chapter aims to develop and propose a hybrid blade design methodology that can effectively combine a conventional aerofoil, such as the NACA0018, and its J-shaped aerofoil, and thus improve the self-starting performance of the H-type VAWT and maintain high efficiency at the normal operating condition. The benefit of utilising the J-shaped aerofoil, which great large positive drag, in the hybrid profile design is to generate sufficient torque to start the turbine when it is needed and accelerate the turbine up to the point where the conventional aerofoil becomes efficient. An effective hybrid blade design can provide an adequate starting torque at low tip speed ratios without a large penalty in the aerodynamic efficiency at high tip speed ratios. To the best of my knowledge, the performance of the H-type VAWT with the proposed hybrid blade has never been explored in the literature.

The chapter is structured as follows: Section 8.2 describes the 3D modelling strategy and the validation of the model against the 2D CFD start-up model and the experimental data. Section 8.3 presents the philosophy of the proposed design used in the present Hybrid blade design. In addition, the estimated performance of the turbines with the proposed hybrid blade design is presented in this chapter. Furthermore, the need for a hybrid blade design to enhance the self-starting characteristics of the turbine is also demonstrated. Finally, in Section 8.4, the overall and the self-starting performance of the turbine with the proposed hybrid blade configurations have been investigated.

8.2   3D CFD turbine study

Due to the straight characteristics of the VAWTs blade, most CFD works have simplified the model into a two-dimensional problem because two-dimensional simulations are much simpler and faster compared to the three-dimensional simulations. Although the two-dimensional CFD model appears sufficient to

evaluate the performance of the H-type VAWT application with acceptable accuracy, 2D simulations generally over-predict the overall performance since they neglect the spanwise secondary flow and vortices from the tip end [188]. In the present investigation, a full three-dimensional CFD simulation of the H-type VAWT is required due to the inherent shape of the proposed hybrid blade design. For this reason, in order to make the design in the present study more reliable, a three-dimensional CFD model has been built with new user-defined function (UDF) after conducting a mesh independency analysis. The details of the UDF can be found in Appendix.

8.2.1 Numerical settings and modelling strategies

As mentioned in Section 2.3.1, there are few experimental studies available in the literature in terms of the turbine self-starting characteristics. For this reason, as in Chapter 4, a published experimental data, conducted by Rainbird [137], has been used in order to validate the 3D CFD start-up model. The detailed information of the selected experimental study can be found in Chapter 4. Based on the work of Rainbird, a 3-bladed H-type VAWT with symmetrical NACA0018 aerofoils, the chord length (*c*) of 0.083m, the height (*H*) of 0.6m and the turbine radius (*R*) of 0.375m has been simulated for the 3D CFD turbine validation study.

Figure 8.1 shows the schematic of the computational domain and the location of the selected boundary conditions. For the present study, the geometry of the 3D computational domain has been obtained by extending the previously employed 2D CFD model, which was explained in Chapter 4. Due to the symmetrical behaviour of the flow around the hybrid blade, only the upper half of the turbine has been considered in the numerical process to reduce the computational cost, and in order to achieve this, a symmetrical boundary condition has been applied to the bottom surface of the computational domain. The velocity inlet condition has been applied to the left side of the computational domain with a constant wind velocity profile of 6m/s, the same as was used in the experiments. A zero gauge pressure-outlet boundary condition has been imposed on the right hand side of the computational domain. Furthermore, the

SIMPLE scheme has been employed to pressure-velocity coupling with gradient called Green Node Based. The second-order upwind scheme is used for the discretization of the momentum and turbulence model equations [153]. The three-dimensional Reynolds-Averaged Navier-Stokes equations and the two-equation turbulence model SST $k - \omega$ have been employed in the present simulations. A detailed discussion of the selection of the turbulence model can also be found in Chapter 4.
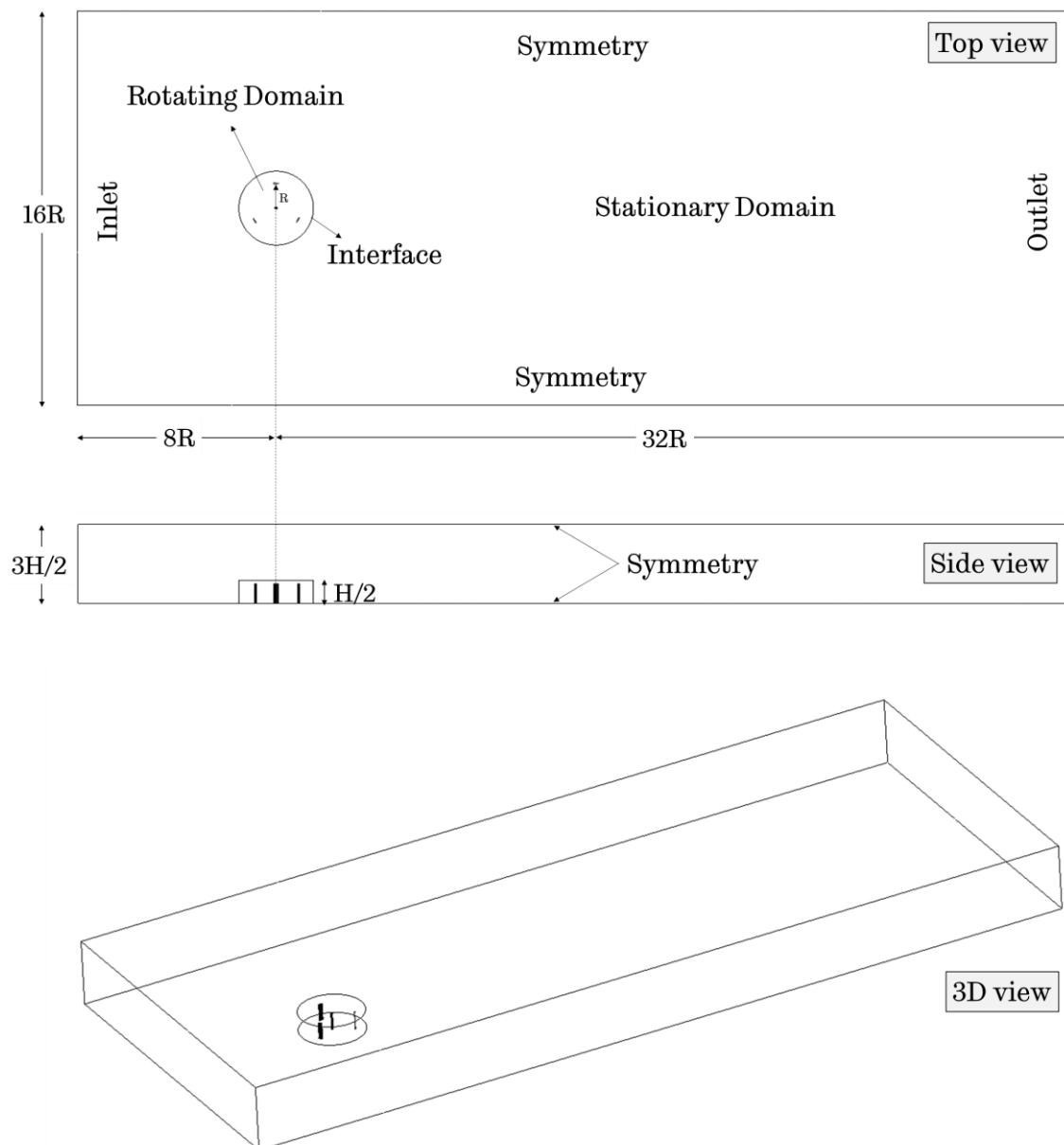
Figure 8.1. Schematic of the 3D computational domain and the location of the boundary conditions.

Furthermore, the time step is another factor, which influences the accuracy and efficiency of the CFD simulations. Thus, the time step size independency study has been conducted in Chapter 4 and based on the findings, the time step size of 0.00072s has been considered appropriate in the present study. Additionally, the residual convergence criterion has been set as 1×10^{-5} for all the variables.

8.2.2   Mesh independency analysis

Although the 3D CFD simulations of an H-type VAWT can produce more accurate results compared to the 2D CFD simulations, the meshing and the calculation process can be very time-consuming. Therefore, it is crucial to conduct a mesh independency analysis in order to select the appropriate number of mesh around the aerofoil to satisfy the calculation accuracy and the computational cost.

In the present study, the computational domain, shown in Figure 8.2 consists of a rotating domain, where the turbine is located, and a stationary domain. As can be seen in the figure, structured mesh topologies have been applied to all the computational domains. In addition, the sliding mesh approach has been employed in order to consider the data exchange between these two adjacent domains with an interface boundary condition. The size of the meshes on the interface is consistent to ensure that the continuity, accuracy, and fast convergence of the CFD simulations are established. It is also important to note that two mesh domain files, namely stationary and rotating domains, have been created separately to simplify the meshing steps, and then, the generated meshes have been re-attached by using the appended function in the solver stage.
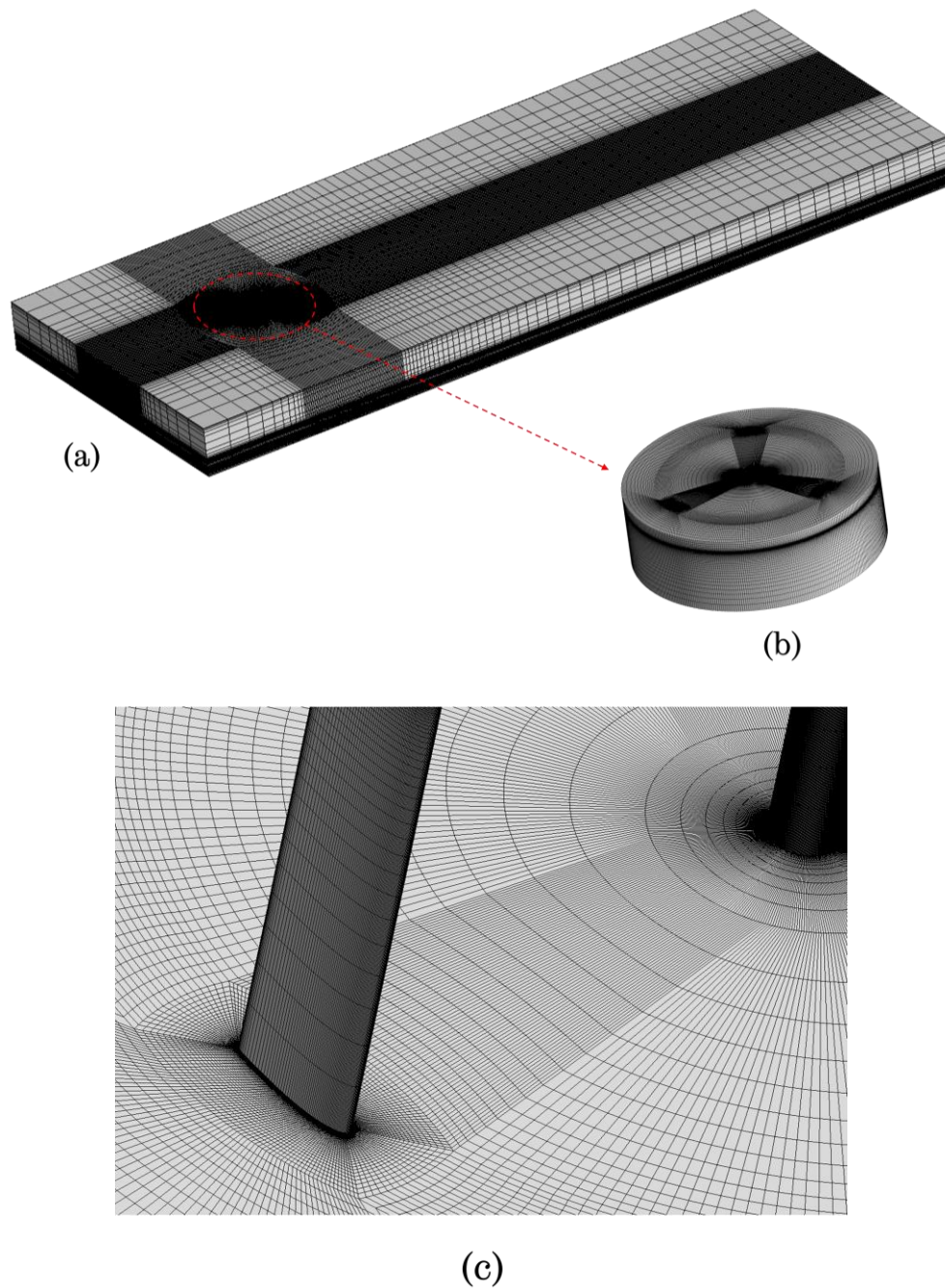
Figure 8.2. Mesh configuration for the (a) stationary domain, (b) rotating domain, and (c) at the vicinity of the blade.

The mesh independency analysis has been carried out by using the three different sets of the nodes, i.e. Node 1, Node 2, and Node 3, as shown in Table 8.1. Although the number of meshes in the vicinity of the blade changes, the non-dimensional wall distance y^+ is kept constant in order to obtain the value that

is recommended for the enhanced wall treatment turbulence models [152]. In the present study, the first mesh close to the aerofoil surface is refined in order to obtain a dimensionless y^+ value with a maximum wall distance 2.5 and average $y^+ < 1$. Additionally, 60 spanwise mesh divisions have been employed to the blade half-length, which is consistent with the study by [188]. Figure 8.3 illustrates the comparison of the results on the moment coefficient for the different number of nodes at the two λ values. As can be seen from the figures, the moment coefficient obtained by Node 2 and Node 3 are very close at both λ values while Node 1 is different. Therefore, Node 2 can be selected for the further simulations, so that not only the computational accuracy is ensured, but also the additional computational cost is not caused.

Table 8.1. The different nodes employed for the three sets of meshes.

Nodes	Number of nodes around the blade 2D profile	Number of elements
Node 1	128	2,198,956
Node 2	184	3,161,265
Node 3	280	4,679,448
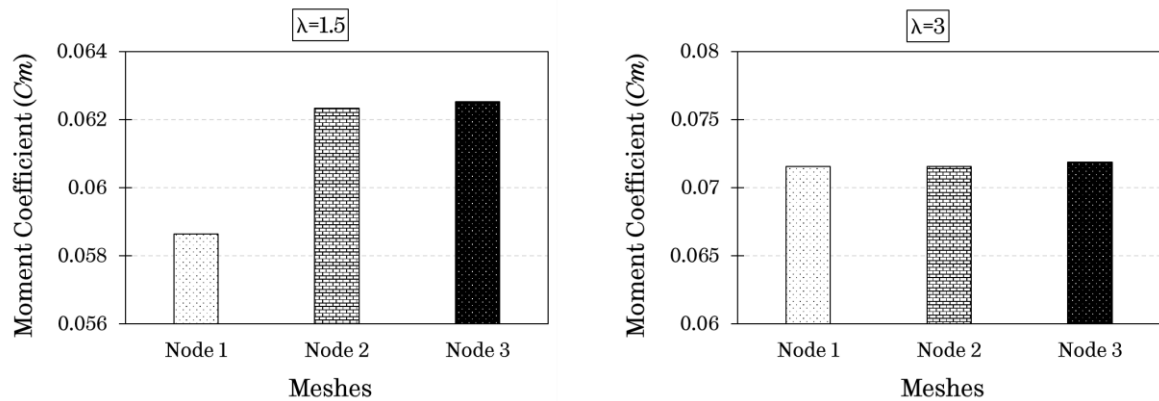
Figure 8.3. The predicted of the turbine overall moment coefficient for the different meshes at λ=1.5 and λ=3.

8.2.3   3D model verification

Figure 8.4 shows the current 3D CFD simulation result with comparisons with the experimental data of Rainbird [137] and the previously obtained 2D CFD model result in Chapter 4. As can be seen from the figure, the 3D CFD model is able to predict the self-starting characteristics of the H-type VAWT investigated. However, to make it easier to understand the comparison between the current CFD results and the experimental data, similar as in Chapter 4, the non-dimensional time axis, which is defined as t/T (T is the time when the turbines reach the steady-state conditions) is employed. As mentioned in Chapter 4, the time required to reach the steady-state condition in the experiment and the 2D CFD simulation is 150s and 15s, respectively; however, it has been found that approximately 31s is required in the current 3D CFD simulation to do so. Furthermore, the deviation in the λ values at the steady-state conditions between the experimental data and the present 3D CFD prediction is found to be around 8.5% while it is 22% between the 2D CFD prediction and the experimental data. It is postulated that the difference between the 3D and experimental data may be due to the fact that additional negative torque sources, such as the bearing and supporting arms, etc. have not been considered in the 3D simulations. Nevertheless, 3D simulations can still provide important insight into the fluid dynamics of the self-starting process of the VAWTs and can produce a more accurate prediction of the self-starting compared to the 2D CFD simulations.

Although there is an understandable degree in the difference between the results obtained from the CFD simulations and experimental study, the behaviour of the self-starting curve of the H-type VAWT obtained from the 3D CFD simulation is in good agreement with the results obtained from an experimental study. Therefore, the current 3D CFD model setup can be used, with confidence, to investigate the effect of the proposed Hybrid blade on the aerodynamic performance and the self-starting behaviour of the H-type VAWT.
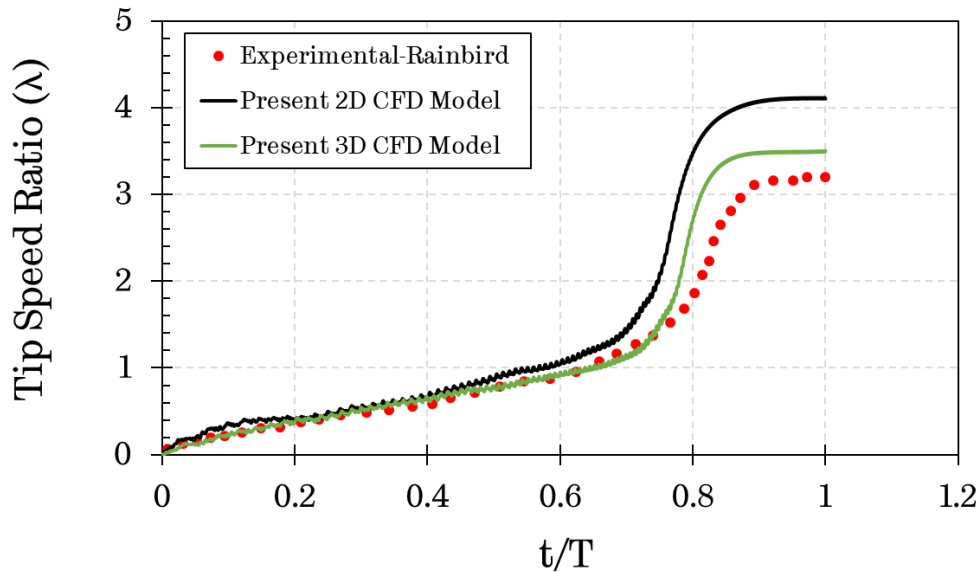
Figure 8.4. The variation of the tip speed ratio as a function of the non-dimensional time for comparisons of the current 3D CFD model with the experimental data and previously obtained 2D CFD results.

8.3 The philosophy of the design

As previously mentioned, the main objective of the present chapter is to design, simulate, and evaluate the performance of the proposed hybrid blade design for self-starting H-type VAWT. In this regard, the philosophy of the design employed with the innovative hybrid blade design is explained in this section. It is important to note that in the current design process, as in Chapter 7, the same turbine configuration has been used; however, the constant free wind speed of *5m/s* is employed since, as shown in the previous chapter, the turbine is not self-starting under this circumstance. The optimised hybrid blade design will make the turbine self-start.

The proposed hybrid blade design consists of three major design and analysis steps, which is summarised, in Figure 8.5 and the details of the procedure of the hybrid blade design are explained systematically as follows:

Procedure of
the Hybrid
Blade Design

Step 1

For turbine with
J-shaped
aerofoils

Calculate Ct and Cp
based on 2D CFD
simulations

For turbine with
conventional
aerofoil

Step 2

Estimate the initial
value of $OLP_{Initial}$

Calculate
C_{t_Hybrid} and C_{p_Hybrid}

Does the turbine
produce positive
torque at λ=0.5 and
λ=1?

No

Yes

Step 3

Consider the losses due
to the 3D effects at low λ
values

Obtain the final
value of OLP_{final}

Comparison
between Hybrid
Design and Original
turbine

Performance
evaluation
at **low** λ values

Performance
evaluation
at **high** λ values

Comparison
between Hybrid
Design and J-
shaped aerofoil

Run 3D CFD turbine dynamic start-up
simulations with Hybrid Designs considering
OLP_{final}

Figure 8.5. Summary of the proposed hybrid blade design method.

Step 1: Performance evaluation of the individual H-type VAWT in 2D with the conventional aerofoil and the J-shaped profiles considering the different range of the opening ratios over the aerofoil surface is conducted. The torque coefficient (Ct) is calculated for the turbines investigated based on the 2D CFD calculations and the results are illustrated in Figure 8.6. As can be seen from the figure, the turbines with the conventional aerofoil and the J-shaped profile with a 10% opening ratio produce a negative torque at low tip speed ratios, such as λ=0.5 and λ=1, which indicates a non-self-starting capability. Furthermore, as found in Chapter 7, when the estimated value for the resistance due to the bearing friction is implemented in the calculations, the turbine with the J-shaped profile with 20% and 30% opening ratios also do not show the self-starting capability. Therefore, in the current hybrid design study, the NACA0018 aerofoil profile has been selected as a conventional aerofoil, while the 40% and 90% opening ratios have been selected for the J-shaped profile. The reason for selecting these opening ratios for the J-shaped profiles investigated is due to the high computational cost required for the additional 3D CFD simulations and no significant difference is expected between the hybrid blade with the J-shaped profile with 40% and 60% opening ratios.
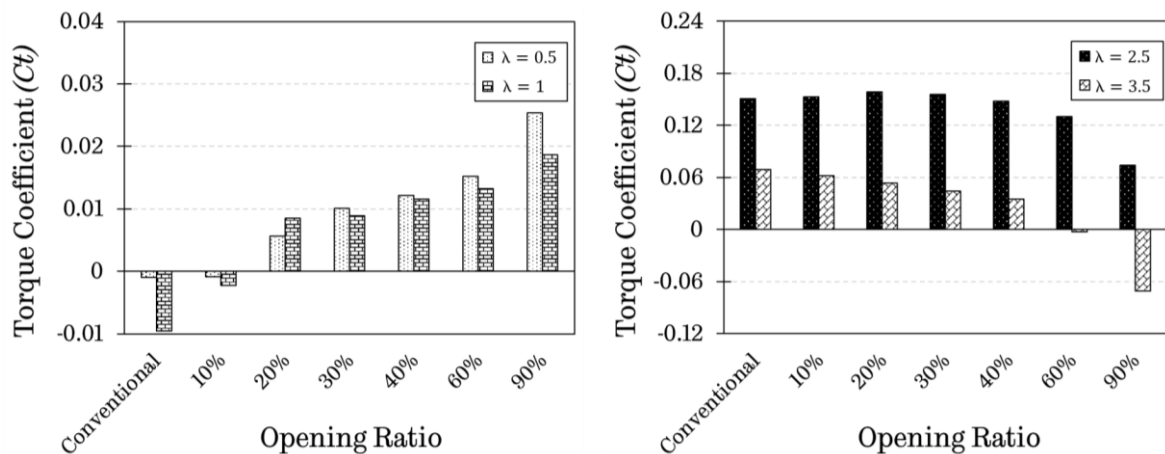
Figure 8.6. The turbine torque coefficient as a function of the conventional aerofoil and the J-shaped profiles with different opening ratios over the aerofoil surface at different tip speed ratios.

Step 2: The most crucial part of the Step 2 is to estimate the initial opening length percentage ($OLP_{initial}$) for the J-shaped profile used in the hybrid blade design, which is related to the ratio of the length of the J-shaped profile along z direction to the length of the whole blade span. The values estimated for the $OLP_{initial}$ are changed from 0% to 100%. Since the torque coefficient values of the turbines with the conventional aerofoil ($Ct_{conventional}$) and the J-shaped profile ($Ct_{J-shaped}$) have been calculated in Step 1, the torque coefficient (Ct_{Hybrid}) of the turbine with the hybrid blade can be calculated with the estimated $OLP_{initial}$ value at the tip speed ratios investigated using the Eq. 8.1.

$$Ct_{Hybrid} = Ct_{J-shaped} \times OLP + Ct_{conventional} \times (1 - OLP) \qquad (8.1)$$

This process continues by changing the value of the $OLP_{initial}$ until the positive torque coefficient (Ct_{Hybrid}) for the turbine with a hybrid blade profile at λ=0.5 and λ=1 is obtained. For instance, when the $OLP_{initial}$ is selected as 45% for the J-shaped profile with a 40% opening ratio used in the Hybrid Blade 1 (which is the combination of the conventional aerofoil and the J-shaped profile with a 40% opening ratio), although the turbine with the Hybrid Blade 1 profile produces a positive torque at the λ=0.5, a negative torque generation is obtained at the λ=1; however, it is positive when $OLP_{initial}$ is selected as 46% at both selected λ values. Therefore, the minimum required $OLP_{initial}$ value for the Hybrid Blade 1 to produce a positive torque coefficient at both low λ values is 46%. On the other hand, the minimum required $OLP_{initial}$ value to obtain a positive torque generation at the λ=0.5 and λ=1 is found to be as 34% for the J-shaped profile with a 90% opening ratio used in the Hybrid Blade 2 (which is a combination of the conventional aerofoil and the J-shaped profile with a 90% opening ratio). Although a further increment on the $OLP_{initial}$ value increases the torque generation at the low λ values, which is desirable for the turbine self-starting capability, it will cause a significant performance reduction at the high λ values. Therefore, the optimum value of the $OLP_{initial}$ values should also be determined by considering the turbine performance at the relatively high λ values.

Step 3: Since the estimation of the $OLP_{initial}$ values have been determined based on the 2D CFD calculations, the existence of the 3D effects, such as tip losses and the blade supporting arms, have not been considered. Therefore, the values of the $OLP_{initial}$ may not be sufficient for the hybrid blades to provide the required torque to self-start the turbine. Even though the discrepancy between the 2D and 3D CFD simulations varies depending on the tip speed ratio [189], in the critical tip speed ratio region, where λ<1, a maximum deviation can be observed around 10% [190, 191, 192]. For this purpose, an additional factor, which is determined by considering this deviation, has been taken into account in the calculations of the final values of the opening length percentages (OLP_{final}). Since the λ=1 appears to be more sensitive than the λ=0.5 in terms of the negative torque generation (see Step 2), the additional factor, which was selected as 10% in the present study, has been only added to the torque coefficient (Ct_{Hybrid}) of the hybrid bladed turbines with the $OLP_{initial}$ values at λ=1. Thus, the OLP_{final} values have been estimated as 50% and 38% for the proposed Hybrid Blade 1 and Hybrid Blade 2, respectively.

From the data presented in Figure 8.7, it is apparent that the turbine with the J-shaped profiles indicates the best performance at the low tip speed ratios, while the turbine with the conventional aerofoil profile produces much more torque at the relatively higher tip speed ratios. However, the turbine with the proposed hybrid blade designs can effectively produce much more sufficient torque compared to the turbine with a conventional aerofoil at low tip speed ratios, while there are less performance losses compared to the turbine with the J-shaped profiles at the high tip speed ratios. Therefore, as mentioned earlier, the proposed Hybrid Blades may address the disadvantages of each turbine design using a single aerofoil profile, such as obtaining self-starting characteristics at low tip speed ratios and high Ct at high tip speed ratios. In order to further illustrate the advantages of the hybrid blade designs over the conventional aerofoil at the low λ values and the J-shaped profiles at the high λ values, the estimated torque coefficient generation of the proposed hybrid blade

designs in a comparison with their conventional and the J-shaped profiles at different tip speed ratios are also demonstrated in Figure 8.8. As can be seen in the figure, the turbines with the proposed hybrid blade designs produce much higher torque coefficients compared to the turbine with the conventional aerofoil at the λ = 0.5 and λ = 1. On the other hand, at relatively high tip speed ratios such as λ = 2.5 and λ = 3.5, the proposed designs also superior compared to the J-shaped aerofoil, in particular at the highest tip speed ratio investigated. Therefore, the observed findings in this estimation process clearly demonstrate the need for the hybrid blade design used in the H-type VAWT in order to increase the self-starting capability without a large penalty at the higher tip speed ratios.
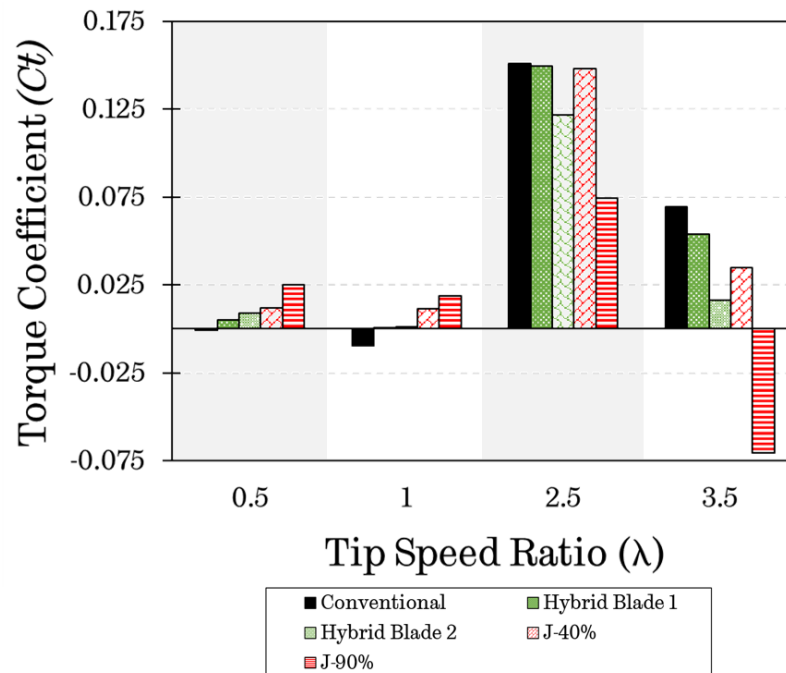
Figure 8.7. Estimated torque coefficient as a function of the tip speed ratio for the turbines with different blade profiles.
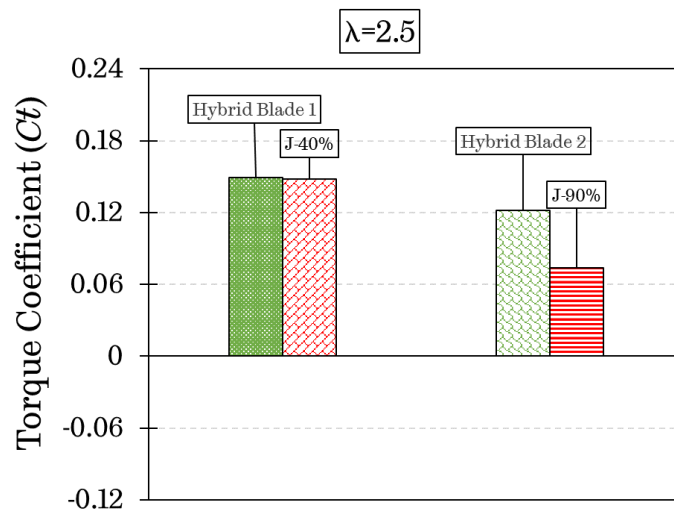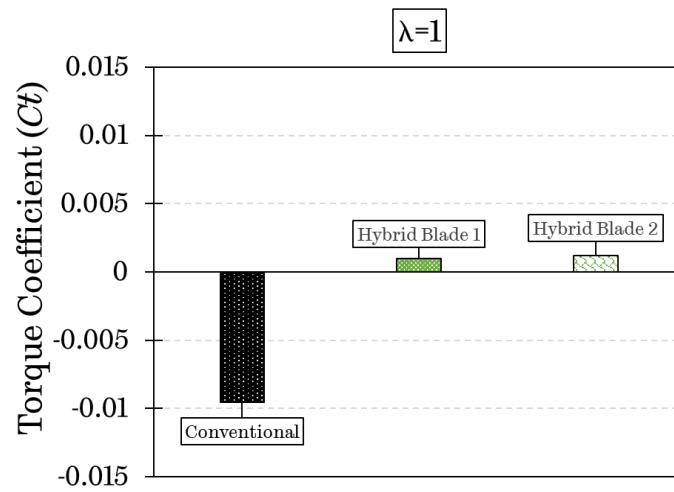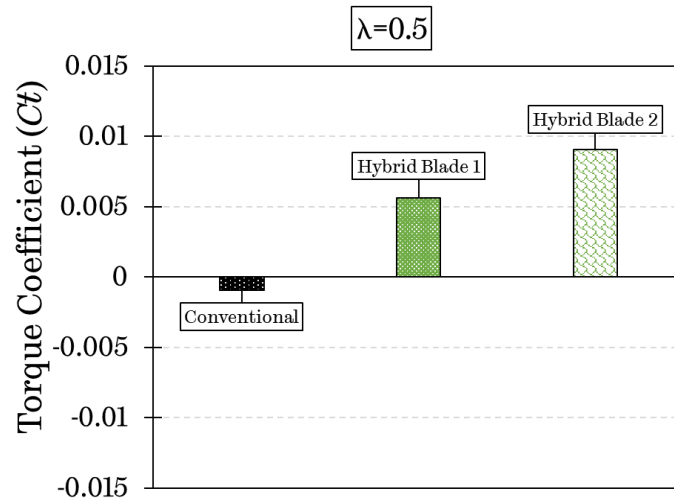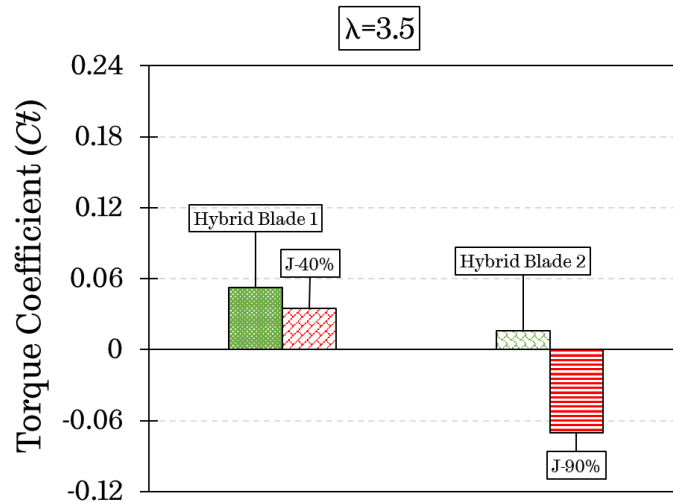
Figure 8.8. The estimated torque coefficient of the hybrid blade designs in comparison with the conventional and J-shaped aerofoil profiles at different tip speed ratios.

According to the design method explained above, the proposed Hybrid Blade 1 and Hybrid Blade 2 are presented in Figure 8.9 and Figure 8.10, respectively. Since the effect of the location of the J-shaped profile along the z direction on the turbine performance cannot be considered with the 2D-based design methodology, three different scenarios have been selected in order to evaluate the effect of the proposed hybrid blade design on the overall and self-starting performance of the H-type VAWTs for the current 3D CFD investigations. The three scenarios are (a) the J-shaped being placed at the top and the bottom of the blade with an open tip end, (b) the J-shaped being placed at the top and the bottom of the blade with a closed tip, and (c) the J-shaped being placed at the middle of the blade span.
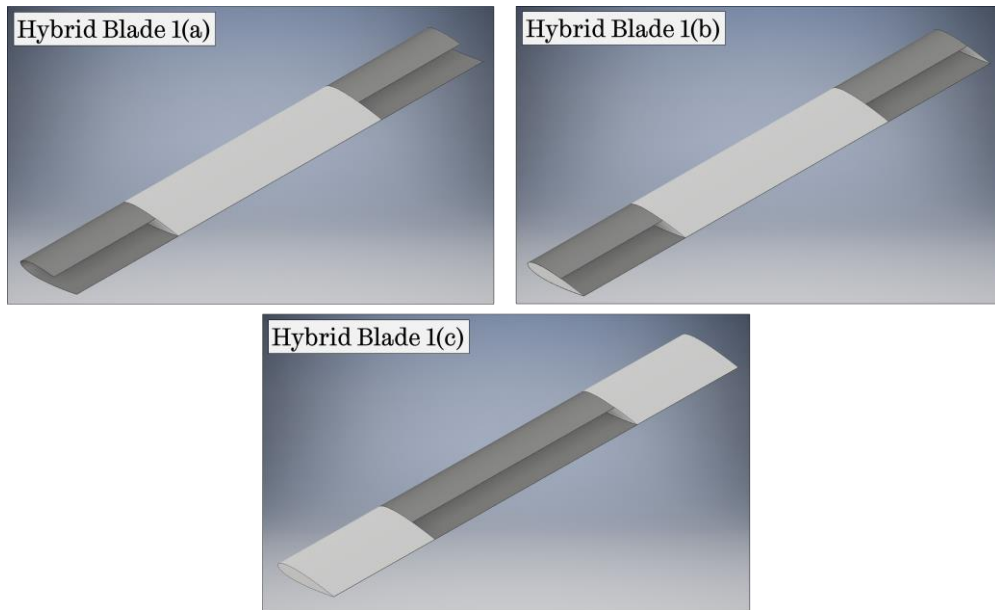
Figure 8.9. Schematic of the proposed Hybrid Design 1 (a) J-shaped is located at the top and the bottom of the blade with an open tip, (b) J-shaped is located at the top and the bottom of the blade with a closed tip, and (c) J-shaped is located at the middle of the blade.
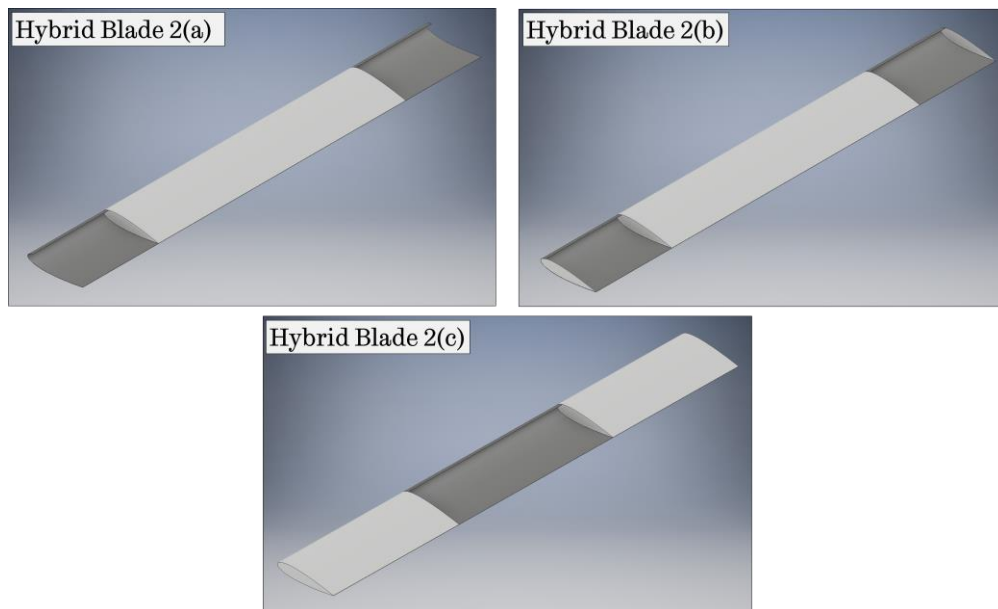
Figure 8.10. Schematic of the proposed Hybrid Design 2 (a) J-shaped is located at the top and the bottom of the blade with an open tip, (b) J-shaped is located at the top and the bottom of the blade with a closed tip, and (c) J-shaped is located at the middle of the blade.

8.4 Self-starting performance of the turbine with hybrid blades

The purpose of the present section is to investigate the effect of the proposed hybrid blade configurations, namely Hybrid Blade 1 (a,b, and c) and Hybrid Blade 2 (a,b, and c), on the overall performance and the self-starting behaviour of the H-type VAWT by using the 3D CFD start-up modelling. For the current investigations, same as Section 8.2, the turbine with a radius of 0.375m, the blade chord length of 0.083m, and the height of 0.6m has been employed under the free wind speed of 5m/s.

Figure 8.11 shows the effect of the different hybrid blade configurations on the turbine dynamic start-up behaviour in comparison with their conventional blade profile. The results show that the turbine with the conventional aerofoil, which is NACA0018 in the present study, does not illustrate the self-starting characteristics. However, from the data in Figure 8.11, it is apparent that the turbines with the J-shaped profiles placed at the top and bottom of the blade with a closed tip exhibit much better performance in terms of the final tip speed ratio and the start-up time required to reach the steady-state condition compared to their open tip configuration in both proposed designs. Moreover, no significant difference has been observed between the hybrid blade configurations b and c in both Hybrid Blade designs. The results clearly illustrate that even though the location of the J-shaped profile does not have much impact on the turbine self-starting characteristics, a significant discrepancy in the self-starting behaviour of the turbine can be observed when closed and open tip is used at the blade tip. It is believed that the reason behind this situation is that the tip vortex generated at the blade tip, which causes a different vortex structure and changes the severity of the pressure interactions between the two sides of the blade. Therefore, a more detailed illustration will be provided using the vorticity contours for the comparison of the effect of the shape of the tip on the performance of the turbine in the following sections.

The results obtained from the analyses of the effect of the hybrid blade designs on the turbine dynamic start-up behaviour in terms of the self-starting time and

the final tip speed ratio are summarised in Table 8.2. As can be seen in the table, the turbine with the Hybrid Blade 1(b) configuration has the maximum final tip speed ratio with a value of 3.35 so that its self-starting performance is the best among all the six configurations investigated. On the other hand, the turbines with the Hybrid Blade 1(a) and Hybrid Blade 2(a) extend the time required to reach steady-state conditions with a much lower final tip speed ratio.
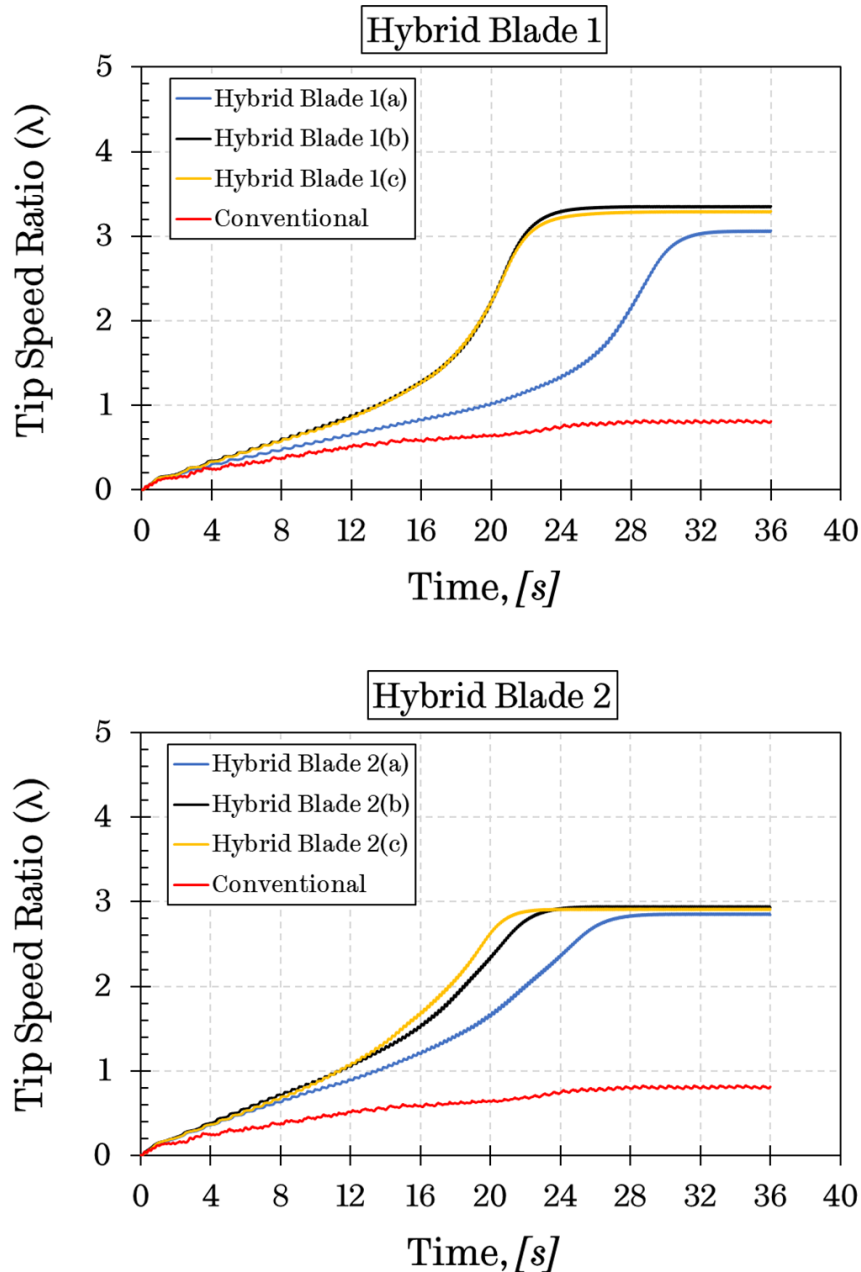
Figure 8.11. The variation of the tip speed ratio as a function of the time for comparison of the self-starting performance of the proposed hybrid blade configurations.

Table 8.2. The comparison of the self-starting capabilities of the proposed hybrid blade designs investigated in terms of the self-starting time and final tip speed ratio.

	Conventional	Hybrid Blade 1			Hybrid Blade 2		
		a	b	c	a	b	c
Self-starting capability	No	Yes	Yes	Yes	Yes	Yes	Yes
Self-starting time	—	34.2	26.8	26.9	30.4	26.2	24.1
Final λ	—	3.07	3.35	3.29	2.85	2.93	2.9

In order to discuss the effect of the different hybrid blade configurations on the aerodynamic performance of the turbine, the torque coefficients and power coefficients as a function of the tip speed ratio curve during the dynamic start-up process for the Hybrid Blade 1(a), 1(b), and 2(b) are plotted in Figure 8.12 and Figure 8.13. The comparison between the Hybrid Blade 1(a) and 1(b) will provide a further better understanding of the effect of the closed and open tip on the aerodynamic performance in the complete operating conditions. On the other hand, the comparison between Hybrid Blade 1(b) and (2b) illustrates the effect of the utilisation of the different J-shaped profiles in the hybrid blade designs on the turbine overall performance.

As can be observed from Figure 8.12, the turbine with the Hybrid Blade 1(b) has the best performance at the all tip speed ratios investigated compared to the Hybrid Blade 1(a). Therefore, this result supports the findings from the dynamic start-up behaviour. For example, the generation of the higher torque coefficient at low and high tip speed ratio results in a faster start-up and a higher final rotational speed at the steady-state condition, respectively. On the other hand, when we compare the performance of the Hybrid Blade 1(b) and Hybrid Blade 2(b), it can be seen in Figure 8.13 that Hybrid Blade 2(b) has the higher

performance at the low λ region (0<λ<1.5) while the highest performance at the relatively high λ region (1.5<λ<3.35) can be achieved with the Hybrid Blade 1(b). This leads to a faster turbine acceleration with the Hybrid Blade 2(b) and a higher final rotational speed at the steady-state condition with the Hybrid Blade 1(b) (see Figure 8.11).
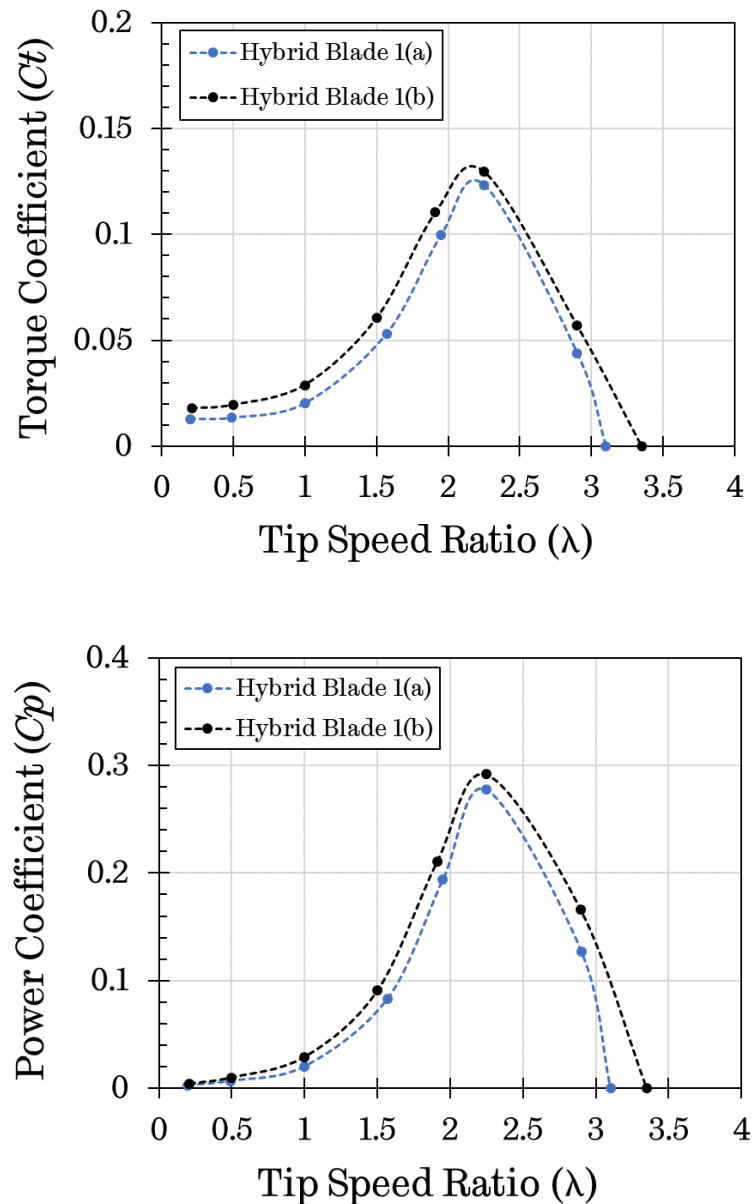
Figure 8.12. The torque and power coefficients as a function of the tip speed ratio for comparison of the aerodynamic performance of the Hybrid Blade 1(a) and Hybrid Blade 1(b).
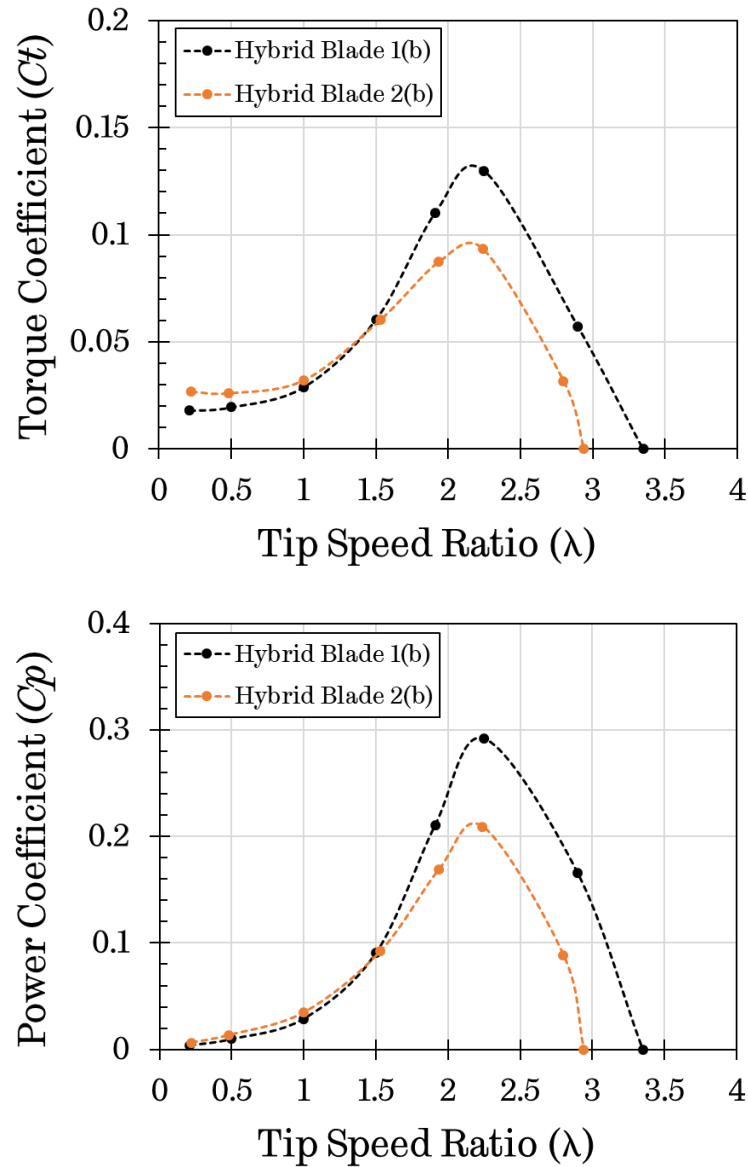
Figure 8.13. The torque and power coefficients as a function of the tip speed ratio for comparison of the aerodynamic performance of the Hybrid Blade 1(b) and Hybrid Blade 2(b).

As mentioned before, although the same configuration, except the closed and open tip, is used in the Hybrid Blade 1(a) and Hybrid Blade 1(b), the difference on the overall performance between the turbines with these configurations is apparent. This may be due to the effect of the tip vortex generated at the blade tips. However, the aerodynamic performance difference between the Hybrid Blade 1(b) and Hybrid Blade 2(b) is considered to be the utilisation for the different J-shaped profile in these configurations. For instance, the J-shaped

profile with a 40% opening ratio is used for the Hybrid Blade 1(b) while the J-shaped profile with a 90% opening ratio is used in Hybrid Blade 2(b). To better analyse and explain the difference between these configurations, the blade torque coefficient as a function of the azimuthal angle at different tip speed ratios is illustrated in Figure 8.14. This figure shows that a slightly higher torque coefficient can be obtained in the upstream part of the turbine with the Hybrid Blade 2(b) configuration while torque pattern of these three configurations is similar at the low tip speed ratios, such as λ=0.5 and λ=1. This results in a higher torque coefficient generation at these two tip speed ratios (see Figure 8.13). The plausible explanation for this situation may be due to the fact that the usage of a J-shaped profile with the larger opening ratio, such as 90%, increases the torque generation in the upstream part of the turbine, especially at the low λ values, while it decreases the torque generation in the downstream part of the turbine, especially at the relatively higher λ values. This finding appears to be consistent with the 2D CFD turbine simulations that have been conducted in Section 7.3.2 to investigate the effect of the J-shaped profiles with different opening ratios on the turbine overall and self-starting performance.

On the other hand, at the relatively higher tip speed ratios, such as λ=2.25 and λ=2.9, a much obvious difference in the torque generation can be observed between the different hybrid blade configurations compared to the low λ values. Although the Hybrid Blade 1(b) and Hybrid Blade 2(b) have a similar torque generation in the upstream part of the turbine ($0 < \theta < 180$), the Hybrid Blade 1(b) performs the best in the downstream part of the turbine ($180 < \theta < 360$). This discrepancy may be due to the utilisation of the J-shaped aerofoil with a 40% opening ratio, which has a lower performance loss in the downstream part of the turbine, in the Hybrid Blade 1(b) while the J-shaped aerofoil with a 90% opening ratio, which has relatively higher performance loss, in the Hybrid Blade 2(b). The results obtained are also consistent with those of Section 7.3.2. Furthermore, when the Hybrid Blade 1(b) is compared to the Hybrid Blade 1(a), the difference in the torque generation, in particular in the upstream part of the turbine, may be due to the effect of the blade tip.
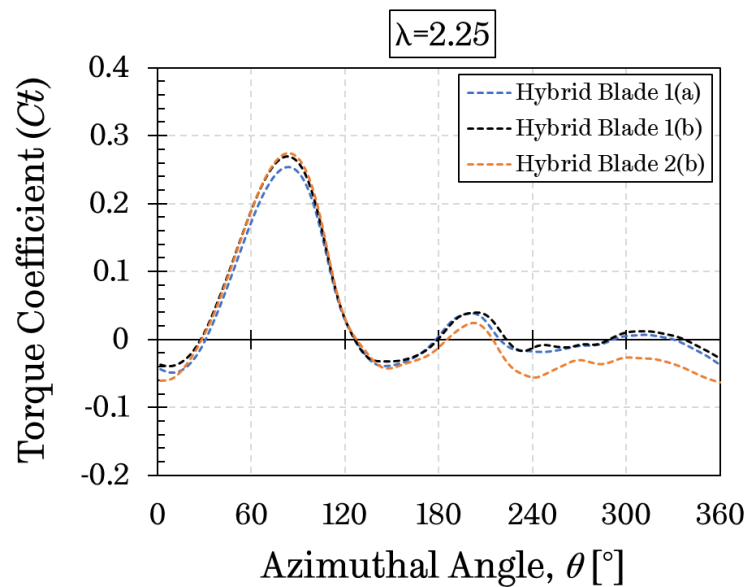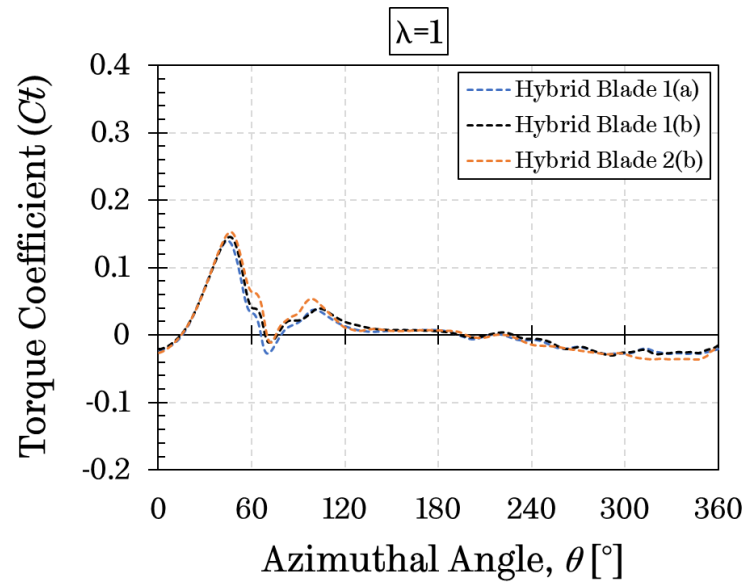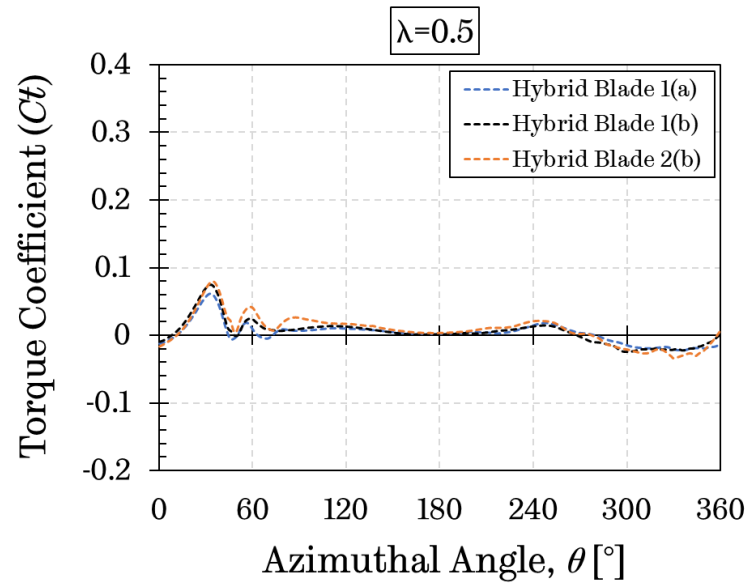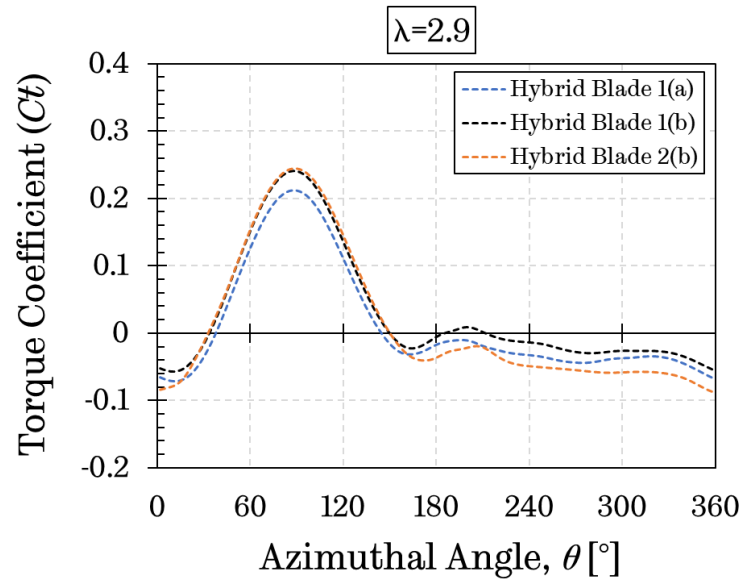
Figure 8.14. The torque and power coefficients as a function of the tip speed ratio for comparison of the aerodynamic performance of the Hybrid Blade 1(b) and Hybrid Blade 2(b).

Furthermore, the lift and drag coefficient of the three configurations at the optimum λ of 2.25 are illustrated in Figure 8.15. As can be seen from this figure, although no significant difference in the lift coefficient is observed between the hybrid blade configurations in the positive angles of attack region, which is corresponding to the upstream part of the turbine, the Hybrid Blade 1(a) produces a much higher drag coefficient in the upstream part of the turbine, which results in much lower performance at the λ investigated (see Figure 8.14). On the other hand, a lower torque coefficient in the downstream part of the turbine is obtained with the Hybrid Blade 2(b) at λ=2.25 as illustrated in Figure 8.14. The reason for this is the generation of the higher drag coefficient in the negative angles of attack region, which is corresponding to the downstream part of the turbine, due to the utilisation of the J-shaped aerofoil with a 90% opening ratio. This finding is consistent with those found in Section 6.2.3 and Section 6.3.2, where the aerodynamics of the J-shaped profiles with the different opening ratios have been examined under the dynamic and static conditions.
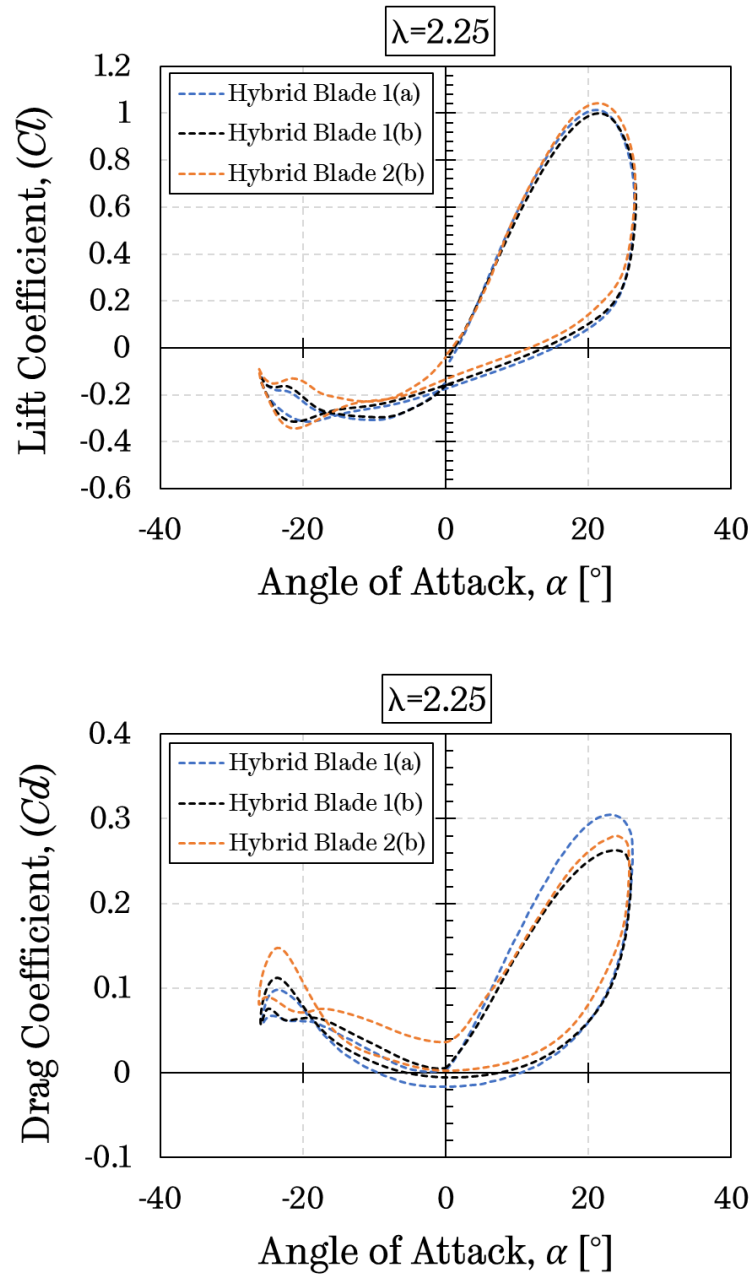
Figure 8.15. The lift and drag coefficient as a function of the angle of attack for comparison between the hybrid designs investigated.

For further analyses on the difference between the Hybrid Blade 1(a) and Hybrid Blade 1(b), Figure 8.16 and Figure 8.17 illustrate the iso-surface contours for the instantaneous vortex structures generated in the vicinity of the blades at the optimum λ of 2.25 at the same turbine position. The comparison of the iso-

surface contours between these two configurations provides a more in-depth understanding of the effect of the closed and open tips on the hybrid blade performance.

The utilisation of the closed tip can affect the distribution of the vorticities over the blade tip. The vortex structure over the blades with the open and closed tips at the same turbine positions are shown by the iso-surface of Q=100 coloured by the vorticity magnitude in Figure 8.16 and Figure 8.17. As can be observed from the figures, a larger vortex structure has been generated with the hybrid blade with an open tip (Hybrid Blade 1(a)) compared to the closed tip. Since a larger vortex structure at the blade tip results in a more intense pressure interaction between the pressure and the suction sides, this leads to a reduction in the pressure difference between two sides of the blade and as a result a decrease in the power efficiency. On the contrary, when we consider the Hybrid Blade 1(b), a reduced tip vortex structure can be observed and it can visually demonstrate a much weaker pressure interaction between the pressure and suction sides at the closed tip and an improvement in the turbine performance. Moreover, in the case of the Hybrid Blade 1(a), it appears that air finds its own way to escape from the blade tips, which may result in a lower pressure difference between the inner and outer sides of the J-shaped profile used in the Hybrid Blade 1(a) and lower performance compared to the Hybrid Blade 1(b).
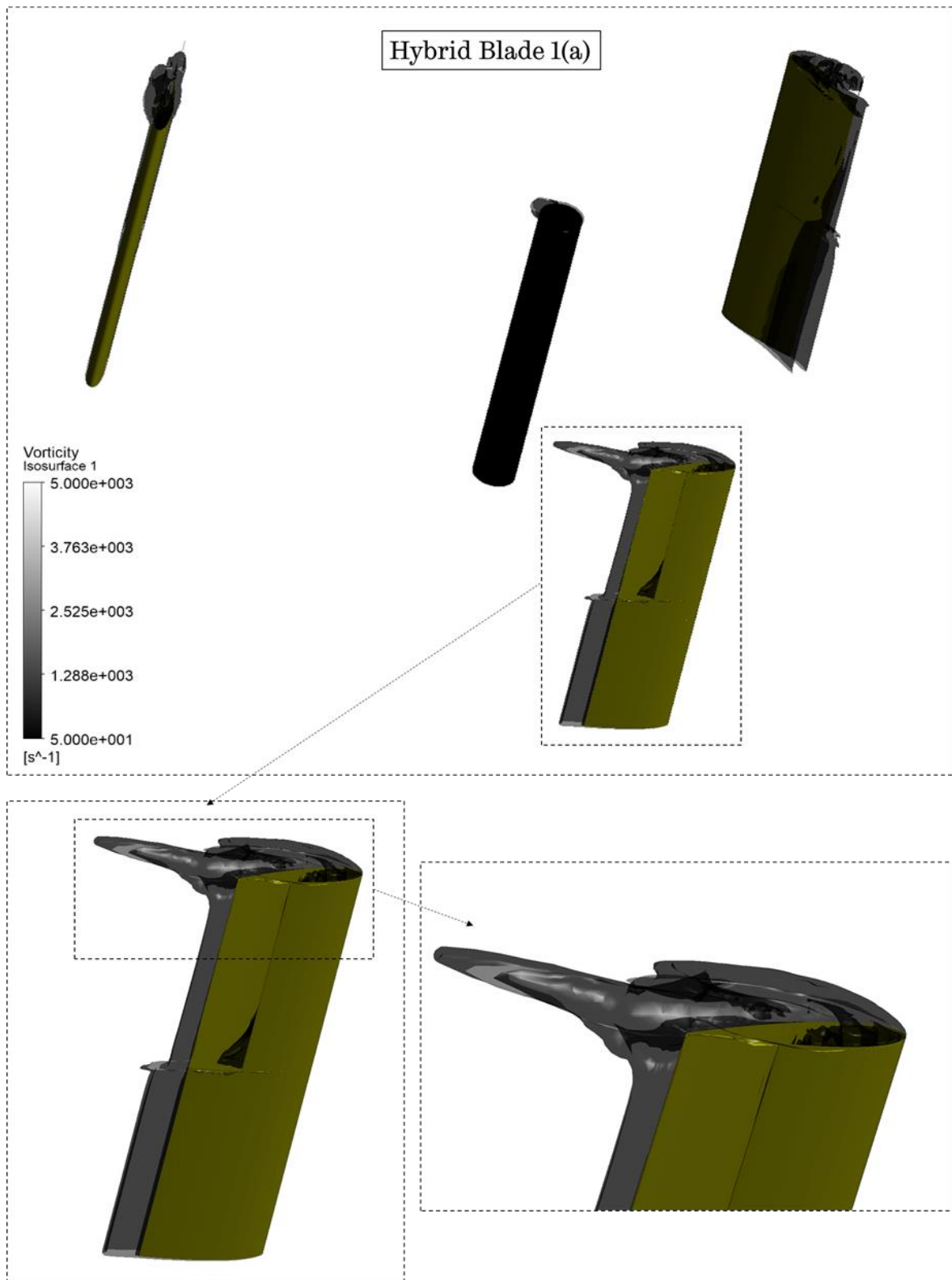
Figure 8.16. The iso-surface contours for the vortex structures generated around the turbine with the Hybrid Blade 1(a) configuration with an enlarged view of the blade tip.
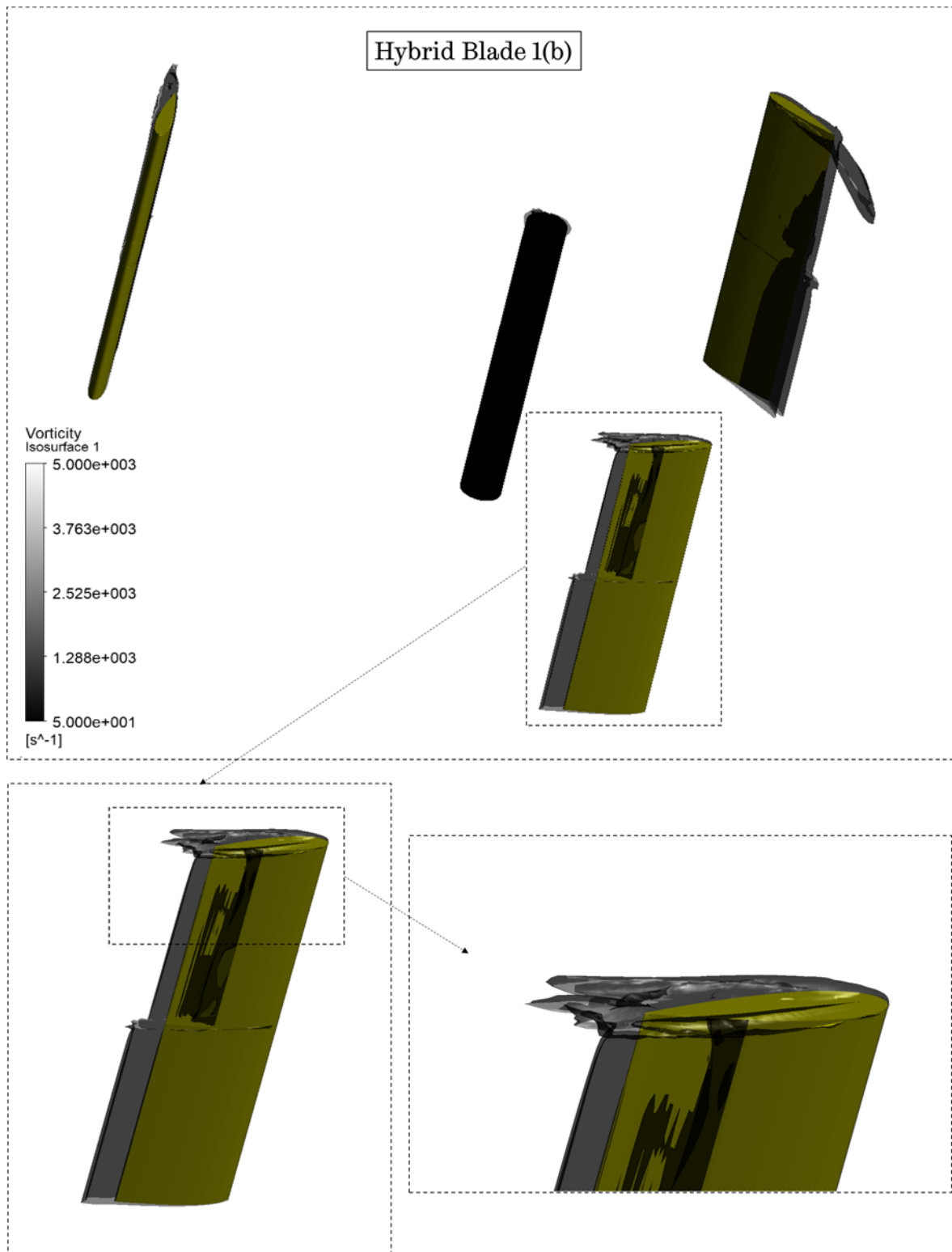
Figure 8.17. The iso-surface contours for the vortex structures generated around the turbine with the Hybrid Blade 1(b) configuration with an enlarged view of the blade tip.

8.5 Conclusion

In this chapter, a 3D CFD start-up modelling strategy and validation study for the model in comparison with the 2D CFD start-up model and the experimental study has been conducted. A computationally affordable 3D CFD model has been employed for the analyses of the hybrid blade designs from the overall performance and self-starting behaviour point of view. Then, a design methodology based on the 2D CFD calculations has been proposed in order to accurately predict the torque and power generations of the turbine with different hybrid blades at low and high tip speed ratio regions. Finally, the turbine with the proposed hybrid blade configurations has been investigated considering the dynamic start-up characteristics and the aerodynamic efficiency at several tip speed ratios.

According to the results obtained in the present chapter, the following conclusions can be drawn:

- Even though the 3D CFD start-up model has been found to be more accurate compared to the 2D CFD start-up model, there is still a discrepancy on the final tip speed ratio at the steady-state condition between the current 3D CFD model and the experimental data for the original design reported by Rainbird [137]. The reason for this may be due to the additional negative torque sources, such as the bearing and the supporting arms, which have not been taken into account in the current investigation. However, it has been shown in Section 7.6 that the friction has a significant influence on the time that is required to accelerate the turbine and its final speed.

- Although the proposed design methodology has been based on the 2D CFD calculations, the predicted aerodynamic performance can provide the first insight on the performance of the turbine with the different hybrid blade designs at the low and high tip speed ratio regions. Furthermore, the estimated results have shown the need for the hybrid blade design to overcome the lower torque generation capability of the conventional aerofoil at low λ values and higher torque losses of the pure J-shaped profiles at the higher λ values.

- According to the proposed design methodology, two hybrid blade designs, namely Hybrid Blade 1 and Hybrid Blade 2 with different configurations (a,b, and c) have been proposed and evaluated in terms of their self-starting capabilities. The 3D CFD results revealed that the finding observed are consistent with the proposed methodology applied to the Hybrid Blade design.

- A significant difference has been observed between the turbine with the Hybrid Blade 1(a), which has an open-tip, and Hybrid Blade 1(b), which has a closed-tip, in terms of the final rotational speed at the steady-state conditions and the start-up time. This discrepancy has been found due to the intensity of the vortex structures generated at the blade tips, which affects the pressure difference between the two side blades at the tip. The tip vortex has been weakened by appending of the closed-tip in the Hybrid Blade 1(b), which results in a reduction in the pressure interaction between the pressure and suction sides at the blade tip and thus the efficiency of the blade is enhanced.

- Even though the Hybrid Blade 1(b) and Hybrid Blade 2(b) can show the similar torque generation in the upstream part of the turbine, Hybrid Blade 2(b) illustrates a less torque generation in the downstream part of the turbine, especially at the relatively higher λ values. This may be due to the utilization of the J-shaped profile with a larger opening (e.g. 90%), which provides a much higher negative drag contribution.

- Among all the designs investigated, the turbine with Hybrid Blade 1(b), which consists of the conventional aerofoil NACA0018 and its closed-tip J-shaped profile with a 40% opening ratio, demonstrates a better overall and the self-starting performance.

Chapter 9

Conclusions and future works

9.1 Conclusions

One of the ultimate goals of the present thesis is to investigate the performance of the small-scale H-type VAWTs in order to provide a much better understanding of how these kinds of turbines can self-start which is a major weakness of the VAWT over the HAWT. Although the majority of the studies in the literature have evaluated the turbine self-starting performance with the calculated torque and power coefficients at the fixed low tip speed ratios (e.g. $\lambda<1$) individually, the turbine time-varying start-up process, as well as the overall performance obtained from the dynamic start-up simulations, have been analysed in the present thesis, together with the influences of the mass and friction of the turbine. This investigation sheds significantly more light on the further understanding of the self-starting behaviour of the turbine at different start-up stages.

Furthermore, the J-shaped aerofoil produced by cutting off part of the NACA0018 has been also investigated under the dynamic and static conditions in order to provide an in-depth understanding of the J-shaped profile for its optimum blade design that would be possible to increase the self-starting performance of the VAWTs and decrease its potential performance loss at high λ values. Contrary to the existing literature, in the present thesis, the J-shaped aerofoil with different opening ratios have been analysed under the Darrieus motion considering the crucial operation conditions that mimic those of the VAWTs. Thus, the current study sheds much light on the characteristics of the J-shaped aerofoil from an aerodynamic point of view when it is used in the turbine applications.

Moreover, the self-starting characteristics of the H-type VAWT with the different configurations of the J-shaped profiles have been also analysed based on the 2D CFD start-up simulations. Although several studies in the literature have been conducted to analyse the effect of the J-shaped aerofoil on the turbine self-starting performance, inconsistent results, which prevents a full understanding of the effect of the J-shaped aerofoil, have been observed in the existing literature. Therefore, in the present thesis, a detailed investigation has been carried out in order to provide an in-depth understanding of the effect of the J-shaped aerofoil on the turbine overall and self-starting performance considering the different design parameters.

Additionally, the novel hybrid blade design has been proposed in order to overcome the drawbacks of the conventional aerofoil, which is the low torque generation at the low λ values, and the J-shaped aerofoil, which is the high performance loss at the high λ values. For this purpose, a detailed 3D CFD investigation has been carried out in order to evaluate the performance of the different hybrid blade configurations in terms of the turbine overall and self-starting behaviour.

The main conclusions of the present thesis are summarised in the following subsections. Recommendations for the future works are also presented.

9.1.1 The analyses of the self-starting performance of the H-type VAWT

In order to provide a better understanding of how an H-type VAWTs can gain a self-starting characteristic, a detailed investigation of the turbine start-up process has been conducted. For this purpose, physical properties, such as the inertia of the blades, the number of blades, the chord length, and the mechanical resistance on its dynamic self-starting behaviour and power performance have been investigated by using the dynamic start-up model instead of employing several constant rotational speeds of the turbine. This is discussed in detail in Chapter 5 and conclusions are summarised as follows:

- Even though the H-type VAWTs are lift-driven turbines, in the critical region ($\lambda<1$), the positive drag contribution plays a significant role at some of the blade azimuthal positions to enhance the turbine overall torque generation, thus assists the turbine to self-start. However, in order to achieve a complete start-up process, the lift-driven should be maintained after the λ of 1.

- It has been found that increasing the moment of inertia of the turbine increases the time required to reach the final rotational speed. On the other hand, although the moment of inertia does not significantly affect the final value of the tip speed ratio, the results show that increasing the moment of inertia decreases the amplitude of the fluctuation of the rotational speed at the steady-state conditions.

- Increasing the number of blades has been found to be beneficial for the turbine self-starting capability; however, it significantly reduces the turbine overall performance at high λ values.

- Although the turbine start-up time increases with the decrease in the blade chord length, a much higher final speed is achieved at the steady-state conditions. In addition, a further decreasing in the blade chord length beyond the optimum value is also found to be detrimental to the turbine self-starting behaviour. On the other hand, regardless of the performance at the higher tip speed ratios, the optimum self-starting performance in terms of the faster acceleration is achieved with the higher blade chord length.

- The more reliable results can be obtained when the real resistance due to the bearing, etc. is implemented to the CFD calculations.

9.1.2 Aerodynamics of the J-shaped aerofoils

The most influential parameters, such as tip speed ratio and pitch angle, that affect the turbine performance have been selected in order to analyse their effect on the aerodynamic performance of the J-shaped aerofoil undergoing the Darrieus motion. In addition, the simulations have been performed over a stationary J-shaped aerofoil profile with different opening ratios, and then the results were compared between the NACA0018 and its J-shaped profiles at both positive and negative angles of attack regions. The simulation results also provide a comprehensive analysis of both quantitatively and qualitatively of the differences in the aerodynamic performance of the conventional and J-shaped aerofoil profiles. Based on the investigations that have been carried out in Chapter 6, the following conclusions are drawn:

- Under the dynamic and static aerofoil conditions, the current findings have enhanced the understanding of the aerodynamic behaviour of the J-shaped profile in the positive and the negative angles of attack regions.

- Regardless of the fact that the simulation has been carried out under the dynamic or static conditions, it has been found that a much greater lift force coefficients of the aerofoils investigated increases with the increase in the opening ratio on the aerofoil surface in the positive angles of attack region. However, increasing in the opening ratio decreases the lift performance in the negative angles of attack region while the conventional aerofoil has better lift performance.

- A further delayed dynamic and static stall angles have been found when the opening ratio is increased over the aerofoil surface. This assists the turbine to generate more torque in a wider range of the azimuthal positions, in particular in the upstream part of the turbine.

- The J-shaped aerofoil exhibits a larger peak value of the lift coefficient but also produces a greater drag coefficient compared the conventional aerofoil,

especially in the upstroke motion in the negative angles of attack region where the opening section is located in the suction side of the aerofoil.

- The reason why the J-shaped aerofoil produces a much higher drag at the negative angles of attack region has been found due to the generation of a much greater pressure over the suction side of the J-shaped aerofoil when compared with the conventional aerofoil, particularly in the negative angles of attack region.

9.1.3   H-type VAWT performance considering J-shaped aerofoils

To obtain a better understanding of the effect of the J-shaped aerofoils on the turbine dynamic self-starting behaviour, a series of the 2D CFD-based simulations have been conducted using the J-shaped profiles with the different values of the opening ratio considering the various design parameters. This is discussed in detail in Chapter 7 and the main conclusion are summarised as follows:

- The selection of the surface where the opening is located has a significant influence on the self-starting capability of the turbine. The results show that the turbine with the J-shaped aerofoil having the openings located at the inner surface has been found to be not beneficial for the turbine self-starting at all the opening ratios investigated when compared with those located at the outer surface.

- The performance of the turbine with the J-shaped aerofoil differs depending on the tip speed ratios. It has been observed that increasing the opening ratio increases the torque generation at the low λ values while it decreases the torque generation at the high λ values. Furthermore, at each λ investigated, the J-shaped aerofoil with a larger opening ratio has a higher performance in the upstream part of the turbine while the conventional aerofoil has a higher performance in the downstream. The results obtained in this study appear to support the findings in Chapter 6.

- The advantage of the J-shaped aerofoil over its conventional profile is found to be having a higher positive contribution of the lift force in the upstream

part of the turbine as well as having a higher positive contribution of the drag at the azimuthal position between 120° and 240° at the low λ values.

- At relatively high λ values, although a more significant positive lift contribution has been still obtained with the J-shaped aerofoil in the upstream part of the turbine, it losses the popularity due to a lower positive lift and much higher negative drag contributions in the downstream part of the turbine.

- Among all the aerofoils investigated in the present study, the thinner aerofoil NACA0012 and highly cambered aerofoil NACA4518 do not appear to bring any benefit for the turbine self-starting performance. However, the reversed versions of the cambered aerofoils demonstrate a better self-starting capability compared to their original profiles.

- The optimum self-stating performance for the turbine investigated has been obtained with the J-shaped aerofoil having a slightly positive pitch angle ($\beta = 2°$) while the negative pitch angles do not bring any benefits to the H-type VAWT with the J-shaped aerofoil.

- Applying a real-situation based resistance to the turbine, a range of the opening ratio that assists the turbine to self-start has been found as between 40% and 90%. This finding will help to optimise the future design of the J-shape blade for self-starting VAWTs.

9.1.4 Hybrid Blade performance

Based on the 2D CFD simulations, a hybrid blade design methodology has been developed and the torque performance of the turbine with the proposed hybrid blade designs at the different λ values has been analysed. A series of 3D CFD simulations have been conducted to find out the 3D effect of the opening location of the J-shaped profile along the z direction of the blade's length on the turbine overall and self-starting performance. This is discussed in detail in Chapter 8 and conclusions are summarised as follows:

- Although the proposed design methodology has been based on the 2D CFD calculations, it enables a quicker prediction of the aerodynamic performance of the proposed hybrid blades compared to the 3D-based CFD simulations.

- Different hybrid blade configurations that were thought to have a significant impact on the turbine self-starting performance have been proposed. The J-shaped profile has been placed at both tips and middle of the blades considering the open and closed tips.

- The open and closed-tips of the J-shaped aerofoil used in the hybrid blade design at the top and bottom sides have a significant influence on the turbine self-starting behaviour in terms of the start-up time and final tip speed ratio at the final steady-state conditions. The intensity of the vortex structures generated at the blade tips, which affects the pressure difference, has been found the result of the performance difference between these configurations.

- In contrast with the J-shaped aerofoil with an open or closed-tips, it has been observed that the location of the J-shaped profile in the hybrid blade span does not significantly affect the turbine self-starting performance.

9.2   Recommendations and future works

The work presented in this thesis has provided a very important step towards a further understanding of the self-starting capability of the small-scale H-type VAWTs considering the J-shaped aerofoil. The self-starting behaviour of the H-type VAWT with conventional and the J-shaped aerofoil has been explained using a combination of the turbine performance coefficients, dynamic start-up characteristics and flow physics. According to the interesting research carried out in this thesis, several recommendations and the future works are summarised as follows:

- It would be interesting to experimentally-investigate the effect of the moment of inertia on the turbine self-starting performance, especially the final rotational speed at the steady-state condition.

- In the present thesis, a 2D CFD model has been used due to its simplicity. However, a full 3D CFD model is recommended to investigate the effect of the J-shaped aerofoil on the turbine start-up and overall performance since the 2D CFD simulations in which the blade span and supporting arms were not taken

into account. This will enable a better comparison between the conventional and J-shaped aerofoils.

- In order to generalise the effect of the J-shaped aerofoil with different opening ratios on the turbine performance, a further investigation would be interesting under various operating conditions, such as different high and low wind speeds.

- Since a relatively thin sheet material used for the J-shaped profile compared to the conventional aerofoil, an investigation on the types and the thickness of the material would be an interesting research topic by considering variation and high-strength design method of the H-type VAWT having a J-shaped aerofoil.

- It is recommended to conduct further studies on the hybrid blade design to provide an in-depth understanding of the different design configurations and solid conclusions about the blade behaviour.

- It would be beneficial to conduct a study that investigates the effect of the different types of tips of the 3D hybrid blade design, such as winglet, on the self-starting performance.

- Apart from the aerodynamic performance comparison between the Hybrid blade and the Hybrid turbine, a further study on the techno-economic analysis and Life Cycle analysis is recommended in order to indicate the advantages of the Hybrid blade over the Hybrid turbine.

- In order to provide a further understanding of the effect of the hybrid blade design on the turbine overall and self-starting performance, carrying on an experimental investigation would be beneficial.

References

[1]   Kaya MN, Kose F, Ingham D, Ma L, Pourkashanian M. Aerodynamic performance of a horizontal axis wind turbine with forward and backward swept blades. J Wind Eng Ind Aerodyn 2018;176:166–73.

[2]   Abolhosseini S, Heshmati A, Altmann J. A review of renewable energy supply and energy efficiency technologies. IZA Discuss Pap Ser 2014:1–36.

[3]   Juneja SK, Sobti N, Wais A. Solar Energy: A Clean Energy System. 2012.

[4]   Lee J, Zhao F. GWEC Global Wind Report. Wind Energy Technol 2020:78.

[5]   Toja-Silva F, Colmenar-Santos A, Castro-Gil M. Urban wind energy exploitation systems: Behaviour under multidirectional flow conditions - Opportunities and challenges. Renew Sustain Energy Rev 2013;24:364–78.

[6]   Lee YT, Lim HC. Numerical study of the aerodynamic performance of a 500W Darrieus-type vertical-axis wind turbine. Renew Energy 2015;83:407–15.

[7]   Deshmukh SA. International Journal of Pure and Applied Research in Engineering and Technology 2013;1:187–91.

[8]   Albadi M. On Techno-economic Evaluation of Wind-based DG 2016.

[9]   Bos R. Self-starting of a small urban Darrieus rotor 2012:1.

[10]   Sheldahl RE, Klimas PC, Feltz L V. Aerodynamic performance of a 5-metre-diameter Darrieus turbine with extruded aluminum NACA-0015 blades. 1980;4.

[11]   Kentfield JA. Fundamentals wind-driven water. CRC Press 1996.

[12]   Baker JR. Features to aid or enable self starting of fixed pitch low solidity vertical axis wind turbines. J Wind Eng Ind Aerodyn 1983;15:369–80.

[13]   Hill N, Dominy R, Ingram G, Dominy J. Darrieus turbines : the physics of self-starting 2008;223:21–9.

[14]   Dominy R, Lunt P, Bickerdyke A, Dominy J. Self-starting capability of a Darrieus turbine. Proc Inst Mech Eng Part A J Power Energy 2007;221:111–20.

[15]   Almohammadi KM. Optimization of a CFD Based Design of a Straight blade Vertical Axis Wind Turbine (SB-VAWT). The University of Leeds, PhD thesis, 2014.

[16]   Longhuan DS. Numerical and Experimental Investigations of Darrieus Wind Turbine Start-up and Operation. Durham University, PhD Thesis, 2016.

[17] Worasinchai S. Small Wind Turbine Starting Behaviour. Durham University, PhD Thesis, 2012.

[18] Kinzel M, Mulligan Q, Dabiri JO. Energy exchange in an array of vertical-axis wind turbines. J Turbul 2012;13:1–13.

[19] Dabiri JO. Potential order-of-magnitude enhancement of wind farm power density via counter-rotating vertical-axis wind turbine arrays. J Renew Sustain Energy 2011;3.

[20] Mertens S, Van Kuik G, Van Bussel G. Performance of an H-Darrieus in the skewed flow on a roof. J Sol Energy Eng Trans ASME 2003;125:433–40.

[21] B. K. Kirke. Evaluation of Self-Starting Vertical Axis Wind Turbines for Stand-Alone Appllications. Griffith University, Australia, PhD Thesis, 1998.

[22] Ragheb M. Optimal rotor tip speed ratio, 2014.

[23] Afgan I. Marine Energy: Wind, Wave and Tidal. 2015.

[24] Templin RJ. Aerodynamic performance theory for the NRC vertical-axis wind turbine. STIN 1974;16618:76.

[25] Mays, I., & Holmes BA. Commercial development of the variable geometry vertical axis windmill. Int Power Gener Surrey, UK 1979.

[26] Consul C a, Willden RHJ, Ferrer E, McCulloch MD. Influence of Solidity on the Performance of a Cross-Flow Turbine. Proc 8th Eur Wave Tidal Energy Conf Uppsala, Sweden 2009:484–93.

[27] Sheldahl RE, Blackwell BF, Feltz L V. Wind Tunnel Performance Data for Two- and Three-Bucket Savonius Rotors. J Energy 1978;2:160–4.

[28] Worstell MH. Aerodynamic performance of the 17-m-diameter Darrieus wind turbine in the three-bladed configuration An addendum. STIN 1980;80:26857.

[29] Aerospace A, Meeting S. Revisiting the Vertical-axix Wind-Trubine Design using Advanced Computational Fuild Dynamics 2005.

[30] Howell R, Qin N, Edwards J, Durrani N. Wind tunnel and numerical study of a small vertical axis wind turbine. Renew Energy 2010;35:412–22.

[31] Castelli MR, Betta S De, Benini E. Effect of Blade Number on a Straight-Bladed Vertical-Axis Darreius Wind Turbine. World Acad Sci Eng Technol 2012;6:256–62.

[32] Mays, I. and Musgrove PJ. Performance of the variable geometry vertical axis wind turbine at high and low solidities. Wien 1979:48–56.

[33] Simhan KA. Review of Calculation Methods for the Determination of Performance Characteristics of Vertical Axis Wind Energy Converters with Special Reference to the Influence of Solidity and Starting Characteristics

Proc. Eur Wind Energy Conf, Hamburg, Ger n.d.

[34] Kirke, B.K. and Lazauskas L. Enhancing the performance of vertical axis wind turbine using a simple variable pitch system. Wind Eng 1991;187–195.

[35] Mohamed MH. Performance investigation of H-rotor Darrieus turbine with new airfoil shapes. Energy 2012;47:522–30.

[36] Eboibi O, Danao LA, Howell R, Edwards JM. A numerical study of the influence of blade profile and solidity on the performance of Vertical Axis Wind Turbines. 51st AIAA Aerosp Sci Meet Incl New Horizons Forum Aerosp Expo 2013 2013:1–16.

[37] Migliore, P.G. and Fritschen JR. Darrieus wind-turbine airfoil configurations. STIN 1982;83:21600.

[38] Berg DE. Customized airfoils and their impact on VAWT cost of energy. Sandia Natl Labs, Albuquerque, NM 1990:25–8.

[39] Klimas PC. Tailored airfoils for vertical axis wind turbines. Sandia Natl Labs, Albuquerque, NM 1984;4.

[40] Masson C, Leclerc C, Paraschivoiu I. Appropriate Dynamic-Stall Models for Performance. Int J Rotating Mach 1998;4:129–39.

[41] Healy JV. The influence of blade camber on the output of vertical-axis wind turbines. Wind Eng 1978:146–55.

[42] Bianchini A. GT2011-45882 2011:1–10.

[43] Angell, R. K., Musgrove, P. J., & Galbraith RM. Unsteady wind tunnel testing of thick section aerofoils for use on large scale vertical axis wind turbines. Proceeding 10th BWEA Conf 1988:195–203.

[44] Islam M, Ting DSK, Fartaj A. Desirable airfoil features for smaller-capacity straight-bladed VAWT. Wind Eng 2007;31:165–96.

[45] McIntosh SC. Wind energy for the built environment. 2009.

[46] Claessens MC. The design and testing of airfoils for application in small vertical axis wind turbines. Masters Thesis 2006:1–137.

[47] Staelens, Y., Saeed, F. and Paraschivoiu I. A straight-bladed variable-pitch VAWT concept for improved power generation. Wind Energy Symp 2003;75944:146–54.

[48] Bossanyi EA. Wind turbine control for load reduction. Wind Energy An Int J Prog Appl Wind Power Convers Technol 2003;6(3):229–44.

[49] Grylls, W., Dale, B., & Sarre PE. A theoretical and experimental investigation into the variable pitch vertical axis wind turbine. Second Int Symp Wind Energy Syst 1978;3.

[50] Soraghan, C.E., Leithead, W.E., Feuchtwang, J. and Yue H. Double multiple

streamtube model for variable pitch vertical axis wind turbines. 31st AIAA Appl Aerodyn Conf 2013:2802.

[51] Klimas, P.C. and Worstell MH. Effects of blade preset pitch/offset on curved-blade Darrieus vertical axis wind turbine performance 1981.

[52] Manwell, J.F., McGowan, J.G. and Rogers AL. Wind energy explained theory, design and application. John Wiley Sons 2010.

[53] McCroskey, W.J., McAlister, K.W., Carr, L.W. and Pucci SL. An experimental study of dynamic stall on advanced airfoil section. Press Force Data 1982;Volume 2.

[54] Carr, L.W., McAlister, K.W. and McCroskey WJ. Analysis of the development of dynamic stall based on oscillating airfoil experiments 1977.

[55] Simão Ferreira CJ, Bijl H, Van Bussel G, Van Kuik G. Simulating Dynamic Stall in a 2D VAWT: Modeling strategy, verification and validation with Particle Image Velocimetry data. J Phys Conf Ser 2007;75.

[56] Tsang KKY, So RMC, Leung RCK, Wang XQ. Dynamic stall behavior from unsteady force measurements. J Fluids Struct 2008;24:129–50.

[57] Wang S, Ingham DB, Ma L, Pourkashanian M, Tao Z. Numerical investigations on dynamic stall of low Reynolds number flow around oscillating airfoils. Comput Fluids 2010;39:1529–41.

[58] Fujisawa N, Shibuya S. Observations of dynamic stall on turbine blades. J Transp Eng 1999;125:201–14.

[59] Leishman GJ. Principles of helicopter aerodynamics with CD extra. Cambridge Univ Press 2006.

[60] Ebert PR, Wood DH. Observations of the starting behavior of a small horizontal- axis wind turbine. Renew Energy 1997;12:245–57.

[61] Lunt PAV. An aerodynamic model for a vertical-axis wind turbine. 2005.

[62] Chua KL. Darrieus Wind turbine-analysis 2002:Available from httpwindturbine-analysis.com.

[63] Hill N, Dominy R, Ingram G, Dominy J. Darrieus turbines: The physics of self-starting. Proc Inst Mech Eng Part A J Power Energy 2009;223:21–9.

[64] Dominy RG, Lunt P, Bickerdyke A, Dominy J. Self-starting capability of a Darrieus turbine. Proc Inst Mech Eng Part A J Power Energy 2007;221:111–20.

[65] Dumitrescu, H., Dumitrache, A., Popescu, C.L., Popescu, M.O., Frunzulica, F. and Craciunescu A. Wind tunnel experiments on vertical-axis wind turbines with straight blades. Int Conf Renew Energies Power Qual 2004.

[66] Du L, Ingram G, Dominy RG. Experimental study of the effects of turbine

solidity, blade profile, pitch angle, surface roughness, and aspect ratio on the H-Darrieus wind turbine self-starting and overall performance. Energy Sci Eng 2019;7:2421–36.

[67] Beri H, Yao Y. Numerical Simulation of Unsteady Flow to Show Self-starting of Vertical Axis Wind Turbine Using Fluent. J Appl Sci 2011:962–70.

[68] Untaroiu A, Wood HG, Allaire PE, Ribando RJ. Investigation of self-starting capability of vertical axis wind turbines using a computational fluid dynamics approach. J Sol Energy Eng Trans ASME 2011;133:1–8.

[69] Worasinchai S, Ingram GL, Dominy RG. The Physics of H-Darrieus Turbines Self-Starting Capability: Flapping-Wing Perspective. Proc ASME Turbo Expo 2012 2012.

[70] Rossetti A, Pavesi G. Comparison of different numerical approaches to the study of the H-Darrieus turbines start-up. Renew Energy 2013;50:7–19.

[71] Chen CC, Kuo CH. Effects of pitch angle and blade camber on flow characteristics and performance of small-size Darrieus VAWT. J Vis 2013;16:65–74.

[72] Batista NC, Melício R, Matias JCO, Catalão JPS. New blade profile for darrieus wind turbines capable to self-start. IET Conf Publ 2011;2011.

[73] Zhu J, Huang H, Shen H. Self-starting aerodynamics analysis of vertical axis wind turbine. Adv Mech Eng 2015;7:1–12.

[74] Zhu J yang, Jiang L, Zhao H. Effect of wind fluctuating on self-starting aerodynamics characteristics of VAWT. J Cent South Univ 2016;23:2075–82.

[75] Torabi M, Zal E, Mustapha F, Wiriadidjaja S. Study on start-up characteristics of H-Darrieus vertical axis wind turbines comprising NACA 4-digit series blade airfoils. Energy 2016;112:528–37.

[76] Sengupta AR, Biswas A, Gupta R. Studies of some high solidity symmetrical and unsymmetrical blade H-Darrieus rotors with respect to starting characteristics, dynamic performances and flow physics in low wind streams. Renew Energy 2016;93:536–47.

[77] Douak M, Aouachria Z, Rabehi R, Allam N. Wind energy systems: Analysis of the self-starting physics of vertical axis wind turbine. Renew Sustain Energy Rev 2018;81:1602–10.

[78] Hosseini A, Goudarzi N. Design and CFD study of a hybrid vertical-axis wind turbine by employing a combined Bach-type and H-Darrieus rotor systems. Energy Convers Manag 2019;189:49–59.

[79] Gavaldà J, Massons J, Díaz F. Experimental study on a self-adapting Darrieus-Savonius wind machine. Sol Wind Technol 1990;7:457–61.

[80] Gupta R, Biswas A. CFD analysis of flow physics and aerodynamic performance of a combined three-bucket Savonius and three-bladed darrieus turbine. Int J Green Energy 2011;8:209–33.

[81] Bhuyan S, Biswas A. Investigations on self-starting and performance characteristics of simple H and hybrid H-Savonius vertical axis wind rotors. Energy Convers Manag 2014;87:859–67.

[82] Liang X, Fu S, Ou B, Wu C, Chao CYH, Pi K. A computational study of the effects of the radius ratio and attachment angle on the performance of a Darrieus-Savonius combined wind turbine. Renew Energy 2017;113:329–34.

[83] Chen J, Yang H, Yang M, Xu H. The effect of the opening ratio and location on the performance of a novel vertical axis Darrieus turbine. Energy 2015;89:819–34.

[84] Zamani M, Maghrebi MJ, Varedi SR. Starting torque improvement using J-shaped straight-bladed Darrieus vertical axis wind turbine by means of numerical simulation. Renew Energy 2016;95:109–26.

[85] Mohamed MH. Criticism study of J-Shaped darrieus wind turbine: Performance evaluation and noise generation assessment. Energy 2019;177:367–85.

[86] Sastry S. Lyapunov Stability Theory In Nonlinear Systems. Interdisciplinary Applied Mathematics, vol 10. Springer 1999, New York, NY.

[87] Abdalrahman G, Pitch angle control for a small-scale Darrieus vertical axis wind turbine with straight blades (H-Type VAWT). Phd Thesis in University of Waterloo, 2019.

[88] I. Paraschivoiu. Wind turbine design: with emphasis on Darrieus concept. Presses inter Polytechnique; 2002.

[89] Templin RJ. Aerodynamic performance theory for the NRC vertical-axis wind turbine. NASA STI/Recon Tech Rep N 1974:76.

[90] Islam M, Ting DSK, Fartaj A. Aerodynamic models for Darrieus-type straight-bladed vertical axis wind turbines. Renew Sustain Energy Rev 2008;12:1087–109.

[91] R. E. Wilson and P. B. S. Lissaman. Machines power wind of aerodynamics. Natl Sci Found 1974.

[92] Strickland JH. A performance prediction model for the Darrieus turbine. Cambridge Univ Press 1976.

[93] Paraschivoiu I. Double-multiple streamtube model for Darrieus wind turbines. Second DOE/NASA Wind Turbines Dyn Work NASA CP-2186, Cleveland, OH 1981:19–25.

[94] E. E. Lapin. Theoretical performance of vertical axis wind turbines. Am.

Soc. Mech. Eng. 1, 1975.

[95]   I. Paraschivoiu and F. Delclauxt. Double Multiple Streamtube Model with Recent Improvements. Energy 1982;7:250–5.

[96]   Saber HE, Attia EM, El Gamal HA. Analysis of Straight Bladed Vertical Axis Wind Turbine. Int J Eng Res Technol 2015;4:714–23.

[97]   Larsen HC. Summary of a vortex theory for the Cyclogyro. Proc. Second US Natl. Conf. Wind Eng. Res., 1975.

[98]   J. Fanucci and R. Walter. Innovative wind machines: the theoretical performance of a vertical-axis wind turbine. Proc. Vert. -axis Wind turbine Technol. Work. Sandia Lab. SAND 76-5586, 1976, p. 61–95.

[99]   H. Dumitrescu, V. Cardos, A. Dumitrache and FF. The Publishing House Low-Frequency Noise Prediction of Vertical Axis Wind Turbines. Proceedings 2010;11:47–54.

[100] Ffowcs Williams, J. E. and Hawkings DL. Sound generation by turbulence and surface in arbitrary motion. Trans R Soc Lond A 1969:321–42.

[101] Pawsey NCK. Development and evaluation of passive variable-pitch vertical axis wind turbines. PhD Thesis, School of Mechanical and Manufacturing Engineering, University of New South Wales, Australia, 2002.

[102] Ir. H. Hirsch and A.C. Manda. A Cascade Theory for the Aerodynamic Performance of Darrieus Wind Turbines. Wind Eng 1987;11:164–75.

[103] R. E. Gormont. A mathematical model of unsteady aerodynamics and radial flow for application to helicopter rotors. Boeing Vertol Co Philadelphia Pa 1973.

[104] F. L. Ponta and P. M. Jacovkis. A vortex model for Darrieus turbine using finite element techniques. Renew Energy 2001;24:1–18.

[105] Blazek J. Computational fluid dynamics: principles and applications. Butterworth-Heinemann 2015.

[106] Jain S, Saha UK. The State-of-the-Art Technology of H-Type Darrieus Wind Turbine Rotors. J Energy Resour Technol 2020;142.

[107] Ferziger JH. Large Eddy Simulation: Its Role in Turbulence Research, in Theoretical Approaches to Turbulence. Springer, New York, NY 1985:51–72.

[108] Reynolds WC. The potential and limitations of direct and large eddy simulations. In Whither turbulence? Springer, Berlin, Heidelberg 1990:313–43.

[109] Batchelor G. Introduction to Fluid Mechanics. 2000.

[110] Deardorff JW. A numerical study of three-dimensional turbulent channel

flow at large Reynolds numbers. J Fluid Mech 1970;41:453–80.

[111]   Davidson L. An introduction to turbulence models. 2015.

[112]   Yakhot, V. S. A. S. T. B. C. G., Orszag, S. A., Thangam, S., Gatski, T. B., & Speziale CG. Development of turbulence models for shear flows by a double expansion technique. Phys Fluids A Fluid Dyn 1992:510–152.

[113]   Pouraria, H., & Park WG. Comparison of different two equation turbulence models for studying the effect of cold outlet diameter on cooling performance of vortex tube. 2010 Int Conf Mech Electr Technol 2010:304–8.

[114]   Patel, V. C., Rodi, W., & Scheuerer G. Turbulence models for near-wall and low Reynolds number flows-a review. AIAA J 1985;23(9):1308–19.

[115]   Wilcox DC. Turbulence modeling for CFD. La Canada, CA DCW Ind 1998;Vol 2:103–217.

[116]   d'Alençon, J. P., & Silva-Llanca L. Two-dimensional numerical analysis of a low-re turbulent impinging synthetic jet. 2016 15th IEEE Intersoc. Conf. Therm. Thermomechanical Phenom. Electron. Syst., 2016.

[117]   Menter FR. Two-equation eddy-viscosity turbulence models for engineering applications. AIAA J 1994;32:1598–605.

[118]   Menter, F. R., Langtry, R. B., Likki, S. R., Suzen, Y. B., Huang, P. G., & Völker S. A correlation-based transition model using local variables—part I: model formulation. 2006.

[119]   Menter FR, Langtry R, Vollker S, Huang PG. Transition Modelling for General Purpose CFD Codes. Eng Turbul Model Exp 6 2005:31–48.

[120]   Raciti Castelli M, Englaro A, Benini E. The Darrieus wind turbine: Proposal for a new performance prediction model based on CFD. Energy 2011;36:4919–34.

[121]   Edwards JM, Angelo Danao L, Howell RJ. Novel Experimental Power Curve Determination and Computational Methods for the Performance Analysis of Vertical Axis Wind Turbines. J Sol Energy Eng 2012;134:031008.

[122]   Amet E, Maître T, Pellone C, Achard JL. 2D numerical simulations of blade-vortex interaction in a darrieus turbine. J Fluids Eng Trans ASME 2009;131:1111031–11110315.

[123]   Danao LA, Qin N, Howell R. A numerical study of blade thickness and camber effects on vertical axis wind turbines. Proc Inst Mech Eng Part A J Power Energy 2012;226:867–81.

[124]   Akay B, Ragni D, Ferreira CS, Bussel GJW Van. Investigation of the root flow in a Horizontal Axis. Wind Energy 2013:1–20.

[125]   Lanzafame R, Mauro S, Messina M. 2D CFD modeling of H-Darrieus Wind

Turbines using a transition turbulence model. Energy Procedia 2014;45:131–40.

[126] Daróczy L, Janiga G, Petrasch K, Webner M, Thévenin D. Comparative analysis of turbulence models for the aerodynamic simulation of H-Darrieus rotors. Energy 2015;90:680–90.

[127] Balduzzi F, Bianchini A, Maleci R, Ferrara G, Ferrari L. Critical issues in the CFD simulation of Darrieus wind turbines. Renew Energy 2016;85:419–35.

[128] Subramanian A, Yogesh SA, Sivanandan H, Giri A, Vasudevan M, Mugundhan V, et al. Effect of airfoil and solidity on performance of small scale vertical axis wind turbine using three dimensional CFD model. Energy 2017;133:179–90.

[129] McLaren KW. A numerical and experimental study of unsteady loading of high solidity vertical axis wind turbines. Doctoral dissertation, 2011.

[130] Chandramouli S, Premsai TP, Prithviraj P, Mugundhan V, Velamati RK. Numerical analysis of effect of pitch angle on a small scale vertical axis wind turbine. International Journal of Renewable Energy Research (IJRER). 2014 Dec 25;4(4):929-35.

[131] Wang Y, Shen S, Li G, Huang D, Zheng Z. Investigation on aerodynamic performance of vertical axis wind turbine with different series airfoil shapes. Renew Energy 2018;126:801–18.

[132] Ma N, Lei H, Han Z, Zhou D, Bao Y, Zhang K, et al. Airfoil optimization to improve power performance of a high-solidity vertical axis wind turbine at a moderate tip speed ratio. Energy 2018;150:236–52.

[133] Elsakka MM, Ingham DB, Ma L, Pourkashanian M. CFD analysis of the angle of attack for a vertical axis wind turbine blade. Energy Convers Manag 2019;182:154–65.

[134] Li Q, Maeda T, Kamada Y, Murata J, Kawabata T, Shimizu K. Wind tunnel and numerical study of a straight-bladed vertical axis wind turbine in three-dimensional analysis (Part I: For predicting aerodynamic loads and performance). Energy 2016;106:443–52.

[135] Mohamed MH, Dessoky A, Alqurashi F. Blade shape effect on the behavior of the H-rotor Darrieus wind turbine: Performance investigation and force analysis. Energy 2019;179:1217–34.

[136] Mazarbhuiya HM, Biswas A, Sharma KK. Blade thickness effect on the aerodynamic performance of an asymmetric NACA six series blade vertical axis wind turbine in low wind speed. International Journal of Green Energy. 2020 Jan 26;17(2):171-9.

[137] Rainbird J. The aerodynamic development of a vertical axis wind turbine. MEng Proj ReporSchool Eng Univ Durham, UK 2007.

[138] Wekesa DW, Wang C, Wei Y, Zhu W. Experimental and numerical study of turbulence effect on aerodynamic performance of a small-scale vertical axis wind turbine. J Wind Eng Ind Aerodyn 2016;157:1–14.

[139] Zhu J, Huang H, Shen H. Self-starting aerodynamics analysis of vertical axis wind turbine. Advances in Mechanical Engineering. 2015 Dec 8;7(12):1687814015620968.

[140] Song C, Zheng Y, Zhao Z, Zhang Y, Li C, Jiang H. Investigation of meshing strategies and turbulence models of computational fluid dynamics simulations of vertical axis wind turbines. J Renew Sustain Energy 2015;7.

[141] D'Alencon JP, Silva-Llanca L. Two-dimensional numerical analysis of a low-re turbulent impinging synthetic jet. Proc 15th Intersoc Conf Therm Thermomechanical Phenom Electron Syst ITherm 2016 2016:921–9.

[142] Menter FR. Review of the shear-stress transport turbulence model experience from an industrial perspective. Int J Comut Fluid Dyn 2009;23:305–16.

[143] Langtry RB, Menter FR, Likki SR, Suzen YB, Huang PG, Völker S. A correlation-based transition model using local variables - Part II: Test cases and industrial applications. J Turbomach 2006;128:423–34.

[144] Menter FR, Langtry R, Völker S, Huang PG. Transition Modelling for General Purpose CFD Codes. Eng Turbul Model Exp 6 2005:31–48.

[145] Castelli MR, Ardizzon G, Battisti L, Benini E, Pavesi G. Modeling Strategy and Numerical Validation. Proc ASME 2010 Int Mech Eng Congr Expo 2010:1–10.

[146] Bedon G, De Betta S, Benini E. A computational assessment of the aerodynamic performance of a tilted Darrieus wind turbine. J Wind Eng Ind Aerodyn 2015;145:263–9.

[147] Nobile R, Vahdati M, Barlow JF, Mewburn-Crook A. Unsteady flow simulation of a vertical axis augmented wind turbine: A two-dimensional study. J Wind Eng Ind Aerodyn 2014;125:168–79.

[148] Zhang LX, Liang YB, Liu XH, Jiao QF, Guo J. Aerodynamic performance prediction of straight-bladed vertical axis wind turbine based on CFD. Adv Mech Eng 2013;2013.

[149] Posa A. Influence of Tip Speed Ratio on wake features of a Vertical Axis Wind Turbine. J Wind Eng Ind Aerodyn 2020;197:104076.

[150] Li Q, Maeda T, Kamada Y, Hiromori Y, Nakai A, Kasuya T. Study on stall behavior of a straight-bladed vertical axis wind turbine with numerical and experimental investigations. J Wind Eng Ind Aerodyn 2017;164:1–12.

[151] Rezaeiha A, Kalkman I, Blocken B. CFD simulation of a vertical axis wind turbine operating at a moderate tip speed ratio: Guidelines for minimum

domain size and azimuthal increment. Renew Energy 2017;107:373–85.

[152] ANSYS Inc. Introduction to Ansys Fluent-Turbulence Modeling 2014.

[153] Launder B. E., B. SD. MAN - ANSYS Fluent User's Guide Releasde 15.0. Knowl Creat Diffus Util 2013;15317:724–46.

[154] Sun X, Zhu J, Hanif A, Li Z, Sun G. Effects of blade shape and its corresponding moment of inertia on self-starting and power extraction performance of the novel bowl-shaped floating straight-bladed vertical axis wind turbine. Sustain Energy Technol Assessments 2020;38:100648.

[155] Roache PJ. Quantification of Uncertainty in Computational Fluid Dynamics. Annu Rev Fluid Mech 1997;29:123–60.

[156] Rezaeiha A, Montazeri H, Blocken B. Towards accurate CFD simulations of vertical axis wind turbines at different tip speed ratios and solidities: Guidelines for azimuthal increment, domain size and convergence. Energy Convers Manag 2018;156:301–16.

[157] Untaroiu A, Wood HG, Allaire PE, Ribando RJ. Investigation of Self-Starting Capability of Vertical Axis Wind Turbines Using a Computational Fluid Dynamics Approach. J Sol Energy Eng 2011;133:041010.

[158] Rezaeiha A, Montazeri H, Blocken B. Characterization of aerodynamic performance of vertical axis wind turbines: Impact of operational parameters. Energy Convers Manag 2018;169:45–77.

[159] Sheldahl RE, Klimas PC. Aerodynamic characteristics of seven symmetrical airfoil sections through 180-degree angle of attack for use in aerodynamic analysis of vertical axis wind turbines. 1981.

[160] Zamani M, Nazari S, Moshizi SA, Maghrebi MJ. Three dimensional simulation of J-shaped Darrieus vertical axis wind turbine. Energy 2016;116:1243–55.

[161] Li Q, Maeda T, Kamada Y, Murata J, Furukawa K, Yamamoto M. Effect of number of blades on aerodynamic forces on a straight-bladed Vertical Axis Wind Turbine. Energy 2015;90:784–95.

[162] Aso T, Aida T, Seki K. Bearing resistance of wind turbine generator system. Electr Eng Japan (English Transl Denki Gakkai Ronbunshi) 2016;194:64–73.

[163] Anderson WJ. Rolling-Element Bearings Rolling-Element Bearings 1983.

[164] Leishman, J. G., & Beddoes TS. A generalised model for airfoil unsteady aerodynamic behaviour and dynamic stall using the indicial method. Proc. 42nd Annu. forum Am. Helicopter Soc., 1986, p. 243–65.

[165] McCroskey, W. J., Carr, L. W., & McAlister KW. Dynamic stall experiments on oscillating airfoils. Aiaa J 1976:57–63.

[166] Tarzanin FJ. Prediction of control loads due to blade stall. J Am Helicopter

Soc 1972.

[167] Larsen JW, Nielsen SRK, Krenk S. Dynamic stall model for wind turbine airfoils. J Fluids Struct 2007;23:959–82.

[168] Lee T, Gerontakos P. Investigation of flow over an oscillating airfoil. J Fluid Mech 2004;512:313–41.

[169] Bangga G. Numerical studies on dynamic stall characteristics of a wind turbine airfoil. J Mech Sci Technol 2019;33:1257–62.

[170] Yu GH, Zhu XC, Du ZH. Numerical simulation of a wind turbine airfoil: Dynamic stall and comparison with experiments. Proc Inst Mech Eng Part A J Power Energy 2010;224:657–77.

[171] Gharali K, Johnson DA. Numerical modeling of an S809 airfoil under dynamic stall, erosion and high reduced frequencies. Appl Energy 2012;93:45–52.

[172] Allet A, Hallé S, Paraschivolu I. Numerical simulation of dynamic stall around an airfoil in darrieus motion. J Sol Energy Eng Trans ASME 1999;121:69–76.

[173] Mazarbhuiya HMSM, Biswas A, Sharma KK. Low wind speed aerodynamics of asymmetric blade H-Darrieus wind turbine-its desired blade pitch for performance improvement in the built environment. J Brazilian Soc Mech Sci Eng 2020;42:1–16.

[174] Eboibi O, Danao LAM, Robert J. Experimental Investigation of the Influence of Solidity on the Performance and Flow Field Aerodynamics of Vertical Axis Wind Turbines at Low Reynolds Numbers 2016:0–21.

[175] Li Q, Maeda T, Kamada Y, Murata J, Shimizu K, Ogasawara T, et al. Effect of solidity on aerodynamic forces around straight-bladed vertical axis wind turbine by wind tunnel experiments (depending on number of blades). Renew Energy 2016;96:928–39.

[176] Rosado Hau N, Ma L, Ingham D, Pourkashanian M. A critical analysis of the stall onset in vertical axis wind turbines. J Wind Eng Ind Aerodyn 2020;204.

[177] Geng F, Kalkman I, Suiker ASJ, Blocken B. Sensitivity analysis of airfoil aerodynamics during pitching motion at a Reynolds number of 1.35×105. J Wind Eng Ind Aerodyn 2018;183:315–32.

[178] Gharali K, Johnson DA. Dynamic stall simulation of a pitching airfoil under unsteady freestream velocity. J Fluids Struct 2013;42:228–44.

[179] Karbasian, H. R., & Kim KC. Numerical investigations on flow structure and behavior of vortices in the dynamic stall of an oscillating pitching hydrofoil. Ocean Eng 2016;127:200–11.

[180] Celik Y, Ma L, Ingham D, Pourkashanian M. Journal of Wind Engineering

& Industrial Aerodynamics Aerodynamic investigation of the start-up process of H-type vertical axis wind turbines using CFD. J Wind Eng Ind Aerodyn 2020;204.

[181] A. Sharma MRV. Airfoil Thickness Effects on Dynamic Stall Onset. 23rd AIAA Comput. Fluid Dyn. Conf., 2013.

[182] Zhang T, Wang Z, Huang W, Ingham D, Ma L, Pourkashanian M. A numerical study on choosing the best configuration of the blade for vertical axis wind turbines. J Wind Eng Ind Aerodyn 2020;201:104162.

[183] Gerakopulos R, Boutilier M, Yarusevych S. Aerodynamic characterization of a NACA 0018 airfoil at low Reynolds numbers. In 40th Fluid dynamics conference and Exhibit 2010 (p. 4629).

[184] Wekesa DW, Wang C, Wei Y, Danao LAM. Influence of operating conditions on unsteady wind performance of vertical axis wind turbines operating within a fluctuating free-stream: A numerical study. J Wind Eng Ind Aerodyn 2014;135:76–89.

[185] Shukla DL, Mehta AU, Modi K V. Dynamic overset 2D CFD numerical simulation of a small vertical axis wind turbine. Int J Ambient Energy 2020;41:1415–22.

[186] Kirke, B.K. and Lazauskas L. Enhancing the performance of vertical axis wind turbine using a simple variable pitch system. Wind Eng 1991:187–95.

[187] Sagharichi A, Maghrebi MJ, Arabgolarcheh A. Variable pitch blades: An approach for improving performance of Darrieus wind turbine. J Renew Sustain Energy 2016;8.

[188] Zhang T tian, Elsakka M, Huang W, Wang Z guo, Ingham DB, Ma L, et al. Winglet design for vertical axis wind turbines based on a design of experiment and CFD approach. Energy Convers Manag 2019;195:712–26.

[189] Franchina N, Kouaissah O, Persico G, Savini M. Three-dimensional CFD simulation and experimental assessment of the performance of a h-shape vertical-axis wind turbine at design and off-design conditions. Int J Turbomachinery, Propuls Power 2019;4.

[190] Mannion B, Leen SB, Nash S. A two and three-dimensional CFD investigation into performance prediction and wake characterisation of a vertical axis turbine. J Renew Sustain Energy 2018;10.

[191] Orlandi A, Collu M, Zanforlin S, Shires A. 3D URANS analysis of a vertical axis wind turbine in skewed flows. J Wind Eng Ind Aerodyn 2015;147:77–84.

[192] Franchina N, Persico G, Savini M. Three-dimensional unsteady aerodynamics of a H-shaped vertical axis wind turbine over the full operating range. J Wind Eng Ind Aerodyn 2020;206:104273.

Appendix

UDF library

The appendix provides the source of the User-defined Function codes that have been linked to the ANSYS Fluent solver under the dynamic mesh zone sections. In UDF 1, a UDF that includes the physical properties such as turbine mass and moment of inertia has been employed in the 2D and 3D CFD simulations to calculate the turbine rotational speed. The moment of the inertia of the turbine has been calculated depending on the per unit span. In UDF 2, a UDF code has been utilised in the 2D CFD turbine dynamic start-up simulations in order to consider the resistance due to the bearing friction. In UDF 3, in order to calculate the aerodynamic force coefficients, such as lift, drag and moment, of the oscillating aerofoil, a UDF has been employed in 2D CFD oscillating aerofoil simulations. In UDF 4, a UDF has been employed in the 2D CFD oscillating aerofoil simulations in order to replicate the angle of attack motion of the H-type VAWT considering the Darrieus motion investigations at the selected tip speed ratio. In UDF 5, a UDF has been utilised in 2D CFD oscillating aerofoil simulations in order to consider the constantly-changing relative velocity.

UDF 1:

```
#include "udf.h"

DEFINE_SDOF_PROPERTIES(rotor, prop, dt, time, dtime)
{
   prop[SDOF_MASS]        = 0.213;
   prop[SDOF_IXX]         = 0.03;
   prop[SDOF_IYY]         = 0.03;
   prop[SDOF_IZZ]         = 0.03;

   prop[SDOF_ZERO_TRANS_X] = TRUE;
   prop[SDOF_ZERO_TRANS_Y] = TRUE;
   prop[SDOF_ZERO_TRANS_Z] = TRUE;

   prop[SDOF_ZERO_ROT_X] = TRUE;
   prop[SDOF_ZERO_ROT_Y] = TRUE;
   prop[SDOF_ZERO_ROT_Z] = FALSE;

   printf ("\n Blade updated 6DOF properties");
}
```

UDF 2:

```c
#include "udf.h"

DEFINE_SDOF_PROPERTIES(rotor, prop, dt, time, dtime)
{
    prop[SDOF_MASS]        = 0.213;
    prop[SDOF_IXX]         = 0.03;
    prop[SDOF_IYY]         = 0.03;
    prop[SDOF_IZZ]         = 0.03;

    prop[SDOF_ZERO_TRANS_X] = TRUE;
    prop[SDOF_ZERO_TRANS_Y] = TRUE;
    prop[SDOF_ZERO_TRANS_Z] = TRUE;

    prop[SDOF_ZERO_ROT_X] = TRUE;
    prop[SDOF_ZERO_ROT_Y] = TRUE;
    prop[SDOF_ZERO_ROT_Z] = FALSE;

    prop[SDOF_LOAD_M_X]    = 0;
    prop[SDOF_LOAD_M_Y]    = 0;
    prop[SDOF_LOAD_M_Z]    = -0.002*DT_OMEGA_CG(dt)[2];  /* variable
resistive torque */

    printf ("\n Blade updated 6DOF properties");
}
```

UDF 3:

```c
/*******************************************************
UDF to define the angular velocity of the oscillating wing
********************************************************
omega= pitching rate
thetamax= pitching amplitude
w= angular frequency, 2*pi*f
********************************************************/
#include "udf.h"
DEFINE_TRANSIENT_PROFILE(angular_velocity,time)
{
real omega;
double thetamax=15*M_PI/180 , w=2*14*0.1/0.15;
omega =-1*thetamax*(w)*cos(w*time);
return omega;
}
```

UDF 4:

```c
/*******************************************************
UDF to define the angular velocity of the oscillating wing
********************************************************
omega= pitching rate
thetamax= pitching amplitude
w= angular frequency, 2*pi*f
********************************************************/
#include "udf.h"
DEFINE_TRANSIENT_PROFILE(angular_velocity,time)
```

```
{
real omega;
double TSR=2.5 , w=2*3.9*0.1/0.15;
omega =-1*w*(1+TSR*cos(w*time))/(1+2*TSR*cos(w*time)+TSR*TSR);
return omega;
}
```

UDF 5

```
/************************************************************************
   Transient UDFs inlet velocity profile and for AoA function
 ************************************************************************/

#include "udf.h"

#define TSR 2.5     /* constants , tip speed ratio*/
#define w 9.33334


DEFINE_TRANSIENT_PROFILE(angular_velocity,time)
{
real omega;
omega =-1*w*(1+TSR*cos(w*time))/(1+2*TSR*cos(w*time)+TSR*TSR);
return omega;
}

DEFINE_PROFILE(unsteady_velocity, thread, position)
{
  face_t f;
  real t = CURRENT_TIME;
  real theta = w*t;
  begin_f_loop(f, thread)
    {
      F_PROFILE(f, thread, position) =
(7/2.5)*sqrt(1+pow(TSR,2)+2*TSR*cos(theta));
    }
  end_f_loop(f, thread)
}
```